Synthesis, Surface Engineering and Stability of CsPbX$_3$ (X = Cl, Br, I) and BaZrS$_3$ Perovskite Nanocrystals

A Thesis

Submitted in Partial Fulfillment of the Requirements

for the Degree of

Doctor of Philosophy

By

Vikash Kumar Ravi

(ID: 20142018)

IISER PUNE

Department of Chemistry,
Indian Institute of Science Education and Research (IISER Pune)
Pune, India - 411008

July 2020

DECLARATION

I declare that this written submission represents my ideas in my own words and wherever other's ideas have been included, I have adequately cited and referenced the original sources. I also declare that I have adhered to all principles of academic honesty and integrity and have not misrepresented or fabricated or falsified any idea / data / fact / source in my submission. I understand that violation of the above will cause for disciplinary action by the Institute and can also evoke penal action from the sources which have thus not been properly cited or from whom proper permission has not been taken when needed.
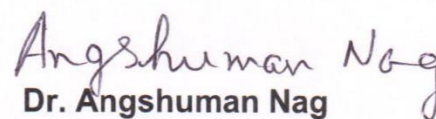
Date: 30th July 2020

Vikash Kumar Ravi

(ID: 20142018)

[III]

CERTIFICATE

This is to certify that this thesis entitled "**Synthesis, Surface Engineering and Stability of CsPbX₃ (X= Cl, Br, I) and BaZrS₃ Nanocrystals** " towards the partial fulfilment of the Integrated PhD dual degree programme at the Indian Institute of Science Education and Research, Pune represents original research carried out by Vikash Kumar Ravi at IISER Pune under my supervision. Part of the work was completed at Prof. Prashant Kamat's laboratory at the University of Notre Dame (USA) under the Bhaskara Advanced Solar Energy (BASE) fellowship. The work presented here or any part of it has not been included in any other thesis submitted previously for the award of any degree or diploma from any other university or institution.

Date: 30th July 2020

Angshuman Nag

Dr. Angshuman Nag

(Research Supervisor)

Acknowledgements

I would like to acknowledge and thank all the people that directly or indirectly have helped me in my PhD journey. This thesis is dedicated all those people who have positively impacted me at some or other point of time. While I cannot name all of you, I would like to say a big thank you to all of you. You all have "butterfly effect" effect on my career and I really owe every one of you.

First and foremost, I would like to thank my PhD mentor Dr. Angshuman Nag. I have learnt a lot from you about research and how to be more critical and rigorous towards any statement or data. I still remember the first time when I asked you to allow me to work in your group. I did not know anything about research back then (somewhat true for the present situation also) and still you gladly welcomed me in your lab. Slowly (sometimes too slowly) and gradually I learned, and I thank you for your motivation, guidance, patience and support during my research journey. I thank you for not being too hard on me even when I made a lot of mistakes. I really consider myself lucky, for the freedom you gave in choosing projects and having flexible working hours. You are the best mentor that a young researcher can ask for. I do hope that in my future labs and endeavour, I get to work with the same enthusiasm and freedom as in your lab.

I am grateful and lucky to work with talented labmates who not only taught me a lot but also kept me happy and energetic. In order of my interaction with those legends, I would like to mention some of them. Dr. Abhishek Swarnkar, you were my first point of contact in IISER and I learned a lot in all those projects that we completed together. Kiran Kadlag, if you are reading this, I really am grateful of you for helping me in the lab and getting things started. Dr. Jagadeesh Metikoti, I enjoyed a lot our singing session while working late hours in the lab. Dr. Shiva Shankar, I have fond memories of us cooking together or going out to have dinner (biryani was our soul food) or devoting our entire evening to badminton. Dr. Bharat Tandon, you are a gem of a person. Always ready to help and have so much confidence. Your advice is always great and I do hope that we keep in touch in future also. And not to forget, our underdog performance in IBL that led me addicted to badminton. Tariq Sheikh, you are such a calm person and sorted person. Last couple of years are memorable because of your biryani treats, cooking and cards playing and I thank you for that. Rayan Chakraborty, it is great that you are such an efficient multitasker. Then, there are new PhDs in our lab with whom I have spent past couple of years while sipping

tea and discussing what not. Arfin, Parikshit, Barnali and Taniya you all are fine researcher and I do know that you guys will do great. Parikshit especially, you interacted more with me and I thank you for helping in various experiments and being a co-author in of our paper.

I also had privilege of working with some talented postdocs. Dr. Ganesh Markad, thank you for teaching me cyclic voltammetry and all those tasty lunches that you had brought. Dr. Anuraj Kshirsagar, I hardly know you more than a year but I have learned a lot form you. Thanks for having useful discussion both related to scientific and non-scientific problems.

I also had the chance to interact with some of the project students mainly the BS MS students. Sajid, Shivam and Vaibhav, I interacted more with you guys because of the more time I had spent in lab and also thank you for being a co-author in our paper. Vaibhav, thank you for all motivation and help that led me to finish this thesis. I learned new things from you and also cherish your word of encouragement to finish writing the thesis.

I was a visiting research fellow at University of Notre Dame under Bhaskara Advanced Solar Energy Program (BASE). I thank Prof. Prashant Kamat for giving me an opportunity to work with him. I remember from the first day, the care you showed for me. Very little I realized, I was in foreign country and away from home. I still remember the sandwich lunches you used to bring me. I remember when you used to come in the lab and work with me (be it electrophoretic deposition or solar cell measurement). Your energy and enthusiasm regrading research are infectious and I hope I get some of that. And yes, coffee machine helped a lot. My colleagues there, Rebecca, Jeffrey, Olivia, Steven, thank you all for supporting and helping me whenever I needed. Also, a big thanks to Daniel, my landlord at South Bend, you are a great friend and especially great human being. You are the one who first introduced me to "Walk the Moon" concert and after that I am hooked. I also got influenced by you deep thoughts and cherish our heated discussions.

Outside lab, I want to thank some of my friends who kept me sane during my PhD and when I was at a very low point. Sarang, Deepak, Punita, Saurabh, Abhijit, Yashwant, you all have impacted me positively at some or other point of time at IISER. My friends Sushant, Rahul, Vinit, talking to you all made me happy and gave me energy to go on. Sushant especially, you know how big positive impact our talk had on me. Our long

phone conversation (even when I was in US, time difference didn't matter) had motivated to keep me going. You were always with me even when I was down and depressed and encouraged me to finish. You believed in me when even I didn't. I really owe you for that.

With all this, I thank whoever is reading this for taking out your precious time and going through it. I hope that you would enjoy reading this thesis and would forgive me if any errors are there.

Dedicated to

To my family, your support means a lot

more than you know.

To Chanchal, you were my guiding light.

List of Abbreviations

ACN: Acetonitrile

CB: Conduction band

CBM: Conduction band minimum

Cs-Oleate: Cesium oleate

CV: Cyclic voltammetry

DC: Direct current

DFT: Density functional theory

DLS: Dynamic light scattering

DOSY = Diffusion ordered spectroscopy

ECM: Electrochemical

EDAX: Energy dispersive X-ray spectroscopy

EPD: Electrophoretic deposition

EQE: External quantum efficiency

ETL: Electron transport layer

FET: Field effect transistor

FF: Fill factor

FFT: Fast Fourier transform

FTIR: Fourier transformed infrared spectroscopy

FTO: Fluorine doped tin oxide

FWHM: Full width at half maximum

HTL: Hole transport layer

HRTEM: High resolution transmission electron microscopy

HWHM: Half width at half maximum

ICs: Integrated circuits

ITO: Indium doped tin oxide

J_{sc}: Short circuit current

LEDs: Light emitting diodes

MA: Methylammonium

MB: Methylene blue

MeAc: Methyl acetate

NCs: Nanocrystals

NHE: Normal hydrogen electrode

NIR: Near infrared

NMR: Nuclear magnetic resonance

NMP: N-methyl-2-pyrrolidinone

NOESY: Nuclear Overhausser effect spectroscopy

OA: Oleic acid

OAm: Oleylamine

OAmBr: Oleylammonium bromide

OLA$^+$: Oleylammonium

ODE: 1- Octadecene

PL: Photoluminescence

PLD: Pulsed layer deposition

PXRD: Powder X-ray diffraction

RB: Round bottom

RPM: Rotation per minute

SAED: Selected area electron diffraction

SEM: Scanning electron microscopy

TBAP: Tetrabutylammonium perchlorate

TBAHS: Tetrabutylammonium hydrogen sulfate

TBAPF$_6$: Tetrabutylammonium hexafluorophosphate

TCSPC: Time correlated single photon counting

TEM: Transmission electron microscopy

TGA: Thermogravimetric analysis

V$_{oc}$: Open circuit voltage

VB: Valence band

VBM: Valence band maximum

XPS: X-ray photoelectron spectroscopy

Zn(DDTC)$_2$: Zinc diethyldithiocarbamate

Synopsis

Synopsis

The main focus of this thesis is the nanocrystals (NCs) of cesium lead halide perovskites, $CsPbX_3$ (X= Cl, Br, I), which has received much attention in recent years, because of their defect tolerant nature and excellent optoelectronic properties. Their synthesis methodology is simple and forgiving where the high quality $CsPbX_3$ NCs can be synthesized even at room temperature. $CsPbX_3$ NCs shows a near unity photoluminescence (PL) quantum yield without requiring any surface treatment. This makes them attractive for application in optoelectronic devices, namely light emitting devices (LEDs), solar cells, and photodetectors. However, instability and lead toxicity issues have raised concern about their use in commercial applications. In this rapidly emerging field, the understanding about band edge energies, exciton transition probabilities, interaction between the NC surface and organic ligands and more importantly, solution of the instability issues of $CsPbX_3$ NCs was found to be inadequate in the literature. Therefore, experimental results presented in current thesis gives elaborative discussions on the above-mentioned important aspects of $CsPbX_3$ NCs.

This thesis starts by giving an introduction about the colloidal semiconductor NCs with a special attention to $CsPbX_3$ NCs. The current challenges that are faced by $CsPbX_3$ NCs are discussed along with the overview of our approach to address them. The knowledge of band edge positions and the absorption and emission probabilities across the edges is an important parameter for choosing semiconductor NCs for any application. These important optical parameters for $CsPbX_3$ NCs have been determined. Similarly, surface of a NC plays an important role in governing the optoelectronic properties. The inorganic surface composition and organic ligand binding mechanism on $CsPbBr_3$ NC surface are elucidated using variety of experimental techniques. Instability of $CsPbX_3$ NCs against reactive environments leads to unwanted anion exchange reactions, water and light induced degradation. These instability issues are addressed by encapsulating the $CsPbX_3$ NCs without negatively affecting the optical properties of pristine $CsPbX_3$ NCs. The toxicity of lead is also a challenge which demands exploration of non-toxic semiconducting materials. Chalcogenide perovskite like $BaZrS_3$ is a promising candidate and is considered an alternative to the $CsPbX_3$ perovskites as per

theoretical predictions. BaZrS$_3$ NCs are synthesized and then surface modified to made colloidal dispersion. These colloidal dispersion of BaZrS$_3$ NCs are then used for making thin film devices.

A brief overview of each of the chapter is given below:

Chapter 1: Introduction

Introduction of the thesis starts with a brief history of semiconductor and is followed by the discussion on their electronic band structure. Colloidal semiconductor NCs are then discussed with a focus on the inorganic and organic part of the NCs. Synthesis mechanism of colloidal NCs as proposed by LaMer is discussed in short. The semiconducting material of choice of this thesis work, i.e. CsPbX$_3$ perovskite NCs is introduced and the plausible reason for its defect tolerant nature is given. Subsequently, the various challenges faced by CsPbX$_3$ NCs are given which needs special attention to find commercial success. These challenges are in the form of anion migration or segregation and instability to water, heat and light exposure combined with the lead toxicity concern. Finally, scope of this thesis work is discussed by describing importance of relevant optical parameters and plausible ways to solve some of the instability issues of CsPbX$_3$ NCs.

Chapter 2: Band Edge Energies and Excitonic Transition Probabilities of CsPbX$_3$ (X = Cl, Br, I) Nanocrystals

This chapter discusses about how the halide (X) compositions in CsPbX$_3$ NCs control the band edge energy positions and the excitonic transition probabilities between the band edges. Cyclic voltammetry technique is employed to show that the valence band maximum (VBM) shifts significantly to higher energies by 0.80 eV, upon going from X = Cl to Br to I. Whereas shift in the conduction band minimum (CBM) is small (0.19 eV) but systematic. This trend confirms that the halides contribute more to VBM. Their contribution to CBM was less, but definitely not negligible. Excitonic transition probabilities for both absorption and emission of visible light decreases probably because of the increasing dielectric constant from X = Cl to Br to I.

Chapter 3: Mechanism of Ligand Binding on the Surface of CsPbBr$_3$ Perovskite Nanocubes

In this chapter, we focused on the understanding of the inorganic and organic surface composition of CsPbBr$_3$ nanocubes. We have used synchrotron-based X-ray photoelectron spectroscopy (XPS) to understand the inorganic surface composition of the CsPbBr$_3$ nanocubes. Nuclear magnetic resonance (NMR) spectroscopy was employed to characterize the organic ligands present on their surface. We find that the oleylammonium ions acts as capping ligands by substituting some of the Cs$^+$ ions from the surface of CsPbBr$_3$ nanocubes. The origin of this substitution mechanism is in stark contrast to the more common adsorption binding mechanism of organic ligands on the surface of typical NCs.

Chapter 4A: Capping of CsPbX$_3$ (X = Cl, Br, I) Nanocrystals by PbSO$_4$-Oleate to Suppress Anion Exchange

In this chapter, a strategy to encapsulate CsPbX$_3$ NCs by PbSO$_4$-Oleate has been shown. This capping successfully suppresses the halide ion exchange between two or more CsPbX$_3$ NCs having different halide (X) compositions. Taking CsPbBr$_3$ and CsPbI$_3$ NC as examples, it has been shown that the pristine NCs, when mixed, undergoes halide ion exchange confirmed by change in absorption and PL spectra. However, capping of CsPbBr$_3$ and CsPbI$_3$ NCs by PbSO$_4$-Oleate suppressed the halide ion exchange when they are mixed together. Further, these capped CsPbX$_3$ NCs are electrophoretically deposited on the FTO/TiO$_2$ electrodes which gives a very simple way to make films having controlled thickness. Different halide compositions of CsPbX$_3$ NCs can be mixed to give gamut of emission including white light both in colloidal dispersion as well as in films.

Chapter 4B: CsPbBr$_3$/ZnS Core/Shell Type Nanocrystals for Enhanced Water Stability

In this chapter, first a strategy is developed to stabilize the CsPbBr$_3$ NCs dispersion under high temperature (~ 180 °C), so that it can be further processed for making core/shell heterostructures. Then, the already prepared CsPbBr$_3$ NCs serving as "seeds" are used to synthesize CsPbBr$_3$/ZnS core/shell type nanostructure *via* treatment with a single molecular precursor namely, zinc diethyldithiocarbamate.

CsPbBr$_3$/ZnS core/shell type nanostructure has been synthesized that showed enhanced water- and photo- stability. Understanding of the band structure suggests the formation of pseudo type II CsPbBr$_3$/ZnS core/shell type nanostructure where electron wavefunction gets confined within the core while hole wavefunction is delocalized over core and shell.

Chapter 5: Colloidal BaZrS$_3$ Chalcogenide Perovskite Nanocrystals for Thin Film Device Fabrication

In this chapter, BaZrS$_3$ NCs are first prepared using a solid-state synthesis route, and the subsequent surface modifications lead to colloidal dispersion of NCs in both polar N-methyl-2-pyrrolidinone and non-polar chloroform solvents. Colloidal BaZrS$_3$ NCs in chloroform are then used to make field effect transistors showing ambipolar properties with hole mobility 0.059 cm^{2}V^{-1}s^{-1} and electron mobility 0.017 cm^{2}V^{-1}s^{-1}. The NCs exhibit thermal (15 – 673 K) and aqueous stability confirmed by high temperature X-ray diffraction pattern and dye degradation of methylene blue in aqueous system. This first report of solution processed chalcogenide perovskite thin film with reasonable carrier mobility and strong optical absorption and emission, is exciting for application of these material in optoelectronic devices.

Thesis Summary and Future Directions

In this section, a summary of this thesis is given and the major findings are highlighted. Future research directions are also proposed based on Chapter 4 and Chapter 5 of this thesis. Encapsulation method developed for CsPbX$_3$ NCs can pave its use for application in blue LEDs or photocatalysis which still remains challenging problem for perovskite researchers. Also, the development of size and shape controlled colloidal BaZrS$_3$ NCs can find its application for various optoelectronic applications including solar cells.

Chapter 1. Introduction to Colloidal Semiconductor and Lead Halide Perovskite Nanocrystals

Chapter 2. Band Edge Energies and Excitonic Transition Probabilities of CsPbX₃ (X = Cl, Br, I) Perovskite Nanocrystals

Chapter 3. Mechanism of Ligand Binding on the Surface of CsPbBr₃ Perovskite Nanocubes

Chapter 4A. Capping of CsPbX₃ (X = Cl, Br, I) Nanocrystals by PbSO₄-Oleate to Suppress Anion Exchange

Chapter 4B. CsPbBr$_3$/ZnS Core/Shell Type Nanocrystals for Enhanced Water Stability

Chapter 5. Colloidal BaZrS$_3$ Chalcogenide Perovskite Nanocrystals for Thin Film Device Fabrication

Chapter 1

Introduction to Colloidal Semiconductor and

Lead Halide Perovskite Nanocrystals

1.1 A brief history of semiconductors:

A semiconductor in its pristine condition does not conduct electricity, which can be referred as off state. But a small perturbation, be it in form of applied electrical bias, or light, or some kind of doping, increases the electrical conductivity by many orders of magnitude (termed as on state). This highly sensitive on-off state modulation by a small external perturbation makes semiconductor a special and interesting class of material. In contrast, metals remain largely in the on state and insulators largely remain in the off state. Figure 1.1 shows this behaviour for a typical semiconductor silicon, where conductivity can be varied by atleast 6 orders of magnitude by changing the doping concentration.
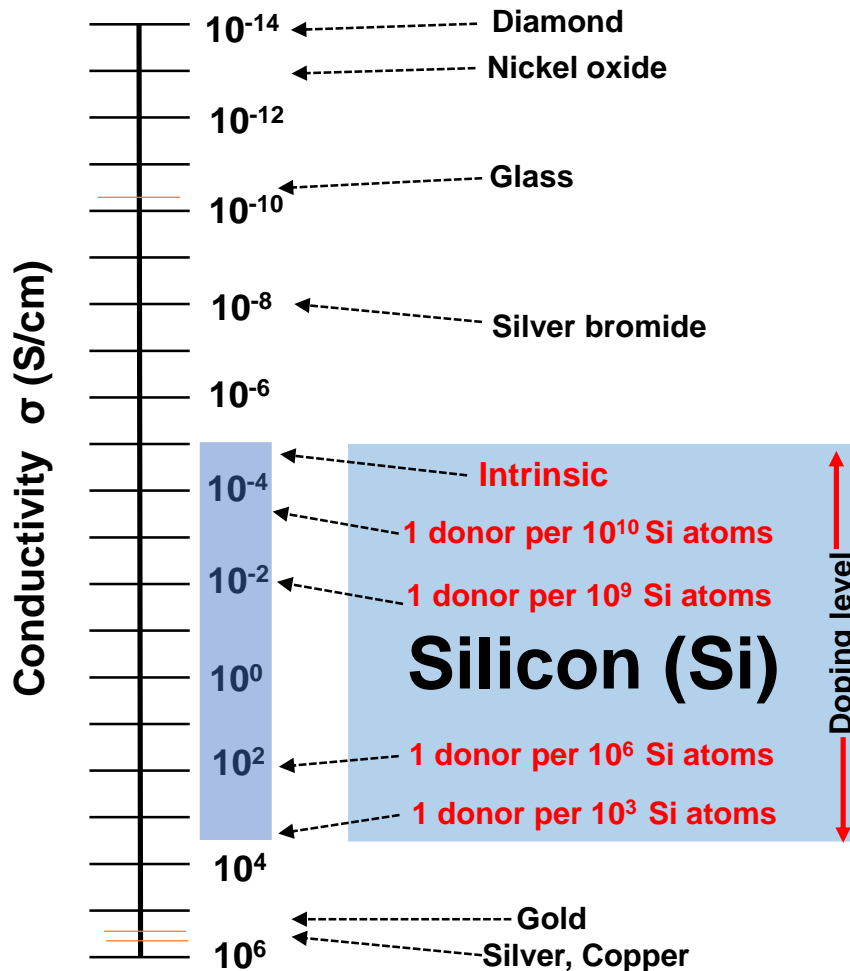

Figure 1.1: Electrical conductivities of pure and doped silicon are compared with the metals and insulators. The value for conductivity has been taken from reference[1].

"Semiconductor" word was first coined by Alessandro Volta in 1782[2] and the first-time semiconductor effect was observed and documented by Michael Faraday in

1833.[3] He noticed that the resistance of silver sulfide (Ag_2S) was decreased with increase of temperature which was different than the dependence of resistance in metals with temperature. Further work in 1874 by Karl Braun showed the rectifier effect of semiconductor.[4] In 1901, Jagdish Chandra Bose used a semiconductor device called "Cat Whiskers" for detection of radio waves.[5] Better understanding of semiconducting behaviour was developed after the Einstein's work on photoelectric effect[6] and the subsequent work by Wilson, Schottky and Mott. The first ever transistor was invented by John Bardeen, Walter Brattain and William Shockley at Bell Labs[7] in 1947 leading to their Nobel prize of Physics in 1956.[8, 9, 10, 11] The discovery of transistor brought the technological revolution leading to the smaller and cheaper inventions of computers, radios, smartphones among other things.

Semiconductors have impacted our life immensely finding its use in our daily lives from how we communicate to how we acquire energy. All the mobile phones, television, laptops have semiconductors in them and are essential for their working. Similarly, solar cell devices use semiconductor to convert light energy to electrical energy. Other applications of semiconductors are in field of lightning devices, catalysis etc. Before going further deeper into the thesis, we first must understand how semiconductor is different from metals and insulators by examining their electronic band structure.

1.2 Electronic structure of semiconductors:

To understand the optical and electronic properties of semiconductors, it is important to understand its electronic band structure that is derived from atomic orbitals. Bohr model of atoms states that, in an individual atom, electrons occupy different discrete energy levels known as orbitals (s, p, d, f). The outermost occupied orbital is known as valence orbital and they are mainly responsible for an element's chemical property. When two identical atoms are brought close together, they interact and the atomic orbitals overlap, causing formation of two molecular orbitals i.e. bonding (σ) and antibonding (σ^*) molecular orbitals. Similarly, for n atoms, n atomic orbitals overlap leading to formation of band (because energy levels are now very closely spaced) as shown in Figure 1.2. Valence orbitals overlap to form valence band while the band just above that is called conduction band. It is called conduction band because the electrons in the conduction band are free to move

and conduct heat and electricity. Electrons from valence band can be excited to conduction band either through light, heat or electrical perturbation.
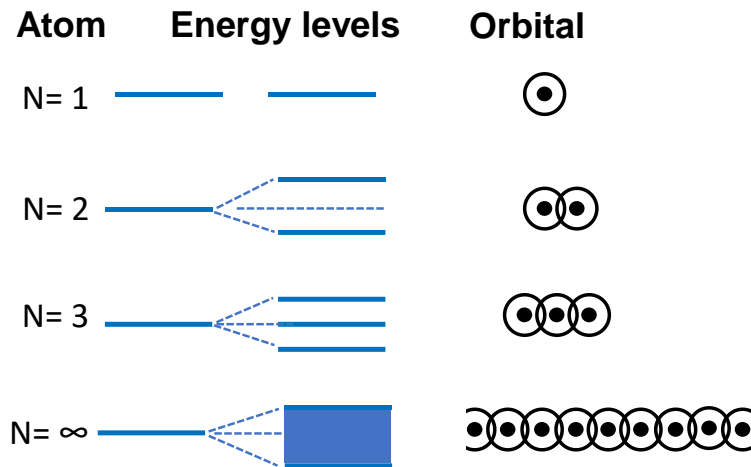
Figure 1.2: Schematic of splitting of energy level when two or more atoms combine.

The energy difference between the valence band edge (maximum) and conduction band edge (minimum) is called bandgap. Figure 1.3a and 1.3b shows the occupied valence and unoccupied conduction band formed by the valence orbitals for the case of Si and CdS semiconductors respectively. In case of Si, outermost 3p orbitals overlap to form valence band having bonding nature (lower in energy) and conduction band having antibonding nature (higher in energy). Similarly, in case of CdS, 5s orbitals of Cd and 3p orbitals of S, hybridize and form valence band and conduction band.
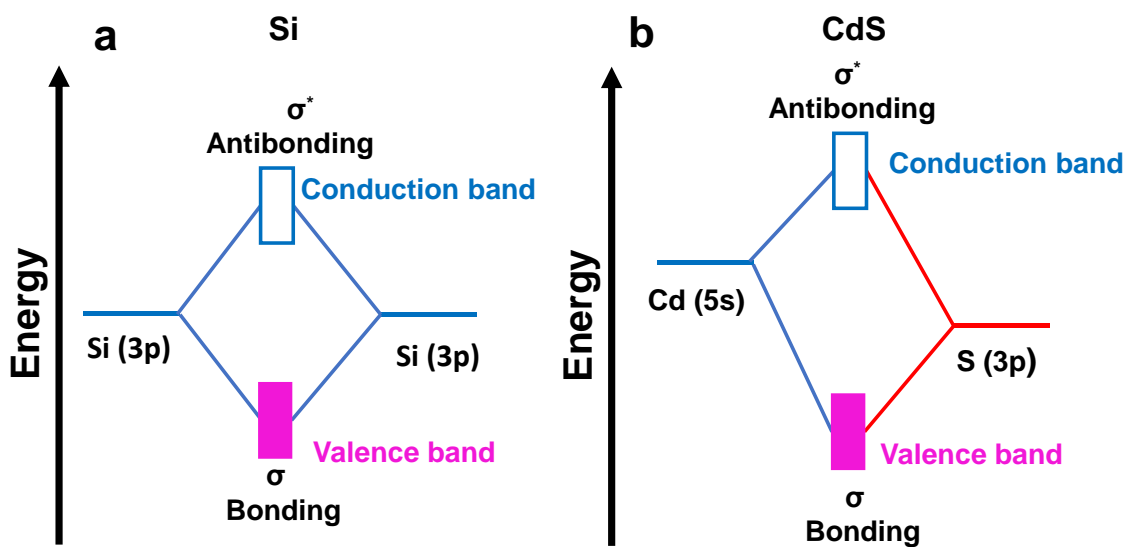
Figure 1.3: Simplified molecular orbital diagram for (a) covalent Si semiconductor (b) binary CdS semiconductor.

Depending on the electronic structure of a material, it can be divided into metals and non-metals as shown in Figure 1.4. In a metal, the Fermi energy level (E$_f$) resides inside a band whereas in non-metals like semiconductors and insulators, E$_f$ resides in the bandgap region. Typically, bandgap (E$_g$) of insulators are higher than semiconductors (E$_g$ > 4 eV for an insulator).
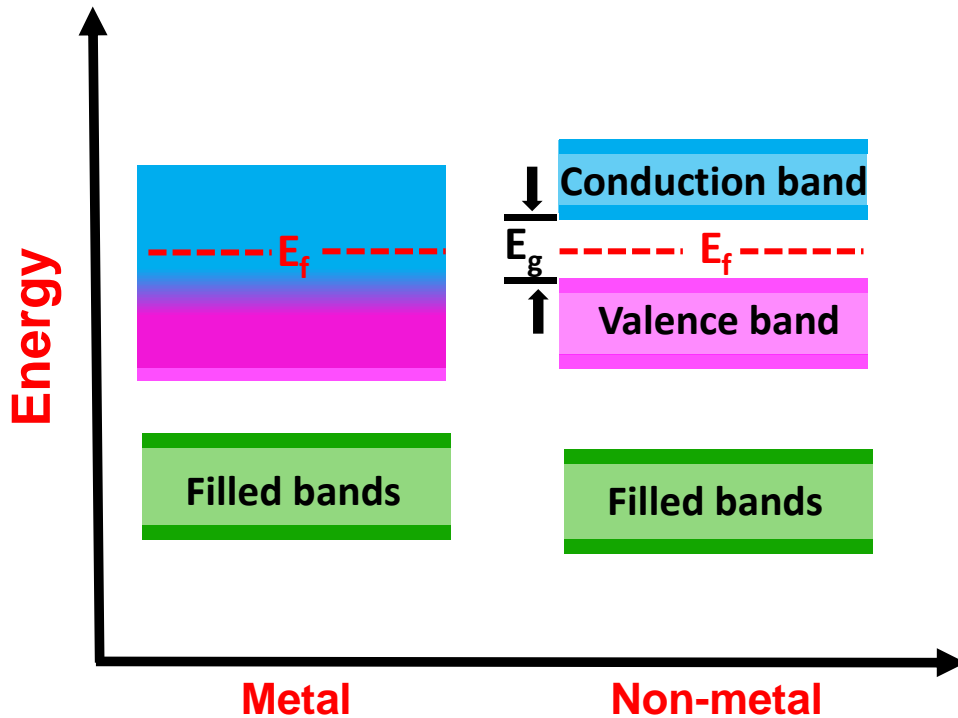
Figure 1.4: Schematics showing electronic band structures of metal and non-metal.

The Fermi level (E$_f$) is defined as the energy level where the probability of finding the electrons is 50 %. The probability of finding an electron at an energy level "E" is given by Fermi-Dirac distribution, $f(E) = \frac{1}{1+e^{(E-E_f)/k_BT}}$, where E$_f$ is the Fermi energy, T is the temperature and k_B is the Boltzmann constant. The electron population is then given as product of Fermi-Dirac function and the density of states at that energy level. At T = 0 K, density of states is 0 at the Fermi level of semiconductors and insulators. So, there is no electron at the Fermi level of a semiconductor at 0 K. When T > 0 K, then there is a finite value of f(E) near the conduction band minimum. An increase in T increases the f(E) and therefore increasing the electrical conductivity of non-metals. Also, at a given T, a decrease in bandgap increases the f(E) near the conduction band minimum. So, electrical conductivity of lower bandgap non-metals (semiconductors) are usually higher than that of wider bandgap non-metal (insulators).

The most popular semiconductor is silicon that is majorly used in electronic components like integrated circuits (ICs). Also, the solar cell industry is largely based on silicon. This is attributed to the excellent electronic properties of the silicon. The natural abundance of silicon and its minimal toxicity have propelled semiconducting industries to be based around silicon.

However, silicon is not suitable in all the cases. First, for excellent semiconducting properties of silicon, it needs to be defect free and that demands very high-quality silicon crystals which are very expensive to process. More importantly, silicon has an indirect bandgap of around 1.1 eV. Having an indirect bandgap means it is not as efficient in absorbing light and emitting light. It cannot be used for display devices which require high photoluminescence (PL). The thickness of silicon material required to capture solar light will be more than other direct bandgap material having same bandgap. Also, 1.1 eV bandgap corresponds to infrared photons and thus to emit color in visible region, wider direct bandgap material is required like GaN, CdS, ZnS.

1.3 Semiconductor nanocrystals (NCs):

There is a famous saying by Nobel laureate Richard Feynman that "There is plenty of room at the bottom". What he meant by that statement is the exciting properties and applications of a material has, when it is reduced to smaller size. As semiconductor size gets decreased, a major change in the electronic structure and properties begins to happen. The continuous valence and conduction bands begin to have more and more discrete energy levels as the size gets decreased (Figure 1.5). Also, the bandgap of the semiconductor starts to widen resulting in blue shift in absorbance and emission spectra. This effect is known as quantum confinement effect and is more pronounced when the size of the NCs approaches a certain size called exciton Bohr radius. Absorption of light excites an electron from valence band to conduction band, leaving behind a hole in the valence band. This electron and hole are bound to each other by Coulomb force. Such electron-hole pairs are called excitons. Exciton Bohr radius is then defined as the natural distance between the bound electron and hole. As the size of semiconductor gets smaller than the exciton Bohr radius, the electron and hole are not able to maintain themselves far apart as they would prefer in a normal situation. This physical confinement is called quantum

confinement. Spherical semiconductor NCs showing such quantum confinement are called quantum dots.
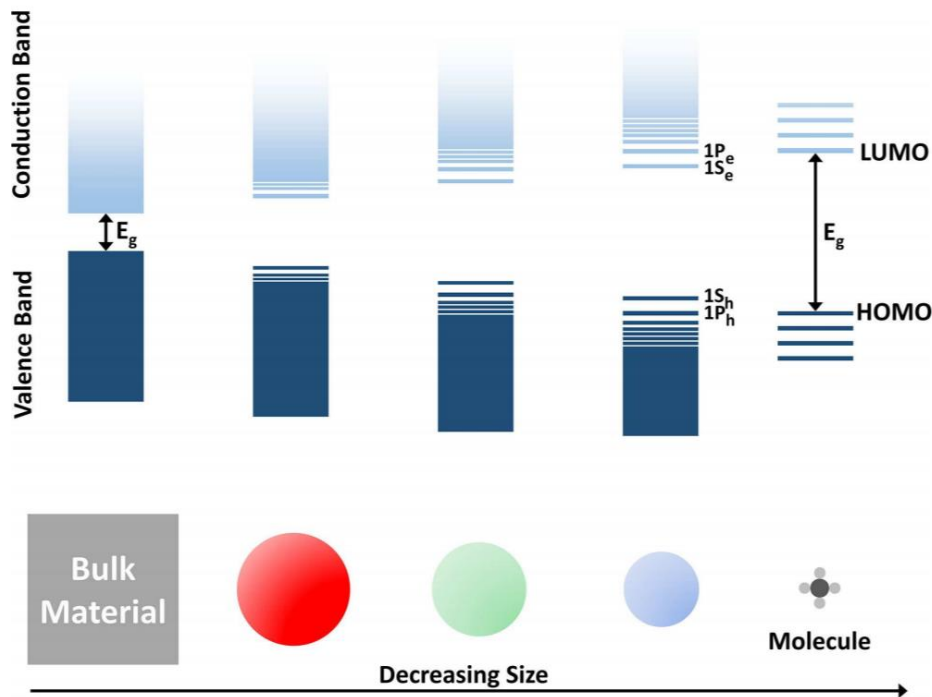
Figure 1.5: Schematics of electronic energy states, as the size of a semiconducting materials gets reduced from bulk to NC to molecule. Adapted from reference[12] with permission. Copyright © 2019, John Wiley and Sons.

Exciton Bohr radius vary from semiconductor to semiconductor like CdS has exciton Bohr radius of 2 nm while PbTe has exciton Bohr radius of 104 nm.[13] The formula for exciton Bohr radius (r_B) is: $r_B = \varepsilon_r \frac{m_o}{\mu} a_0$ where ε_r is dielectric constant of the semiconductor, m_o is the rest mass of the electron, μ is the reduced mass of exciton ($\frac{1}{\mu} = \frac{1}{m_e^*} + \frac{1}{m_h^*}$; where m_e^* and m_h^* are effective mass of electron and hole respectively) and a_o is the Bohr radius of hydrogen atom (0.053 nm). When the size of a NC becomes smaller than the r_B, excitons are spatially confined analogous to particle in a box model which also causes an increase in energy,. Here the particle would be exciton and box would be the NC. Thus, the increased bandgap for a semiconducting spherical NC is given by Brus-Kayanuma[14] equation:

$$E_{QD} = E_{gap} + \frac{h^2}{8r^2}\left(\frac{1}{m_e^*} + \frac{1}{m_h^*}\right) - \frac{1.786\,e^2}{4\pi\varepsilon_o\varepsilon_r r} - 0.248\,(E * R_y)$$ where E$_{QD}$ is the bandgap of the quantum dot having radius r and bulk bandgap of E$_{gap}$, $E * R_y$ is the Rydberg energy. The first term of the right-hand equation gives the bulk bandgap of the

material. The second term gives increase in energy due to the quantum confinement effect. The third subtractive term accounts for the Coulombic interaction energy of exciton while the fourth term stands for the spatial correlation effect and can be neglected for low dielectric materials. This equation is based on effective mass theory approximation and often fails in case of very small NCs.

Confinement of an exciton in a semiconductor can be in one, two, or all three spatial dimensions. If the exciton is confined in one direction meaning one of its physical size is less than r_B then it would be termed as nanosheet, while confinement in two dimensions give rise to quantum wire. If the semiconductor is confined in all three directions it is termed as quantum dots or 0D material. A Semiconductor not confined to any spatial dimension is considered as bulk material. The density of states (DOS) varies as the confinement of exciton varies. Figure 1.6 shows the DOS as the dimension of the material changes resulting in various degrees of confinement for the exciton.
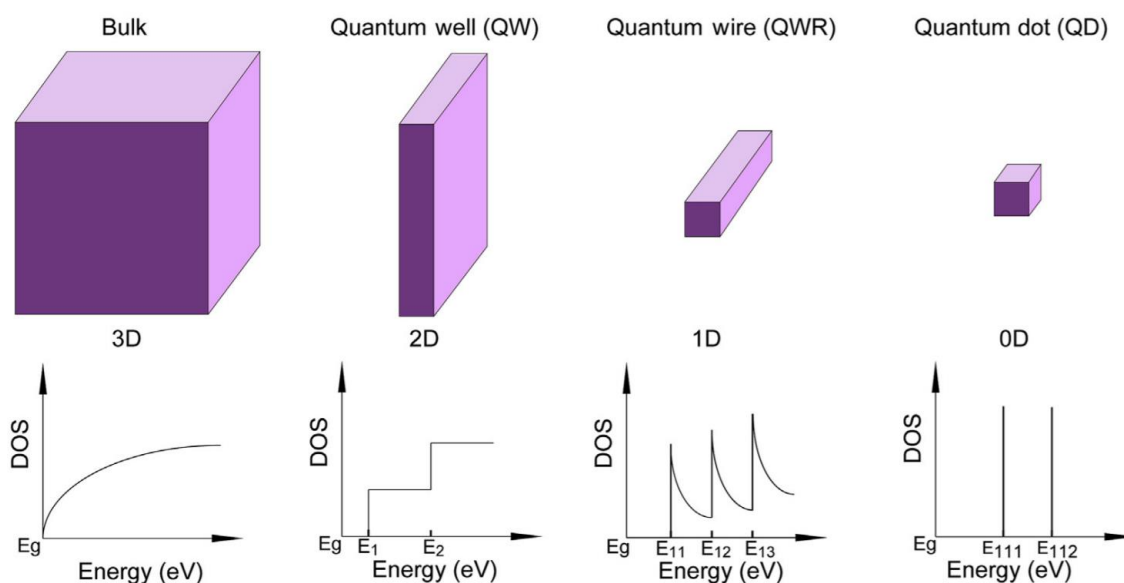
Figure 1.6: Schematic of bulk (3D), quantum well (2D), quantum wire (1D) and quantum dot (0D) and its corresponding density of states (DOS). Adapted from reference[15] with permission. Copyright © 2015, Elsevier.

1.4 Colloidal semiconductor NCs:

Semiconductor NCs properties do not only depend on the composition but also on the size, shape and its surface structure. Therefore, control over the synthesis to obtain high quality NCs is desired. High quality mainly refers to the NCs having very low density of charge trap carriers and monodispersed size.

The semiconductor NCs that are often synthesized by liquid phase method and forms a stable colloidal dispersion in a liquid solvent are referred to as colloidal semiconductor NCs. Colloidal NCs provide atomic level control of the size of a NCs, therefore, size dependent properties like reduction in melting temperature, increase in the bandgap and other parameters can be greatly controlled by tuning the size of NCs. For example, as the semiconductor NC size decreases, the luminescence efficiency increases because of strong electron and hole overlap which are then suited for light emitting applications. In addition to that, colloidal semiconductor NCs offer way of very inexpensive device fabrication by spray painting or inkjet printing. These are also scalable meaning it can be made on large scale. One of the most important advantage is that colloidal form of semiconductor NCs allows to have thin film devices on flexible substrate. Flexible devices are needed for many applications like as wearable on our hand or clothes.

The colloidal NCs typically consist of two parts: i) a semiconducting inorganic core ii) organic ligand shell (Figure 1.7). So, the optoelectronic properties are not only dependent on the composition of the semiconductor but also on the ligand shell present on the NC surface.
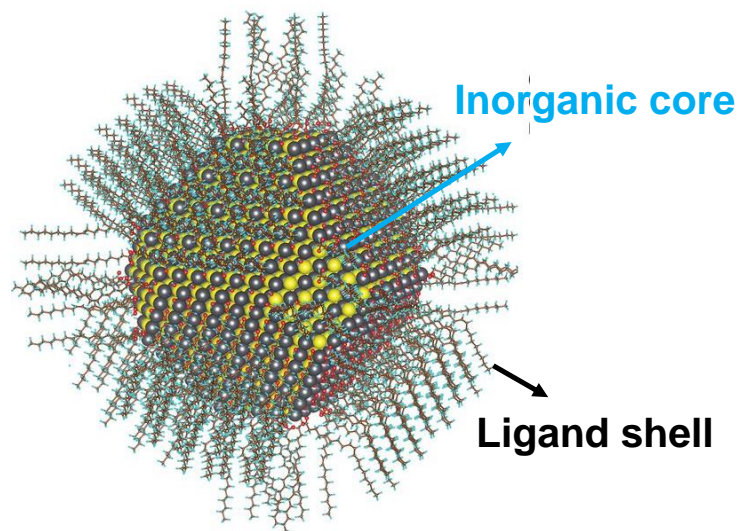
Figure 1.7: Atomic structure of 5 nm diameter NC having PbS as core and oleate and hydroxides as ligands. Adapted from reference[16] with permission. Copyright © 2014, American Association for the Advancement of Science.

a. The inorganic core

Inorganic core of semiconductor can be simple semiconductor like Si, CdS, PbS or more complex like $CuInS_2$, $CsPbBr_3$ or even $Cu_2ZnSnSe_4$. The core can also be of

type where two or more semiconductors combine. These are called heterostructures NCs. In the heterostructures NCs, it can be of type, Janus NC (segmented NC), or core/shell NCs (Figure 1.8). In a Janus NC, the NC contains two separate semiconductor parts. In a core/shell NC, one semiconductor is covered with another semiconductor. The advantage of having heterostructure is that it can impart multiple functionalities to a single NC and also in some cases can stabilise the NC. This stabilization of NC can be in metastable state or protection from external reactive environment.[17-19]
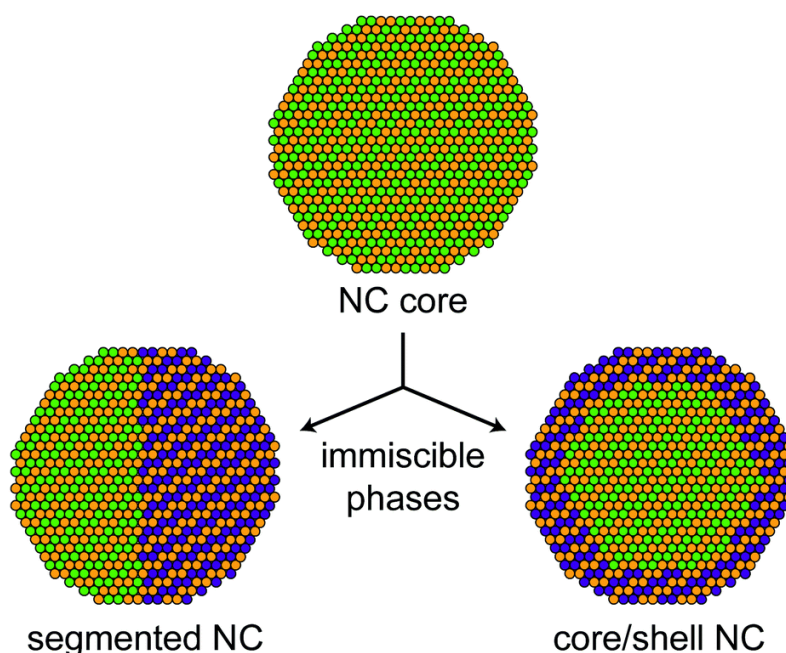
Figure 1.8: Segmented (Janus) NC and core/shell NC obtained from the cation exchange of a core NC. Adapted from reference[20] with permission. Copyright © 2018, Royal Society of Chemistry.

Core/shell NCs structure are important class of heterostructure NCs. Figure 1.9 shows different type of core/shell structures for a semiconductor. Type I core/shell structure refers to the band structure where core valence band maxima (VBM) and conduction band minima (CBM) lies within the VBM and CBM of shell material. Here both electron and hole wavefunctions get confined to the core material. Here, the shell material is of higher bandgap than the core material. These type I core/shell NCs are one of the brightest emitting materials as the surface defects of core are now passivated. In reverse type I core/shell material, the shell bandgap is lower than the core bandgap and the VBM and CBM of the shell lies in between the CBM and VBM of the core material. Here both electron and hole wavefunctions get

confined to the shell material and thus they are desirable for charge carrier separation and find their use in photocatalysis etc. In type II core/shell semiconductor, there is an offset between the CBM or VBM of core and shell semiconducting materials. This type of band alignment helps in the separation of charge carrier and therefore important for applications like photovoltaics etc. Here, either electron or hole wavefunction gets confined to the core while the other one goes to shell material. This causes an increase in radiative recombination lifetime as effective overlap between the electron and hole wavefunction have decreased. In pseudo Type II core/shell NC, either CBM or VBM of shell is close to the CBM or VBM of the core resulting in one of the charge carrier wavefunction spread out to both core and shell material. This also decreases the effective overlap of electron and hole wavefunction resulting in the increase in PL lifetime.
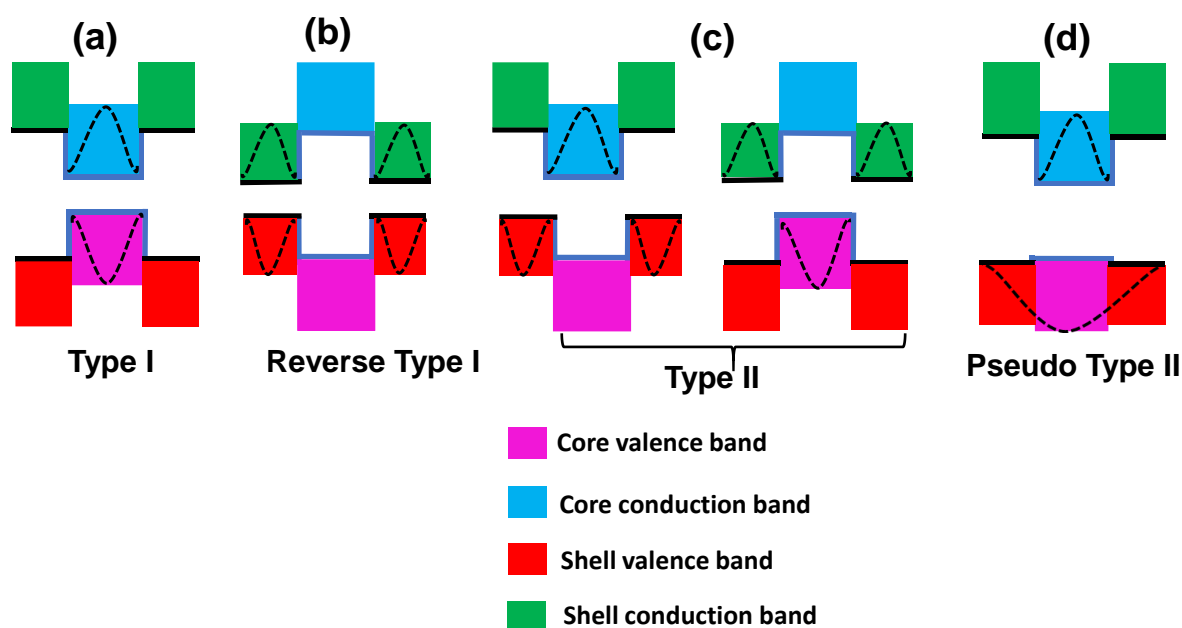
Figure 1.9: Schematic diagram of core/shell NCs of various types (a)Type I NC: both electron and hole wavefunctions get confined in the core (b) Reverse Type I NC: both electron and hole wavefunctions get confined to the shell (c) Type II NC: either electron or hole wavefunction gets to shell while the other remained in core causing separation of electron and hole wavefunction. (d) Pseudo Type II NC: either electron or hole wavefunction gets delocalized over both core and shell while other one gets confined to the core.

Core/shell structure has various advantages like it protects the NCs towards external environment like heat, light, oxygen, moisture etc. As shown in Figure 1.9, choosing a specific shell material for a core NCs, can tailor the application according to the needs. Further role of shell is in separating the charge carriers in the

semiconducting core depending on the band alignment of core shell structure. However, designing core/shell structure is not trivial and growing a shell on a core NC requires that core and shell have very little lattice mismatch. Also, the other problem that exists while growing shell material is the self-nucleation or formation of other heterostructures.

b. The ligand shell and its versatile role:

Molecules known as ligand are bound to the surface of the NC and are responsible for the solubility of the NCs in a given solvent. Ligands are very important for a NC because of their versatile role. It greatly influences the electronic, optical and catalytic properties of the NCs. Not only it does help in the solubility of NCs but also affects the growth and finally the shape and size of the NCs. The ligands can selectively bind to one of the facets, thereby reducing the energy of these facets relative to others. This selective binding of ligand to a facet, control the size of the NCs and give rise to different shape like rods and platelets.

However, ligands can also negatively impact the properties of the NCs. The ligands are generally long chain organic molecules present on the NC surface.[21, 22] These organic molecules are insulating in nature and thus hinder charge transfer between two NCs (in a film) separated by the organic ligands. Also, ligand act as poison for many catalytic activities because it can block the active sites on the NC surface. Usually post synthetic ligand treatments are performed where the long organic chain ligand is replaced with short chain ligands or with inorganic ligands. Also, methods like sintering (heating the NCs film) or treating the NCs film with a polar solvent can get rid of the ligand and make the NC film conductive. Therefore, understanding of the surface of the NC (composition and ligand binding) is of utmost importance for their utilization in any applications or devices. The ligands are broadly classified based on bonding nature with NCs surface as: X type, L type or Z type as shown in Figure 1. 10.[23, 24] L type ligands are neutral ligands where they donate electron to the metal atoms at the surface. Example include amies and phosphines. X type ligands are ionic ligands that bound to the NCs surface as ionic pairs. Examples are like ammonium bromide ($RNH_3^+Br^-$). Z type ligands are charge neutral ligand which accept electrons from non-metal atoms at the NCs surface. Example include cadmium chloride ($CdCl_2$) or lead oleate ($Pb(COOR)_2$).
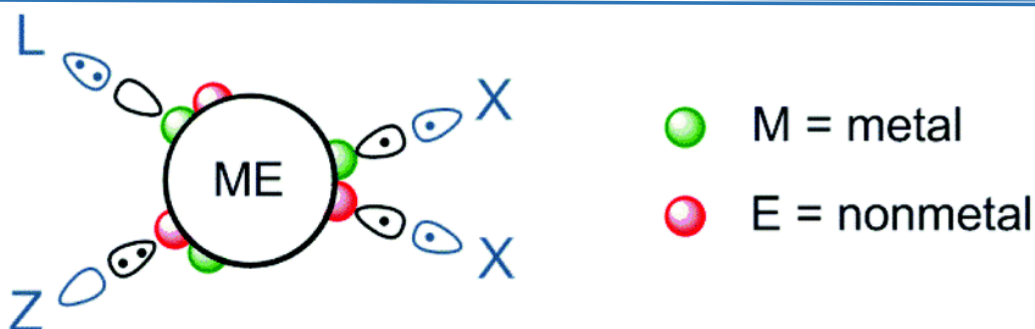
Figure 1.10: Classification of ligands as L, X and Z type. Adapted from reference[24] with permission. Copyright © 2016, Royal Society of Chemistry.

The ligand at the NCs surface not only required for making colloidal dispersion but also for passivating trap states. The trap states arise from the non-bonding orbitals of the under-coordinated surface atoms (dangling bonds). Ligands are needed to make the bonds with these undercoordinated surface atoms. This gives the electronic states which lies in the bandgap region of the semiconductor and which can trap charge carriers, electrons and holes. In a NC, due to its high surface to volume ratio, large number of atoms are present on the surface and so greater number of these trap states. Take the case of CdS semiconductor NC, where in an ideal case there are no electronic states in the bandgap region (Figure 1.11a). However, this situation is never realized in real life and the semiconductor NCs have lot of defects which contribute to the electronic states in between the bandgap region. Surface atoms on the NCs have different environment than the atoms in the core region. They are undercoordinated which results in weaker bonds as well as electronic states within the bandgap region. Such electronic sates in the bandgap region, traps the photoexcited electron or holes before they can combine radiatively. In Figure 1.11b, undercoordinated surface Cd^{2+} form empty electronic states below the conduction band and can trap electrons. Similarly, undercoordinated surface S^{2-} forms filled electronic states above the valence band and can trap holes. Therefore, it is extremely important for the NCs to passivate these defects by using appropriate ligand. Cd^{+2} electronic states need L type ligand (electron donating ligand) to hybridize with Cd^{+2} electronic states to give bonding orbital lower than valence band edge of CdS and antibonding orbital above than conduction band edge of CdS (Figure 1.11c). Similarly, S^{2-} electronic states need Z type ligand (electron acceptor ligand) to hybridize with and to give bonding and antibonding orbital outside of the bandgap region.
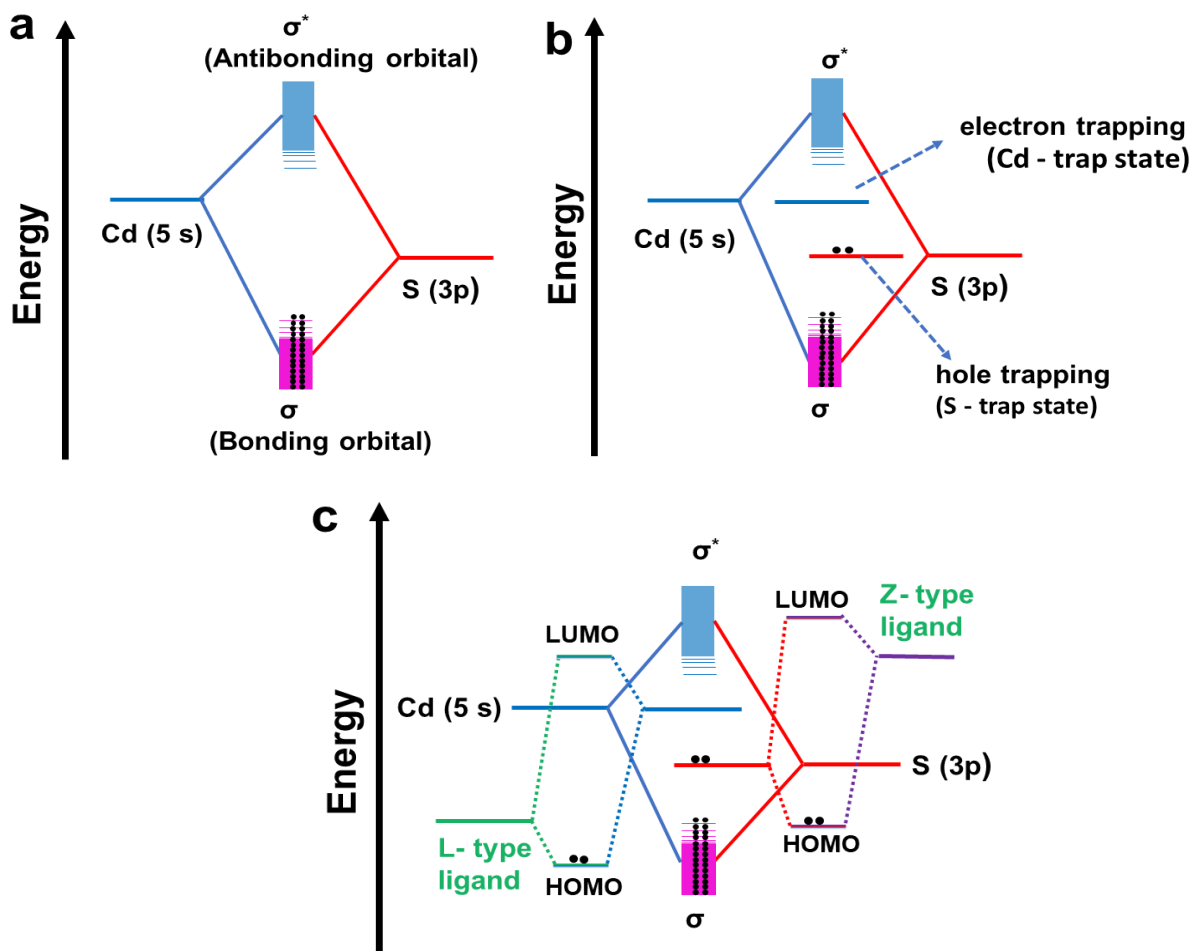
Figure 1.11: Schematic of electronic structure of (a) ideal CdS semiconductor (b) CdS having surface defect in the form of undercoordinated Cd and S electronic states (c) passivation by ligand to passivate the mid gap trap states.

1.5 Synthesis mechanism of colloidal NCs:

The synthesis of colloidal NCs can be done in either aqueous or organic medium, depending on the reaction solvent used for the synthesis. The aqueous synthesis has advantage of being environmentally friendly but it doesn't produce high quality NCs because of the moderate synthesis temperature used. The organic route to synthesize colloidal NCs are the most common and preferred one where high boiling solvent is employed. This usually gives rise to high quality NCs having excellent crystallinity, less defects and narrow size distribution. But the problem exists with the environmental concern of the organic chemicals employed for the synthesis.

The mechanism of NCs formation has three stages: monomer formation, nucleation, and growth. After the completion of the reaction, the NCs are washed and stored. Usually colloidal NCs synthesis is performed in a round bottom flask

having inert atmosphere (maintained through Schlenk line). Inert condition is maintained by applying alternate nitrogen and vacuum condition. This process ensures removal of oxygen and moisture from the reaction medium and precursor. It is necessary because NCs are prone to oxidation and it quench the PL properties of the NCs.

a. Monomer formation: Monomer formation involves reaction of metal or non-metal salts to form complexes. Commonly, metal salts like acetates, halides or oxides and non-metals like sulphur, tellurium, bromide, etc. are complexed with organic molecules like oleic acid, oleylamine at high temperature (> 100 °C) to give the corresponding complex. Sometimes other precursor like dodecanethiol, zinc diethyldithiocarbamate, benzylhalides etc. are also used which do not require complex formation.[25-27]

b. Nucleation: In the nucleation step, monomers react to form cluster and then to nuclei. Nuclei is defined as the smallest size cluster that can grow to be a crystal. Thus, nucleation is the step where the nuclei formation happens that serves as seeds for the growth of the crystal. Most common method to prepare nuclei is by hot injection method. In hot injection method, one of the precursors is injected into the reaction mixture at a high temperature (100- 300 °C). Hot injection method gives a way to separate nucleation and growth and thus gives better control over size and shape of NCs but it has a disadvantage of large scalability and reproducibility. Other method involves heat up synthesis where all the precursors are mixed and they are heated at desired temperature and the nucleation happens. Heat up synthesis method is more reproducible and scalable but it has size distribution problem as well as application are limited to growth of complex composition NCs.

c. Growth: After nuclei reaches a certain critical size it doesn't redissolve in the reaction medium and starts to form smaller crystals or NCs. Growth happens where bigger NCs grow on the expense of smaller NCs which is known as Ostwald ripening.[20] This is also the step where the size and the shape of the NCs are determined.

After the completion of the reaction (reaching desired shape or size), the growth is stopped by either cooling with ice bath or by injecting solvent from room temperature to this high temperature reaction medium. Fast cooling of NCs reaction medium is required to stop the NCs from further growing and thus maintain narrow size

distribution. The NCs are then purified by centrifuging the crude product and throwing out the supernatant and keeping the precipitate. The precipitate which is mostly NCs along with unreacted solvent and precursor, is further washed with a mixture of nonpolar (say hexane) and polar (say 1-butanol) solvent. Finally, the purified NCs are then stored in non-polar solvent like hexane or toluene for further use.

A more physical view of the mechanism of colloidal NCs is proposed by LaMer in 1950 (shown in Figure 1.12). According to that, upon reaction, there is increase in the concentration of monomers until the point it reaches supersaturation (Figure 1.12, stage I). After reaching the supersaturation concentration the solution becomes thermodynamically unstable and fast nucleation happens thereby reducing the monomer concentration and degree of supersaturation (figure 1.12, stage II). Then the growth of the nuclei happens by different mechanism like diffusion growth where the monomers are added to the already formed nuclei or by Ostwald ripening (figure 1.12, stage III), where the smaller NCs dissolve and bigger NCs grow or by coalescence where multiple nuclei come together and grow.
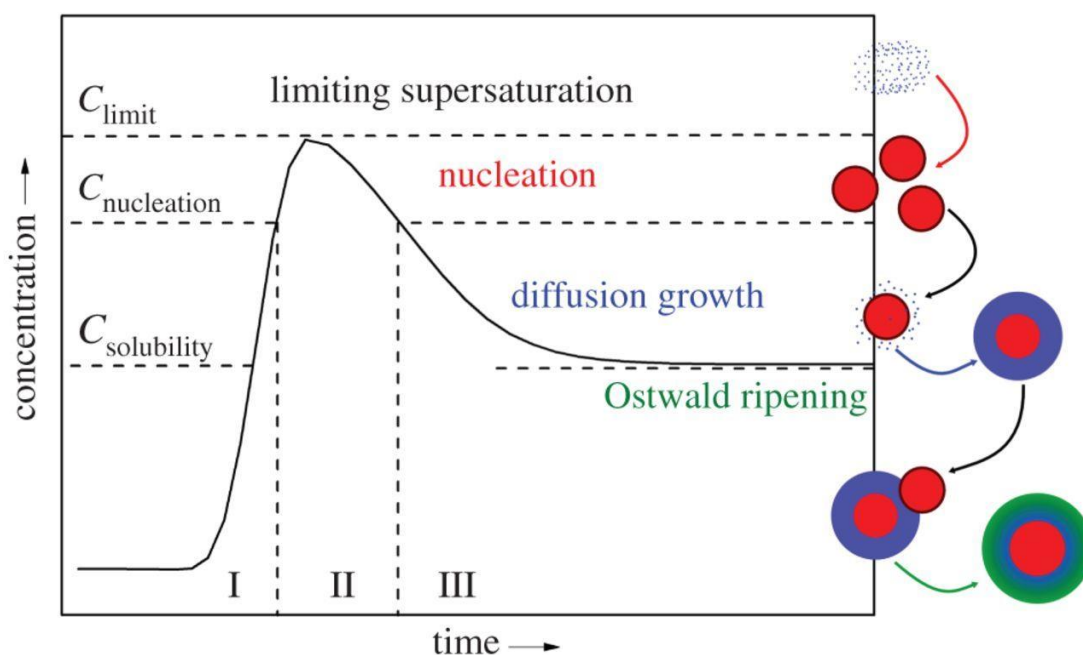
Figure 1.12: Schematic of growth model of colloidal NCs as proposed by LaMer. Adapted from reference[28] with permission. Copyright © 2015, Royal Society of Chemistry.

With this learning about the colloidal semiconductor NCs, we introduce the semiconducting material of choice in this thesis i.e. cesium lead halide perovskite,

$CsPbX_3$ (X = Cl, Br, I) NCs. Majority of the thesis work and hence the subsequent chapters are focussed on $CsPbX_3$ and barium zirconium sulfide chalcogenide, $BaZrS_3$ perovskite NCs. The challenges that these $CsPbX_3$ NCs face towards their commercial success along with the strategy developed to address some of them are discussed in this PhD thesis work.

1.6 Introduction to lead halide perovskite:

Perovskite is the crystal structure of the mineral $CaTiO_3$ i.e. of formula ABX_3. Here, A and *B* are cation and X is an anion. *B* cation and X anion forms an interconnected octahedra while A cation sits in the cavity formed by the BX_6 interconnected octahedra as shown in Figure is 1.13.
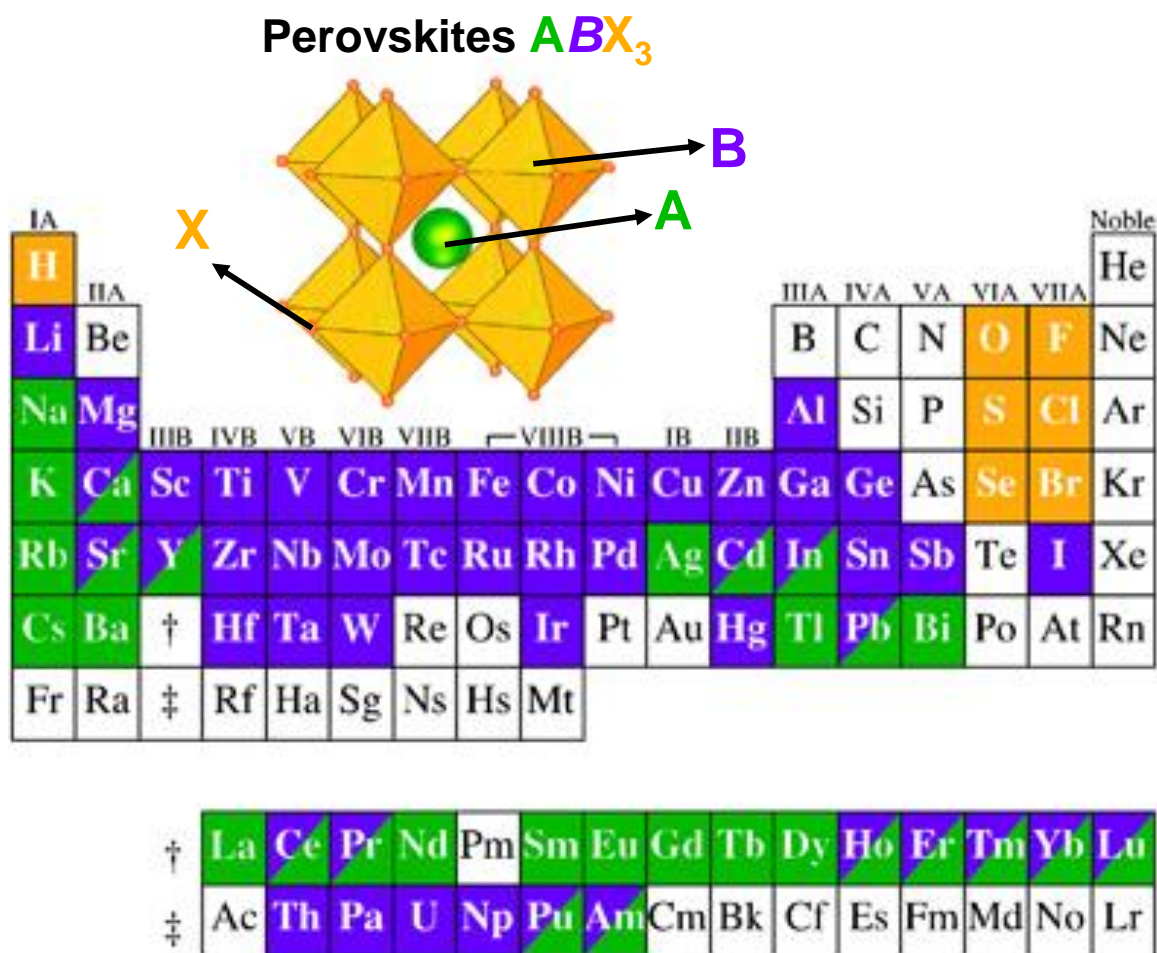
Figure 1.13: Ideal cubic perovskite structure of ABX_3 composition having A site cation (green color) in the cavity of BX_6 octahedra formed by *B* site cation (purple color) and X site anion (orange color). Map of elements from the periodic table occupying A, *B* or X site forming stable perovskite structure. Adapted from reference[29] with permission. Copyright © 2015, John Wiley and Sons.

Perovskites are very versatile class of material structure where almost every element of the periodic table forms this structure given that they satisfy certain size requirement. The size requirement is given by Goldschmidt tolerance factor, $t = \frac{r_A + r_X}{\sqrt{2}\,(r_B + r_X)}$, where r_A, r_B and r_X are the ionic radii of A and B cations and the X anion, respectively.[30] Generally, if value of t is between 0.9 < t ≤ 1, then the perovskite structure formed would be cubic while 0.8 < t ≤ 0.9 corresponds to tetragonal or orthorhombic perovskite structure. There is another parameter called octahedral factor, $\mu = \frac{r_B}{r_X}$ which is considered while predicting the stability of the perovskite. It governs the stability of BX_6 octahedra. μ in the range of 0.4 to 0.9 signifies the formation of stable BX_6 octahedra.[31] However, predicting the stability of perovskite based only on the value of t has limited success. Recently researcher have proposed new tolerance factor,[32] $\tau = \frac{r_x}{r_B} - n_A \left(n_A - \frac{r_A/r_B}{\ln r_A/r_B} \right)$ for predicting the stability of oxide and halide-based perovskites where n_A is the oxidation state of A site cation.

Perovskites are naturally occurring mineral in earth's crust. A large fraction of earth's minerals has various compositions of metal oxides having perovskite structure. Depending A and B site cation in oxide perovskites, it can give a lot of different and exciting properties like piezoelectric, thermoelectric, antiferromagnetic, superconducting and so on.[33-38] These oxide-based perovskites are very stable and generally synthesized above > 1000 °C. First time in 1893, H. L. Wells synthesized halide-based $CsPbX_3$ (X= Cl, Br, I) compound[39] and its perovskite structure was confirmed by Møller.[40, 41] Halide-based perovskite are formed at lower temperature from solution and exhibit interesting properties like magnetic, ferromagnetic, semiconducting, luminescence and electroluminescence.[42-45] The ease of forming high quality films from solution at low temperature make the halide-based perovskite interesting for electronic and optoelectronic applications. Lead halide-based perovskite has Pb^{2+} for B site cation and halides as X site anion. A site is occupied with either inorganic cation like Cs^+, Rb^+ or organic cation like $CH_3NH_3^+$ (MA^+) or $NH_2CHNH_2^+$ (FA^+) as shown in Figure 1. 14. Interest in lead halide perovskites mainly emerged from its exceptional photovoltaic properties. Excellent optoelectronic properties coupled with the ease of synthesis makes them ideal candidate for solar cells. Hybrid lead halide perovskite like methylammonium lead

halide perovskite have already proven to be a serious contender of silicon in field of PV and regarded as next generation solar cell material. They have reached a record efficiency of 25.2%[46] within few years of research and now are in the process of commercialization as alone or in tandem with silicon.

X⁻ = Cl⁻, Br⁻, I⁻

B^{2+} = Pb²⁺

Organic-Inorganic
halide perovskite
A⁺ = CH₃NH₃⁺, HC(NH₂)₂⁺

All-Inorganic
halide perovskite
A⁺ = Cs⁺ Rb⁺
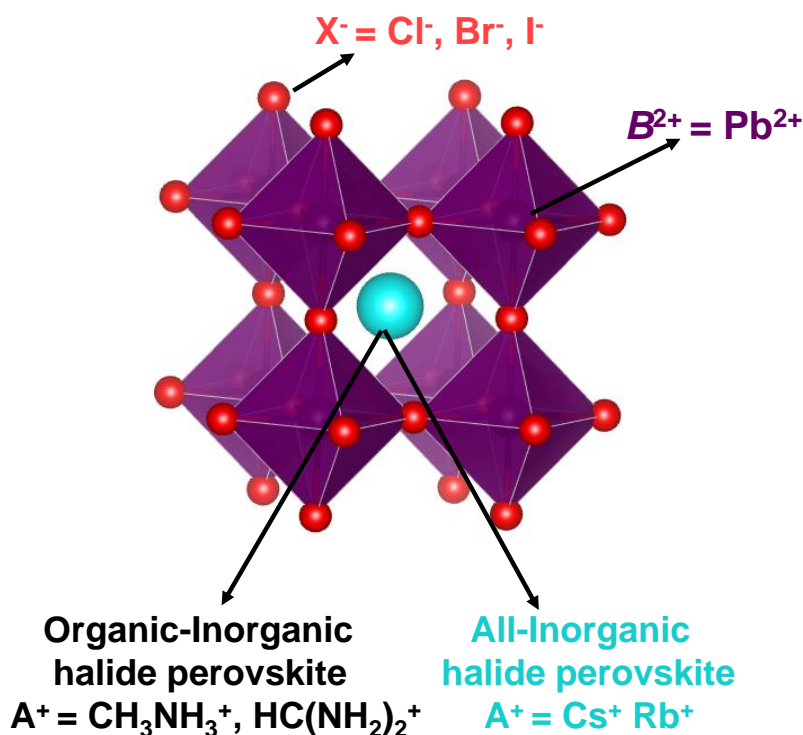
Figure 1.14: Crystal structure of lead halide perovskite where *B* site is Pb²⁺, X site is Cl⁻ or Br⁻ or I⁻. Depending on the A site cation, it can be hybrid lead halide perovskite (organic A site cation) or all-inorganic lead halide perovskite (inorganic A site cation).

However, their all inorganic counterpart like CsPbX₃ (X= Cl, Br, I) shows better thermal and moisture stability compared to hybrid organic-inorganic lead halide perovskite. Especially, the colloidal NCs of CsPbX₃ have attracted lot of interest in recent years due to its superior optoelectronic properties. Synthesis of colloidal CsPbX₃ NCs was first reported by Kovalenko group in 2015.[47] They have synthesised NCs of CsPbX₃ (X = Cl, Br, I) of size around ~ 11 nm using hot injection method. The bandgap (and so absorption and emission) of these NCs can be varied from the UV region (for CsPbCl₃ composition) to near NIR region (for CsPbI₃ composition) just by changing halide anion (X anion). Also, the NCs obtained have very high PL quantum yield reaching upto 100% along with narrow emission width without any surface treatment as shown in Figure 1.15. This narrow emission width (characterized by their full width at half maximum, FWHM of emission spectrum)

suggests the high color purity which is much desirable for display technologies. Compared to traditional NCs like CdS, ZnS which have color inconsistency due to batch by batch variation in NCs synthesis, the lead halide perovskite NCs have very high consistency in the optical property. The above-mentioned advantages of $CsPbX_3$ NCs have made them interesting for next generation optoelectronic applications like light emitting diodes (LEDs), solar cells and photodetectors.
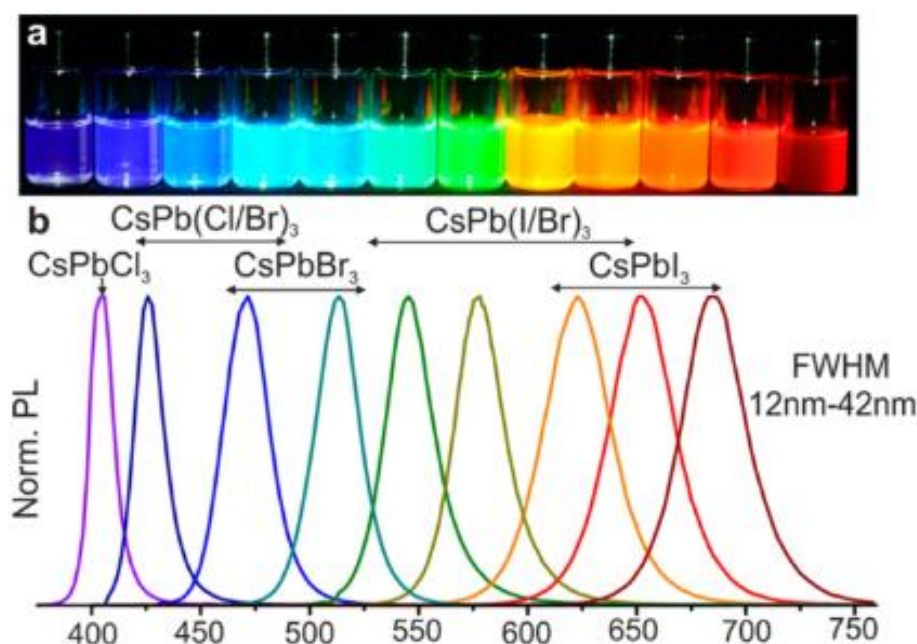
Figure 1.15: (a) Vial of colloidal dispersion of $CsPbX_3$ NCs under UV light showing emission color ranging from violent to the red. (b) The emission spectra corresponding to $CsPbX_3$ NCs having sharp and narrow PL. Adapted from reference[47] with permission. Copyright © 2015, American Chemical Society.

So, what makes these lead halides perovskite so special? Why they have such excellent optoelectronic properties? Following section look at the possible answer to these questions.

1.7 Defect tolerant nature of $CsPbX_3$ NCs:

Traditional semiconductor like Si, GaAs, CdTe require very high crystal quality meaning ultralow concentration of defects to work as good solar cell material. Therefore, their synthesis is highly complex and expensive, requiring ultrapure chemicals and very clean and inert processing environment. However, lead halide perovskites differ from them in this manner. The synthesis of lead halide perovskite NCs are facile. It does not require very high purity chemicals or high purity environment for the synthesis of good quality of NCs. Lead halide perovskite are

also excellent light emitters reaching PLQY upto 100 % without any surface treatment.

The bonding in lead halide perovskites are more ionic compared to traditional semiconductors. This increased ionicity is responsible for the easy synthesis of NCs at lower temperature (even at room temperature). They can be synthesised at high temperature following traditional hot injection method or synthesised at room temperature using ligand assisted reprecipitation (LARP) method. Various synthesis method for CsPbX$_3$ NCs are shown in Figure 1.16.
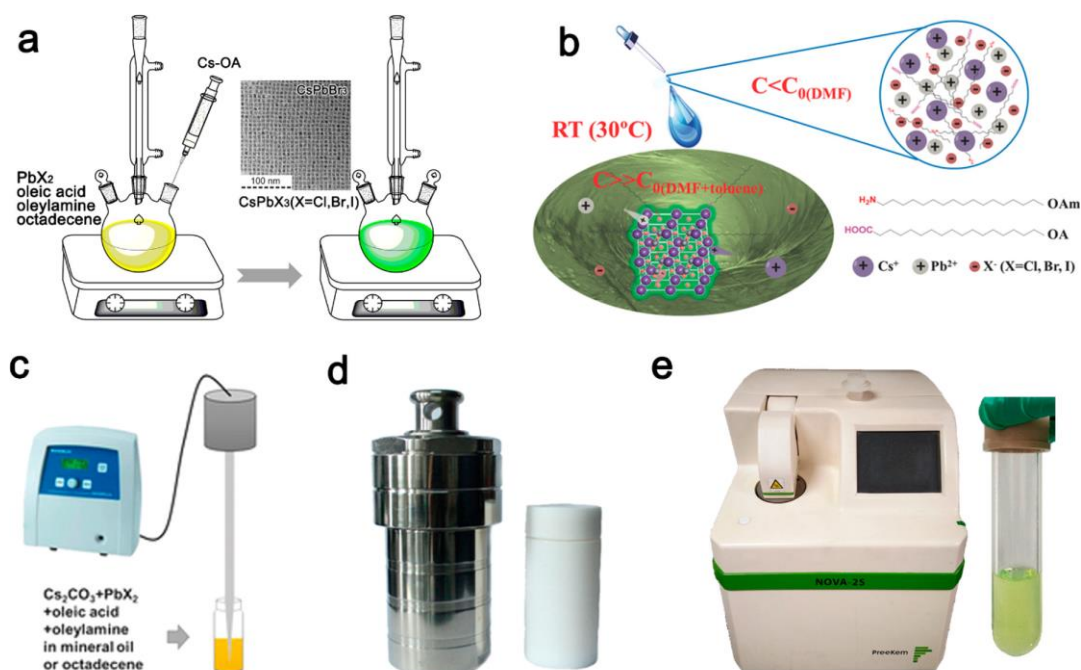
Figure 1.16: Schematic of various synthesis technique of CsPbX$_3$ NCs: (a) hot-injection method (b) supersaturated recrystallization method (c) ultrasonic-assisted method (d) solvothermal method and (e) microwave assisted method. Adapted from reference[48] with permission. Copyright © 2018, American Chemical Society.

These excellent optoelectronic properties of lead halide perovskites are attributed to the defect tolerance nature of the perovskite. In the case of lead halide perovskite, despite of the presence of defects it acts as an excellent optoelectronic material implying that the defects states do not trap the charge carriers. The plausible reasons for defect tolerant nature of these lead halide perovskite are listed below:

a. Defects present in lead halide perovskite are mainly in the form of vacancies like halide vacancies. These vacancies form shallow defects level (does not lie deep in the bandgap region) that they do not trap charge carriers (Figure 1.17a). Fortunately, other types of defects like interstitial defect or anti-site defects which

would form deep trap states are almost absent in the lead halide perovskites as they are energetically unfavourable to form.[49, 50]
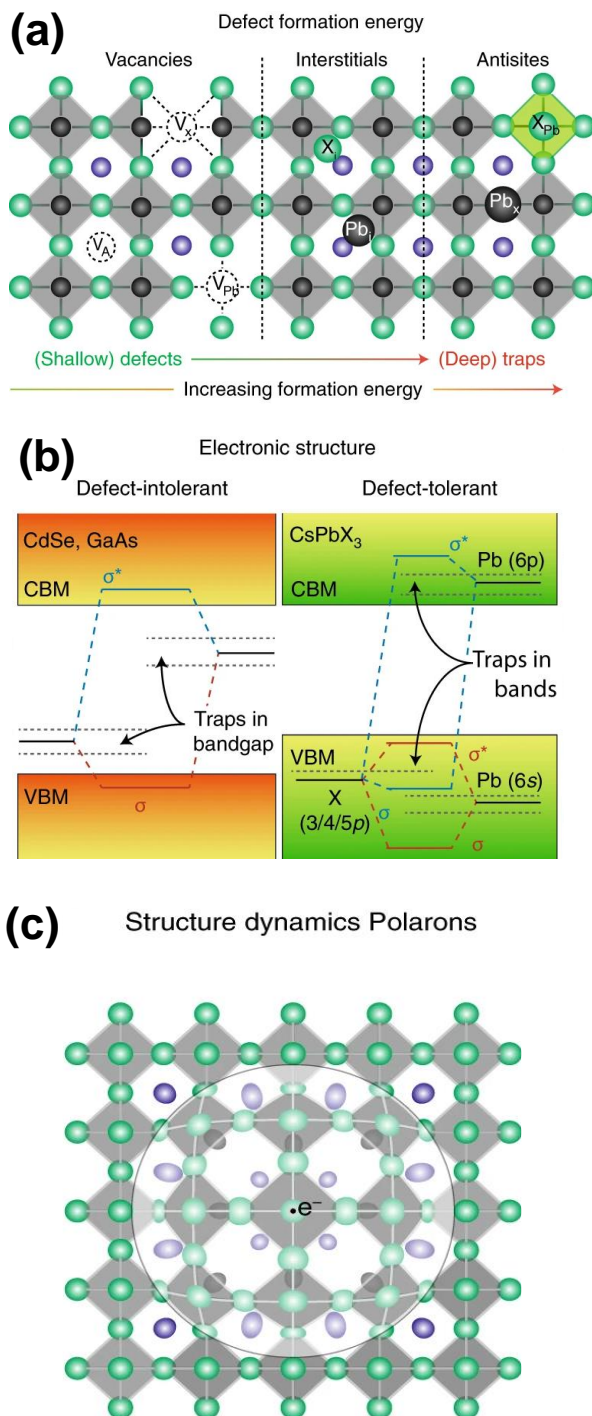
Figure 1.17: Plausible reasons for defect tolerant nature of lead halide perovskite. (a) vacancy shallow defect is more prominent in lead halide perovskite than other interstitial or antisite deep defects. (b) simplified schematic of electronic bandgap structure of lead halide perovskite compared with that of traditional semiconductor like GaAs. (c) local deformation of crystal structure along with electron and hole gives rise to polarons which then reduced charge carrier trapping and scattering. Adapted from reference[51] with permission. Copyright © 2018, Springer Nature.

b. Halide vacancies form shallow defect levels because of the nature of bonding in lead halide perovskite where both valence band and conduction band are antibonding in character (Figure 1.17 b). Also, the spin orbit coupling effect (due to the heavy Pb atom) in conduction band further stabilizes the conduction band by lowering the energy of conduction band.

c. Due to the soft and ionic nature of lead halide crystal structure, they are easily deformed. This deformation of crystal structure along with charge carrier (electron or hole) give rise to formation of polaron. The formation of Polarons is very feasible in lead halide perovskites due to the coupling of electron and holes with the soft and ionic lattice of perovskite. Polarons are proposed to screen coulombic potential and reduce the carrier trapping and scattering (Figure 1.17c).

1.8 Challenges faced by $CsPbX_3$ NCs:

However, all is not so shiny for these $CsPbX_3$ NCs. $CsPbX_3$ NCs undergoes rapid degradation when exposed to external environments like moisture, heat and light. These instability issues associated with them, impedes their utilization in commercial applications. Their instability arises because of the ionic bonding of lead and halide as well as the labile binding of the ligands on the $CsPbX_3$ NCs surface. Further, concern about the toxicity of lead complicates the problem. The problems that $CsPbX_3$ NCs must overcome are highlighted below:

a. Anion exchange and segregation problem: Anions in the lead halide perovskite are very mobile. Also, due to the low formation energy of anion vacancies, it is very easy to form halide vacancy defect. This causes movement of other anions in the crystals to fill those vacancies. This property of lead halide perovskite proved to be extremely beneficial in some cases like easy anion exchange of one of the compositions of lead halide perovskite to other composition. This gives a way to tune the bandgap of the lead halide perovskite. However, the easy anion exchange poses a problem like spontaneous exchange of anions in two different composition of $CsPbX_3$ films. It results in a film having a single composition, losing the identity of individual layers. Figure 1.18 shows a schematic where, if you make thin films of two halide perovskite i.e. $CsPbI_3$ NCs and $CsPbBr_3$ NCs on top of each other then, they would get anion exchange to give films of mixed composition $CsPbBr_xI_{3-x}$ .This poses a problem to use these halide perovskite in a

tandem fashion where different bandgap should be placed on top of each other so that they can capture solar light efficiently. Similarly, in case of colloidal dispersion of NCs, when two NCs are mixed, they undergo anion exchange to give a single composition of NCs. So, to obtain emission color like white light from lead halide perovskite, it should emit red, green and blue together so that these color can be perceived as white light.

Other problem that lead halide perovskite faces is the anion segregation in mixed halide perovskite under influence of light or electric field. Segregation of halides in mixed halide perovskites gives rise to individual halide rich region leading to color instability. For example, $CsPb(Cl/Br)_3$ NCs which are used for blue emitting LEDs, suffers from this problem.
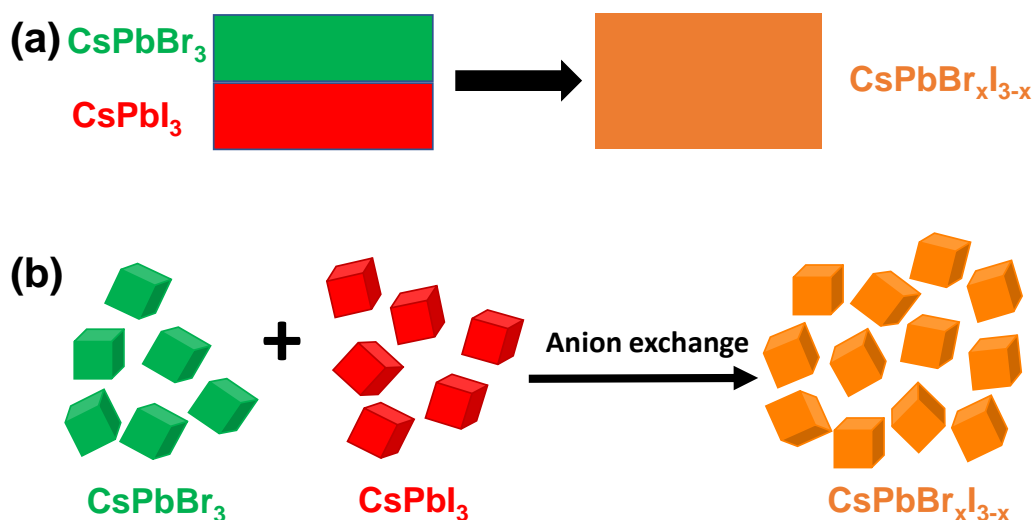
Figure 1.18: Schematic showing halide exchange for $CsPbX_3$ NCs (a) a film of $CsPbBr_3$ deposited on top of $CsPbI_3$ NCs undergoes anion exchange to give a film of single composition of $CsPbBr_xI_{3-x}$. (b) NCs of $CsPbBr_3$ and $CsPbI_3$ undergoes anion exchange in colloidal dispersion.

b. Moisture instability: The lead halide perovskite is known to break in the polar environment or even in moisture due to its ionic nature.[52-54] This instability to water limits their applications in devices as well as long term performance. For example, lead halide perovskite cannot be used for photocatalysis in water despite being excellent solar absorbing material. The mechanism proposed for the degradation is that, first the water molecules react with PbX_6 octahedra. This causes chemical bonds between A site cation (Cs^+) and PbX_6 to break leading to transformation to

0D structure (Figure 1.19). Further treatment with the water lead to complete degradation to the corresponding salts of PbX_2 and CsX.[55]

3D CsPbBr$_3$ **0D Cs$_4$PbBr$_6$**   CsBr + PbBr$_2$
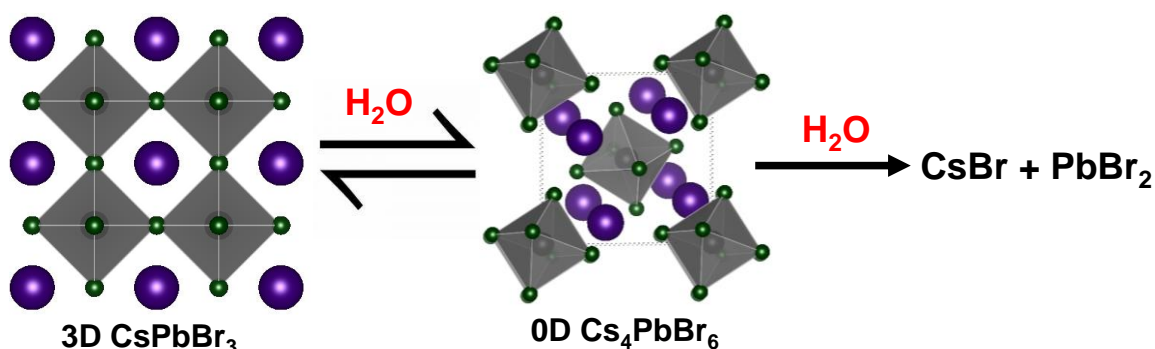
Figure 1.19: Schematic of degradation of CsPbBr$_3$ NCs under moisture/water where initially CsPbBr$_3$ transformed to Cs$_4$PbBr$_6$ which then finally gets degraded to corresponding CsBr and PbBr$_2$ salts.

Similar instability of lead halide perovskite exists with the polar solvent like methanol, dimethyl sulfoxide and dimethylformamide where the lead halide perovskite dissolves and undergoes degradation.

c. Degradation due to light: CsPbX$_3$ NCs are also reported to be unstable when continuously irradiated with the blue LED light or sunlight.[56, 57] The NCs undergo morphological and structural change upon illumination along with the heavy loss of PL. Figure 1.20 shows the model proposed by Chen et al.[58] where the CsPbBr$_3$ NCs loses its optical properties under continuous irradiation of light.
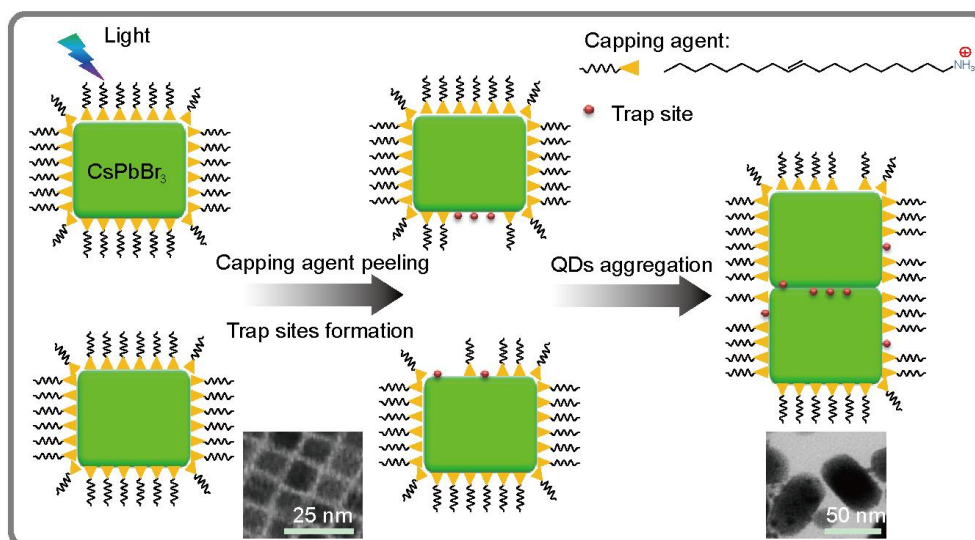
Figure 1.20: Schematic showing the photodegradation mechanism of CsPbBr$_3$ NCs dispersed in toluene. Adapted from reference[58] with permission. Copyright © 2016, Springer Nature.

The prolonged irradiation of light causes the photogenerated charge carriers to diffuse towards the surface where they are capture by the ligands. Some of this surface ligand then irreversibly dissolve in the solvent leading to the trap formation on the surface of the NCs. Removal of the ligand promotes the NCs to aggregate together to grow into bigger NCs having trap states leading to loss of PL properties.

d. Degradation due to heat: Although the inorganic lead halide perovskite like $CsPbBr_3$ NCs are thermally stable upto 550 °C but its optical properties are not. It shows great loss in PL when heated which are not reversible. The loss of PL is attributed to the loss of surface ligand which then creates the defect states. These defects then act as charge trap centres and thus quench the PL. Further the loss of ligand promotes the structural degradation to lower dimensional counterparts like $CsPb_2Br_5$ or Cs_4PbBr_6 as shown in Figure 1.21
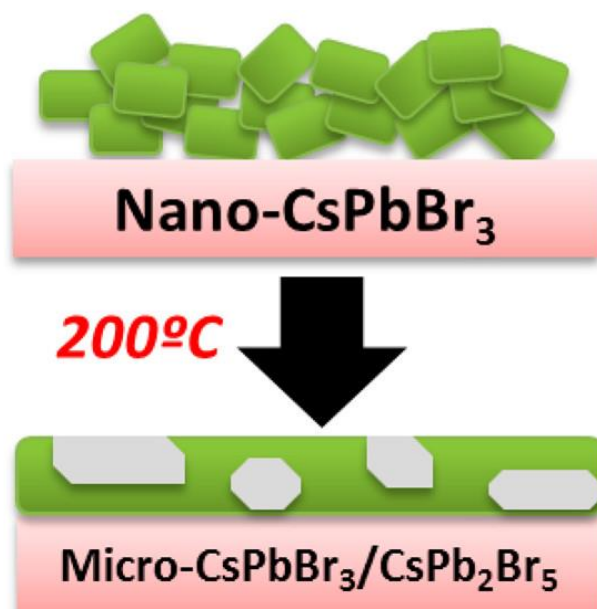
Figure 1.21: Transformation of $CsPbBr_3$ NCs to $CsPb_2Br_5$ driven by the loss of organic ligand from the surface when NCs are thermally treated at higher temperature. Adapted from reference[59] with permission. Copyright © 2017, American Chemical Society.

Report by Diroll et al.[60] have studied the PL quenching of $CsPbX_3$ NCs as a function of temperature and they have found that the thermal quenching is reversible upto 450 K while above than it is irreversible. The reversible behaviour is attributed to thermally assisted trapping due to halogen vacancy centre whereas the irreversible behaviour of PL quenching is attributed to loss of surface ligand followed by agglomeration. The worse effect of degradation by heat is seen as it amplifies the

degradation caused by light, moisture and oxygen. Therefore, the instability problem of perovskite QDs to thermal effect must be addressed as it is an important and universal for all of the lead halide perovskites.

e. Toxicity of lead: The toxicity of lead is a major concern for the $CsPbX_3$ NCs or for general lead halide perovskites. Although the device on lead halide perovskite can be properly sealed and even the amount of lead used in a lead halide PV device is within allowed limit, it still poses an environmental and health concern.[61-63] This is because the lead salts (PbX_2 normally used as precursor) are soluble in water and can enter the ground water once the devices based on lead halide perovskite break and lead leaches out. Also because of their water solubility, they are readily bioavailable to plants and other organisms. A very recent report by Li et al.[64] have studied the lead uptake by plant in lead halide perovskite-contaminated soil. They have found out that the lead leaking into the ground from lead halide perovskite can enter into the plant and then to food cycle almost ten times effectively than the other lead contaminants (from lead acid battery or from electronic components) already present. Figure 1.22 shows the concentration of Pb^{2+} in mint plants grown in natural soil and one with deliberately contaminated with the halide perovskite.

Pb²⁺ in leaves: 7.5–8.4

Stems: 2.8–3.9

Roots: 9.3–15.2

(mg kg⁻¹)

Pb^{2+} in leaves: 7.5–8.4 | Stems: 2.8–3.9 | Roots: 9.3–15.2 | (mg kg⁻¹) | Natural soil | Perovskite-contaminated soil | Pb^{2+} in leaves: 384.7–426.8 | Stems: 179.0–240.1 | Roots: 3404.1–4896.8 | (mg kg⁻¹)
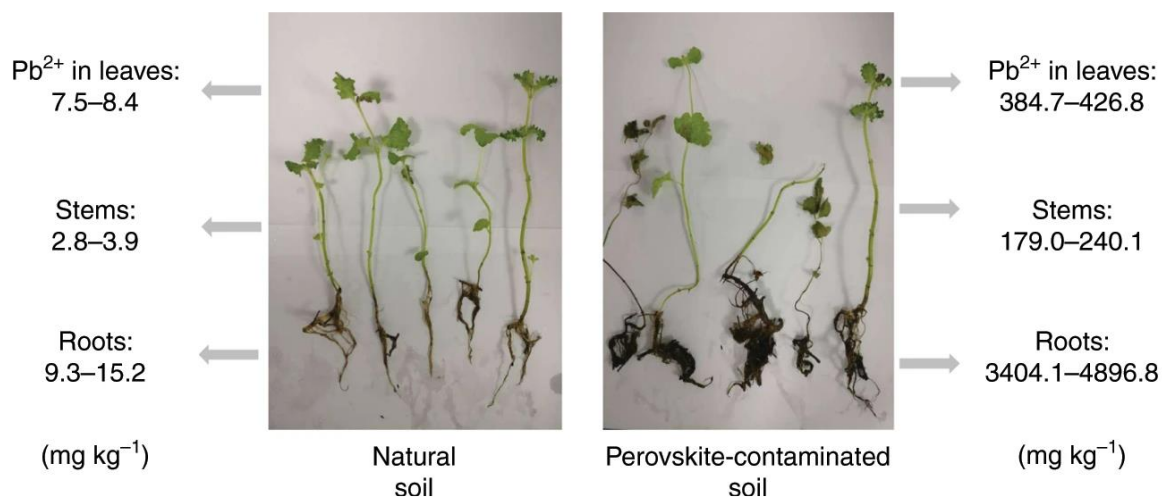
Figure 1.22: The value of Pb^{2+} content in leaves, stems and roots in mint plants grown in a. control soil (36.3 mg Kg⁻¹ of Pb^{+2}) b. soil contaminated with lead halide perovskite (250 mg Kg⁻¹ of Pb^{+2}). Adapted from reference[64] with permission. Copyright © 2020, Springer Nature.

The highest lead concentration that is allowed in agricultural land is 250 mg Kg⁻¹ which is already higher than the natural lead content of 36 mg Kg⁻¹ in earth's crust.

They have shown that lead concentration in different parts of mint plants can well above the tolerant limit of plant and they died due to lead intoxication.

This demands a need for either safer option for lead halide perovskite or putting strict regulation where permissible Pb^{2+} limit is lower than the current allowed value.

1. 9 Scope of this thesis:

As outlined above are the problems of lead halide perovskites. This thesis takes a shot at addressing some of those problems in various chapters.

Generally, while choosing a system of semiconductor NCs for a device application, we need to know some of their important structural and optical parameters along with the stability aspects of the NCs. For $CsPbX_3$ NCs, we have started first with their colloidal synthesis by the reported method and have determined its optical band edge energies along with the excitonic transition probabilities. Further, we have determined how the surface composition of the $CsPbBr_3$ NCs is, its termination and the ligand present on the surface. Then we went to tackle the instability problem of $CsPbX_3$ NCs by doing surface engineering of the NCs. This surface engineering was done by encapsulating the $CsPbX_3$ NCs by proper shell material. Finally, we have addressed the inherent stability problem and toxicity of $CsPbX_3$ NCs by doing the compositional engineering. We have explored more stable and environment friendly but less explored chalcogenide perovskite namely, $BaZrS_3$ NCs. Before discussing those work in details let us look at which are the parameters and why they are important for the working of a semiconductor device:

a.   **Determination of optical parameters***:* It is very important to know about the relevant optical parameters of a semiconductor like its bandgap, its band edge energy levels and its excitonic transition probabilities in terms of its absorption and emission to use them for a specific application.

Say for example if we wish to use a semiconductor for solar cell application, then the choice for the bandgap of active semiconducting material, electron transport layer (ETL) and hole transport layer (HTL) need to be such that they can facilitate charge transfer between these layers as shown in Figure 1.23.

Similarly, knowledge about the excitonic transition probability is also important for using a semiconductor for an application. Exciton transition probability in terms of its absorption coefficient is important for application like solar cell or photovoltaics

where the maximum absorption of light is desired whereas excitonic transition probability in terms of PL emission is desirable for application in LEDs. Figure 1.24 shows the schematic of transition probabilities in terms of absorption and emission at its excitonic edge.
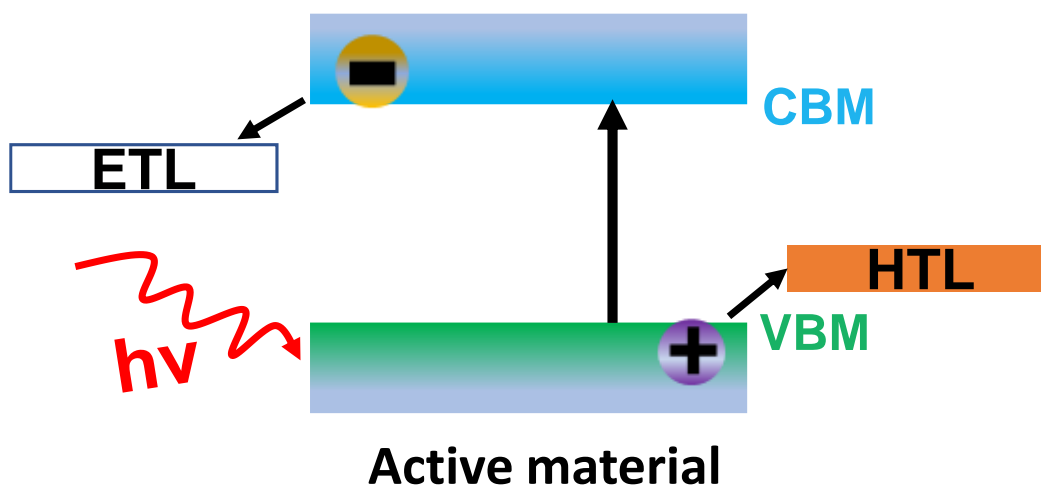
Figure 1.23: Schematic for solar cell device having semiconductor of appropriate bandgap as active layer.
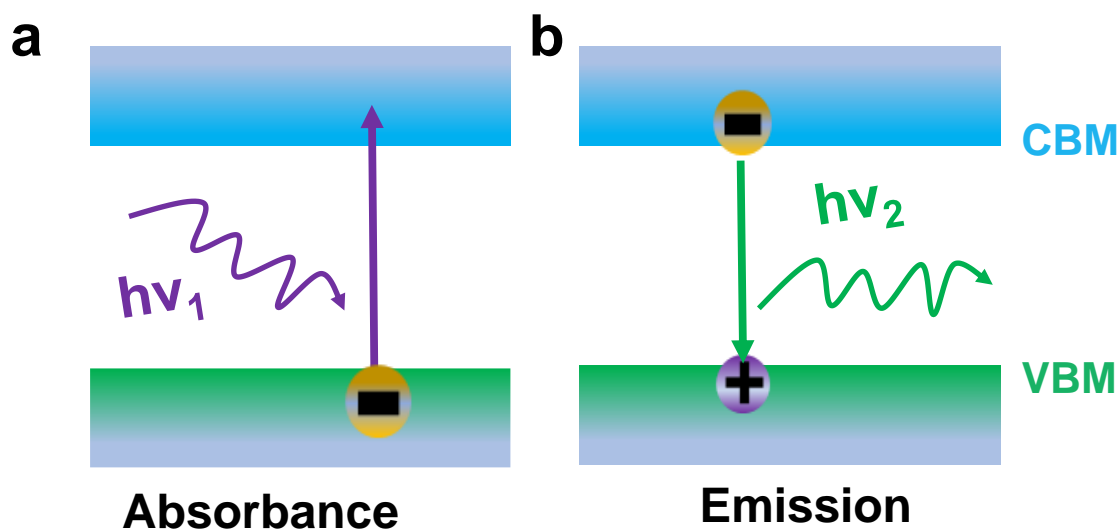
Figure 1.24: Schematic showing (a) absorbance of light leading to excitation of electron from valence band to conduction band (b) recombination of electron and hole (exciton) by radiative emission.

In Chapter 2, we have done just that by synthesising $CsPbX_3$ NCs and measured its optical bandgap and band edge energies (CBM and VBM) as X anion varies from Cl to Br to I. The excitonic transition probabilities measured in terms of molar extinction coefficient and PL decay lifetime show a systematic decreasing trend from $CsPbCl_3$ to $CsPbBr_3$ to $CsPbI_3$ NCs.

b. Surface chemistry: The surface of the NCs plays a major role in determining the optoelectronic properties of the NCs. The organic ligands used during the synthesis of the NCs provide steric stabilization which then helps to make the colloidal dispersion of NCs. Also, it passivates the surface defects which would otherwise trap charge carriers and so decrease their optoelectronic performance. But the downside is that these long chain organic ligands inhibit charge transfer between the NCs in the films and thus severely limits the device performance. This calls for careful selection of the ligand or to replace the existing long chain organic ligand with shorter carbon chain or inorganic ligand to facilitate charge transfer. It is therefore important to know about the surface of the NCs and the nature of ligand that binds to it.

Chapter 3 of this thesis answers these questions about $CsPbBr_3$ nanocubes by employing various experimental and theoretical techniques to understand inorganic surface composition and organic ligand on the surface. The developed understanding from this chapter can be extended for other composition of $CsPbX_3$ NCs, if they have similar synthesis method.

<div align="center">

Inorganic composition   **Organic ligand**   **NCs capped with ligand**

</div>
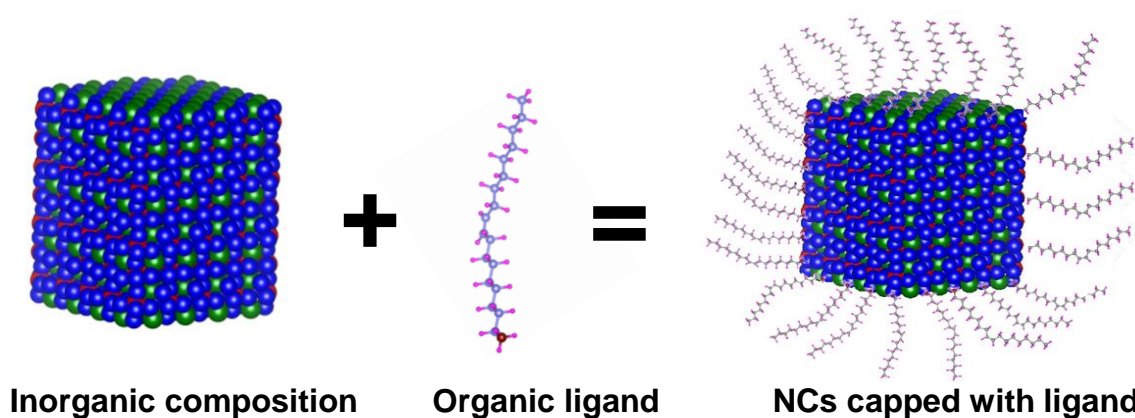
Figure 1.25: Colloidal $CsPbBr_3$ NC composed of inorganic $CsPbBr_3$ core and organic ligand.

c. Stability by surface engineering: To use the semiconductor in a device, it must be stable under given operating condition without undergoing significant decrease in efficiency and performance. It means that the devices like solar cells or LEDs based on these materials should be stable against the external environment like moisture, oxygen, light and heat. For example, it is reported that the blue LEDs based on mixed lead halide perovskite loses its efficiency and color purity after certain operating hours. This is mainly due to the ion migration problem which leads

to segregation of individual halide rich regions. Similarly, PV devices based on lead halide perovskite slowly loses its efficiency due to the degradation caused by heating of the device and the moisture present in the device.

Chapter 4 of this thesis is devoted to solving the instability problem of $CsPbX_3$ NCs by surface engineering. In Chapter 4A, the anion exchange problem between different composition of $CsPbX_3$ NCs has been dealt with. The $CsPbX_3$ NCs are capped with inorganic $PbSO_4$-Oleate which suppresses the anion exchange between NCs both in colloidal dispersion as well as in films (Figure 1.26a). In Chapter 4B, the instability issue of $CsPbBr_3$ NCs towards water and light induced degradation has been addressed by making a core/shell type structure of $CsPbBr_3/ZnS$ NCs (Figure 1.26b).

Stability by Surface Engineering
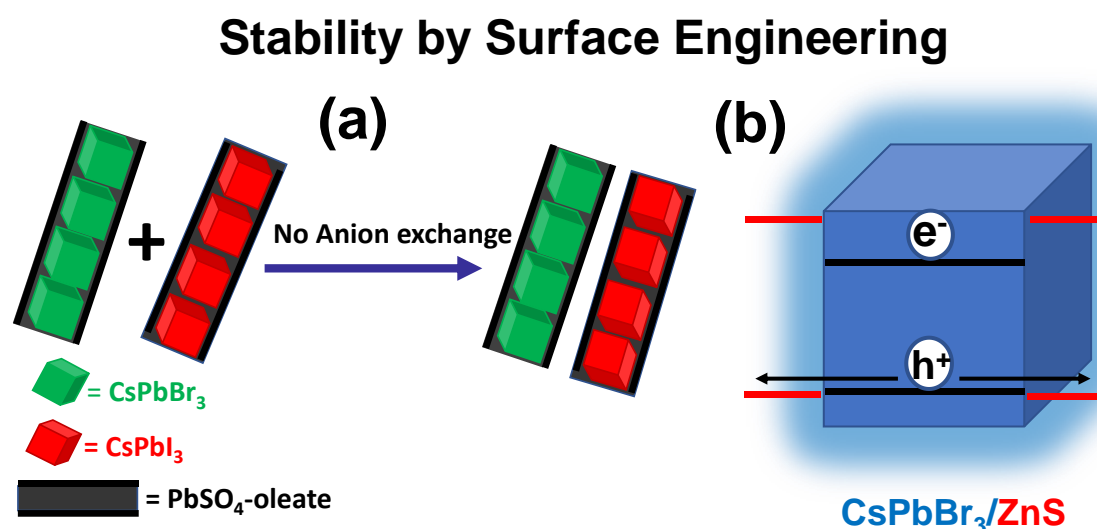
Figure 1.26: Surface engineering of $CsPbX_3$ NCs by encapsulating with (a) $PbSO_4$-Oleate to suppress anion exchange (b) ZnS semiconducting shell to make it more stable towards water and light induced degradation.

d. Stability by compositional engineering: The lead halide perovskite has low formation energy meaning they can form at low temperature. So, reverse of this is also valid, that it can degrade easily too. Additionally, because of their ionic nature they are unstable to water/moisture. Therefore, they are inherently unstable and so alternative semiconducting material having similar optoelectronic properties like of lead halide perovskite is desirable. Further, the lead halide perovskite still faces resistance in commercialization because of presence of toxic lead.

Chalcogenide perovskites have recently been emerged as potential alternative to lead halide perovskites. Chalcogenide perovskites as the name suggests have

chalcogenides like S, Se or Te at the X site anion. This means to balance the charge on the perovskite, A site cation have +2 charge while *B* site cation has +4 charge (Figure 1.27). The chalcogenide perovskite has possibility to combine high stability of oxide perovskite and good optoelectronic properties of lead halide perovskite. Oxide perovskites are very stable but usually they have very large bandgap which makes them unsuitable for optoelectronic applications in visible and infrared region.[65] On the other hand, lead halide perovskite have excellent optoelectronic properties but they have their issues with instability and lead toxicity discussed above. Chalcogenide perovskites represent middle way of both oxide and halide perovskite. Recent theoretical papers on the chalcogenide perovskites also predict it to have optoelectronic properties on par with the lead halide perovskites.[66, 67]
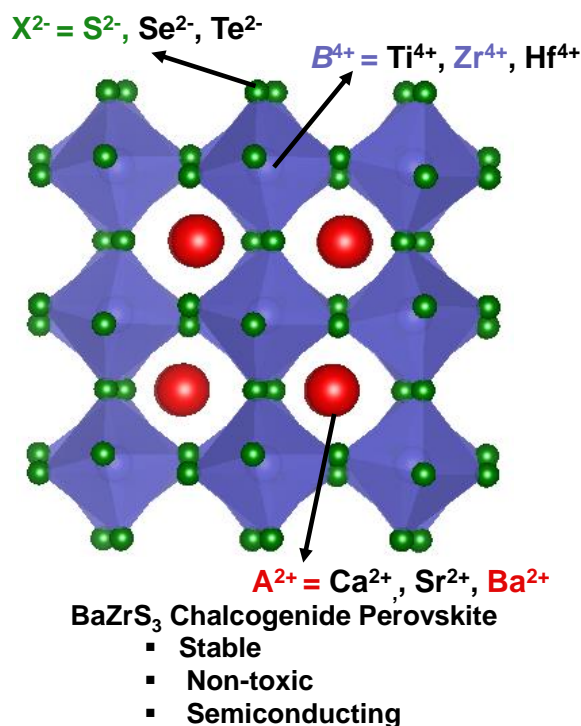
Figure 1.27: Crystal structure of BaZrS$_3$ chalcogenide perovskite.

In Chapter 5, we have explored one such chalcogenide perovskite, namely BaZrS$_3$ to overcome the inherent instability problem as well as the toxicity concern associated with the lead halide perovskites. Indeed, thermal and water stability test performed on BaZrS$_3$ NCs does suggest the better stability of chalcogenide perovskite over CsPbX$_3$ NCs. BaZrS$_3$ NCs shows strong absorption in visible region and being a direct bandgap material has potential for optoelectronic devices like solar cells.

1.10 References:

1. Queisser, H. J.; Haller, E. E., Defects in Semiconductors: Some Fatal, Some Vital. *Science* **1998**, *281*, 945-950.

2. Busch, G., Early history of the physics and chemistry of semiconductors – from doubts to fact in a hundred years. *Eur. J. Phys.* **1989**, 10, 254–263.

3. Faraday, M., Experimental researches in electricity. Fourth series. *Philos. Trans. R. Soc. London* **1833**, *123*, 507–522.

4. *The History of Wireless;* Sarkar, T. K.; Mailloux, R.; Oliner, A. A.; Salazar-Palma, M.; Sengupta, D. L.; Hoboken: Wiley, 2006.

5. P. K. Bondyopathyay, "Sir J. C. Bose's diode detector received Marconi's first transatlantic wireless signal of December 1901 (the "Italian navy coherer" scandal revisited)", *Proc. IEEE* **1998**, 86, 259-285.

6. Einstein, A., Über einen die Erzeugung und Verwandlung des Lichtes betreffenden heuristischen Gesichtspunkt. *Ann. Phys.* **1905**, *322*, 132-148..

7. Schottky, W., Vereinfachte und erweiterte Theorie der Randschicht-gleichrichter. *Z. Phys.* **1942**, *118*, 539-592.

8. Schottky, W., Zur Halbleitertheorie der Sperrschicht- und Spitzengleichrichter. *Z. Phys.* **1939**, *113*, 367-414.

9. Schottky, W., Halbleitertheorie der Sperrschicht. *Naturwissenschaften* **1938**, *26*, 843-843.

10. Mott, N. F., The theory of crystal rectifiers. *Proc. R. Soc. Lond. A* **1997**, *171*, 27–38.

11. Mott, N., Note on the contact between a metal and an insulator or semiconductor. *Proc. Cambridge Philos. Soc.*, **1938**, 34, 568-572.

12. Garoz-Ruiz, J.; Perales-Rondon, J. V.; Heras, A.; Colina, A., Spectroelectrochemistry of Quantum Dots. *Isr. J. Chem.* **2019**, *59*, 679-694.

13. Krauss, T. D.; Peterson, J. J. In *Colloidal Quantum Dot Optoelectronics and Photovoltaics; S*argent, E. H., Konstantatos, G., Eds.; Cambridge University Press: Cambridge, 2013, pp 59-86.

14. Kayanuma, Y., Quantum-size effects of interacting electrons and holes in semiconductor microcrystals with spherical shape. *Phys. Rev. B* **1988,** 38, 9797-9805.

15. Tomioka, K.; Fukui, T. In *Handbook of Crystal Growth (Second Edition);* Nishinaga, T., Eds.; Elsevier: Boston, 2015, 749-793.

16. Z Zherebetskyy, D.; Scheele, M.; Zhang, Y.; Bronstein, N.; Thompson, C.; Britt, D.; Salmeron, M.; Alivisatos, P.; Wang, L. W., Hydroxylation of the surface of PbS nanocrystals passivated with oleic acid. *Science* **2014**, *344*, 1380-1384.

17. Swarnkar, A.; Marshall, A. R.; Sanehira, E. M.; Chernomordik, B. D.; Moore, D. T.; Christians, J. A.; Chakrabarti, T.; Luther, J. M., Quantum dot-induced phase stabilization of alpha-CsPbI$_3$ perovskite for high-efficiency photovoltaics. *Science* **2016**, *354*, 92-95.

18. Swarnkar, A.; Mir, W. J.; Nag, A., Can B-Site Doping or Alloying Improve Thermal- and Phase-Stability of All-Inorganic CsPbX$_3$ (X = Cl, Br, I) Perovskites? ACS *Energy Letters* **2018,** 3, 286-289.

19. Mir, W. J.; Swarnkar, A.; Nag, A., Postsynthesis Mn-doping in CsPbI$_3$ nanocrystals to stabilize the black perovskite phase. Nan*oscale* **2019,** *11*, 4278-4286.

20. Enright, M. J.; Cossairt, B. M., Synthesis of tailor-made colloidal semiconductor heterostructures. Che*m. Commun.* **2018,** 54, 7109-7122.

21. Talapin, D. V.; Lee, J. S.; Kovalenko, M. V.; Shevchenko, E. V., Prospects of colloidal nanocrystals for electronic and optoelectronic applications. Che*m. Rev.* **2010,** 110, 389-458.

22. Kramer, I. J.; Sargent, E. H., Colloidal Quantum Dot Photovoltaics: A Path Forward. ACS *Nano* **2011,** 5, 8506-8514.

23. Owen, J., The coordination chemistry of nanocrystal surfaces. Sci*ence* **2015,** 347, 615.

24. De Roo, J.; De Keukeleere, K.; Hens, Z.; Van Driessche, I., From ligands to binding motifs and beyond; the enhanced versatility of nanocrystal surfaces. *Dalt. Trans.* **2016,** 45, 13277-13283.

25. van der Stam, W.; Akkerman, Q. A.; Ke, X.; van Huis, M. A.; Bals, S.; de Mello Donega, C., Solution-Processable Ultrathin Size- and Shape-Controlled Colloidal Cu$_{2-x}$S Nanosheets. Che*m. Mater.* **2015,** 27, 283-291.

26. Niu, Y.; Pu, C.; Lai, R.; Meng, R.; Lin, W.; Qin, H.; Peng, X., One-pot/three-step synthesis of zinc-blende CdSe/CdS core/shell nanocrystals with thick shells. Nano *Res.* **2017,** 10, 1149-1162.

27. Imran, M.; Caligiuri, V.; Wang, M.; Goldoni, L.; Prato, M.; Krahne, R.; De Trizio, L.; Manna, L., Benzoyl Halides as Alternative Precursors for the Colloidal Synthesis of Lead-Based Halide Perovskite Nanocrystals. J. *Am. Chem. Soc.* **2018,** 140, 2656-2664.

28. Dunne, P. W.; Munn, A. S.; Starkey, C. L.; Huddle, T. A.; Lester, E. H., Continuous-flow hydrothermal synthesis for the production of inorganic nanomaterials. *Philos. Trans. R. Soc., A,* **2015**, *373*, 20150015.

29. Schlom, D. G.; Chen, L.-Q.; Pan, X.; Schmehl, A.; Zurbuchen, M. A., A Thin Film Approach to Engineering Functionality into Oxides. *J. Am. Ceram. Soc.* **2008**, *91*, 2429-2454..

30. Li, C.; Lu, X.; Ding, W.; Feng, L.; Gao, Y.; Guo, Z., Formability of ABX$_3$ (X = F, Cl, Br, I) halide perovskites. *Acta Crystallogr. B* **2008**, *64*, 702-707.

31. Li, Z.; Yang, M.; Park, J.-S.; Wei, S.-H.; Berry, J. J.; Zhu, K., Stabilizing Perovskite Structures by Tuning Tolerance Factor: Formation of Formamidinium and Cesium Lead Iodide Solid-State Alloys. Che*m. Mater.* **2016,** 28, 284-292.

32. Bartel, C. J.; Sutton, C.; Goldsmith, B. R.; Ouyang, R.; Musgrave, C. B.; Ghiringhelli, L. M.; Scheffler, M., New tolerance factor to predict the stability of perovskite oxides and halides. *Sci. Adv.* **2019**, 5, eaav0693.

33. Setter, N.; Damjanovic, D.; Eng, L.; Fox, G.; Gevorgian, S.; Hong, S.; Kingon, A.; Kohlstedt, H.; Park, N. Y.; Stephenson, G. B.; Stolitchnov, I.; Taganstev, A. K.; Taylor, D. V.; Yamada, T.; Streiffer, S., Ferroelectric thin films: Review of materials, properties, and applications. *J. Appl. Phys.* **2006**, 100, 051606.

34. Thomas, R.; Scott, J. F.; Bose, D. N.; Katiyar, R. S., Multiferroic thin-film integration onto semiconductor devices. *J. Phys.: Condens. Matter* **2010**, *22*, 423201.

35. Nechache, R.; Harnagea, C.; Li, S.; Cardenas, L.; Huang, W.; Chakrabartty, J.; Rosei, F., Bandgap tuning of multiferroic oxide solar cells. *Nat. Photonics* **2015,** 9, 61-67.

36. Fan, Z.; Sun, K.; Wang, J., Perovskites for photovoltaics: a combined review of organic–inorganic halide perovskites and ferroelectric oxide perovskites. *J. Mater. Chem. A* **2015**, *3*, 18809-18828.

37. Nakamura, M.; Kagawa, F.; Tanigaki, T.; Park, H. S.; Matsuda, T.; Shindo, D.; Tokura, Y.; Kawasaki, M., Spontaneous Polarization and Bulk Photovoltaic Effect Driven by Polar Discontinuity in $LaFeO_3/SrTiO_3$ Heterojunctions. *Phys. Rev. Lett.* **2016**, *116*, 156801.

38. Paillard, C.; Bai, X.; Infante, I. C.; Guennou, M.; Geneste, G.; Alexe, M.; Kreisel, J.; Dkhil, B., Photovoltaics with Ferroelectrics: Current Status and Beyond. *Adv. Mater.* **2016,** 28, 5153-5168.

39. Wells, H. L., Über die Cäsium- und Kalium-Bleihalogenide. *Anorg. Chem.* **1893**, *3*, 195-210.

40. Moller, C. K., A Phase Transition in Caesium Plumbochloride. *Nature* **1957**, *180*, 981-982.

41. Moller, C. K., Crystal Structure and Photoconductivity of Caesium Plumbohalides. *Nature* **1958**, *182*, 1436-1436.

42. Mitzi, D. B.; Chondroudis, K.; Kagan, C. R., Design, Structure, and Optical Properties of Organic−Inorganic Perovskites Containing an Oligothiophene Chromophore. *Inorg. Chem.* **1999**, *38*, 6246-6256.

43. Mitzi, D. B., Templating and structural engineering in organic–inorganic perovskites. *J. Chem. Soc., Dalton Trans.* **2001**, *1*, 1-12.

44. Cheng, Z.; Lin, J., Layered organic–inorganic hybrid perovskites: structure, optical properties, film preparation, patterning and templating engineering. *CrystEngComm* **2010**, *12*, 2646-2662.

45. Mercier, N.; Louvain, N.; Bi, W., Structural diversity and retro-crystal engineering analysis of iodometalate hybrids. *CrystEngComm* **2009**, *11*, 720-734.

46. National Renewable Energy Laboratory, Best Research-Cell Efficiencies. **2019**. https://www.nrel.gov/pv/cell-efficiency.html.

47. Protesescu, L.; Yakunin, S.; Bodnarchuk, M. I.; Krieg, F.; Caputo, R.; Hendon, C. H.; Yang, R. X.; Walsh, A.; Kovalenko, M. V., Nanocrystals of Cesium Lead Halide Perovskites ($CsPbX_3$, X = Cl, Br, and I): Novel Optoelectronic Materials Showing Bright Emission with Wide Color Gamut. *Nano Lett.* **2015**, *15*,

3692-3696. https://pubs.acs.org/doi/10.1021/nl5048779. Further permission related to the material excerpted should be directed to the ACS.

48. Zhang, Q.; Yin, Y., All-Inorganic Metal Halide Perovskite Nanocrystals: Opportunities and Challenges. *ACS Cent. Sci.* **2018**, *4*, 668-679. https://pubs.acs.org/doi/10.1021/acscentsci.8b00201. Further permission related to the material excerpted should be directed to the ACS.

49. Brandt, R. E.; Stevanović, V.; Ginley, D. S.; Buonassisi, T., Identifying defect-tolerant semiconductors with high minority-carrier lifetimes: beyond hybrid lead halide perovskites. *MRS Commun.* **2015**, *5*, 265-275.

50. Kang, J.; Wang, L.-W., High Defect Tolerance in Lead Halide Perovskite CsPbBr$_3$. *J. Phys. Chem. Lett.* **2017**, *8*, 489-493.

51. Akkerman, Q. A.; Rainò, G.; Kovalenko, M. V.; Manna, L., Genesis, challenges and opportunities for colloidal lead halide perovskite nanocrystals. *Nat. Mater.* **2018**, *17*, 394-405.

52. Peng, C.; Chen, J.; Wang, H.; Hu, P., First-Principles Insight into the Degradation Mechanism of CH$_3$NH$_3$PbI$_3$ Perovskite: Light-Induced Defect Formation and Water Dissociation. *J. Phys. Chem. C* **2018**, *122*, 27340-27349.

53. Wei, W.; Hu, Y. H., Catalytic role of H$_2$O in degradation of inorganic–organic perovskite (CH$_3$NH$_3$PbI$_3$) in air. *Int. J. Energy Res.* **2017**, *41*, 1063-1069.

54. Akbali, B.; Topcu, G.; Guner, T.; Ozcan, M.; Demir, M. M.; Sahin, H., CsPbBr$_3$ perovskites: Theoretical and experimental investigation on water-assisted transition from nanowire formation to degradation. *Phys. Rev. Materials* **2018**, *2*, 034601.

55. Tsvetkov, D. S.; Mazurin, M. O.; Sereda, V. V.; Ivanov, I. L.; Malyshkin, D. A.; Zuev, A. Y., Formation Thermodynamics, Stability, and Decomposition Pathways of CsPbX$_3$ (X = Cl, Br, I) Photovoltaic Materials. *J. Phys. Chem. C* **2020**, *124*, 4252-4260.

56. Huang, S.; Li, Z.; Wang, B.; Zhu, N.; Zhang, C.; Kong, L.; Zhang, Q.; Shan, A.; Li, L., Morphology Evolution and Degradation of CsPbBr$_3$ Nanocrystals under Blue Light-Emitting Diode Illumination. *ACS Appl. Mater. Interfaces* **2017**, *9*, 7249-7258.

57. Li, J.; Bo, B.; Gao, X., The degradation of structure and luminescence in CsPbBr$_3$ perovskite nanocrystals under UV light illumination. *AIP Conf. Proc.* **2018**, *2036*, 030018.

58. Chen, J.; Liu, D.; Al-Marri, M. J.; Nuuttila, L.; Lehtivuori, H.; Zheng, K., Photo-stability of CsPbBr$_3$ perovskite quantum dots for optoelectronic application. *Sci. China Mater.* **2016**, *59*, 719-727.

59. Palazon, F.; Dogan, S.; Marras, S.; Locardi, F.; Nelli, I.; Rastogi, P.; Ferretti, M.; Prato, M.; Krahne, R.; Manna, L., From CsPbBr$_3$ Nano-Inks to Sintered CsPbBr$_3$–CsPb$_2$Br$_5$ Films via Thermal Annealing: Implications on Optoelectronic Properties. *J. Phys. Chem. C* **2017**, *121*, 11956-11961. https://pubs.acs.org/doi/abs/10.1021/acs.jpcc.7b03389, Further permission related to the material excerpted should be directed to the ACS.

60. Diroll, B. T.; Nedelcu, G.; Kovalenko, M. V.; Schaller, R. D., High-Temperature Photoluminescence of CsPbX$_3$ (X = Cl, Br, I) Nanocrystals. *Adv. Funct. Mater.* **2017**, *27*, 1606750.

61. Conings, B.; Babayigit, A.; Boyen, H.-G., Fire Safety of Lead Halide Perovskite Photovoltaics. *ACS Energy Lett.* **2019**, *4*, 873-878.

62. Jiang, Y.; Qiu, L.; Juarez-Perez, E. J.; Ono, L. K.; Hu, Z.; Liu, Z.; Wu, Z.; Meng, L.; Wang, Q.; Qi, Y., Reduction of lead leakage from damaged lead halide perovskite solar modules using self-healing polymer-based encapsulation. *Nat. Energy* **2019**, *4*, 585-593.

63. Hailegnaw, B.; Kirmayer, S.; Edri, E.; Hodes, G.; Cahen, D., Rain on Methylammonium Lead Iodide Based Perovskites: Possible Environmental Effects of Perovskite Solar Cells. *J. Phys. Chem. Lett.* **2015**, *6*, 1543-1547.

64. Li, J.; Cao, H.-L.; Jiao, W.-B.; Wang, Q.; Wei, M.; Cantone, I.; Lü, J.; Abate, A., Biological impact of lead from halide perovskites reveals the risk of introducing a safe threshold. *Nat. Commun.* **2020**, *11*, 310.

65. Swarnkar, A.; Mir, W. J.; Chakraborty, R.; Jagadeeswararao, M.; Sheikh, T.; Nag, A., Are Chalcogenide Perovskites an Emerging Class of Semiconductors for Optoelectronic Properties and Solar Cell? *Chem. Mater.* **2019,** 31, 565-575.

66. Sun, Y.-Y.; Agiorgousis, M. L.; Zhang, P.; Zhang, S., Chalcogenide Perovskites for Photovoltaics. Nano *Lett. 2015***, 15**, 581-585.

67. Perera, S.; Hui, H.; Zhao, C.; Xue, H.; Sun, F.; Deng, C.; Gross, N.; Milleville, C.; Xu, X.; Watson, D. F.; Weinstein, B.; Sun, Y.-Y.; Zhang, S.; Zeng, H., Chalcogenide perovskites – an emerging class of ionic semiconductors. Nano *Energy 2016***, 22,** *1*29-135.

Chapter 2

Band Edge Energies and Excitonic Transition Probabilities of CsPbX$_3$ (X = Cl, Br, I) Perovskite Nanocrystals

The work presented in this chapter has led to the following publication:

Ravi, V. K.; Markad, G. B.; Nag, A. Band Edge Energies and Excitonic Transition Probabilities of Colloidal CsPbX$_3$ (X = Cl, Br, I) Perovskite Nanocrystals *ACS Energy Lett.* **2016**, 1, 4, 665-671. Copyright permission has been taken from ACS publication for full paper.

Declaration:

Dr. Ganesh B. Markad and Vikash K. Ravi together carried out the Cyclic Voltammetry measurements.

Chapter 2
Band Edge Energies and Excitonic Transition Probabilities of CsPbX$_3$ (X = Cl, Br, I) Perovskite Nanocrystals

Abstract:

Cesium lead halide, CsPbX$_3$ (X = Cl, Br, I) nanocrystals bandgap can be easily tuned across the entire visible region just by performing anion exchange reactions. Cesium lead chloride has large bandgap and it can be decreased by exchanging chloride ion with bromide or iodide. These colloidal CsPbX$_3$ (X = Cl, Br and I) nanocrystals have recently emerged as preferred materials for light emitting diode, along with opportunities for photovoltaic applications. Such applications rely on the nature of valence and conduction band edges, and optical transitions across these edges. Present chapter discusses about how halide compositions can control both of these correlated parameters in CsPbX$_3$ nanocrystals. We used cyclic voltammetry technique to show that the valence band maximum (VBM) shifts significantly to higher energies by 0.80 eV, from X = Cl to Br to I, whereas shift in the conduction band minimum (CBM) was small (0.19 eV) but systematic. This confirms that halides contribute more to VBM however; their contribution to CBM is also not negligible. Excitonic transition probabilities for both absorption and emission of visible light decreases probably because of the increasing dielectric constant from X = Cl to Br to I. These band-edge properties will help designing suitable interfaces in both devices and hetero-structured nanocrystals.

Graphical Abstract:
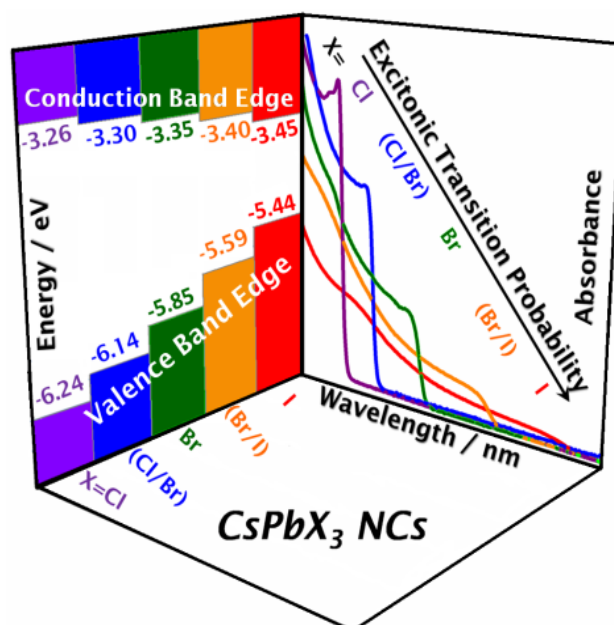
2.1. Introduction:

Organic-inorganic hybrid perovskite such as CH$_3$NH$_3$PbI$_3$ exhibits impressive semiconductor properties with long carrier diffusion length (>1μm), long carrier lifetime (~ 2 μS), narrow Urbach tail (15 meV), and reasonable carrier mobility (~10 cm^{2}V^{-1}S^{-1}), in spite of being processed at a low temperature (<100 °C).[1-3] This combination of excellent semiconductor properties at a low processing cost, along with its suitable optical bandgap, has already made these perovskites as one of the most sought after material to meet today's energy demand.[4-9] Optoelectronic applications like solar cells, light emitting diodes and photodetectors based on these hybrid perovskites are progressing rapidly.[10, 11]

Not far behind is the colloidal nanocrystals (NCs),[12] particularly, the all-inorganic CsPbX$_3$ (X = Cl, Br, I) perovskites NCs that are first reported by Protesescu et al.[13] in 2015. These CsPbX$_3$ NCs exhibited ~90% photoluminescence (PL) quantum yield with narrow PL spectra (FWHM = 85 meV) and reduced PL blinking,[14] along with low lasing threshold.[15] These properties are far superior than the traditional best known semiconductor NCs such as CdSe based ones. It is proposed that the surface defects in CsPbBr$_3$ NCs do not lead to localized deep midgap states to trap charge carriers.[16] Motivated by these photophysical properties, highly efficient light emitting diodes (LEDs) are already being made using CsPbBr$_3$ as the active material.[17, 18] Most of these properties have been explored using green light emitting CsPbBr$_3$ NCs. A systematic change in the halide compositions of NCs from CsPbCl$_3$ to CsPbBr$_3$ to CsPbI$_3$ allows achieving systematic variation in optical bandgap from blue to red without changing the size of NCs.[19-21] For further optoelectronic application of these materials in blue to red LEDs, or in photodetector or in solar cells including tandem cells, we need to understand the nature of band edges namely valance band maximum (VBM) and conduction band minimum (CBM). Two important parameters that governs such optoelectronic applications are (i) charge transfer (injection or ejection) at the interface, and (ii) optical transitions (absorption or emission), and both depends strongly on the nature of VBM and CBM.

In this Chapter, we explore the contribution of halide composition in VBM and CBM of CsPbX$_3$ NCs, and subsequent effect on optical transition probabilities across these states. Cyclic voltammetry (CV) data show a systematic shift in VBM

by 0.80 eV, from -6.24 to -5.44 eV, whereas CBM exhibit a smaller shift of 0.19 eV from -3.26 to -3.45 eV by changing the composition from CsPbCl$_3$ NCs to CsPbI$_3$ NCs through CsPbBr$_3$ NCs and mixed halides CsPb(Cl/Br)$_3$ NCs and CsPb(Br/I)$_3$ NCs. These results, in one hand, predict the charge transfer processes at interfaces both in devices and in heterostructure NCs and on the other hand, suggest that the CBM has contribution from halides as well, though mainly composed of Pb 6p states. Both absorption cross-section and rate of radiative PL decay (that indicate transition probability) across the band edges which are essentially the lowest energy excitonic transitions decreases systematically probably because of the increasing dielectric constant from X= Cl to Br to I.

2.2. Experimental Section:

2.2.1 Chemicals:

Cesium carbonate (Cs$_2$CO$_3$, 99.9%, Aldrich), lead (II) bromide (PbBr$_2$, 99.999%, Aldrich), lead (II) chloride (PbCl$_2$, 99.99%, Aldrich), lead (II) iodide (PbI$_2$, 99.99%, Aldrich), oleic acid (OA, 90%, Aldrich), oleylamine (OAm, technical grade 70%, Aldrich), 1-octadecene (ODE, technical grade 90%, Aldrich), toluene (anhydrous 99.8%, Aldrich), trioctylphosphine (TOP,98%, Aldrich), ethyl acetate (99.5%, Rankem), tetrabutylammonium perchlorate (TBAP, ≥99.0%, Aldrich), tetrabutylammonium hexafluorophosphate (TBAPF$_6$, 98% Aldrich), acetonitrile (anhydrous, 99.8%, Aldrich), dimethyl sulfoxide (anhydrous, 99.9%, Aldrich), ferrocene (98%, Aldrich).

2.2.2 Preparation of Cs-Oleate:

0.407 g (1.25 mmol) Cs$_2$CO$_3$, 1.25 mL OA and 15 mL ODE are mixed in a 50 mL three-necked round bottom flask and the reaction mixture has been kept under vacuum for 15 min at 110 °C, followed by purging with N$_2$ for 10 min along with magnetic stirring. This method of alternate application of vacuum and N$_2$ is repeated 3 times to achieve the removal of moisture and O$_2$ from the reaction mixture. The temperature of the reaction mixture is then increased to 130 °C, and the heating is continued until the Cs$_2$CO$_3$ dissolved completely giving a clear solution. This Cs-Oleate solution in ODE is then used as cesium precursor for the synthesis of CsPbBr$_3$ NCs.

2.2.3 Synthesis of CsPbBr₃ NCs:

Colloidal CsPbBr₃ NCs are synthesized by following a method similar to earlier reported method.[13] 20 mL dried ODE and 0.276 g (0.752 mmol) PbBr₂ are taken in a 50 mL three-necked round bottom flask. The mixture is degassed (under alternate vacuum and nitrogen) at 120 °C for 60 minutes along with magnetic stirring. Dried OA and OAm, each 2.0 mL, is added to the mixture at 120 °C having N₂ flow. After complete dissolution of PbBr₂ in ODE, the reaction temperature is increased to 180 °C. Separately prepared Cs-Oleate (0.1 M, 1.6 mL) solution in ODE, pre-heated to 100 °C, is swiftly injected to the reaction mixture. The reaction mixture became greenish and the reaction is stopped by dipping the reaction flask into an ice bath. The synthesized CsPbBr₃ NCs are precipitated by adding ethyl acetate at room temperature and then centrifuged at 7000 rpm. Finally, the precipitate of the NCs are redispersed in 20 mL toluene and is used as stock dispersion for anion exchange reaction.

2.2.4 Anion Exchange of CsPbBr₃ NCs:

Anion exchange reactions are carried out by modifying earlier reported protocol.[19] 20 mL colloidal CsPbBr₃ NCs in toluene (as discussed above) is divided into 5 parts having 4 mL each. For preparation of CsPbCl₃ NCs and CsPb(Cl/Br)₃ NCs, PbCl₂ in different concentration (0.220 mmol for CsPbCl₃, and 0.094 mmol for CsPb(Cl/Br)₃ NCs) are mixed with ODE (4 mL) in 25 mL three- necked round bottom flask and is degassed and dried by applying alternate vacuum and N₂ flow for 1hour at room temperature. Dried OA (0.5 mL) and OAm (0.5 mL) along with TOP (1 mL) are injected at 200 °C under N₂ flow to make PbCl₂ completely soluble. The reaction mixture is then allowed to cool down to room temperature and then CsPbBr₃ NCs stock dispersion (4 mL) is injected to give anion exchanged CsPbCl₃ and CsPb(Cl/Br)₃ NCs. Similarly, for preparation of CsPbI₃ NCs and CsPb(Br/I)₃ NCs, 0.220 and 0.094 mmol of PbI₂ is used in ODE (4 mL), and dried OA (0.2 mL) and OAm (0.2 mL) are added to reaction mixture at 120 °C under N₂ environ to make PbI₂ soluble. The reaction mixture is then allowed to cool down to room temperature and 4 mL CsPbBr₃ NCs stock dispersion is injected to give anion exchanged CsPbI₃ and CsPb(Br/I)₃ NCs. NCs are then precipitated by adding ethyl acetate (1:1 v/v) and then centrifuged at 7000 rpm for 10 min.

The supernatant is discarded and the wet precipitate is re-dispersed in toluene and used for further characterization.

2.2.5 Characterization:

Perkin Elmer, Lambda-45 UV/Vis spectrometer is used for recording UV-visible absorption spectra. Steady state PL and PL decay measurements are carried out using FLS 980 (Edinburgh Instruments). Powder X-ray diffraction (PXRD) data are recorded using a Bruker D8 Advance X-ray diffractometer using Cu Kα radiation (1.54 Å). Transmission electron microscopy (TEM) studies are carried out using a JEOL JEM 2100F field emission transmission electron microscope at 200 kV. Thermogravimetric analysis (TGA) measurements are carried out using Perkin Elmer STA 6000. The samples are heated from 30 °C to 800 °C at the heating rate of 10 °C/min. Scanning electron microscopy (SEM) and energy dispersive X-ray spectroscopy (EDAX) measurements are performed on Zeiss Ultra Plus SEM instrument.

2.2.6 Calculation of molar extinction coefficient (ε):

Each dispersion of CsPbX₃ NCs are divided into two equal parts and the NCs are precipitated by adding ethyl acetate and centrifuging at 7000 rpm at room temperature. First part of NC is again dispersed in a known volume of toluene for UV-visible absorption measurements, and the second part is vacuum dried in order to obtain the weight of NCs. In order to subtract the weight of organic capping ligands from the total weight of organic capped NCs, TGA data are recorded, showing ~10% weight from organic capping ligand. Therefore, 90% of the total weight of organic capped NCs is used to calculate the molar concentration of inorganic core NCs absorbing the visible light. Considering cubic shape of a NC and using the average size obtained from TEM, weight of a single NC is calculated using the formula, m = d/v, where m is the mass of each NC, d is density of bulk CsPbX₃ ($CsPbCl_3$ = 4.24 g/cm³, $CsPbBr_3$ = 4.86 g/cm³, $CsPbI_3$ = 5.07 g/cm³), and v is the volume of a NC (v = a^3 where a = average edge-length of a NC obtained from TEM). Densities of alloyed $CsPb(Cl/Br)_3$ is extracted from that of their end members $CsPbCl_3$ and $CsPbBr_3$ after weighing with the composition of the alloy. Likewise, density of $CsPb(Br/I)_3$ is extracted from their end-members $CsPbBr_3$ and $CsPbI_3$. Now, the number of NCs in the sample is obtained by dividing the total weight of

inorganic part of the NCs sample with weight of a single NC. These numbers of NCs are then converted to mole of NCs by dividing with Avogadro's number (N_A). Molar concentrations (C) of the NCs are then calculated from knowledge of volume of toluene used in the dispersion. For determination of ε, the absorption spectrum of dilute dispersion of NCs are recorded having different concentrations. ε is then obtained using Beer-Lambert Law: $A = \varepsilon \times C \times l$, where, A is the absorbance, and l is the optical path length (1 cm) taken from cuvette dimension.

In order to account for variations in size distribution causing broadening of absorption peak, the obtained molar extinction coefficient value is multiplied by a normalizing factor, $\Delta E_{HWHM}/\Delta E_x$, where ΔE_{HWHM} (eV) is the fitted half width at half maximum (HWHM) of first absorption peak and ΔE_x is selected as 0.06 eV as it is average HWHM of all the samples used here for the measurement.

2.2.7 Electrochemical measurements:

CV measurements are performed with the help of PAR Potentiostat/Galvanostat (model PARSTAT 2273). A commercial Pt disk electrode (CHI Instruments, USA, 2-mm diameter), Ag wire, and Pt-wire loop were used as working, quasi reference, and counter electrodes, respectively. Prior to use, the working electrode is polished over 0.5 μm alumina powder and rinsed with Milli-Q water. Further it has been pretreated electrochemically with 0.5 M H_2SO_4 by cycling the potential for several times between 1.2 V and -0.55 V (scan rate of 1 V s^{-1}). Electrochemical measurements are performed in a 5-neck glass electrochemical cell. After fixing all the electrodes, 0.171 g of TBAP is transferred into the cell and it is then air tightened inside the glove-box. Cell is then taken out of the glove-box and TBAP is dried under vacuum at 80 °C in the oil bath for a 1 hour. Cell is then allowed to cool down to room temperature naturally and vacuum is released by high purity nitrogen gas. 5 mL acetonitrile and toluene mixture (1:4 v/v) is injected in the cell through the septum and electrochemical measurements are carried out with slight positive pressure of N_2 gas in air tight cell. At the end of each set of experiments, the potentials are calibrated with respect to the normal hydrogen electrode (NHE) using ferrocene as an internal standard. Formal potential of ferrocene/ferrocenium redox couple in 1:4 mixture of acetonitrile/toluene is estimated experimentally using Ag/AgNO₃ (10 mM in acetonitrile) reference electrode. Potentials are reported with

respect to NHE throughout the chapter.

2.3 Results and Discussions:

2.3.1 Anion exchange of CsPbBr₃ NCs:

The colloidal dispersion of CsPbBr₃ NCs are first prepared and then anion exchanged to give different composition of CsPbX₃ NCs. Five samples of CsPbX₃ NCs with different halide compositions are prepared. PXRD patterns of CsPbX₃ NCs are shown in Figure 2.1.
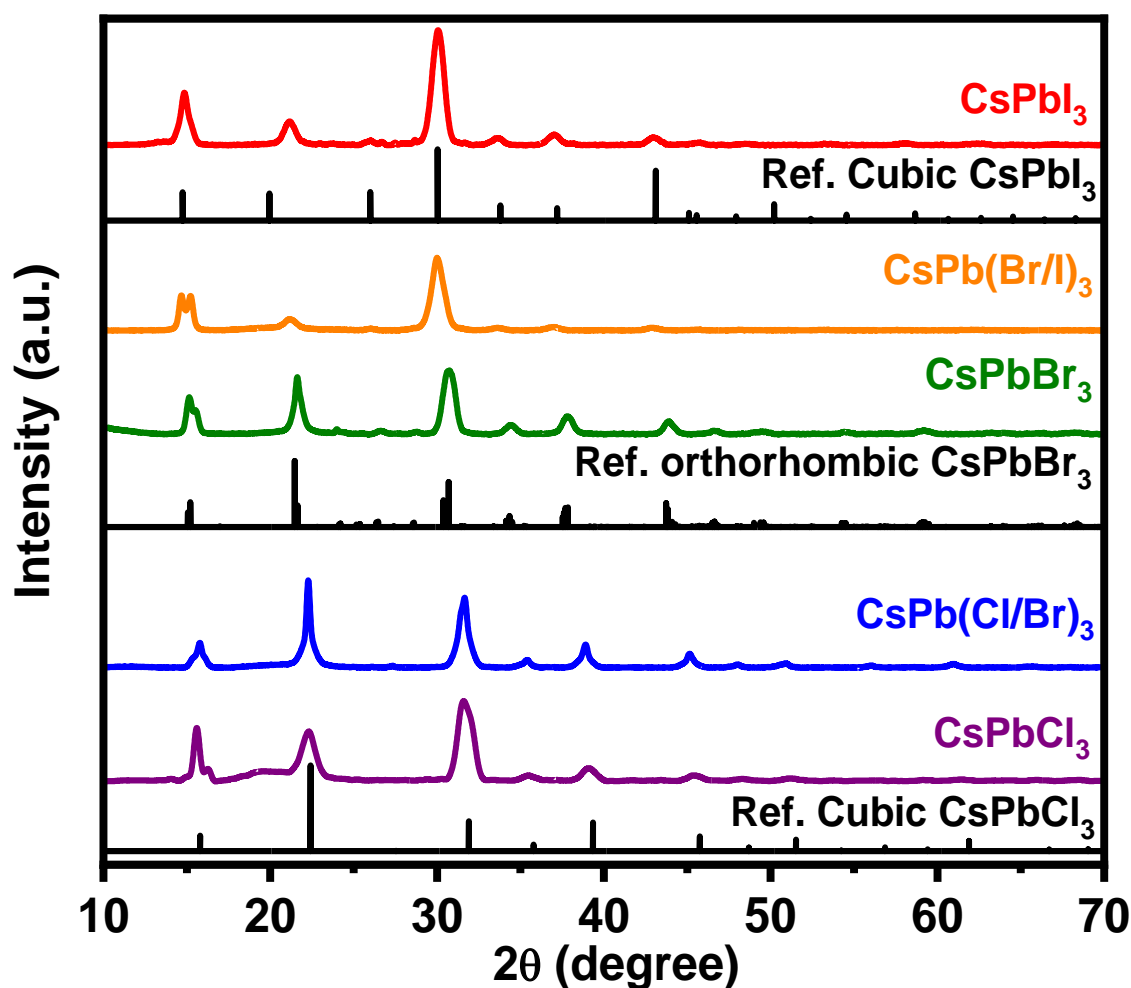
Figure 2.1: PXRD patterns of CsPbX₃ NCs with overlay of reference patterns of their respective bulk materials. PXRD patterns are shifted vertically for better clarity.

It shows a systematic shift in peak positions (lattice parameters) and matched well with their corresponding reference phase, confirming that the composition of CsPbX₃ is indeed systematically tailored after anion exchange reactions. Starting with CsPbBr₃ NCs having orthorhombic phase, the anion exchange with chlorine

shifts the peaks to higher 2θ value because of smaller size of chlorine and to lower 2θ values when exchanged with iodide. Figure 2.2 shows the TEM image of CsPbBr₃ NC along with representative anion exchanged sample of CsPbCl₃ and CsPbI₃ NCs, exhibiting cubic morphology with an average edge length of 11 nm. TEM data confirms that the size and shape of all samples remained similar apart from the expected minor change in size because of different sizes of exchanged halide ions.
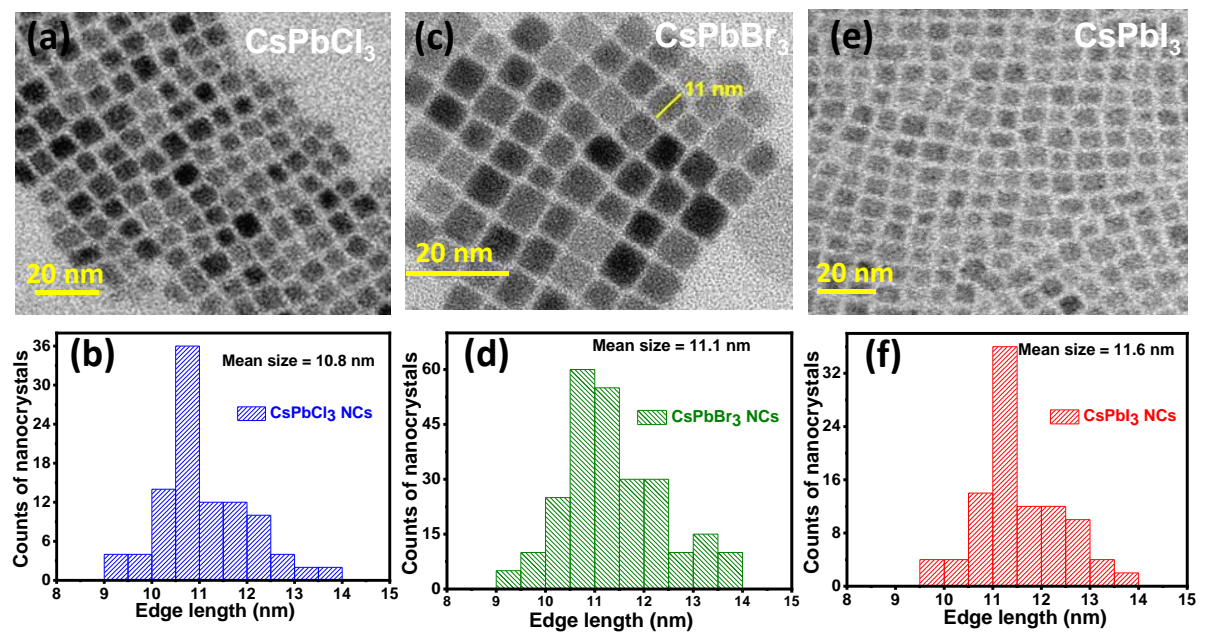
Figure 2.2: TEM images along with their size distribution histogram of (a, b) CsPbCl₃ NCs (c, d) CsPbBr₃ NCs and (e, f) CsPbI₃ NCs.

The SEM images are recorded on the five samples of CsPbX₃ NCs and are shown in Figure 2.3. EDAX are recorded on the same sample of colloidal dispersion of CsPbX₃ NCs, drop casted on silicon wafer, estimated the compositions of these samples as $CsPbCl_{3.1}$, $CsPbCl_{2.0}Br_{1.3}$, $Cs_{0.9}PbBr_{3.2}$, $CsPbBr_{2.3}I_{0.8}$, and $Cs_{0.9}PbI_3$. These different compositions indicate the success of anion exchange reaction. However, it is to be noted that determination of such compositions using EDAX involves some uncertainties. All samples show a slight excess of anionic contribution similar to prior literature, suggesting the possibility of anion-rich surface. For simplicity, these five compositions will be now be simply referred as NCs of, CsPbCl₃, CsPb(Cl/Br)₃, CsPbBr₃, CsPb(Br/I)₃, and CsPbI₃ throughout this chapter. Digital photographs of colloidal CsPbX₃ NCs captured under ambient light as well as under UV light and reaction schemes are shown in Figure 2.4 which highlights

the essential methodology employed for these anion exchange reactions. Figure 2.4a shows the image of CsPbX$_3$ NCs captured under ambient light while the Figure 2.4b shows the digital photograph capture under UV light.
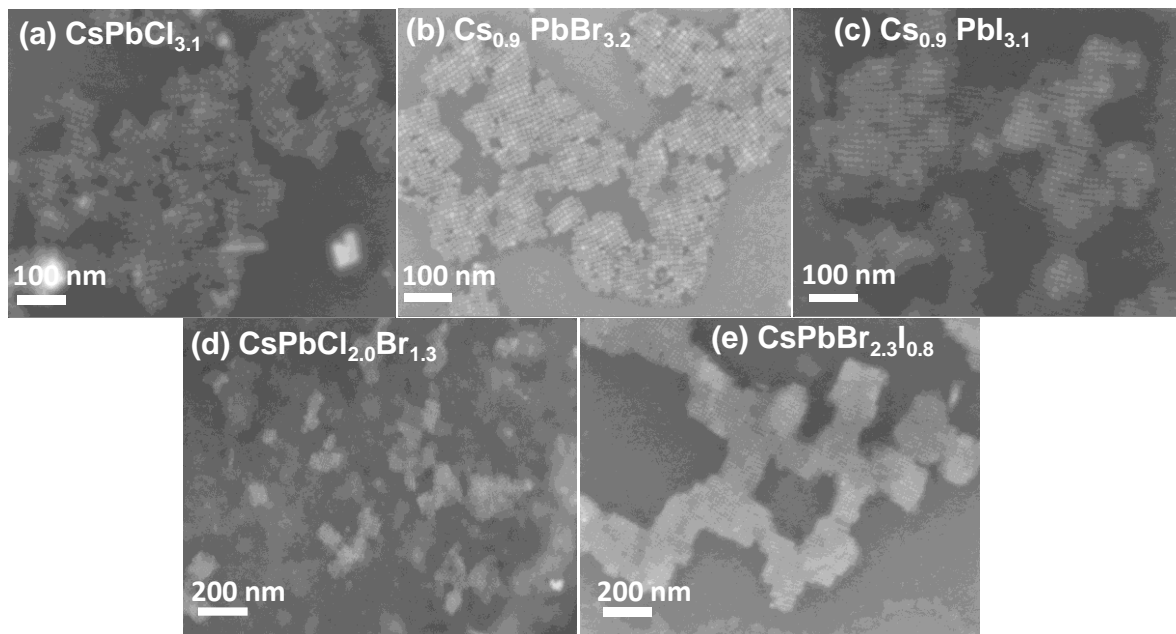
Figure 2.3: SEM images of colloidal NCs of: (a) CsPbCl$_3$, (b) CsPbBr$_3$, (c) CsPbI$_3$ (d) CsPb(Cl/Br)$_3$ and (e) CsPb(Br/I)$_3$ along with their composition determined from EDAX written in their individual panel. Cubic morphology and size are maintained for all the samples.
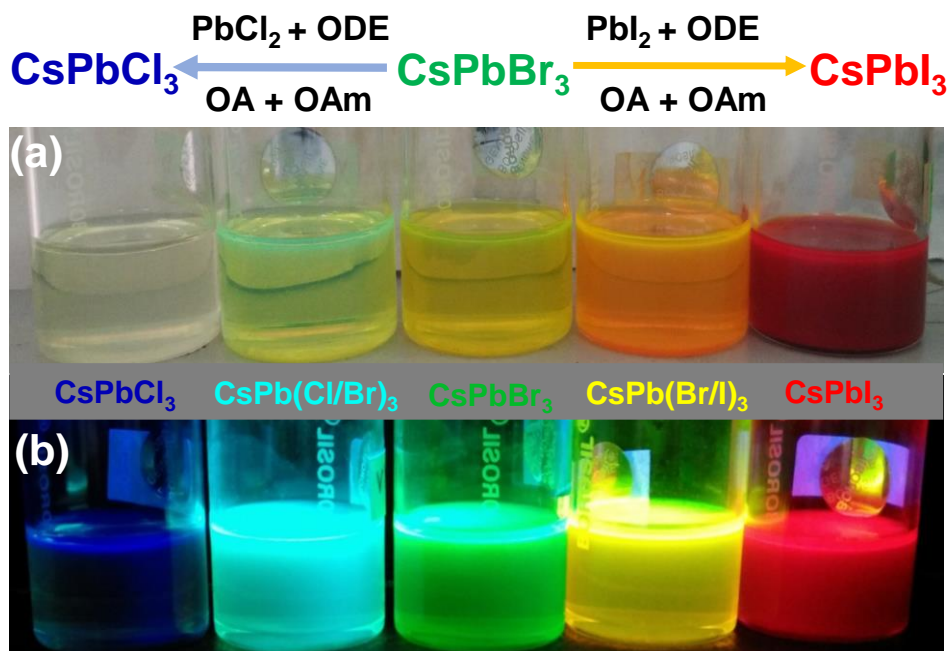
Figure 2.4: Schematic representation of anion exchange reactions along with digital photographs of colloidal dispersion of CsPbX$_3$ NCs captured under ambient light (a) and UV light (b) with various halide compositions.

UV-visible absorption and PL spectra of CsPbX$_3$ NCs dispersion in toluene is shown in Figure 2.5. It can be seen that with different halide compositions i.e. going from Cl to Br to I, the optical bandgap (determined from absorption spectra) systematically decreases as identified by their redshift in peak positions. This led to the tuning of PL peak positions between 420 nm to 666 nm, covering the entire visible region of spectrum.
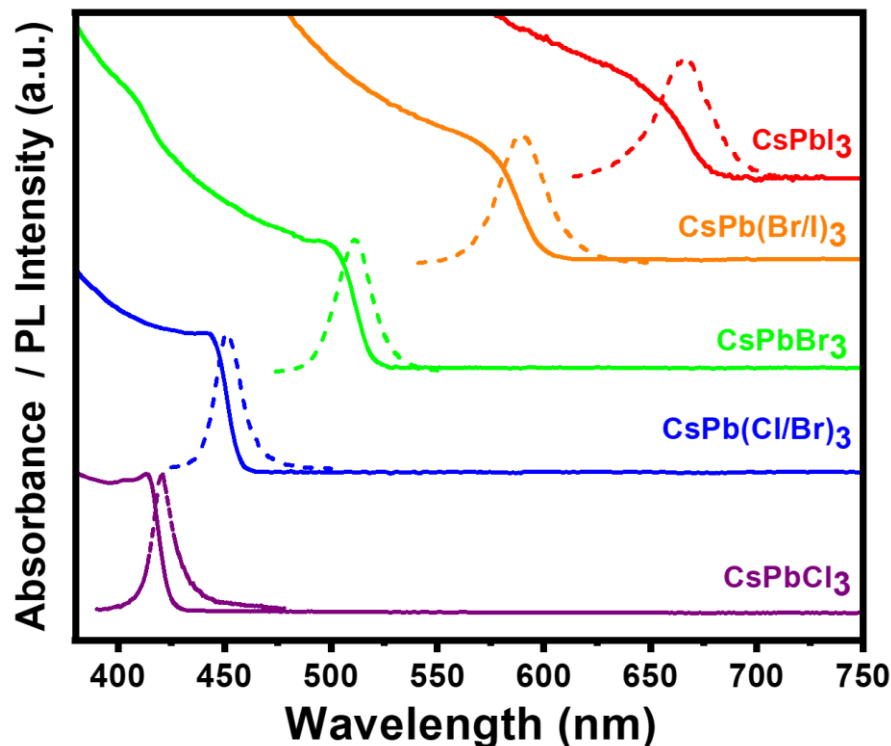
Figure 2.5: UV-visible absorbance spectra (shown by solid lines) and PL spectra (shown by dashed lines) of CsPbX$_3$ NCs dispersed in toluene. Absorbance and PL spectra are shifted vertically for clear presentation. Tuning of bandgap can be seen in the entire visible region just by changing anion composition. The excitation wavelength of 370 nm is used to record PL spectra.

2.3.2 Band edge energy levels of CsPbX$_3$ NCs:

Nature of VBM and CBM of bulk CH$_3$NH$_3$PbI$_3$ is being studied in recent time to optimize solar cell operation. In this regard, theoretical studies are in the forefront however, some of the aspects like how the energy of VBM and CBM changes with halide composition are not yet clear from theoretical studies showing diverging trends.[22, 23] One problem that electronic band structure calculations suffers in comparing band edge energies of different systems (samples) is the absence of a vacuum level, and the energy scale is typically defined relative to an internal reference, which again varies with composition and structure of the system.[22, 24]

Experimental determination of the VBM and CBM of $CH_3NH_3PbX_3$ or $CsPbX_3$ mainly relied on challenging techniques such as ultraviolet photoemission spectroscopy (UPS) and inverse photoemission spectroscopy (IPES) respectively.[25, 26] Only a few of such studies have been reported with emphasis on iodide based low bandgap solar cell materials. These prior literatures show that the dependence of CBM and VBM on halide compositions of bulk or thin film of lead halide perovskite is not yet established, and then there was no experimental study on band edge energies of $CsPbX_3$ NCs. Particularly, for optimization of $CsPbX_3$ NC based LEDs, knowledge of band edge energies of all compositions emitting from blue to red light is important.

CV is an established technique to study band edges in solution phase at room temperature and ambient pressure.[27-33] Such studies involve charge transfer across electrode-NC interface in the situation which is closer to the actual performance of devices. We have employed CV for determining CBM and VBM of $CsPbX_3$ NCs. One advantage of these organic capped NCs is that the NCs can be dispersed in a (less-polar) solvent medium, unlike their bulk counterpart. In present study, CV experiments are performed in mixture of solvents (acetonitrile and toluene (1:4 v/v)) under inert atmosphere and ferrocene/ferrocenium redox couple used as an internal standard as shown in Figure 2.6.
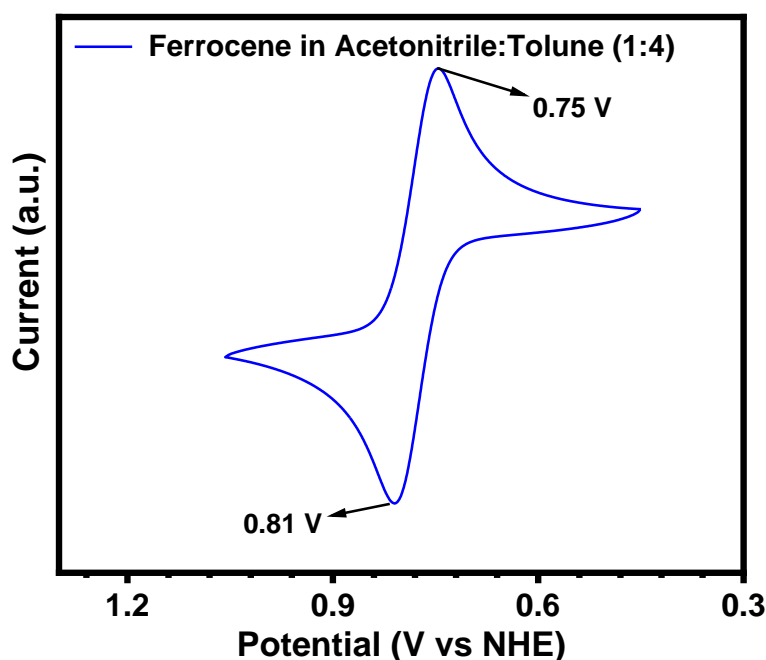
Figure 2.6: Cyclic voltammograms recorded for ferrocene/ferrocenium redox couple in 50 mM TBAP solution in 1:4 v/v mixture of acetonitrile and toluene. Scan rate used is 50 mV/s and the formal potential is 0.78 V.
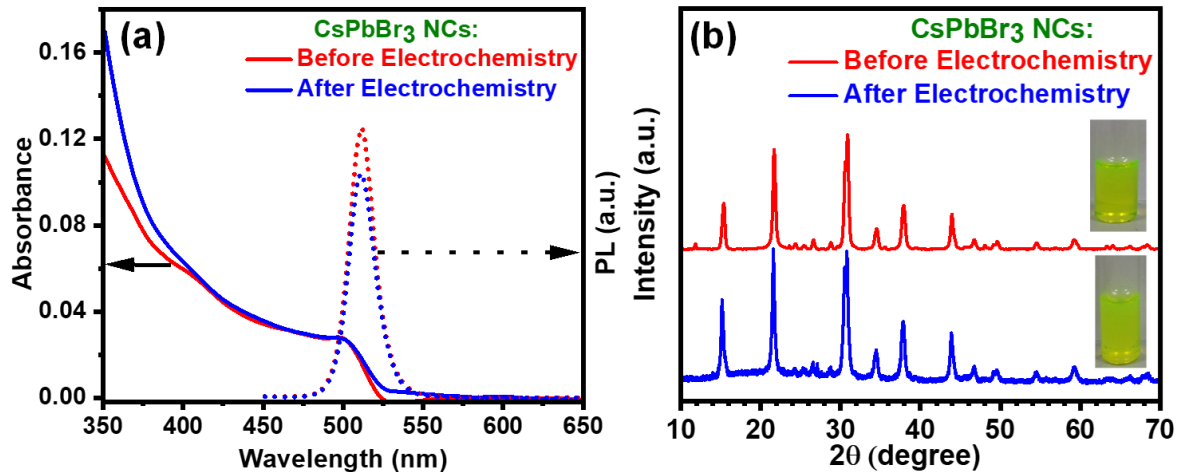
Figure 2.7: (a, b) UV-visible absorption and PL spectra, and (b) PXRD pattern of CsPbBr₃ NCs before and after the 10 cycles of CV measurements. PXRD pattern are shifted vertically for a better presentation. Inset of (b) shows the digital photograph of CsPbBr₃ NCs dispersion in toluene captured before and after CV measurements (after CV measurement, the NCs dispersion is precipitated and redispersed in toluene).

Such dispersion of NCs in a suitable solvent helps CV study because the electrolyte TBAP can be dispersed in the same medium together with the NCs. Since lead halide perovskite compounds have a tendency to degrade in presence of water and other polar solvents, the stability in composition and size of NCs during the CV experiments is confirmed by obtaining UV-visible absorption, PL, and PXRD pattern of NCs before and after the 10 cycles of CV measurements as shown in Figure 2.7. There is no noticeable change in peak position in UV-visible and PL spectra of the colloidal dispersion obtained before and after the CV measurements however, PL peak intensity is decreased somewhat after the CV measurements. Decrease in PL intensity is probably because of minor agglomeration and/or presence of different electrolyte systems. Similar PXRD patterns are observed for both samples before and after CV measurements, confirming the crystal structure remained intact during the CV experiment. Also, widths of PXRD peaks remained unaltered before and after the CV measurements, again suggesting that the crystal size does not change during the CV measurement. All these results confirm that the CsPbX₃ NCs are stable during the CV measurements.

Figure 2.8 compares cyclic voltammograms of CsPbBr₃ NCs with that of blank sample without the NCs. While scanning potential from 0 V towards more positive potential, distinct anodic peak is observed at + 1.35 V (labeled as A₁ in figure 2.8a). After peak A₁, increase in current is observed while going towards more positive

potential which is probably because of further oxidation of NCs. Upon reversal of scan two cathodic peaks are observed at -0.73 V and -1.15 V, which are labeled as C$_1$ and C$_2$ respectively. Reversing the scan again toward less negative potential, two peaks are observed with small intensities and labeled as A$'$ and A$_2$. These small peaks are assigned to interference of reduced product. The peak potential difference between the peak A$_1$ and C$_1$ was 2.07 V while that between A$_1$ and C$_2$ is 2.47 V. This A$_1$-C$_2$ peak potential difference is close to the optical bandgap 2.48 eV (500 nm) obtained from Figure 2.4, and hence peak A$_1$ and C$_2$ can be assigned to electron transfer between NCs and electrode interface *via* VBM and CBM of NCs respectively. We note here that unlike organic semiconductors, VBM and CBM of inorganic semiconductor NCs are assigned at the peak position of the anodic and cathodic peaks respectively, instead of peak onsets.
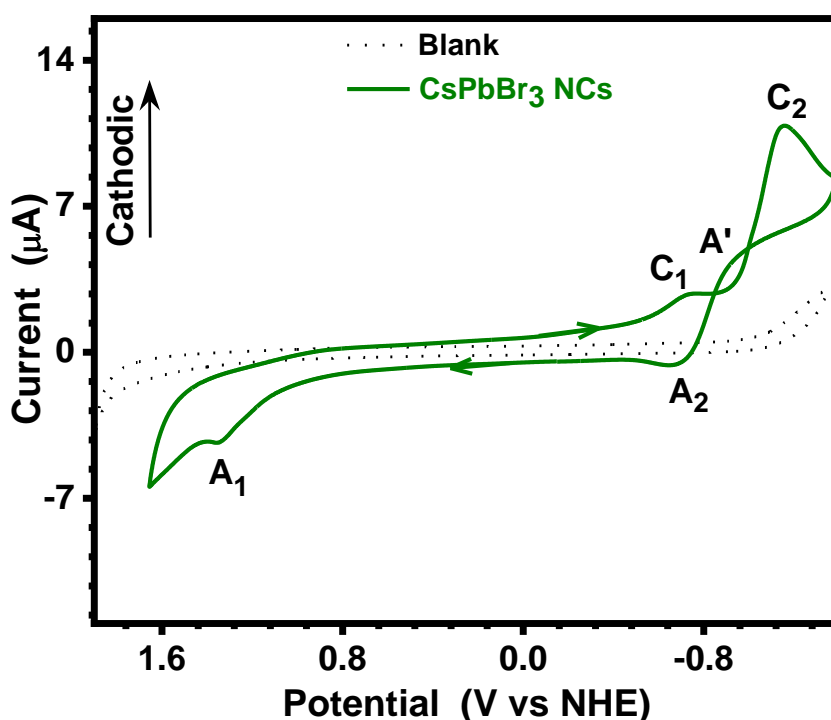
Figure 2.8: Cyclic voltammograms of CsPbBr$_3$ NCs (green line) dispersed in 50 mM TBAP solution in 1:4 v/v mixture of acetonitrile and toluene. Dotted line indicates cyclic voltammogram of blank recorded for electrolyte solution without NCs. Scan rate used is 50 mV/s

Origin of peak C$_1$ is not so clear, but Figure 2.9a shows that the unreacted Pb-Oleate exhibit peak near the potential of C$_1$. Further to check the effect of scan direction on peak potential and intensity we performed measurements both starting from 0 V towards positive and towards negative potentials separately. In both the

cases, peak current and potentials agrees well with the complete cycle measurements as shown in Figure 2.9b.
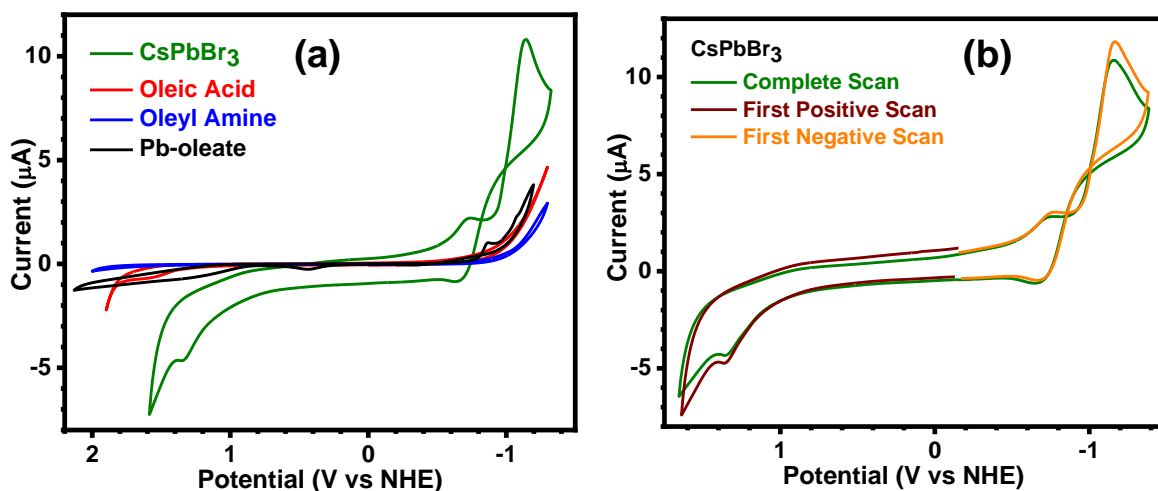
Figure 2.9: (a) Cyclic voltammograms recorded on $CsPbBr_3$ NCs, OA, OAm and Pb-Oleate in 50 mM TBAP solution in 1:4 v/v mixture of acetonitrile and toluene. (b) Cyclic voltammograms recorded on $CsPbBr_3$ NCs with different scan directions in 50 mM TBAP solution in 1:4 v/v mixture of acetonitrile and toluene. Scan rate used is 50 mV/s.
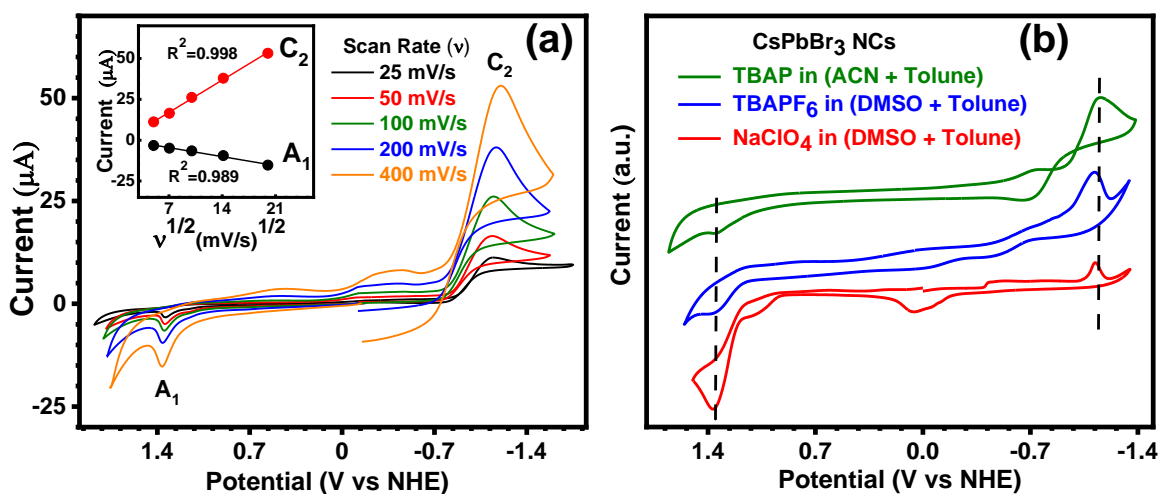
Figure 2.10: (a) Cyclic voltammograms recorded on $CsPbBr_3$ NCs with different scan rates in 50 mM TBAP solution in 1:4 v/v mixture of acetonitrile and toluene. Inset shows plot of peak current of A_1 and C_2 versus square root of scan rate where solid line indicates linear fit. (b) Cyclic voltammograms recorded on $CsPbBr_3$ NCs in different solvent/electrolyte media. Scan rate used is 50 mV/s. Voltammograms are shifted vertically for a better presentation.

In order to check effect of scan rate, CV measurements are performed with different scan rate ranging from 20-400 mV/s as shown in Figure 2.10a. Linear fit of A_1 and C_2 peak current versus square root of scan rate suggests the diffusion-

controlled charge transfer. To check the effect of solvent/electrolyte media on electrochemical behavior of CsPbBr$_3$ NCs, CV measurements are carried out in three different solvent/electrolyte combinations, as shown in Figure 2.10b. In all three solvent/electrolyte media prominent oxidation and reduction peaks are observed. The obtained energies for VBM and CBM of CsPbBr$_3$ NCs in different solvent/electrolyte media matches with each other, suggesting that a particular electrolyte and solvent is not influencing the measure band edge energies. All these above measurements support our assignment of peak A$_1$ to VBM and peak C$_2$ to CBM.
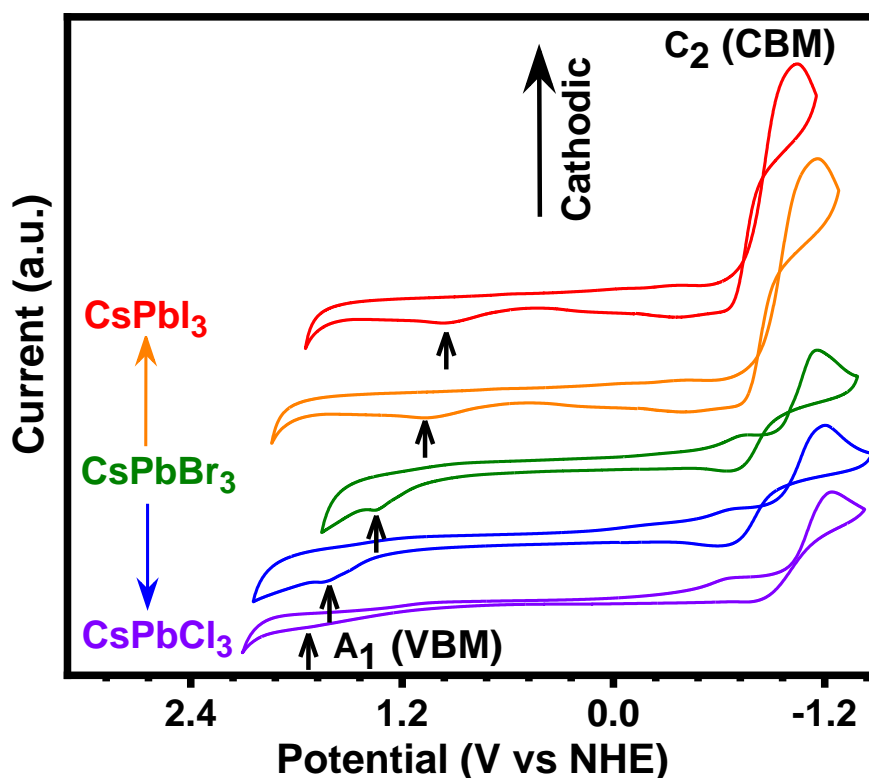
Figure 2.11: CV data of CsPbX$_3$ NCs with different halide compositions. Voltammograms are shifted vertically for a better presentation. Scan rate used is 50 mV/s.

For comparing different CsPbX$_3$ NCs samples, CV measurements are carried out under identical conditions using 50 mV/s scan rate. Cyclic voltammograms in Figure 2.11 show that peak potentials of A$_1$ and C$_2$ systematically changes depending on the halide composition, whereas peak potential of C$_1$ do not have any systematic relation with halide composition. From peak potential of A$_1$ and C$_2$, VBM and CBM of all samples are estimated and their energy levels with respect to vacuum are plotted in Figure 2.12, and also tabulated in Table 2.1. Moving from Cl to Br to I,

VBM shifted prominently towards higher energies (less positive potentials) while a smaller shift is observed for CBM towards lower energies (less negative potentials). This leads to a decrease in electrochemical bandgap for $CsPbX_3$ NCs with X = Cl to Br to I, similar to the change in optical bandgap (Figure 2.4) values as shown in Figure 2.12b.
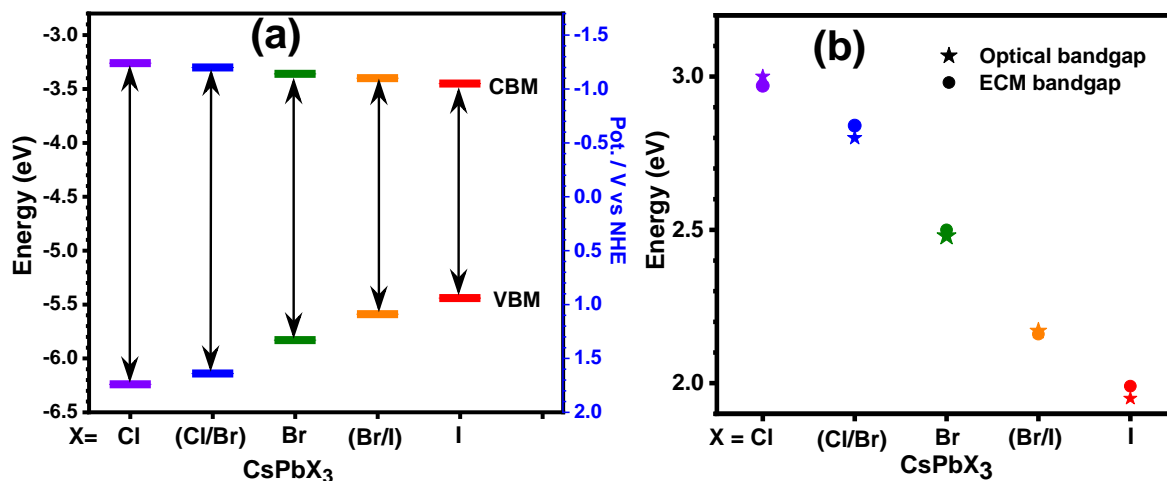
Figure 2.12: (a) Band edge energies of $CsPbX_3$ NCs extracted from Figure 2.11. (b) Comparison of obtained optical and electrochemical (ECM) bandgap values.

Table 2.1: Optical and electrochemical bandgap, VBM and CBM energy levels versus NHE and vacuum of $CsPbX_3$ NCs samples.

Nanocrystals sample	Optical bandgap (eV)	Electro-chemical bandgap (eV)	VBM (V) vs NHE	CBM (V) vs NHE	VBM (V) vs vacuum	CBM(V) vs vacuum
$CsPbCl_3$	3	2.97	1.74	-1.24	-6.24	-3.26
$CsPb(Cl/Br)_3$	2.8	2.84	1.64	-1.2	-6.14	-3.30
$CsPbBr_3$	2.48	2.47	1.35	-1.15	-5.85	-3.35
$CsPb(Br/I)_3$	2.17	2.16	1.09	-1.10	-5.59	-3.40
$CsPbI_3$	1.95	1.99	0.94	-1.05	-5.44	-3.45

A comparison of our data with literature reports showing influence of halide composition on both VBM and CBM for bulk or thin film of $APbX_3$ (A = Cs or CH_3NH_3) are shown in Figure 2.13. VBM and CBM for all $APbI_3$ taken from different literatures have been defined to 0.0 eV and 1.99 eV respectively, and then the shift in VBM and CBM for other $APbX_3$ with different X has been plotted with respect to the

defined values of $APbI_3$, within a given literature report. It is to be noted here both Cs^+ and $CH_3NH_3^+$ do not contribute directly to these band edges,[34, 35] and also size of our NCs are large enough with weak quantum confinement effect. So, inhomogeneity in crystallite size and counter cations Cs^+ vs $CH_3NH_3^+$, among different samples is not expected to significantly influence the results shown in Figure 2.13, and the observed trends are because of the change in halide compositions of PbX_6 octahedra. Inset in Figure 2.13 highlights the inconsistency in reported theoretical results where ref[23] suggests both CBM and VBM shift almost by equal extent with change in halide compositions, but ref[22] suggests extent of change in VBM was significantly more prominent than the change in CBM. Our CV data show VBM depends more strongly on halide composition compared to CBM. UPS and IPES data available for limited compositions suggest a good agreement of prior experimental data[25, 26] with a subset of our data, and also the theoretical calculations reported in ref[22] agree with our data.
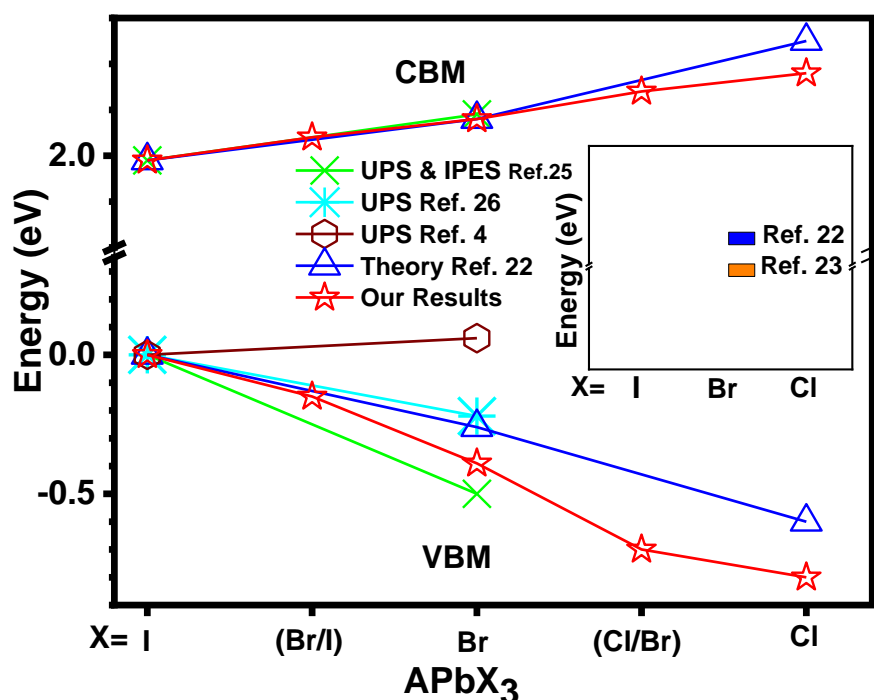
Figure 2.13: (a) Comparison of observed VBM and CBM of $APbX_3$ (A = Cs and CH_3NH_3) shifts with prior literature. VBM and CBM of $APbI_3$ have been fixed at 0.0 eV and 1.99 eV respectively, for all reported literatures. Shift in VBM and CBM for other halide compositions within a given report has been plotted with respect to the fixed values of $APbI_3$. (Where UPS: ultra-violet photoelectron spectroscopy, IPES: inverse photoelectron spectroscopy) Inset shows comparison of theory result from two different sources showing the extent of calculated shifts in VBM and CBM with halide composition do not agree with each other.

A simplified schematic representation of molecular orbital diagram of formation of valence and conduction band for lead halide perovskite is shown in Figure 2.14, after adapting it from ref[36]. It has been shown consistently in different reports[34-36] that the VBM of CsPbX₃ (or CH₃NH₃PbX₃) is mainly constituted by anti-bonding hybridization Pb 6s and X np orbitals, with major contribution from X np. Therefore, as we move from I (5p) to Br (4p) to Cl (3p), the energies of the halide p orbital decreases, shifting the VBM towards more positive potentials. On the other hand, theoretical understanding of the nature of CBM is still somewhat debated, with a section of reports suggest CBM is constituted exclusively by Pb 6p orbital[35], and some other reports suggest CBM arises from anti-bonding mixing of Pb 6p and X np orbitals[34, 36] with dominant contributions from Pb 6p as shown in Figure 2.14. Our CV data showing small changes in CBM with change in halide composition support that CBM is predominantly constituted by Pb orbitals, but still a systematic shift in CBM suggest contribution from halides to CBM cannot be neglected.
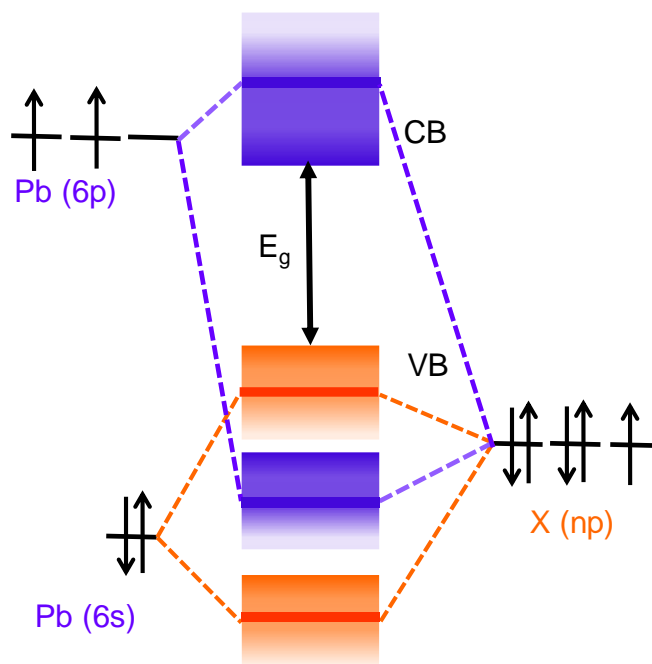
Figure 2.14: Schematic representation of bonding/antibonding orbitals of APbX₃ showing the formation of valence band (VB) and conduction band (CB). This schematic has been redrawn using results given in ref[36], which is based on the density functional theory calculations including spin-orbit interactions.

Another important parameter known to influence CBM energy is the spin-orbit coupling, but for all the halide compositions, X = Cl, Br, and I, spin-orbit coupling constant has been found to be nearly constant around 1.1 eV.[37] Therefore,

the systematic variation of CBM with halide compositions agrees with the section of computation studies suggesting that the CBM is constituted by anti-bonding states with dominant Pb 6*p* and minor X n*p* character as schematically represented in Figure 2.14. Pb-X bond lengths decreases and hence extent of hybridization is expected to increase from X = I to Br to Cl, which in turn can shift the CBM towards higher energies.

Our results explaining the dependency of band edge states on halide composition of CsPbX₃ NCs will be helpful to design suitable interfaces in both new heterostructured materials and optoelectronic devices. For example, if a CsPbI₃/CsPbCl₃ core/shell (or other kinds of heterostructures) NC is prepared, then the hole is expected to be confined within the CsPbI₃ core, whereas electron will be largely delocalized over both the core and shell, providing a pseudo type-II band alignment. A comparison of band edges of CsPbBr₃ NCs with other known semiconductors in bulk state is shown in Figure 2.15. For example, CsPbI₃/ZnS interface will be a type-I interface, whereas CsPbI₃/ZnTe interface will be type-II interface suitable for p-n junction. However, we note here that the synthesis of such heterostructured NCs would be challenging because of possibilities of cation and anion exchange across the interface.
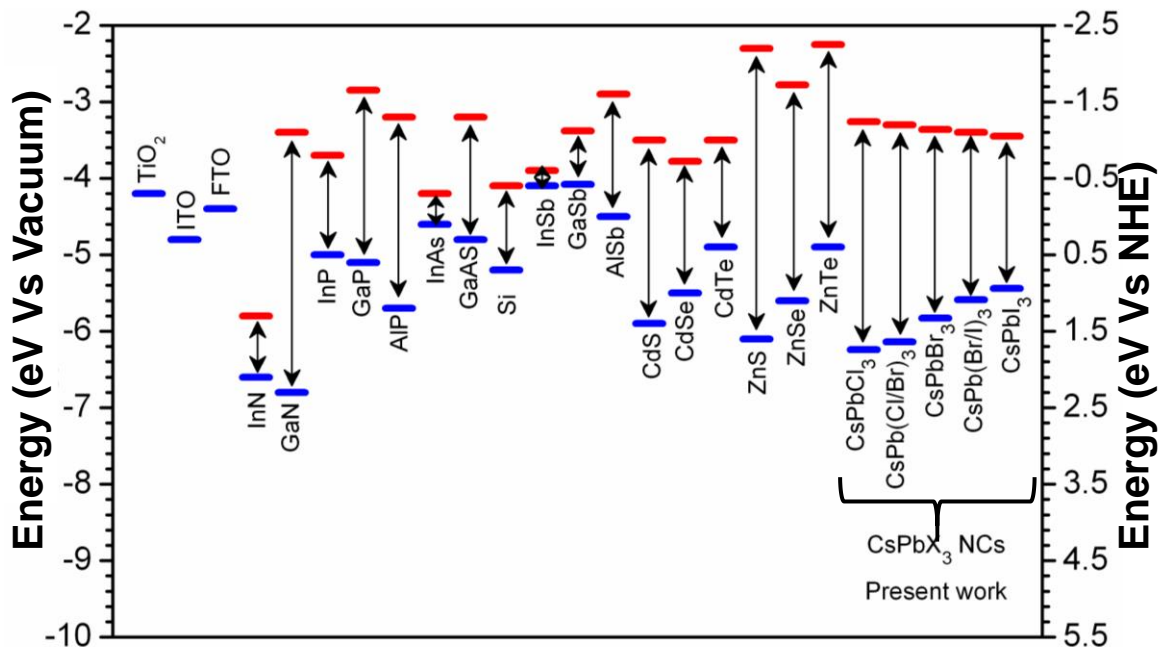
Figure 2.15: Comparison of band edge positions of CsPbX₃ NCs estimated from our CV results with selected III-V and II-VI semiconductors in bulk state. Results for III-V and II-VI semiconductors are taken from ref[38, 39].

Additionally, Figure 2.16 provides the relevant energies of various well-known hole and electron transporting materials relevant for LEDs and solar cell materials, in comparison of the band edge energies of our CsPbX₃ NCs.
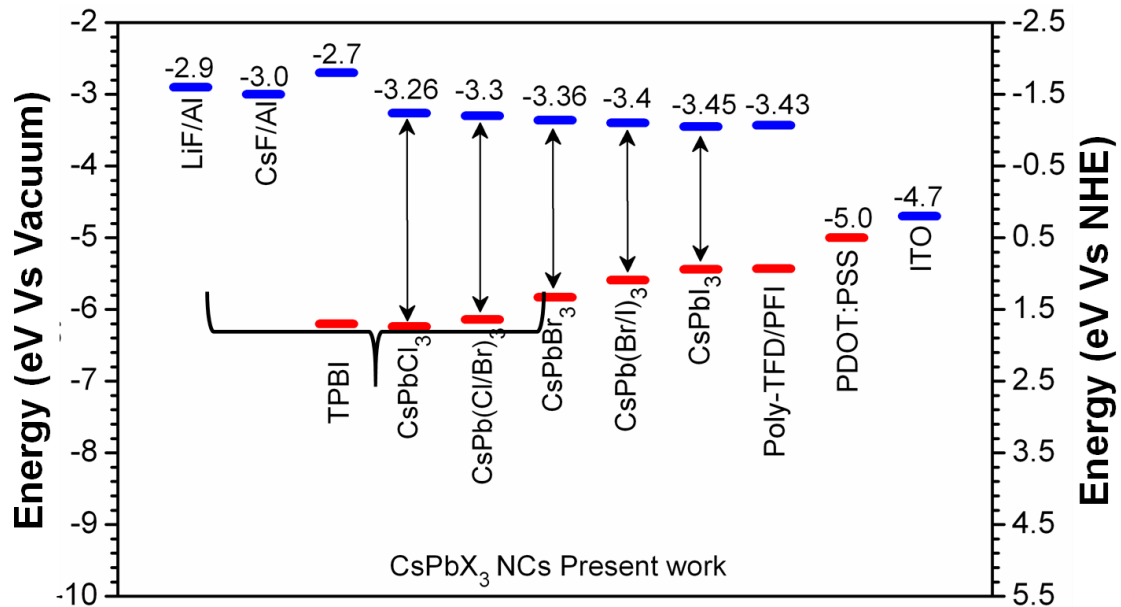
Figure 2.16: Band edge positions of our CsPbX₃ NCs with respect to different hole and electron transport materials used for light emitting diode device preparation, values were adopted from ref[18].

2.3.3 Optical transition probabilities of CsPbX₃ NCs:

After understanding the nature of band edges, it is important to know the probabilities of optical transitions across these band edges, which can be termed as the lowest energy excitonic transitions. For applications like solar cells and photodetectors, absorption cross-section or molar extinction coefficients for excitonic transition is crucial, whereas, for LED applications, transition probability of excitonic emission is important. Figure 2.17 shows the plot of absorbance, A of the lowest energy excitonic transition against molar concentration, C of CsPbX₃ NCs with different halide compositions. The linear behavior of A *vs* C plots shows that all samples obey Beer-Lambert law, $A = \varepsilon \times C \times L$, where ε is the molar extinction coefficient and L is the optical path length = 1 cm, as determined by the dimension of the cuvette. The tricky part here is the determination of C that involves multiple steps where concentration of only inorganic CsPbX₃ part has been measured excluding the contribution from organic capping ligands. The obtained values of ε are used for calculation of absorption cross-section (σ) using the following equation,

$\varepsilon(E) = \frac{N_A * \sigma(E)}{1000 * ln(10)}$ here E is the energy of absorbed light corresponding to the respective lowest energy excitonic transition and N_A (mol^{-1}) is the Avogadro's number.
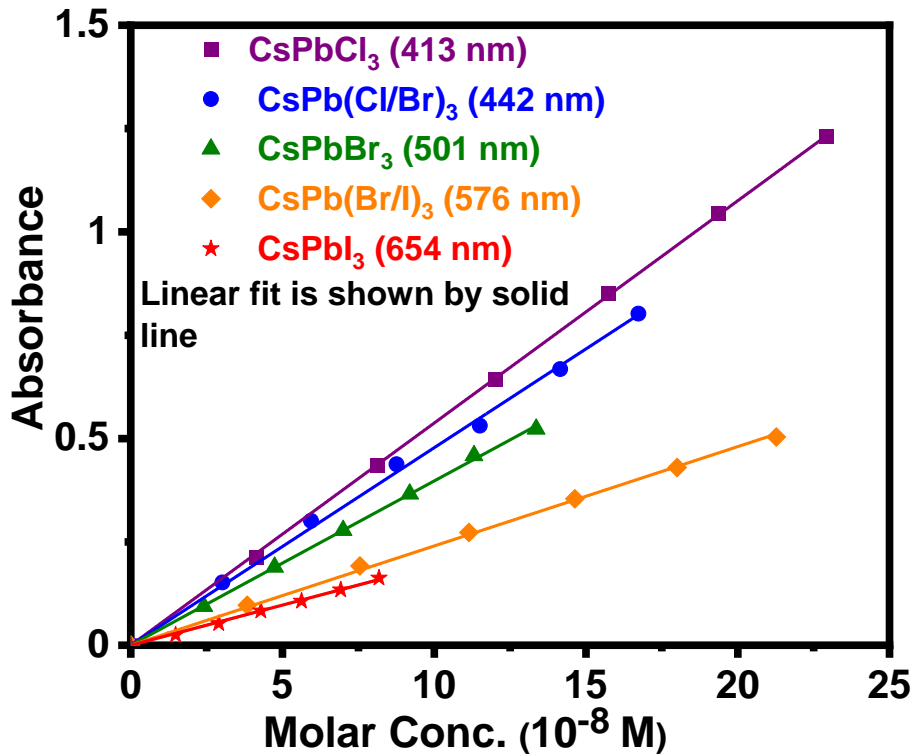
Figure 2.17: (a) Plot of absorbance vs molar concentration of $CsPbX_3$ NCs with different halide composition.

Figure 2.18 shows a systematic increase in the ε from X = I to Br to Cl. Since size of all these NCs are similar, along with similar weak quantum confinement effect, the decrease in dielectric constant from $CsPbI_3$ (6.32) to $CsPbBr_3$ (4.96) to $CsPbCl_3$ (4.07) explain the observed change in ε with halide compositions. Smaller the dielectric screening, larger is the excitonic binding energy, which in turn get reflected into the stronger cross-section for excitonic absorption. Expectedly, reported excitonic binding energies for bulk $CsPbI_3$, $CsPbBr_3$ and $CsPbCl_3$ are 20, 40, and 75 meV respectively.[13] Figure 2.18 also compares ε values of our $CsPbX_3$ NCs with reported values of CdSe NCs[38] with similar optical bandgaps. Clearly, ε for $CsPbX_3$ NCs are about an order of magnitude larger compared CdSe NCs in most part of the visible region. It is to be noted here that the smaller size of CdSe NCs is one of the major causes for its lower ε values. For example, CdSe NCs with optical bandgap at 413 nm has an average diameter of 1.6 nm, whereas, our $CsPbCl_3$ NCs

with similar optical bandgap exhibit 11 nm edge-length of cubes. As the size of CdSe NCs increases, optical bandgap red shifts along with increase in its ε values.
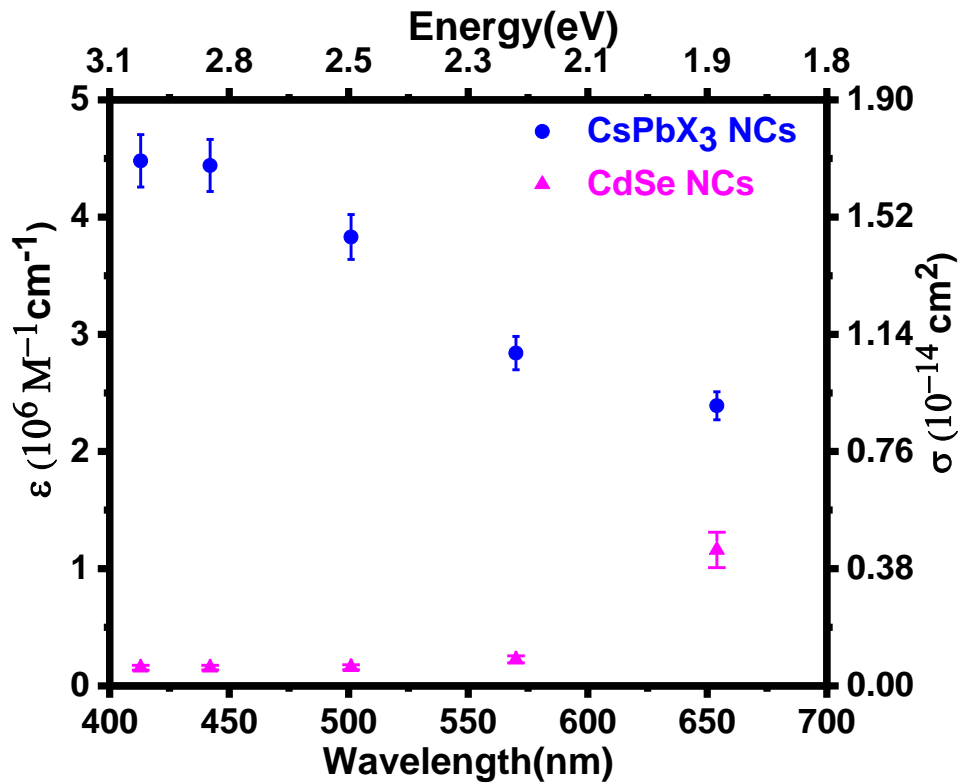
Figure 2.18: Molar extinction coefficient and absorption cross section of CsPbX₃ NCs compared with CdSe NCs with similar optical bandgap.

PL decay dynamics shown in Figure 2.19 (fitting parameters are shown in Table 2.2) suggest that the radiative lifetime decreases systematically as the composition of X varies from I to Br to Cl and similar trend has been observed in literature.[19, 39] Having low PL lifetime (τ), implies higher rate (k = 1/τ), of spontaneous emission and this rate is then characteristic of the material and depends on the dielectric constant or refractive index of the material. So, transition probabilities for excitonic absorption and emission systematically increases as the compositions of CsPbX₃ NCs changed from X = I to Br to Cl. However, we cannot rule out the possibility of halide dependent change in the overlap of electron-hole wavefunctions based on the hybridization of VBM and CBM, and further theoretical study is required for a better understanding. It is to be noted that while a decrease in dielectric constant can be beneficial for increase excitonic absorption cross-section, but in general, a decrease in dielectric constant also decreases the efficiency excitonic dissociation and increases the probability of capturing minority carriers by charged defects.[36] So,

a better performance of an optoelectronic device depends on simultaneous optimization of all these parameters.
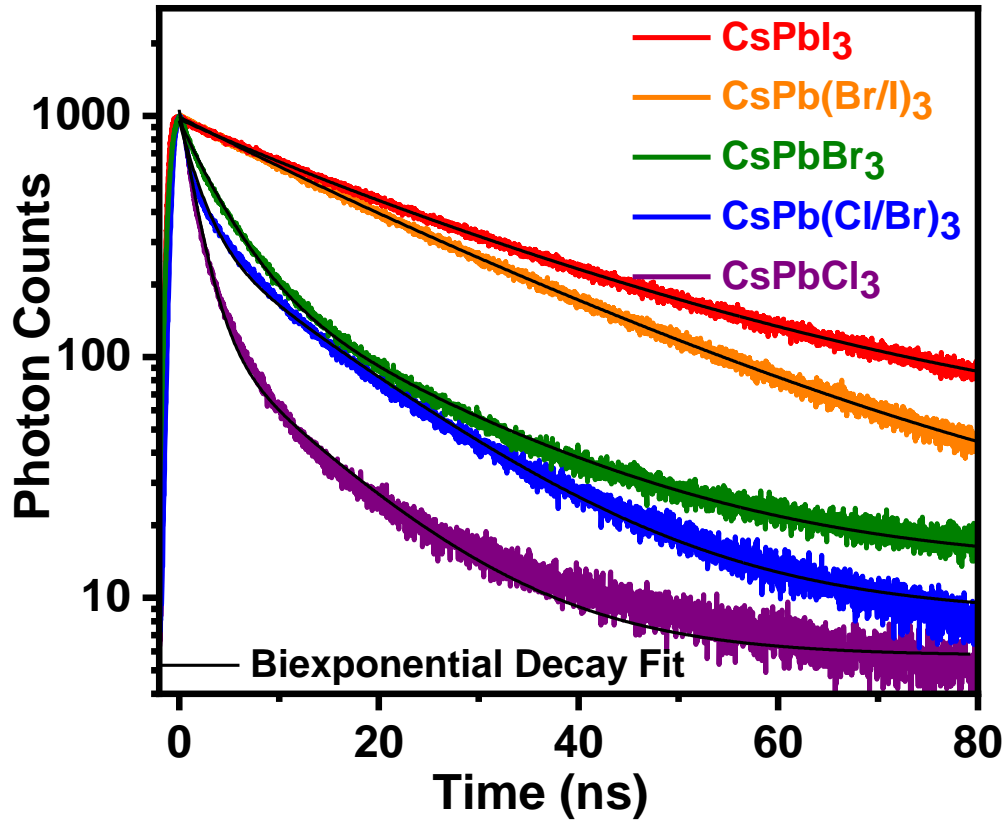
Figure 2.19: PL decay of $CsPbX_3$ NCs recorded at individual PL peak wavelength of each samples. Excitation wavelength is 380 nm. Fitting parameters are given in Table 2.2.

Table 2.2: PL Decay lifetime of $CsPbX_3$ NCs obtained from Figure 2.19 at their emission peak wavelength.

Nanocrystals sample	a_1	τ_1 (ns)	a_2	τ_2 (ns)	τ_{avg} (ns)[a]
$CsPbCl_3$	0.84	1.4	0.16	6.2	3.5
$CsPb(Cl/Br)_3$	0.69	2.2	0.31	6.8	4.9
$CsPbBr_3$	0.64	4.2	0.36	8.4	6.4
$CsPb(Br/I)_3$	0.79	23.4	0.21	12.2	22.0
$CsPbI_3$	0.78	27.9	0.22	11.4	26.2

$$^{a}\tau_{avg} = \frac{\sum a_i \tau_i^2}{\sum a_i \tau_i}$$

2.4 Conclusions:

In conclusion, we have elucidated how halide compositions contribute to the VBM and CBM of colloidal CsPbX$_3$ NCs, including the probability of optical transitions across these states. CV results suggest predominant contribution of VBM in tuning of optical bandgap across the visible region by changing the halide composition from X = Cl to Br to I. Interestingly, CBM also shifts systematically with halide composition though the shift is small. This shift in CBM indicates that the contribution of halides to CBM is not negligible, and agrees with a section of the theoretical studies suggesting CBM is formed by anti-bonding Pb 6p and X np interactions. Probability for optical transition across these band edges, which is essentially the lowest energy excitonic transition also exhibit a systematic trend. ε for lowest energy excitonic absorption decreases from X = Cl to Br to I, probably because of the increase in dielectric screening of the excitonic binding energy with this composition change. Interestingly, the ε values of CsPbX$_3$ NCs are about an order of magnitude higher than that of CdSe NCs with similar optical bandgap. To the best our knowledge, this is the first experimental report showing the influence of halide compositions on valence and conduction band edges for different compositions of CsPbX$_3$ with optical bandgap across the entire visible region, and would be useful in designing suitable interfaces in blue to red LEDs, and also in designing heterostructured NCs with desired interfacial band alignments.

2.5 References:

1. Shi, D.; Adinolfi, V.; Comin, R.; Yuan, M.; Alarousu, E.; Buin, A.; Chen, Y.; Hoogland, S.; Rothenberger, A.; Katsiev, K.; Losovyj, Y.; Zhang, X.; Dowben, P. A.; Mohammed, O. F.; Sargent, E. H.; Bakr, O. M., Low trap-state density and long carrier diffusion in organolead trihalide perovskite single crystals. *Science* **2015,** *347*, 519-522.

2. Manser, J. S.; Christians, J. A.; Kamat, P. V., Intriguing Optoelectronic Properties of Metal Halide Perovskites. *Chem. Rev.* **2016,** *116*, 12956-13008.

3. Zhumekenov, A. A.; Saidaminov, M. I.; Haque, M. A.; Alarousu, E.; Sarmah, S. P.; Murali, B.; Dursun, I.; Miao, X.-H.; Abdelhady, A. L.; Wu, T.; Mohammed, O. F.; Bakr, O. M., Formamidinium Lead Halide Perovskite Crystals with

Unprecedented Long Carrier Dynamics and Diffusion Length. *ACS Energy Lett.* **2016,** *1*, 32-37.

4. Kojima, A.; Teshima, K.; Shirai, Y.; Miyasaka, T., Organometal Halide Perovskites as Visible-Light Sensitizers for Photovoltaic Cells. *J. Am. Chem. Soc.* **2009,** *131*, 6050-6051.

5. Etgar, L.; Gao, P.; Xue, Z.; Peng, Q.; Chandiran, A. K.; Liu, B.; Nazeeruddin, M. K.; Grätzel, M., Mesoscopic $CH_3NH_3PbI_3/TiO_2$ Heterojunction Solar Cells. *J. Am. Chem. Soc.* **2012,** *134*, 17396-17399.

6. Lee, M. M.; Teuscher, J.; Miyasaka, T.; Murakami, T. N.; Snaith, H. J., Efficient hybrid solar cells based on meso-superstructured organometal halide perovskites. *Science* **2012,** *338*, 643-647.

7. Christians, J. A.; Fung, R. C.; Kamat, P. V., An inorganic hole conductor for organo-lead halide perovskite solar cells. Improved hole conductivity with copper iodide. *J. Am. Chem. Soc.* **2014,** *136*, 758-764.

8. Zhou, Y.; Zhu, K., Perovskite Solar Cells Shine in the "Valley of the Sun". *ACS Energy Lett.* **2016,** *1*, 64-67.

9. Arora, N.; Orlandi, S.; Dar, M. I.; Aghazada, S.; Jacopin, G.; Cavazzini, M.; Mosconi, E.; Gratia, P.; De Angelis, F.; Pozzi, G.; Graetzel, M.; Nazeeruddin, M. K., High Open-Circuit Voltage: Fabrication of Formamidinium Lead Bromide Perovskite Solar Cells Using Fluorene–Dithiophene Derivatives as Hole-Transporting Materials. *ACS Energy Lett.* **2016,** *1*, 107-112.

10. Saliba, M.; Matsui, T.; Seo, J.-Y.; Domanski, K.; Correa-Baena, J.-P.; Nazeeruddin, M. K.; Zakeeruddin, S. M.; Tress, W.; Abate, A.; Hagfeldt, A.; Grätzel, M., Cesium-containing triple cation perovskite solar cells: improved stability, reproducibility and high efficiency. *Energy Environ. Sci.* **2016,** *9*, 1989-1997.

11. Yakunin, S.; Sytnyk, M.; Kriegner, D.; Shrestha, S.; Richter, M.; Matt, G. J.; Azimi, H.; Brabec, C. J.; Stangl, J.; Kovalenko, M. V.; Heiss, W., Detection of X-ray photons by solution-processed lead halide perovskites. *Nat. Photonics* **2015,** *9*, 444-449.

12. Schmidt, L. C.; Pertegas, A.; Gonzalez-Carrero, S.; Malinkiewicz, O.; Agouram, S.; Minguez Espallargas, G.; Bolink, H. J.; Galian, R. E.; Perez-Prieto,

J., Nontemplate synthesis of CH$_3$NH$_3$PbBr$_3$ perovskite nanoparticles. *J. Am. Chem. Soc.* **2014,** *136*, 850-853.

13. Protesescu, L.; Yakunin, S.; Bodnarchuk, M. I.; Krieg, F.; Caputo, R.; Hendon, C. H.; Yang, R. X.; Walsh, A.; Kovalenko, M. V., Nanocrystals of Cesium Lead Halide Perovskites (CsPbX$_{(3)}$, X = Cl, Br, and I): Novel Optoelectronic Materials Showing Bright Emission with Wide Color Gamut. *Nano Lett.* **2015,** *15*, 3692-3696.

14. Swarnkar, A.; Chulliyil, R.; Ravi, V. K.; Irfanullah, M.; Chowdhury, A.; Nag, A., Colloidal CsPbBr3 Perovskite Nanocrystals: Luminescence beyond Traditional Quantum Dots. *Angew Chem. Int. Ed.* **2015,** *54*, 15424-15428.

15. Yakunin, S.; Protesescu, L.; Krieg, F.; Bodnarchuk, M. I.; Nedelcu, G.; Humer, M.; De Luca, G.; Fiebig, M.; Heiss, W.; Kovalenko, M. V., Low-threshold amplified spontaneous emission and lasing from colloidal nanocrystals of caesium lead halide perovskites. *Nat. Commun.* **2015,** *6*, 8056.

16. Yettapu, G. R.; Talukdar, D.; Sarkar, S.; Swarnkar, A.; Nag, A.; Ghosh, P.; Mandal, P., Terahertz Conductivity within Colloidal CsPbBr$_3$ Perovskite Nanocrystals: Remarkably High Carrier Mobilities and Large Diffusion Lengths. *Nano Lett.* **2016,** *16*, 4838-4848.

17. Song, J.; Li, J.; Li, X.; Xu, L.; Dong, Y.; Zeng, H., Quantum Dot Light-Emitting Diodes Based on Inorganic Perovskite Cesium Lead Halides (CsPbX$_3$). *Adv. Mater.* **2015,** *27*, 7162-7167.

18. Zhang, X.; Lin, H.; Huang, H.; Reckmeier, C.; Zhang, Y.; Choy, W. C. H.; Rogach, A. L., Enhancing the Brightness of Cesium Lead Halide Perovskite Nanocrystal Based Green Light-Emitting Devices through the Interface Engineering with Perfluorinated Ionomer. *Nano Lett.* **2016,** *16*, 1415-1420.

19. Nedelcu, G.; Protesescu, L.; Yakunin, S.; Bodnarchuk, M. I.; Grotevent, M. J.; Kovalenko, M. V., Fast Anion-Exchange in Highly Luminescent Nanocrystals of Cesium Lead Halide Perovskites (CsPbX$_3$, X = Cl, Br, I). *Nano Lett.* **2015,** *15*, 5635-5640.

20. Akkerman, Q. A.; D'Innocenzo, V.; Accornero, S.; Scarpellini, A.; Petrozza, A.; Prato, M.; Manna, L., Tuning the Optical Properties of Cesium Lead Halide Perovskite Nanocrystals by Anion Exchange Reactions. *J. Am. Chem. Soc.* **2015,** *137*, 10276-10281.

21. Ramasamy, P.; Lim, D.-H.; Kim, B.; Lee, S.-H.; Lee, M.-S.; Lee, J.-S., All-inorganic cesium lead halide perovskite nanocrystals for photodetector applications. *Chem. Commun.* **2016,** *52*, 2067-2070.

22. Butler, K. T.; Frost, J. M.; Walsh, A., Band alignment of the hybrid halide perovskites $CH_3NH_3PbCl_3$, $CH_3NH_3PbBr_3$ and $CH_3NH_3PbI_3$. *Mater. Horiz.* **2015,** *2*, 228-231.

23. Buin, A.; Comin, R.; Xu, J.; Ip, A. H.; Sargent, E. H., Halide-Dependent Electronic Structure of Organolead Perovskite Materials. *Chem. Mater.* **2015,** *27*, 4405-4412.

24. Ihm, J.; Zunger, A.; Cohen, M. L., Momentum-space formalism for the total energy of solids. *J. Phys. C: Solid State Phys.* **1980,** *13*, 3095-3095.

25. Schulz, P.; Edri, E.; Kirmayer, S.; Hodes, G.; Cahen, D.; Kahn, A., Interface energetics in organo-metal halide perovskite-based photovoltaic cells. *Energy Environ. Sci.* **2014,** *7*, 1377-1381.

26. Ryu, S.; Noh, J. H.; Jeon, N. J.; Chan Kim, Y.; Yang, W. S.; Seo, J.; Seok, S. I., Voltage output of efficient perovskite solar cells with high open-circuit voltage and fill factor. *Energy Environ. Sci.* **2014,** *7*, 2614-2618.

27. Haram, S. K.; Quinn, B. M.; Bard, A. J., Electrochemistry of CdS Nanoparticles: A Correlation between Optical and Electrochemical Band Gaps. *J. Am. Chem. Soc.* **2001,** *123*, 8860-8861.

28. Markad, G. B.; Battu, S.; Kapoor, S.; Haram, S. K., Interaction between Quantum Dots of CdTe and Reduced Graphene Oxide: Investigation through Cyclic Voltammetry and Spectroscopy. *J. Phys. Chem. C* **2013,** *117*, 20944-20950.

29. Kucur, E.; Riegler, J.; Urban, G. A.; Nann, T., Determination of quantum confinement in CdSe nanocrystals by cyclic voltammetry. *J. Chem. Phys.* **2003,** *119*, 2333-2337.

30. Inamdar, S. N.; Ingole, P. P.; Haram, S. K., Determination of Band Structure Parameters and the Quasi-Particle Gap of CdSe Quantum Dots by Cyclic Voltammetry. *ChemPhysChem* **2008,** *9*, 2574-2579.

31. Hines, D. A.; Forrest, R. P.; Corcelli, S. A.; Kamat, P. V., Predicting the Rate Constant of Electron Tunneling Reactions at the CdSe–TiO2 Interface. *J. Phys. Chem. B* **2015,** *119*, 7439-7446.

32. Janietz, S.; Bradley, D. D. C.; Grell, M.; Giebeler, C.; Inbasekaran, M.; Woo, E. P., Electrochemical determination of the ionization potential and electron affinity of poly(9,9-dioctylfluorene). *Appl. Phys. Lett.* **1998,** *73*, 2453-2455.

33. Kulbak, M.; Gupta, S.; Kedem, N.; Levine, I.; Bendikov, T.; Hodes, G.; Cahen, D., Cesium Enhances Long-Term Stability of Lead Bromide Perovskite-Based Solar Cells. *J. Phys. Chem. Lett.* **2016,** *7*, 167-172.

34. Umebayashi, T.; Asai, K.; Kondo, T.; Nakao, A., Electronic structures of lead iodide based low-dimensional crystals. *Phys. Rev. B* **2003,** *67*, 155405.

35. Filippetti, A.; Mattoni, A., Hybrid perovskites for photovoltaics: Insights from first principles. *Phys. Rev. B* **2014,** *89*, 125203.

36. Brandt, R. E.; Stevanović, V.; Ginley, D. S.; Buonassisi, T., Identifying defect-tolerant semiconductors with high minority-carrier lifetimes: beyond hybrid lead halide perovskites. *MRS Commun.* **2015,** *5*, 265-275.

37. Yuan, Y.; Xu, R.; Xu, H.-T.; Hong, F.; Xu, F.; Wang, L.-J., Nature of the band gap of halide perovskites ABX₃ (A = CH₃NH₃, Cs; B = Sn, Pb; X = Cl, Br, I): First-principles calculations. *Chin. Phys. B* **2015,** *24*, 116302.

38. Wei, S.-H.; Zunger, A., Calculated natural band offsets of all II–VI and III–V semiconductors: Chemical trends and the role of cation d orbitals. *Applied Phys. Lett.* **1998,** *72*, 2011-2013.

39. Reiss, P.; Protière, M.; Li, L., Core/Shell Semiconductor Nanocrystals. *Small* **2009,** *5*, 154-168.

40. Jasieniak, J.; Smith, L.; van Embden, J.; Mulvaney, P.; Califano, M., Re-examination of the Size-Dependent Absorption Properties of CdSe Quantum Dots. *J. Phys. Chem. C* **2009,** *113*, 19468-19474.

41. Makarov, N. S.; Guo, S.; Isaienko, O.; Liu, W.; Robel, I.; Klimov, V. I., Spectral and Dynamical Properties of Single Excitons, Biexcitons, and Trions in Cesium–Lead-Halide Perovskite Quantum Dots. *Nano Lett.* **2016,** *16*, 2349-2362.

Chapter 3

Mechanism of Ligand Binding on the Surface of CsPbBr₃ Perovskite Nanocubes
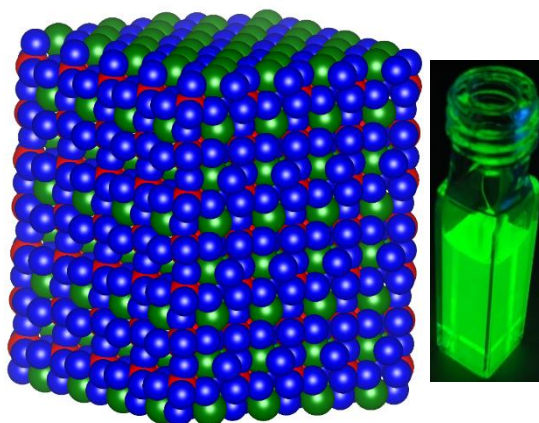
The work presented in this chapter has led to the following publication:

Ravi, V. K.; Santra, P. K.; Joshi, N.; Chugh, J.; Singh, S. K.; Rensmo, H.; Ghosh, P.; Nag, A. Origin of Substitution Mechanism for the Binding of Organic Ligands on the Surface of CsPbBr₃ Perovskite Nanocubes. *J. Phys. Chem. Lett.* **2017**, 8, 20,4988-4994. Copyright permission has been taken from ACS publication for full paper.

Declaration:

X-ray photoelectron spectroscopy is carried out by Dr. Pralay Santra (CENS, Bangalore).

Density functional theory calculations are performed by Dr. Niharika Joshi and Dr. Prasenjit Ghosh (IISER Pune).

Abstract:

As the crystallites size becomes smaller, its surface area to volume ratio increases. Thus, for a nanocrystal, its surface and the interaction of the surface with the surrounding environment plays an important role in governing its properties. For CsPbBr$_3$ perovskite nanocubes, optoelectronic properties depend strongly on the interaction of inorganic surface with the organic ligands passivating the surface. We have used synchrotron-based X-ray photoelectron spectroscopy to understand the inorganic surface composition of the CsPbBr$_3$ perovskite nanocubes and with the help of nuclear magnetic resonance spectroscopy, we characterized the organic ligands present on its surface. We have found that the oleylammonium ion acts as capping ligand by substituting some of the Cs$^+$ ions from the surface of CsPbBr$_3$ nanocubes. First principles density functional theory confirms that the substitution mechanism of Cs$^+$ ion by oleylammonium ion does not require much energy for surface reconstruction and is favoured by the three hydrogen bonds formed between the NH$_3$$^+$ moiety of oleylammonium and surrounding Br$^-$ ion on the surface of the nanocubes and thus stabilizes the nanocubes. The origin of this substitution mechanism is in stark contrast to the more common adsorption binding mechanism of organic ligands on the surface of typical nanocrystals.

Graphical Abstract:
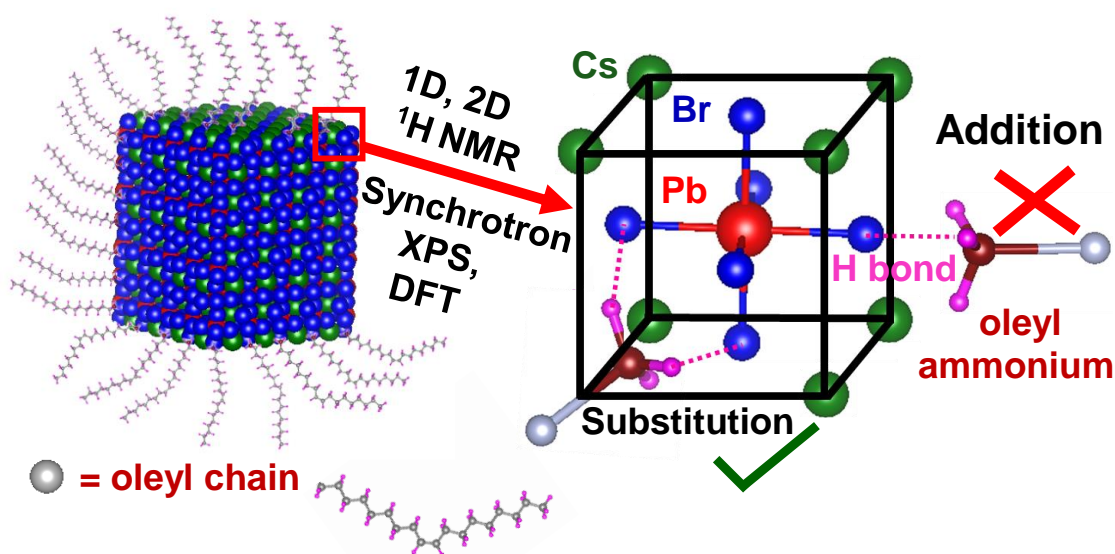
3.1 Introduction:

Colloidal cesium lead halide nanocubes became popular in recent years because of their defect-tolerant nature, where surface defects are inefficient to trap charge carriers.[1-7] Consequently, these nanocubes show promise for applications in light emitting diodes (LEDs),[8-10] solar cells,[11] and photodetectors.[12, 13] To enhance the efficacy of these applications, understanding of both the surface chemistry,[14-19] and the internal structure of nanocubes[20-25] are essential. Surface chemistry of nanocrystals (NCs) have been developed extensively for traditional II-VI, III-V, and IV-VI compound semiconductors.[14] Unfortunately, most of these previous knowledges of surface engineering for different colloidal semiconductor NCs, cannot be directly extended for Pb-halide perovskite nanocubes. One reason for such failure is that the Pb-halide nanocubes degrade in polar medium, and some of the prior surface engineering methodology involves treatment of nanocubes in polar solvents. But even in the non-polar medium, synthesis of a good quality core/shell (or other heterostructures) nanocubes of Pb-halide perovskites is challenging, whereas, heterostructured nanocubes of other semiconductors are routinely made. Therefore, one of the major challenges in this field is to have a better control of the surface chemistry of Pb-halide perovskite nanocubes. In this regard, the first step is to understand the mechanism of binding organic ligands on the surface of CsPbBr$_3$ nanocubes. Nuclear magnetic resonance (NMR) spectroscopy and Fourier transformed infrared spectroscopy (FTIR) based studies in prior literature[26-28] have characterized the passivating organic ligands but did not characterize the inorganic component on the NC surface. On the other hand, Li et al.[29] reported preliminary X-ray photoelectron spectroscopy (XPS) study for inorganic part of CsPbBr$_3$ nanocubes prepared using a different synthesis protocol but did not study the organic ligands.

In this chapter, we combine both synchrotron-based XPS and NMR results for complete elucidation of inorganic and organic moieties on the surface of CsPbBr$_3$ nanocubes, and computational studies explain the thermodynamics of ligand binding. Our experimental results show a unique interaction between the organic capping ligand and the inorganic core. Typically, organic ligands are adsorbed on the NC surface. However, in the present case, we have shown first experimental evidence that oleylammonium ions (OLA$^+$) substitute Cs$^+$ ions on the NC surface.

Calculations showed that the preference of substitution over adsorption is due to a balance between the energy cost of surface restructuring induced by the interaction of MA^+ with the surface and energy gain by MA^+ adsorption through the formation of hydrogen bonds.

3.2 Experimental Section:

3.2.1 Chemicals:

Cesium carbonate (Cs_2CO_3, 99.9%, Sigma-Aldrich), lead (II) bromide ($PbBr_2$, 99.999%, Sigma-Aldrich), oleic acid (OA, 90%, Sigma-Aldrich), oleylamine (OLA, technical grade 70%, Sigma-Aldrich), 1-octadecene (ODE, technical grade 90%, Sigma-Aldrich), acetonitrile (Anhydrous, 99.8%, Sigma-Aldrich), chloroform ($CHCl_3$, 99.5%, Sigma-Aldrich), deuterated chloroform ($CDCl_3$, 99.8 atom % D, Sigma-Aldrich).

3.2.2 Synthesis of CsPbBr₃ nanocubes:

The synthesis of $CsPbBr_3$ nanocubes is carried out in same fashion as reported in the previous chapter at 180 °C. To recap briefly, in a three- necked round bottom flask, 5 mL ODE and 69 mg (0.188 mmol) of $PbBr_2$ are added and the mixture is kept under vacuum at 120 °C for 30 min followed by N_2 purging. This cycle of alternate vacuum and N_2 purging is repeated three times to ensure effective removal of moisture and oxygen (O_2). Dried OA and OLA (0.5 mL each) are added to the mixture at 120 °C under N_2 flow. After solubilization of $PbBr_2$, reaction temperature is increased to 180 °C and 0.4 mL of Cs-oleate (pre-heated at 100 °C) is injected into the solution. The reaction is stopped after 5 sec using ice-bath. The nanocubes are precipitated by adding acetonitrile to the crude reaction mixture and centrifuging at 7000 rpm. The supernatant is discarded and the precipitate is then dissolved in $CHCl_3$ to measure the optical properties.

3.2.3 Characterization:

UV-visible absorption spectra are recorded using a Perkin Elmer, Lambda-45 UV/Vis spectrometer. Photoluminescence (PL) spectra are measured using FLS 980 (Edinburgh Instruments). UV-visible absorption and PL experiments are performed on the colloidal dispersion of $CsPbBr_3$ nanocubes in $CHCl_3$. Powder X-ray diffraction (PXRD) data are recorded using a Bruker D8 Advance X-ray

diffractometer using Cu Kα radiation (1.54 Å). Transmission electron microscopy (TEM) studies are carried out using a JEOL JEM 2100 F field emission transmission electron microscope at 200 kV. The samples for TEM are prepared by putting a drop of the colloidal dispersion of nanocubes on the carbon coated copper grids. Scanning electron microscopy (SEM) measurements are performed on Zeiss Ultra Plus SEM instrument. Dynamic light scattering (DLS) measurements are performed Malvern Zetasizer ZS90 instrument.

3.2.4 NMR spectroscopy:

For preparation of NMR samples, as synthesized $CsPbB_3$ nanocubes were first centrifuged at 7000 rpm for 10 min and the supernatant was discarded. The precipitates were then re-dispersed in $CHCl_3$ and precipitated again by adding ACN and centrifuged at 7000 rpm and supernatant was discarded. This process of washing was repeated for two times, followed by the dispersion of nanocubes in $CDCl_3$ for measuring NMR data. All NMR experiments were carried out using a Bruker Avance III HD spectrometer operating at a ^1H frequency of 400 MHz, at 298 K. ^1H, 2D nuclear Overhausser effect spectroscopy (NOESY) and 2D diffusion ordered spectroscopy (DOSY) were acquired using standard pulse sequences from the Bruker library. For ^1H measurements, spectral width was set to 20 ppm and 64 k data points were sampled with a relaxation delay of 1 s. For NOESY, 2048 data points in the direct dimension and 256 data points in the indirect dimension were sampled having spectral width set to 10 ppm with a mixing time of 500 ms. DOSY spectra were acquired by using "ledbpg2s" pulse program.[30] The gradient strength was varied linearly from 2% to 95% of probe's maximum value in 32 increments to ensure a final attenuation of the signal in the final increment of less than 10% relative to the first increment. 1D ^1H and NOESY spectra were processed in TopSpin 3.5. The diffusion coefficients were obtained by doing Bayesian DOSY transformation of the 2D DOSY spectra in software MestReNova.

3.2.5 XPS measurement:

The XPS measurements are collected at high photon energies at KMC-1 beamline[31] with HIKE end station at BESSY-II[32], Berlin. The photon energy is selected using a double-crystal monochromator (Oxford- Danfysik) and the photoelectron kinetic energies are measured using a Model R4000 analyzer (Scienta) optimized for high

kinetic energies. The photon energy is selected using a double-crystal monochromator (Oxford- Danfysik) and the photoelectron kinetic energies (KE) were measured using a Model R4000 analyzer (Scienta) optimized for high kinetic energies. In our work, we performed experiments at 2500 and 4000 eV photon energies by selecting the first order light from Si (111) and Si (311) crystals respectively. The angle between the incident photon beam and sample surface is ~ 5° and the chamber pressure was ~ 2-5 × 10^{-8} mbar. The samples are prepared by drop casting a colloidal dispersion of CsPbBr$_3$ nanocubes on TiO$_2$ coated on indium doped tin oxide (ITO) substrate.

Overview spectra and core levels are collected with pass energy (E$_p$) of 500 and 200 eV, respectively. The spectra presented in this work are energy-calibrated with Fermi energy at zero binding energy, which is determined by measuring a gold plate collected electrically to the sample and setting Au 4f$_{7/2}$ at 84.0 eV. Experiments at low photon energies (650, 758 and 1100 eV) are performed at I411 beamline at the Swedish National Synchrotron Radiation Laboratory, Max-lab.[33] The photoemission cross-section values for lower photon energies are taken from reference.[34] The higher photon energy cross section data are calculated from interpolation of the data presented in reference.[35] The values of photoemission cross-section for Pb 4f, Cs 4d and Br 3d are also mentioned in Table 3.1.

3.3 Results and Discussions:

3.3.1 Nature of facets on the surface of CsPbBr$_3$ nanocubes:

Figure 3.1 shows the characterization of CsPbBr$_3$ nanocubes by techniques like PXRD, UV-visible absorption and PL spectroscopy. These data conform that the CsPbBr$_3$ nanocubes of orthorhombic phase is formed with absorption peak at 505 nm and emission peak at 515 nm.

TEM image shown in Figure 3.2 shows nanocubes of size around 10.8 nm. High-resolution TEM (HRTEM) image in the inset of Figure 3.2 shows the lattice planes with an interplanar distance 5.8 Å, that can correspond to both (002) or (110) planes of orthorhombic phase terminating the crystal. It has been reported earlier[5, 36, 37] that orthorhombic CsPbBr$_3$ nanostructures are often enclosed by six facets of (002) {or (001) and (110) planes} and our HRTEM results agree with that.
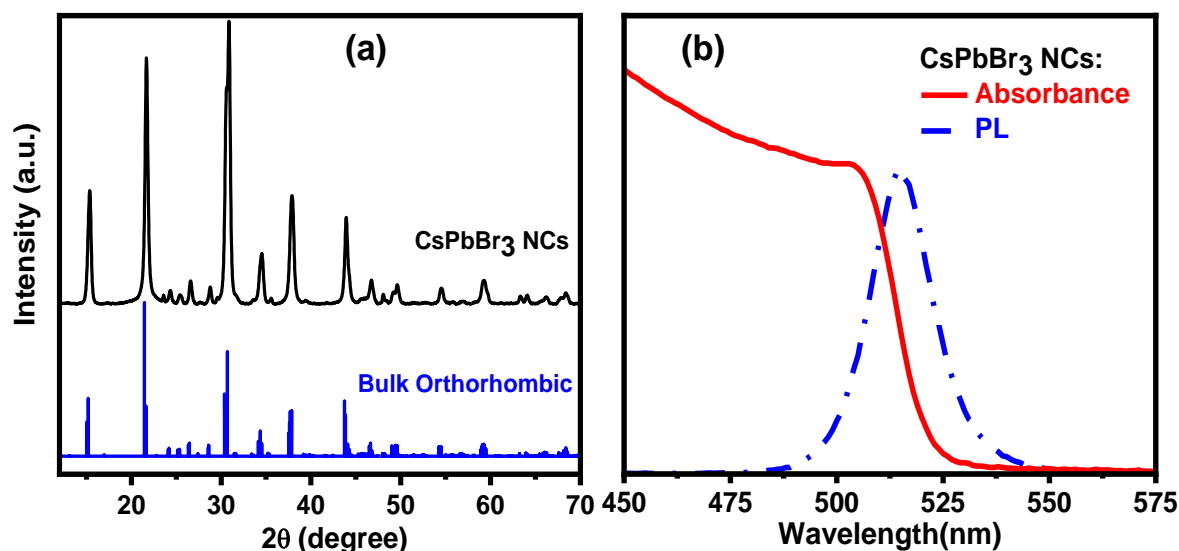
Figure 3.1: (a) PXRD pattern of CsPbBr₃ nanocubes matched with the orthorhombic phase. (b) UV-visible absorbance and PL spectra of the CsPbBr₃ nanocubes. The sample is dispersed in toluene and for PL, the sample is excited with the wavelength of 370 nm.
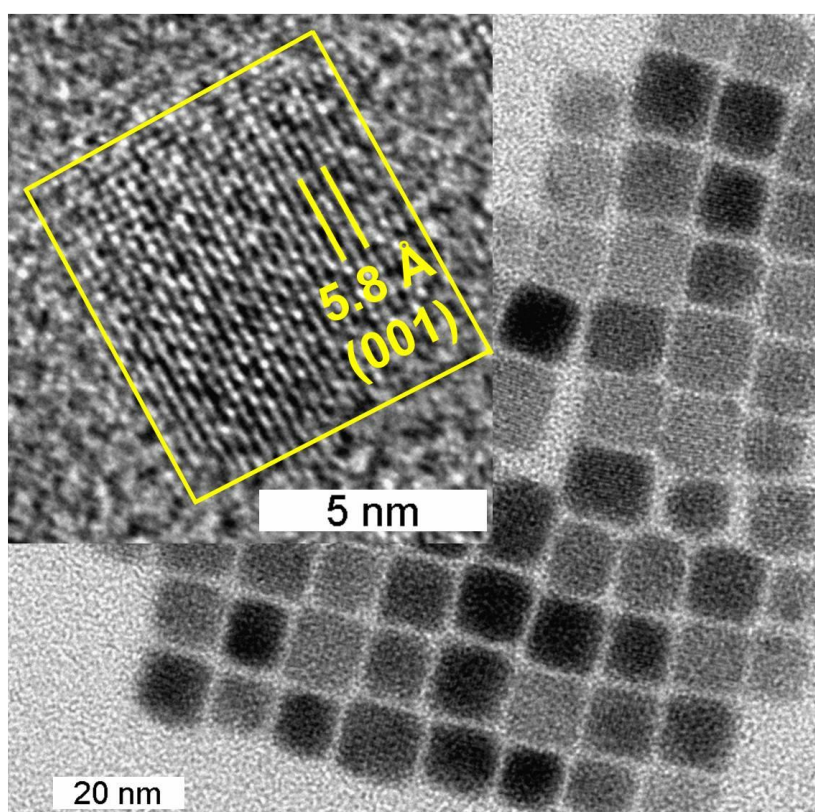
Figure 3.2: TEM image of CsPbBr₃ nanocubes with edge-length 10.8 ± 0.6 nm. HRTEM image in the inset shows the interplanar distance of 5.8 Å corresponding to either (002) or (110) facets.

When the orthorhombic CsPbBr₃ crystal is terminated by any one of (001) or (110) facets, two kinds of charge neutral surfaces can arise as shown in Figure 3.3 and

Figure 3.4. One of the planes with Cs and Br on the surface termed as "CsBr surface", and the other one with Pb and Br on the surface termed as "PbBr$_2$ surface". Note that, for (110) facets, PbBr$_2$ or CsBr are not exactly on the same plane (Figure 3.4b). Such atomic layers are also maintained for the (001) planes of cubic phase of CsPbBr$_3$. The major difference between the cubic and orthorhombic phase is the tilting of the Pb-Br$_6$ octahedrons and such tilting does not influence the present discussion. Computational study by Brinck et al.[5] suggested a model of CsPbBr$_3$ NC with exposed CsBr surface, where ~50% of Cs$^+$ ions were replaced by methylammonium ion (MA$^+$), and electronic band structure of the model could explain the defect tolerant nature of CsPbBr$_3$ nanocubes. In fact, it is intuitive that surface termination at PbBr$_2$ surface will require the breaking of PbBr$_6$ octahedron, and will therefore be energetically less favored, compared to termination by CsBr surface.

Furthermore, substitution of Cs$^+$ with MA$^+$ on the CsBr surface does not require breaking of a covalent bond. Based on above considerations, we extend the model of Brinck et al.[5] to schematics presented in Figure 3.5, where OLA$^+$ (instead of MA$^+$) substitutes a large fraction Cs$^+$ from (001) facets of orthorhombic CsPbBr$_3$ NC. However, the validity of the model in Figure 3.5 needs to be experimentally verified.
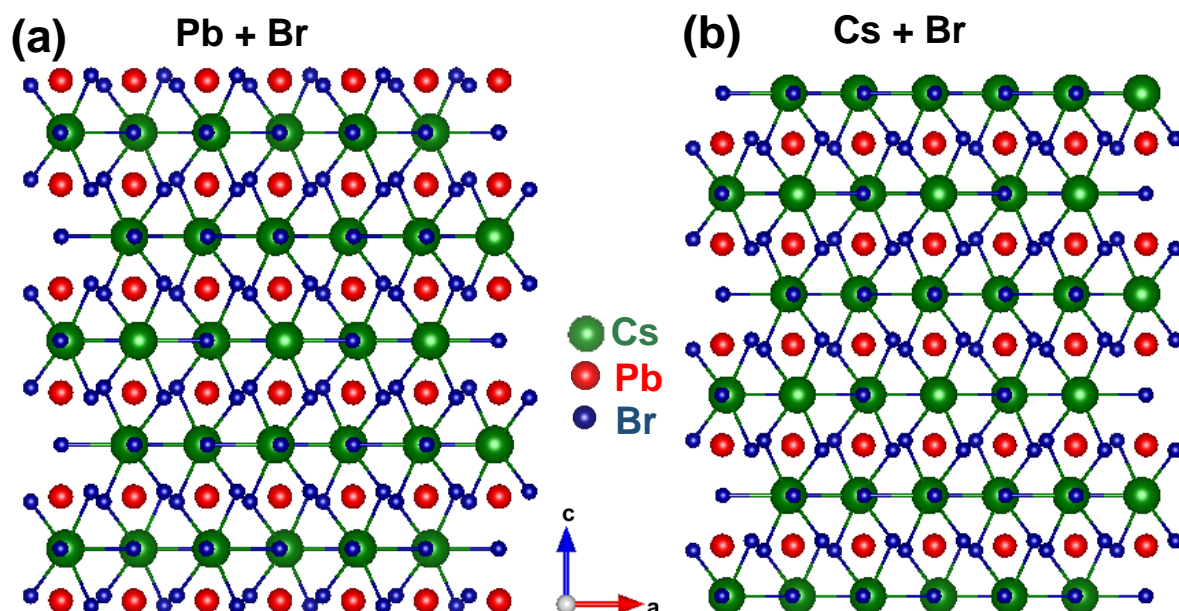
Figure 3.3: Two types of surface arises (a) PbBr$_2$ surface (b) CsBr surface for orthorhombic CsPbBr$_3$ crystals having its termination with (001) plane.
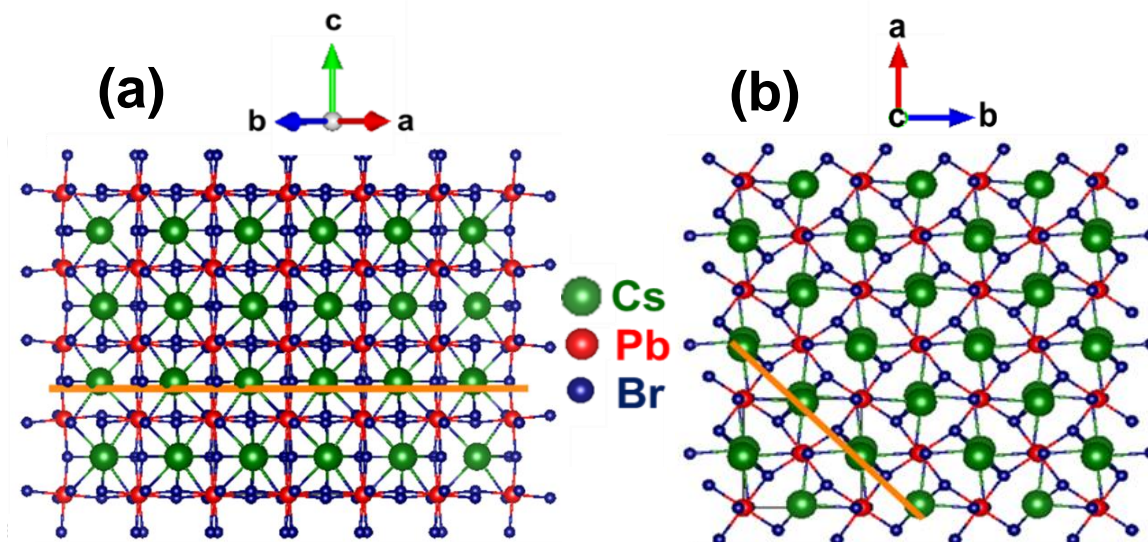
Figure 3.4: Orthorhombic CsPbBr₃ crystals. (a) (001) planes shown by yellow color line having Cs and Br. The immediate next (upward or downward) plane is composed of Pb and Br. Clearly, alternative layers of Cs-Br and Pb-Br are arranged along the [001] direction. (b) (110) plane shown by yellow line. Alternate layers of Cs-Br and Pb-Br are arranged along the [110] direction as well.
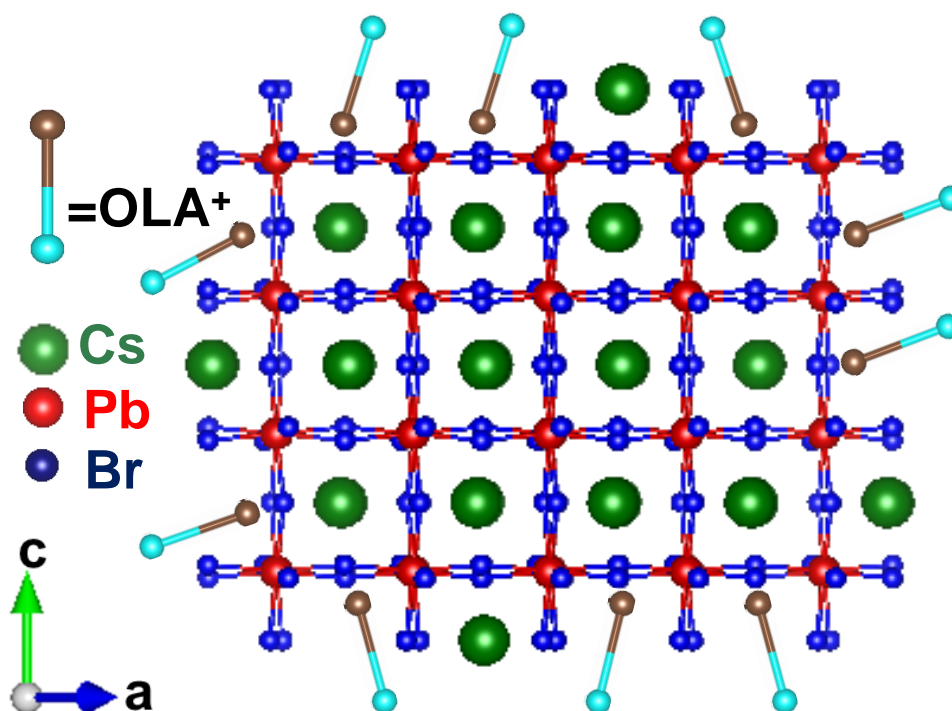
Figure 3.5: Schematic representation of the orthorhombic CsPbBr₃ terminated with (001) facets containing Cs and Pb, where OLA⁺ ions replace most of the Cs+. Similar situation is expected with for (110) facets as well.

3.3.2 Layer-by-layer internal structure of CsPbBr₃ nanocubes:

We have elucidated the compositional inhomogeneity between surface and core of NC in a layer-by-layer fashion by using XPS[38, 39] with the help of Dr. Pralay Santra.

Details of experiments and analysis are given in the above experimental section. The mean free path of a photoelectron increases with increase in the kinetic energy (when kinetic energy > 100 eV) of the photoelectron. Therefore, by increasing the incident photon energy from 650 eV to 4000 eV, we could systematically increase the probe depth to a distance comparable to that from the surface to the centre of CsPbBr$_3$ nanocubes. This tuning of probe depth provides an opportunity to elucidate elemental composition in a layer-by-layer fashion from surface to core of nanocubes.

High resolution Pb 4f core level spectra in Figure 3.6a collected at two different photon energies, show peaks at 139.2 and 144.1 eV corresponding to 4f$_{7/2}$ and 4f$_{5/2}$ respectively with a spin orbit splitting energy of 4.9 eV. The binding energies and the homogeneity of spectral shapes suggest that Pb is present in 2+ oxidation state with nearly identical coordination environment, for both photon energies.[40] However, the samples contain a small amount (3.8%) of metallic Pb as observed at 137.6 and 142.5 eV, which either might have occurred due to beam damage during the measurement[36] or might be present as a minor impurity[41] in the product. Cs 4d and Br 3d core levels have similar binding energies and are presented together in Figure 3.6b.
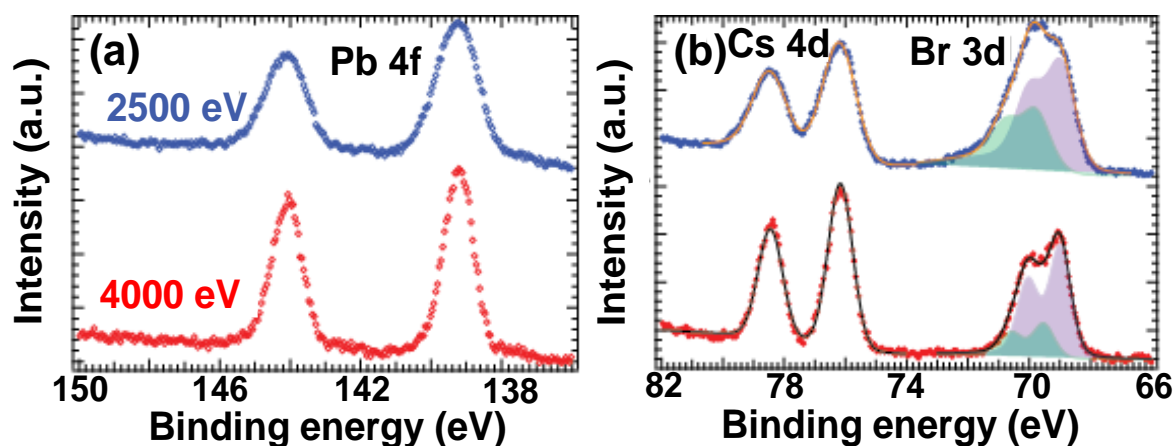
Figure 3.6: (a) Pb 4f, and (b) Cs 4d and Br 3d spectra from CsPbBr$_3$ nanocubes collected at 2500 (blue) and 4000 eV (red) photon energies. Closed circles are experimental data, solid lines are simulated total spectra, and shaded regions are simulated component spectra. Spectra are shifted vertically for clear presentation.

This similarity in binding energies results into similar kinetic energies and thus similar inelastic mean free paths for both the Cs 4d and Br 3d photoelectrons, ensuring that both kinds of photoelectrons originate at the same depth from the

surface of nanocubes. We observed only one type of Cs$^+$ with 4d$_{5/2}$ binding energy at 76.2 eV along with 4d$_{3/2}$ peak separated by a spin orbit splitting of 2.3 eV.[18] In contrast to both Pb and Cs, there are two distinct Br 3d spin orbit split doublets as highlighted in green and magenta shades in Figure 3.6b. The Br species highlighted in magenta has a binding energy of 69.3 eV for 3d$_{5/2}$ core level, while the other one highlighted in green has a binding energy of 70.1 eV for 3d$_{5/2}$ core level. Interestingly, the contribution of the higher binding energy species (shaded in green) decreases with increase in photon energy, suggesting this species to be present more on the surface of the nanocube.
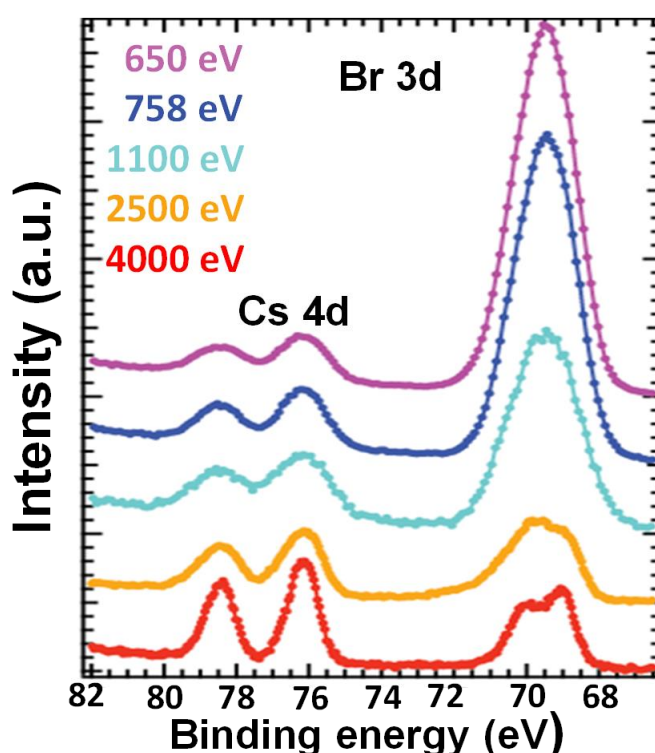
Figure 3.7: Experimental core level spectra of Cs 4d and Br 3d for CsPbBr$_3$ nanocubes, collected at five different photon energies. In order to have higher signal counts, the low photon energy (650-1100 eV) data are collected with higher aperture size, thus having a poor resolution compared to higher photon energy (2500 and 4000 eV) data. The spectra are normalized with respect to Cs 4d raw signal intensity. Also, the spectra are shifted vertically for better presentation.

Similarly, we collected a series of Pb 4f, Cs 4d and Br 3d spectra at five different photon energies namely 650 eV, 758 eV, 1100 eV, 2500 eV, and 4000 eV. Figure 3.7 shows that the total intensity of Br 3d with respect to Cs 4d increases systematically with the decrease in photon energies. The photoemission cross-section (Table 3.1) corrected relative intensity of Br 3d (black) and Pb 4f (red) with

respect to Cs 4d at different photon energies in Figure 3.8. A constant elemental ratio (~1) between Pb and Cs for all photon energies signifies a uniform composition of $CsPbBr_3$ from the surface to the core of nanocubes, which agrees with the expected composition of $CsPbBr_3$.

Table 3.1: Photoemission cross-section values for different core levels at selected photon energies. These values were obtained from Lindau and Scofield.[34, 35]

Photon energy (eV)	Pb 4f Cross section (Mbarn)	Cs 4d Cross section (Mbarn)	Br 3d Cross section (Mbarn)
650	2.6754	0.4262	0.4899
758	1.9517	0.3217	0.317
1100	0.7769	0.1495	0.1041
2500	0.0468	0.0191	0.0072
4000	0.0093	0.0040	0.0011
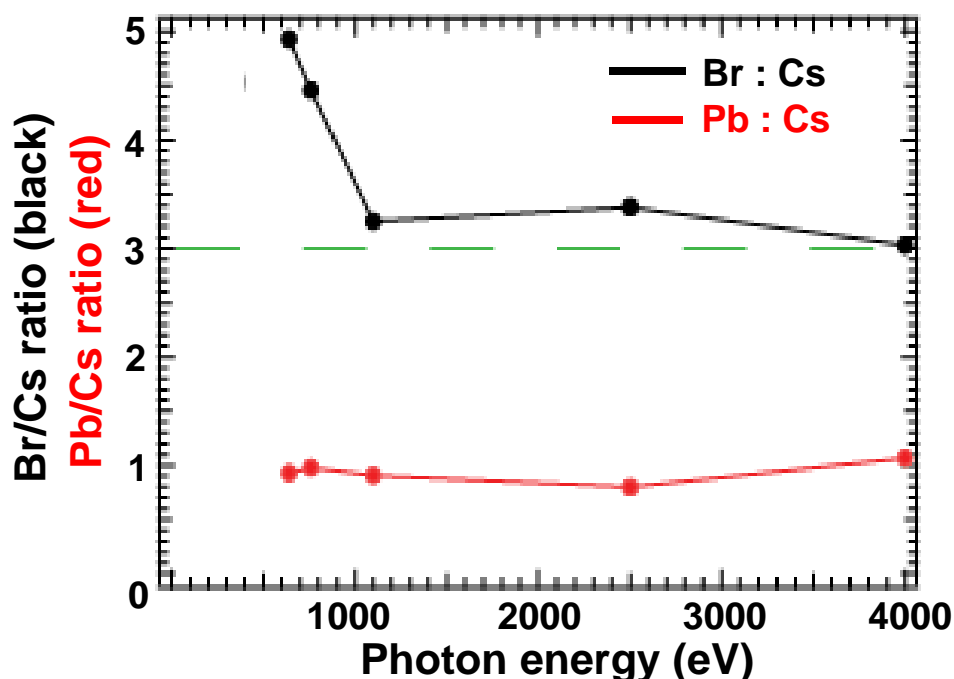
Figure 3.8: Variation in relative intensity of Br (black) and Pb (red) with respect to Cs at different photon energies. These intensity ratios are calculated after correcting the photoemission cross section for respective core levels.

However, at 650 eV photon energy, Br: Cs elemental ratio is ~5, much higher than the expected ratio of 3 in the bulk $CsPbBr_3$. This Br: Cs ratio first decreases

systematically with increase in photon energies becoming ~ 3 at 1100 eV and then remains constant with further increase in photon energy. These results clearly suggest an excess of Br present on the surface of the nanocubes and agrees with the model shown in Figure 3.5. According to this model, termination of NC facets exposing CsBr surface, and then replacing Cs$^+$ with OLA$^+$ provide Cs: Pb ~ 1 in the core, and an excess Br on the surface. Alternatively, if we assume termination with PbBr$_2$ surface, then Pb: Br is expected to be <3, which opposes our experimental findings. Therefore, layer-by-layer compositions obtained from our XPS data suggest the termination of NC with CsBr surface.

3.3.3 Type of organic ligand bound to the CsPbBr$_3$ nanocube surface:

After elucidating the inorganic compositions from the surface to core of CsPbBr$_3$ nanocubes and their contribution to VB, now we discuss the binding of organic capping ligands to this inorganic part utilizing NMR spectroscopy. We probed the passivating ligands around the nanocubes using solution ^{1}H NMR spectroscopy, which is a reliable tool for both qualitative and quantitative characterization of ligands bound on the nanocubes surface. Such characterizations rely on the facts that bound ligands exhibit: (i) ^{1}H resonance which is shifted and broadened relative to the free ligands, (ii) strong positive nuclear Overhausser effect (NOE) cross peaks, and (iii) slow diffusion characteristic as they are attached to the heavier NC. The 1D ^{1}H NMR spectrum of CsPbBr$_3$ nanocubes dispersed in CDCl$_3$ is shown in Figure 3.9, and that for OA, OLA and ODE are provided in Figure 3.10. NMR peaks for CsPbBr$_3$ nanocubes have been assigned in Figure 3.9, though the peaks at chemical shifts lower than 2.2 ppm are difficult to distinguish as OLA, OA and ODE show overlapping chemical shifts in this region. Furthermore, broad peaks at 7.0 ppm and 3.5 ppm are characteristics of OLA$^+$ corresponding to α- proton (NH$_3^+$) and β-proton (CH$_2$-N) respectively, suggesting the binding of OLA$^+$ ions on the surface of CsPbBr$_3$ nanocubes as depicted in the model in Figure 3.5. Peak 4 at 5.36 ppm corresponds to alkene protons, which can come from both OLA and OA. However, the peak at 2.4 ppm is unique for OA, suggesting presence of OA or oleate ion in the final product. But the sharpness of this peak suggests that OA or oleate is not bound to the NC surface. Having said that, the above hint of peak broadening towards ligand bound state is not confirmatory as chemical/conformational

exchange may also contribute towards line broadening. Thus, for further verification of ligand bound status, two-dimensional ^1H-^1H NOESY cross peak intensity and DOSY are measured.
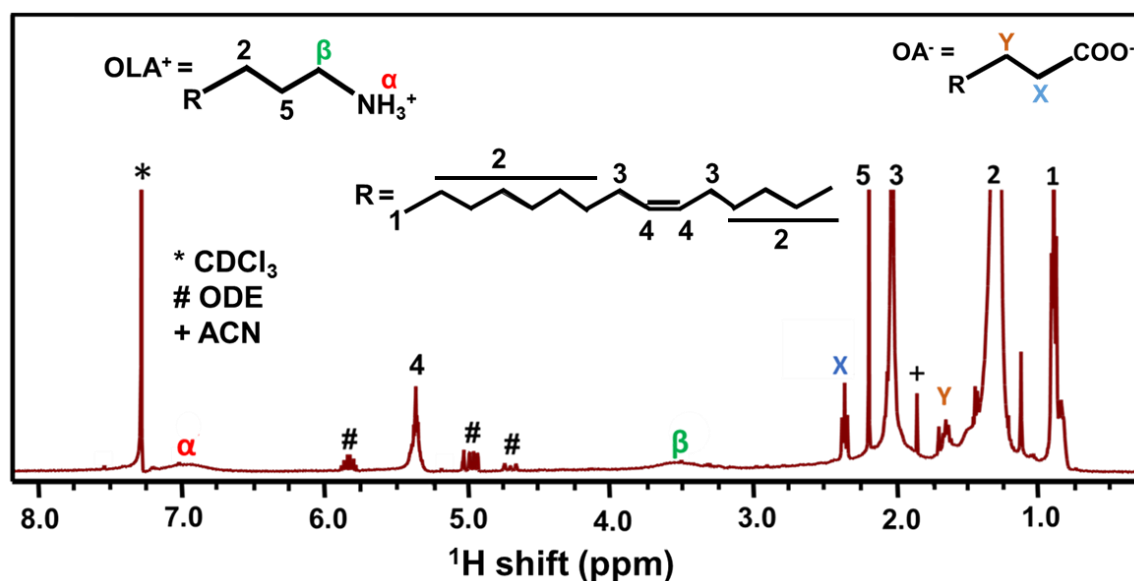
Figure 3.9: (a) 1H NMR spectrum of CsPbBr₃ nanocubes dispersed in CDCl₃. Acetonitrile (ACN) was used for washing of nanocubes, and terminal alkene group of residual ODE solvent are marked. Peak for solvent CDCl₃ is marked with *.

NOESY can effectively distinguish between free and bound ligands. Free ligand molecules behave like small molecules develop slightly negative or even no NOEs due to small negative or zero cross relaxation rate. Whereas ligands bound to NC surface develop large and positive NOEs due to large and positive cross relaxation rate. Thus, a negative NOE will give a cross peak with opposite sign with respect to the diagonal peaks in the 2D NOESY spectrum.[44] NOESY spectra of CsPbBr₃ nanocubes in Figure 3.13 show negative cross peak (red) for OA at 2.4 ppm suggesting OA or oleate are not bound to the surface, while positive cross peak (black) corresponding to OLA⁺ (α, β, and alkene protons) confirms the binding of OLA⁺ to the NC surface. Similarly, DOSY spectra shown in Figure 3.14, displaying relatively smaller diffusion coefficient for bound peak of OLA suggest OLA⁺ is bound to the nanocube surface, though the binding may be labile in nature.

Overall, our NMR results agree with previous report[27] confirming that the OLA⁺ is bound to the nanocube surface, but OA though present in the NC dispersion are not bound to the surface of nanocubes. This absence of bound OA to the nanocube surface, again agrees with earlier conclusion that Pb^{2+} ions are not present on the nanocube surface.
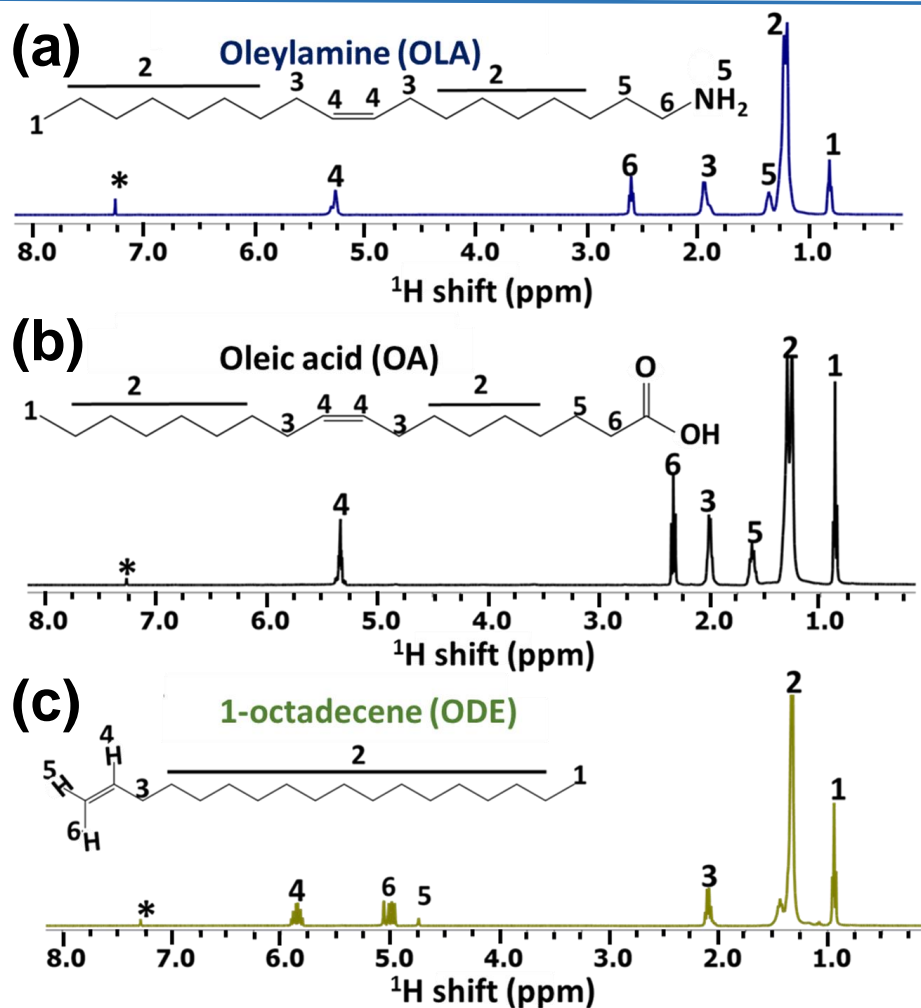
Figure 3.10: ^1H NMR spectra of (a) OLA molecules, (b) OA molecules and (c) ODE molecules. The resonance peaks for corresponding hydrogen in structure and ^1H spectra are numbered accordingly. Peak for solvent CDCl₃ is marked with *.
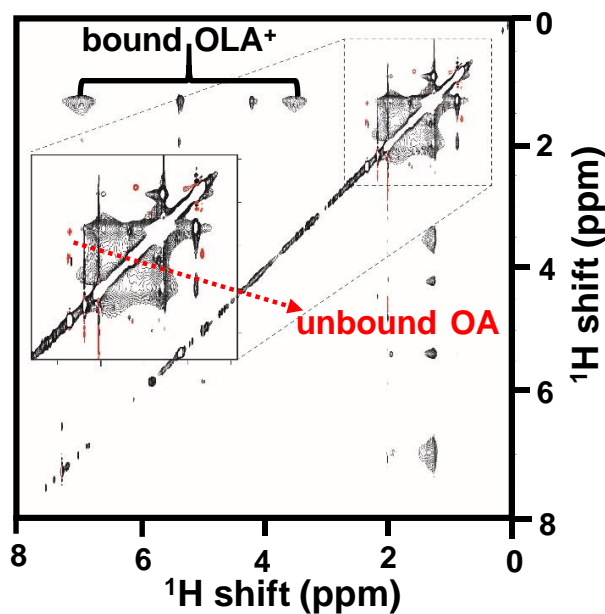
Figure 3.11: NOESY spectrum of CsPbBr₃ nanocubes dispersed in CDCl₃.
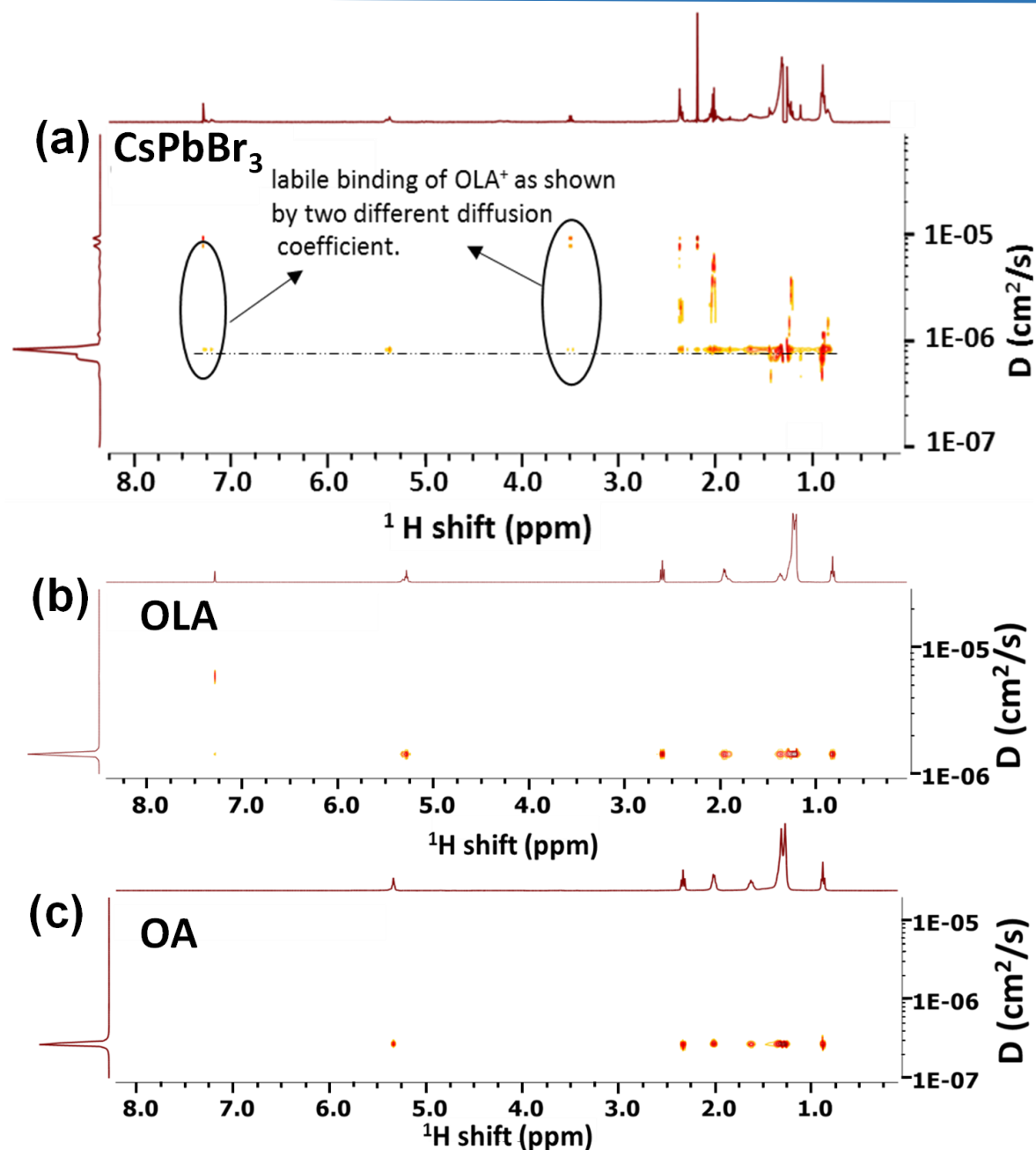
Figure 3.12: DOSY spectra of CsPbBr₃ nanocubes (a), free OLA molecules (b) and free OA molecules (c). The circled black region in a, shows the two types of diffusion coefficient for OLA$^+$ peak which shows its labile binding nature. Free OLA has diffusion coefficient of 6.2×10^{-6} cm^2/s and free OA has diffusion coefficient of 2.1×10^{-6} cm^2/s while in bound state diffusion coefficient corresponding to resonance peak of OLA$^+$ decreases to 8.1×10^{-7} cm^2/s as shown by dashed black line.

Binding of OLA$^+$ is expected on the NC surface, since our XPS results show excess Br$^-$ on the NC surface. The possibility of hydrogen bonding of OLA$^+$ with Br$^-$ has been discussed earlier in the form of addition[27] (or adsorption) of OLA$^+$ to the NC surface (see the addition mechanism in Figure 3.13). Such H⋯Br hydrogen bond can form irrespective of the surface termination with CsBr, or PbBr₂ surface.

However, our XPS data suggest termination of NC selectively by CsBr surface. Therefore, we propose the possibility of a different kind of hydrogen bonding mechanism, where OLA^+ substitutes Cs^+ from the NC surface, as shown by substitution mechanism in Figure 3.13. In this substitution mechanism, $-NH_3^+$ moiety of OLA^+ is surrounded by multiple Br^- sites on the NC surface, with possibility of forming more H····Br hydrogen bonds, compared to the addition mechanism. In fact, both computational and experimental studies have already suggested similar multiple hydrogen bonding scenario between MA^+ and halide ions in the lattice of $MAPbI_3$ perovskites.[45, 46] This possibility of formation of more number of H····Br hydrogen bonds in the substitution mechanism, might favour the substitution mechanism over the addition mechanism. Furthermore, both mechanisms will involve different kinds of surface reconstruction, which will also influence the energetics.
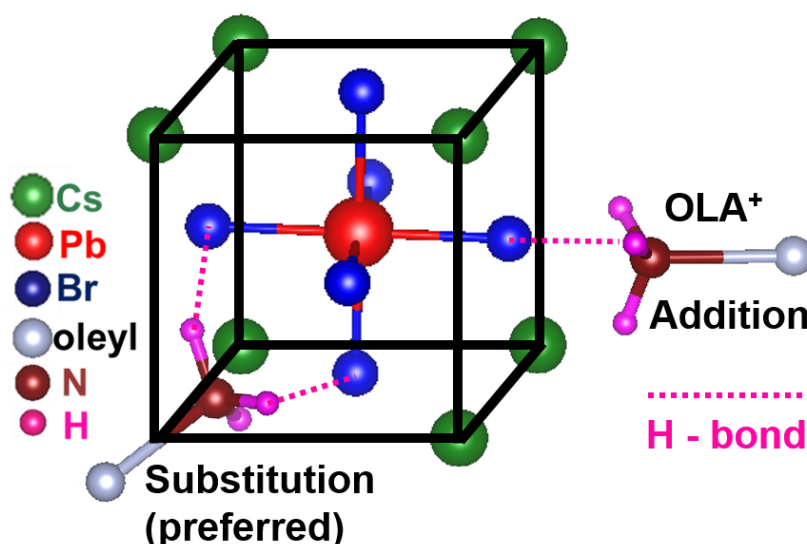
Figure 3.13: Schematic showing the possible binding mechanism of OLA^+ to $CsPbBr_3$ nanocube by forming hydrogen bonds with Br^-. Substitution of Cs^+ with OLA^+ can form multiple hydrogen bonds, whereas addition of OLA^+ to the nanocube surface can form only one hydrogen bond.

3.3.4 Thermodynamics of ligand binding:

To understand the thermodynamics of binding of organic molecules on the surface of the inorganic core of $CsPbBr_3$ nanocube, first principles DFT based calculations have been performed by Dr. Niharika Joshi and Dr. Prasenjit Ghosh at IISER Pune. Details of computational calculations can be found in our published paper (Ravi et al., *J. Phys. Chem. Lett.* **2017,** 8, 4988-4994).[47] Two main experimental results: (i)

substitution of Cs$^+$ with OLA$^+$, and (ii) absence of bound OA molecule at the NC surface, have been explained computationally. The calculation has been carried out for (001) facets, similar scenario is expected for the (110) facets as well (see Figure 3.4b). To optimize the computational cost, the larger OLA$^+$ is replaced with shorter chain MA$^+$. It is to be noted that with the MA$^+$, the chemistry governing the interaction between the nanocube surface with OLA$^+$ can be well explained. Following three scenarios are considered: (a) adsorption (addition) mechanism: MA$^+$ adsorbs on (i) CsBr surface and (ii) on PbBr$_2$ surface (Figure 3.16), (b) substitution mechanism: MA$^+$ replaces surface Cs$^+$ atom, and (c) adsorption of CH$_3$COOH on CsBr and PbBr$_2$ surface (Figure 3.17). For each of these situation, the reaction energies (ΔE, differences in total energies of the reactants and the products) are computed using the following chemical reactions:

(a) MA$^+$ adsorption: CH$_3$NH$_2$ + CsPbBr$_3$^{s} + (½) H$_2$ ----> CsPbBr$_3$^{s}-MA

(b) Cs$^+$ substitution: CH$_3$NH$_2$ + CsPbBr$_3$^{s} + (½) H$_2$ + (x/2) Br$_2$ ----> Cs$_{1-x}$PbBr$_3$^{s}-MA$_x$ + x CsBr, x being the number of Cs atoms replaced by MA$^+$

(c) Acetate adsorption: CH$_3$COOH + CsPbBr$_3$^{s} ----> CsPbBr$_3$^{s}-CH$_3$COO + (½) H$_2$
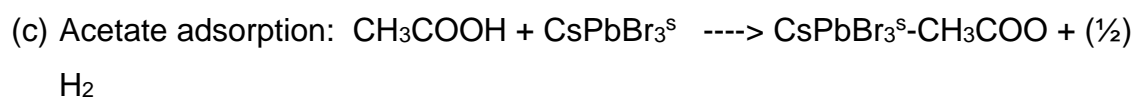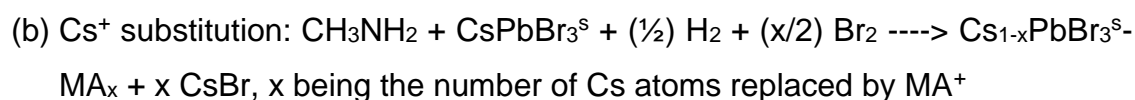
In the above equations, the superscript "s" denotes CsPbBr$_3$ surface. More negative the value of ΔE, more favourable is the reaction. The calculations show that for adsorption of MA$^+$ on CsBr and PbBr$_2$ termination, the ΔE is 0.52 and -0.43 eV. The acetate adsorption on CsBr/PbBr$_2$ termination leads to a ΔE of about 1.26 eV. In contrast to these cases, the substitution of Cs$^+$ by the MA$^+$ has a ΔE of -3.06 eV. These results, in accordance to the experimental observations, show that (i) binding of the acetate ion is thermodynamically unfavourable and (ii) indeed the organic cation replacing the exposed Cs$^+$ ions of the CsBr termination is the most favourable thermodynamic process. To understand why Cs$^+$ substitution is favored, we took a closer look at the CsBr-MA$^+$ interface formed due to substitution (Figure 3.14a) and adsorption (Figure 3.14b). Adsorption of MA$^+$ results in substantially large rumpling of the highly stable clean CsBr surface (about 1.18 and 1.84 Å) compared to that of the substitution Cs$^+$ with MA$^+$ (about 0.30 Å). It is observed that the formation of hydrogen bonds between the protons of the -NH$_3$$^+$ moiety and the nearby Br$^-$ ions

takes place. For the substitution mechanism, there are three H-bonds of which two of them with the surface Br ions are of moderate strength (H·····Br length of about 2.28 Å) while the third one with the Br ion in the layer below is slightly weaker (about 2.51 Å), as shown in the inset of Figure 3.16a. In contrast, for the case of adsorption of MA⁺ on CsBr surface (Figure 3.16b), there are two H-bonds with H·····Br distances of 2.07 and 2.17 Å. We note that the H-bonds are relatively stronger in the case of adsorption compared to that of substitution. Thus, these results indicate towards two competing factors that affect ΔE, the energy cost to induce rumpling in the surface and the energy gain (stabilization) due to the formation of H-bonds.
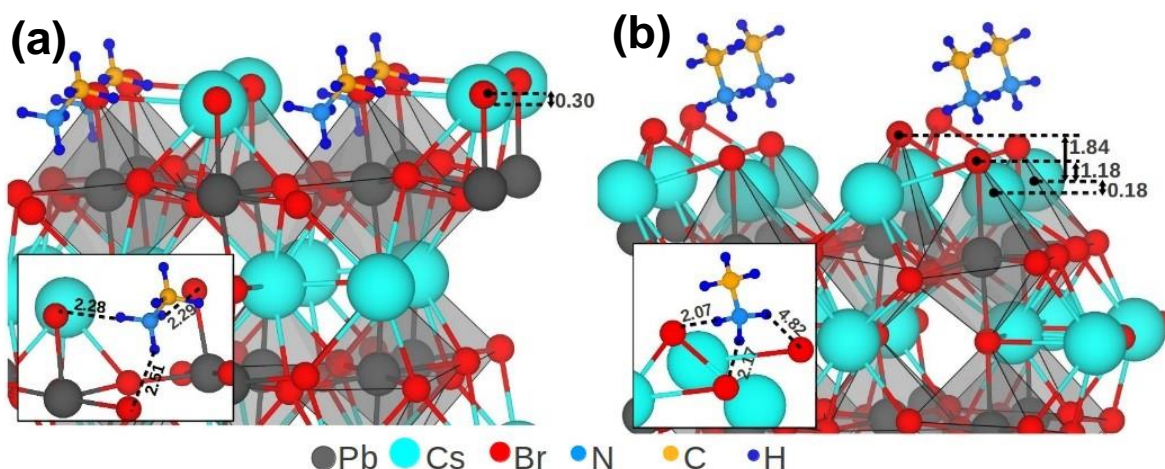
Figure 3.14: The optimized geometry of CsBr terminated (001) surface of orthorhombic CsPbBr₃ when (a) MA⁺ substitutes Cs⁺ ions and (b) when MA⁺ is adsorbed. In both the figures the inset displays the local geometry around the MA⁺ showing the H.....Br distances for each H in the -NH₃⁺ moiety. All distances and bond lengths are given in Å.

Overall finding of experimental and calculation results shows that the surface of our CsPbBr₃ nanocubes is terminated by CsBr surface, and then the capping ligand OLA⁺ replace a large fraction of Cs⁺ ions. Prior reports[5, 48] show that both CH₃NH₃⁺ (as an analog of OLA⁺) and Cs⁺ do not introduce defect state in the bandgap region. Also, it has been shown that such surface Br⁻ gives shallow and delocalized defect states. Therefore, the possible defect states on the surface of NCs are not detrimental for optoelectronic properties, which have been experimentally observed.

3.3.5 Role of OA in maintaining colloidal stability:

It has been already established that an acid-base reaction, in which proton gets exchanged from OA to OLA is necessary for the synthesis of CsPbBr₃ nanocubes. However, OA is not a part of NC surface, but still present in the final colloidal

dispersion obtained after careful washing of nanocubes. We then set out to find the role of OA whether or not it has some role in stabilizing the colloidal dispersion of CsPbBr$_3$ nanocubes. To address this question, some systematic experiments by adding excess ligands to the CsPbBr$_3$ dispersion are performed. To a dispersion (0.2 μM determined from absorption spectrum[49]) of CsPbBr$_3$ nanocubes in CHCl$_3$ (3 mL), an excess (15% by volume) of OLA, OA, and mixture of OLA:OA = 1:5, are added. Addition of excess OLA decomposes CsPbBr$_3$ nanocubes into colorless product, and preliminary PXRD pattern of the product is difficult to assign showing a mixture of phase of CsPbBr$_3$, Cs$_4$PbBr$_6$, PbBr$_2$ as presented in Figure 3.15.
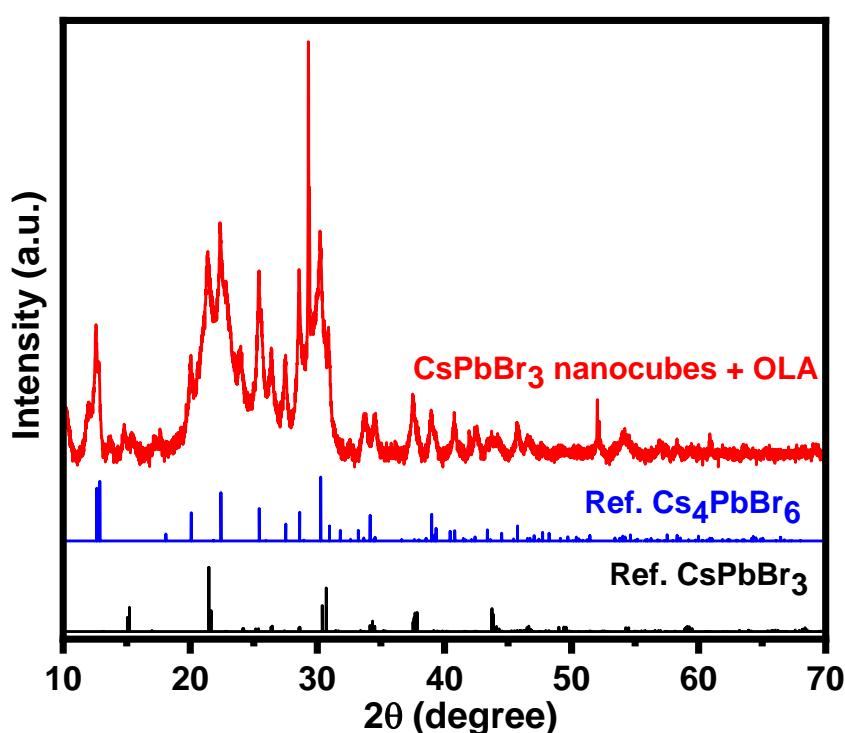
Figure 3.15: PXRD pattern of degraded CsPbBr$_3$ nanocubes after the addition of OLA to the purified nanocubes dispersion. There may be mixture of crystals phases, where Cs$_4$PbBr$_6$ can be one such phase.

On the other hand, when excess OA is added to CsPbBr$_3$ NC dispersion, nanocubes start agglomerating with a subsequent decrease in both colloidal stability and PL efficiency as shown in Figure 3.16. Excitingly, the addition of OLA to this agglomerated sample causes it to regain both colloidal stability and PL efficiency. This reversible behaviour of agglomeration process is shown by DLS data in Figure 3.17, where the hydrodynamic size of the sample increases from ~10 nm to 700 nm after addition of OA and returns back close to original value after addition of OLA in the second step.
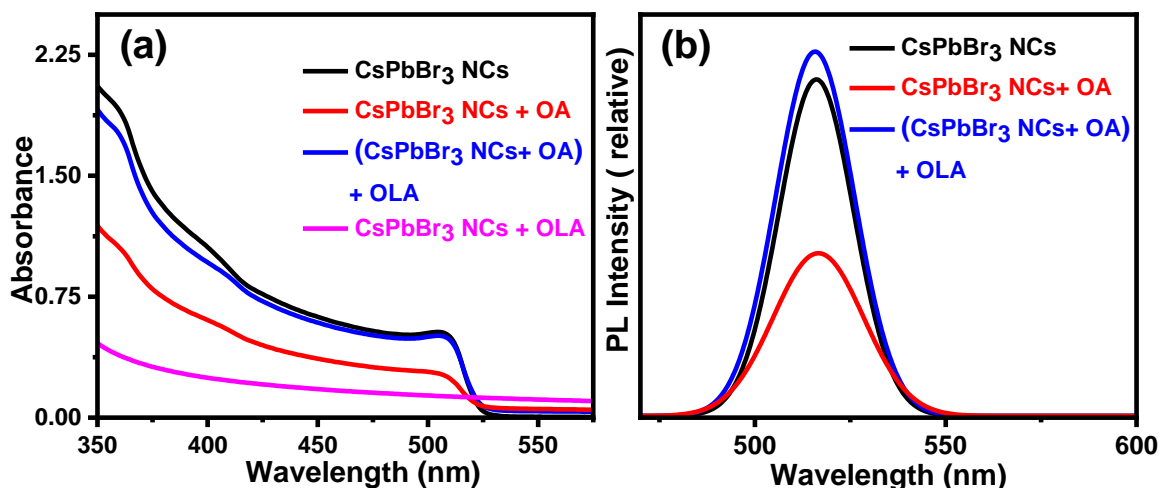
Figure 3.16: UV-visible absorbance and PL spectra of CsPbBr3 nanocubes before and after the addition of OA and OLA to the purified nanocubes dispersion. Addition of OLA to the purified dispersion (no companion OA) causes degradation of perovskite nanocubes and PL disappears. Addition of OA does not change the energy of excitonic absorption and PL, but reduces the PL intensity because of aggregation. However, after the addition of OLA to this aggregated dispersion, the nanocubes dispersion regains its PL intensity.
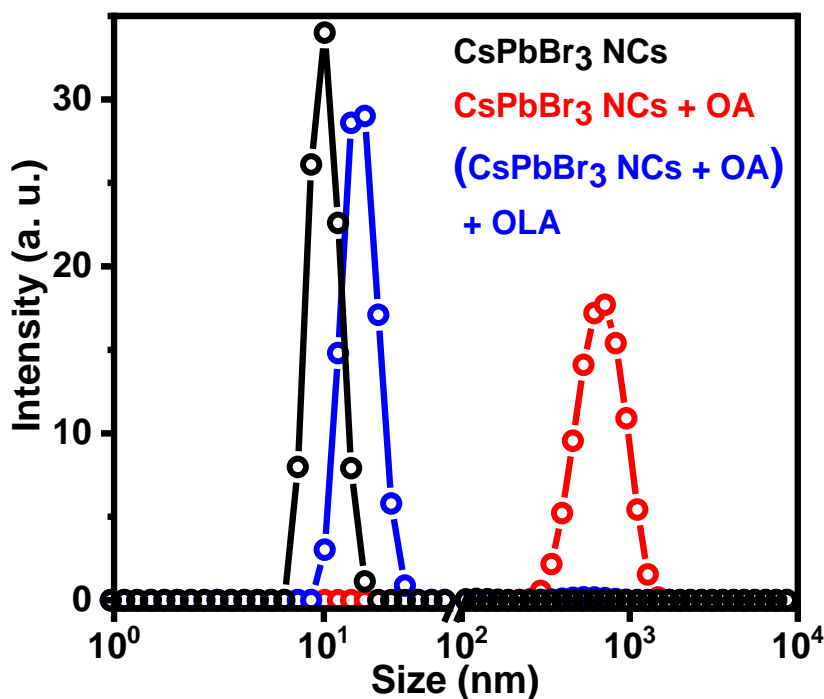
Figure 3.17: DLS data showing effect of addition of OA and OLA to CsPbBr3 nanocubes dispersed in CHCl3. Addition of only OA causes aggregation and therefore observed size seems to increased. With the addition of OLA, the aggregation process reverses back.

The point to note is that only addition of OA or OLA alone cause the quenching of PL intensity. However, a certain ratio of OA and OLA (1:5, V/V) increase the PL

intensity to the maximum. Further increase in the volume of OLA causes the degradation of CsPbBr$_3$ nanocubes to Cs$_4$PbBr$_6$. It can be hypothesized that upto certain ratio of OA and OLA, they form acid base complex and passivate the surface reducing the surface defects which leads to increase in PL intensity. Whereas, the excess OLA lead to extraction of OLA$^+$-PbBr$_2$ complex and therefore transforming it to 0D perovskite phase of Cs$_4$PbBr$_6$. The similar effect by other amines like butylamine, hexylamine, octylamine and octadecylamine can be also observed with difference in rate of degradation/transformation. Figure 3.18 shows the schematics along with the digital photograph of nanocubes to show the effect of adding excess ligand.
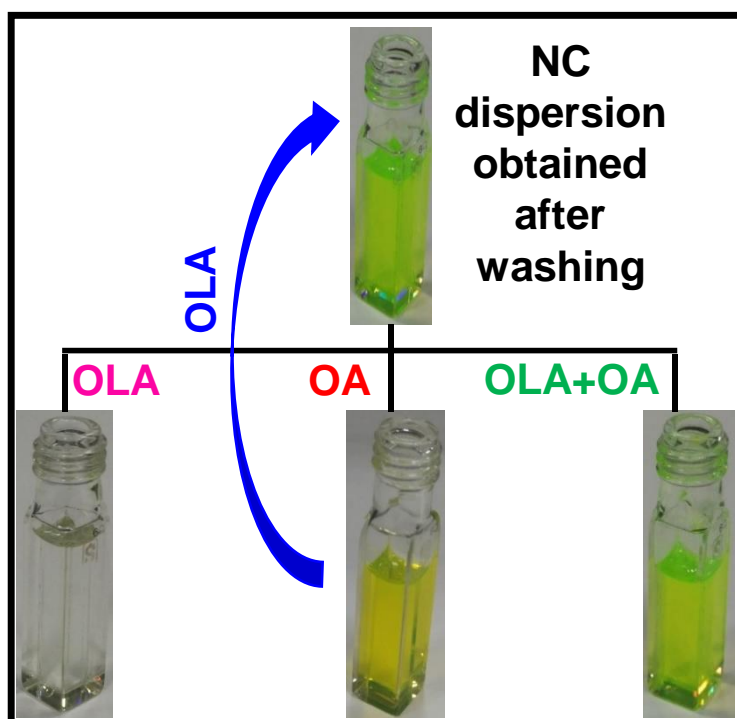
Figure 3.18: Effect of addition of OA and OLA to CsPbBr$_3$ nanocubes dispersed in CHCl$_3$. Photographs of the samples obtained under visible light shows the corresponding changes after addition of the excess ligands.

These results clearly establish that though OA is not bound to the CsPbBr$_3$ nanocube surface, maintaining a ratio of OLA and OA (or OLA$^+$ and oleate) in the final nanocubes dispersion is necessary for the stability of the product. When a mixture of OLA: OA = 1:5 (by volume) is added to the dispersion of CsPbBr$_3$ nanocubes, the colloidal stability and optical properties of nanocubes are completely preserved. These results suggest that the final sample/dispersion is a

mixture containing OLA$^+$-capped CsPbBr$_3$, OA (or oleate), and oleylammonium oleate. An equilibrium between these components is required to be maintained for the desired stability and optical properties of CsPbBr$_3$ nanocubes.

3.4 Conclusions:

In conclusion, XPS, NMR and DFT results show that OLA$^+$ binds to the surface of CsPbBr$_3$ nanocubes by substituting Cs$^+$ ions. This substitution of Cs$^+$ with OLA$^+$ is thermodynamically favored due to reduced surface rumpling of the nanocube and formation of more numbers of H⋯Br hydrogen bonds between the H atoms of the –NH$_3^+$ moiety of OLA$^+$ and the Br$^-$ ions on the nanocube surface. Such substitution reaction of organic ligand with nanocube surface is not observed for other kinds of semiconductors NCs, where organic ligands are typically adsorbed (addition mechanism) on the surface of NCs. Importantly, though OA is not bound to the surface of nanocubes, a critical ratio of OA and OLA (or oleate and OLA$^+$) is necessary for the stability of CsPbBr$_3$ nanocubes in the final washed sample. This understanding of OLA$^+$ binding to the CsPbBr$_3$ nanocube surface, along with further understanding of the role OA in the final dispersion, will be critical for surface modification, shape-control, along with formation hetero-structures and composites of colloidal cesium lead halide NCs.

3.5 References:

1. Protesescu, L.; Yakunin, S.; Bodnarchuk, M. I.; Krieg, F.; Caputo, R.; Hendon, C. H.; Yang, R. X.; Walsh, A.; Kovalenko, M. V., Nanocrystals of Cesium Lead Halide Perovskites (CsPbX$_{(3)}$, X = Cl, Br, and I): Novel Optoelectronic Materials Showing Bright Emission with Wide Color Gamut. *Nano Lett.* **2015,** *15*, 3692-3696.

2. Swarnkar, A.; Chulliyil, R.; Ravi, V. K.; Irfanullah, M.; Chowdhury, A.; Nag, A., Colloidal CsPbBr$_3$ Perovskite Nanocrystals: Luminescence beyond Traditional Quantum Dots. *Angew Chem. Int. Ed.* **2015,** *54*, 15424-15428.

3. Bekenstein, Y.; Koscher, B. A.; Eaton, S. W.; Yang, P.; Alivisatos, A. P., Highly Luminescent Colloidal Nanoplates of Perovskite Cesium Lead Halide and Their Oriented Assemblies. *J. Am. Chem. Soc.* **2015,** *137*, 16008-16011.

4. Yettapu, G. R.; Talukdar, D.; Sarkar, S.; Swarnkar, A.; Nag, A.; Ghosh, P.; Mandal, P., Terahertz Conductivity within Colloidal CsPbBr$_3$ Perovskite

Nanocrystals: Remarkably High Carrier Mobilities and Large Diffusion Lengths. *Nano Lett.* **2016,** *16,* 4838-4848.

5. ten Brinck, S.; Infante, I., Surface Termination, Morphology, and Bright Photoluminescence of Cesium Lead Halide Perovskite Nanocrystals. *ACS Energy Lett.* **2016,** *1,* 1266-1272.

6. Manser, J. S.; Christians, J. A.; Kamat, P. V., Intriguing Optoelectronic Properties of Metal Halide Perovskites. *Chem. Rev.* **2016,** *116,* 12956-13008.

7. Protesescu, L.; Yakunin, S.; Bodnarchuk, M. I.; Bertolotti, F.; Masciocchi, N.; Guagliardi, A.; Kovalenko, M. V., Monodisperse Formamidinium Lead Bromide Nanocrystals with Bright and Stable Green Photoluminescence. *J. Am. Chem. Soc.* **2016,** *138,* 14202-14205.

8. Song, J. Z.; Li, J. H.; Li, X. M.; Xu, L. M.; Dong, Y. H.; Zeng, H. B., Quantum Dot Light-Emitting Diodes Based on Inorganic Perovskite Cesium Lead Halides (CsPbX$_3$). *Adv. Mater.* **2015,** *27,* 7162-7167.

9. Zhang, X. Y.; Lin, H.; Huang, H.; Reckmeier, C.; Zhang, Y.; Choy, W. C. H.; Rogach, A. L., Enhancing the Brightness of Cesium Lead Halide Perovskite Nanocrystal Based Green Light-Emitting Devices through the Interface Engineering with Perfluorinated Ionomer. *Nano Lett.* **2016,** *16,* 1415-1420.

10. Li, J.; Xu, L.; Wang, T.; Song, J.; Chen, J.; Xue, J.; Dong, Y.; Cai, B.; Shan, Q.; Han, B.; Zeng, H., 50-Fold EQE Improvement up to 6.27% of Solution-Processed All-Inorganic Perovskite CsPbBr$_3$ QLEDs via Surface Ligand Density Control. *Adv. Mater.* **2017,** *29,* 1603885.

11. Swarnkar, A.; Marshall, A. R.; Sanehira, E. M.; Chernomordik, B. D.; Moore, D. T.; Christians, J. A.; Chakrabarti, T.; Luther, J. M., Quantum dot-induced phase stabilization of alpha-CsPbI$_3$ perovskite for high-efficiency photovoltaics. *Science* **2016,** *354,* 92-95.

12. Ramasamy, P.; Lim, D.-H.; Kim, B.; Lee, S.-H.; Lee, M.-S.; Lee, J.-S., All-inorganic cesium lead halide perovskite nanocrystals for photodetector applications. *Chem.I Commun.* **2016,** *52,* 2067-2070.

13. Dong, Y.; Gu, Y.; Zou, Y.; Song, J.; Xu, L.; Li, J.; Xue, J.; Li, X.; Zeng, H., Improving All-Inorganic Perovskite Photodetectors by Preferred Orientation and Plasmonic Effect. *Small* **2016,** *12,* 5622-5632.

14. Talapin, D. V.; Lee, J. S.; Kovalenko, M. V.; Shevchenko, E. V., Prospects of colloidal nanocrystals for electronic and optoelectronic applications. *Chem. Rev.* **2010,** *110*, 389-458.

15. Kadlag, K. P.; Rao, M. J.; Nag, A., Ligand-Free, Colloidal, and Luminescent Metal Sulfide Nanocrystals. *J. Phys. Chem. Lett.* **2013,** *4*, 1676-1681.

16. Krause, M. M.; Jethi, L.; Mack, T. G.; Kambhampati, P., Ligand Surface Chemistry Dictates Light Emission from Nanocrystals. *J. Phys. Chem. Lett.* **2015,** *6*, 4292-4296.

17. Li, W.; Zhong, X., Capping Ligand-Induced Self-Assembly for Quantum Dot Sensitized Solar Cells. *J. Phys. Chem. Lett.* **2015,** *6*, 796-806.

18. Pan, J.; Sarmah, S. P.; Murali, B.; Dursun, I.; Peng, W.; Parida, M. R.; Liu, J.; Sinatra, L.; Alyami, N.; Zhao, C.; Alarousu, E.; Ng, T. K.; Ooi, B. S.; Bakr, O. M.; Mohammed, O. F., Air-Stable Surface-Passivated Perovskite Quantum Dots for Ultra-Robust, Single- and Two-Photon-Induced Amplified Spontaneous Emission. *J. Phys. Chem. Lett.* **2015,** *6*, 5027-5033.

19. Li, X.; Yu, D.; Cao, F.; Gu, Y.; Wei, Y.; Wu, Y.; Song, J.; Zeng, H., Healing All-Inorganic Perovskite Films via Recyclable Dissolution–Recyrstallization for Compact and Smooth Carrier Channels of Optoelectronic Devices with High Stability. *Adv. Funct. Mater.* **2016,** *26*, 5903-5912.

20. Hines, M. A.; Guyot-Sionnest, P., Synthesis and Characterization of Strongly Luminescing ZnS-Capped CdSe Nanocrystals. *J. Phys. Chem.* **1996,** *100* (2), 468-471.

21. Peng, X.; Schlamp, M. C.; Kadavanich, A. V.; Alivisatos, A. P., Epitaxial Growth of Highly Luminescent CdSe/CdS Core/Shell Nanocrystals with Photostability and Electronic Accessibility. *J. Am. Chem. Soc.* **1997,** *119*, 7019-7029.

22. Dabbousi, B. O.; Rodriguez-Viejo, J.; Mikulec, F. V.; Heine, J. R.; Mattoussi, H.; Ober, R.; Jensen, K. F.; Bawendi, M. G., (CdSe)ZnS Core−Shell Quantum Dots: Synthesis and Characterization of a Size Series of Highly Luminescent Nanocrystallites. *J. Phys. Chem. B* **1997,** *101*, 9463-9475.

23. Sarma, D. D.; Nag, A.; Santra, P. K.; Kumar, A.; Sapra, S.; Mahadevan, P., Origin of the Enhanced Photoluminescence from Semiconductor CdSeS Nanocrystals. *J. Phys. Chem. Lett.* **2010,** *1* (14), 2149-2153.

24. Zhang, J.; Yang, Q.; Cao, H.; Ratcliffe, C. I.; Kingston, D.; Chen, Q. Y.; Ouyang, J.; Wu, X.; Leek, D. M.; Riehle, F. S.; Yu, K., Bright Gradient-Alloyed CdSe$_x$S$_{1-x}$ Quantum Dots Exhibiting Cyan-Blue Emission. *Chem. Mater.* **2016,** *28*, 618-625.

25. Grandhi, G. K.; Viswanatha, R., Demystifying Complex Quantum Dot Heterostructures Using Photogenerated Charge Carriers. *J. Phys. Chem. Lett.* **2017,** *8*, 2043-2048.

26. Kim, Y.; Yassitepe, E.; Voznyy, O.; Comin, R.; Walters, G.; Gong, X.; Kanjanaboos, P.; Nogueira, A. F.; Sargent, E. H., Efficient Luminescence from Perovskite Quantum Dot Solids. *ACS Appl. Mater. Interfaces* **2015,** *7*, 25007-25013.

27. De Roo, J.; Ibanez, M.; Geiregat, P.; Nedelcu, G.; Walravens, W.; Maes, J.; Martins, J. C.; Van Driessche, I.; Kovalenko, M. V.; Hens, Z., Highly Dynamic Ligand Binding and Light Absorption Coefficient of Cesium Lead Bromide Perovskite Nanocrystals. *ACS Nano* **2016,** *10*, 2071-81.

28. Pan, A.; He, B.; Fan, X.; Liu, Z.; Urban, J. J.; Alivisatos, A. P.; He, L.; Liu, Y., Insight into the Ligand-Mediated Synthesis of Colloidal CsPbBr$_3$ Perovskite Nanocrystals: The Role of Organic Acid, Base, and Cesium Precursors. *ACS Nano* **2016,** *10*, 7943-54.

29. Li, X.; Wu, Y.; Zhang, S.; Cai, B.; Gu, Y.; Song, J.; Zeng, H., CsPbX3 Quantum Dots for Lighting and Displays: Room-Temperature Synthesis, Photoluminescence Superiorities, Underlying Origins and White Light-Emitting Diodes. *Adv. Funct. Mater.* **2016,** *26*, 2435-2445.

30. Wu, D. H.; Chen, A. D.; Johnson, C. S., An Improved Diffusion-Ordered Spectroscopy Experiment Incorporating Bipolar-Gradient Pulses. *J. Magn. Reson. Se.r A* **1995,** *115*, 260-264.

31. Schaefers, F.; Mertin, M.; Gorgoi, M., KMC-1: A high resolution and high flux soft x-ray beamline at BESSY. *Rev. Sci. Instrum.* **2007,** *78*, 123102.

32. Gorgoi, M.; Svensson, S.; Schäfers, F.; Öhrwall, G.; Mertin, M.; Bressler, P.; Karis, O.; Siegbahn, H.; Sandell, A.; Rensmo, H.; Doherty, W.; Jung, C.; Braun, W.; Eberhardt, W., The high kinetic energy photoelectron spectroscopy facility at BESSY progress and first results. *Nuc. Instrum. Methods Phys. Res., Sect. A: Accelerators, Spectrometers, Detectors and Associated Equipment* **2009,** *601*, 48-53.

33. Bässler, M.; Forsell, J. O.; Björneholm, O.; Feifel, R.; Jurvansuu, M.; Aksela, S.; Sundin, S.; Sorensen, S. L.; Nyholm, R.; Ausmees, A.; Svensson, S., Soft X-ray undulator beam line I411 at MAX-II for gases, liquids and solid samples. *J. Electron Spectrosc. Relat. Phenom.* **1999,** *103*, 953-957.

34. Yeh, J. J.; Lindau, I., Atomic subshell photoionization cross sections and asymmetry parameters: $1 \leqslant Z \leqslant 103$. *Atomic Data and Nuclear Data Tables* **1985,** *32*, 1-155.

35. Scofield, J. H., Hartree-Slater subshell photoionization cross-sections at 1254 and 1487 eV. *J. Electron Spectrosc. Relat. Phenom.* **1976,** *8*, 129-137.

36. Akkerman, Q. A.; Motti, S. G.; Srimath Kandada, A. R.; Mosconi, E.; D'Innocenzo, V.; Bertoni, G.; Marras, S.; Kamino, B. A.; Miranda, L.; De Angelis, F.; Petrozza, A.; Prato, M.; Manna, L., Solution Synthesis Approach to Colloidal Cesium Lead Halide Perovskite Nanoplatelets with Monolayer-Level Thickness Control. *J. Am. Chem. Soc.* **2016,** *138*, 1010-1016.

37. Dang, Z.; Shamsi, J.; Palazon, F.; Imran, M.; Akkerman, Q. A.; Park, S.; Bertoni, G.; Prato, M.; Brescia, R.; Manna, L., In Situ Transmission Electron Microscopy Study of Electron Beam-Induced Transformations in Colloidal Cesium Lead Halide Perovskite Nanocrystals. *ACS Nano* **2017,** *11*, 2124-2132.

38. Borchert, H.; Dorfs, D.; McGinley, C.; Adam, S.; Möller, T.; Weller, H.; Eychmüller, A., Photoemission Study of Onion Like Quantum Dot Quantum Well and Double Quantum Well Nanocrystals of CdS and HgS. *J. Phys. Chem. B* **2003,** *107*, 7486-7491.

39. Sarma, D. D.; Santra, P. K.; Mukherjee, S.; Nag, A., X-ray Photoelectron Spectroscopy: A Unique Tool To Determine the Internal Heterostructure of Nanoparticles. *Chem. Mater.* **2013,** *25*, 1222-1232.

40. Endres, J.; Kulbak, M.; Zhao, L.; Rand, B. P.; Cahen, D.; Hodes, G.; Kahn, A., Electronic structure of the CsPbBr₃/polytriarylamine (PTAA) system. *J. Appl. Phys.* **2017,** *121*, 035304.

41. Udayabhaskararao, T.; Kazes, M.; Houben, L.; Lin, H.; Oron, D., Nucleation, Growth, and Structural Transformations of Perovskite Nanocrystals. *Chem. Mater.* **2017,** *29*, 1302-1308.

42. Heidrich, K.; Schäfer, W.; Schreiber, M.; Söchtig, J.; Trendel, G.; Treusch, J.; Grandke, T.; Stolz, H. J., Electronic structure, photoemission spectra, and

vacuum-ultraviolet optical spectra of CsPbCl₃ and CsPbBr₃. *Phys. Rev. B* **1981,** *24*, 5642-5649.

43. Endres, J.; Egger, D. A.; Kulbak, M.; Kerner, R. A.; Zhao, L.; Silver, S. H.; Hodes, G.; Rand, B. P.; Cahen, D.; Kronik, L.; Kahn, A., Valence and Conduction Band Densities of States of Metal Halide Perovskites: A Combined Experimental-Theoretical Study. *J. Phys. Chem. Lett.* **2016,** *7*, 2722-2729.

44. Tekely, P., Malcolm H. Levitt. Spin dynamics: basics of nuclear magnetic resonance. John Wiley & Sons, Chichester, UK, 2001.

45. Liu, S.; Zheng, F.; Koocher, N. Z.; Takenaka, H.; Wang, F.; Rappe, A. M., Ferroelectric Domain Wall Induced Band Gap Reduction and Charge Separation in Organometal Halide Perovskites. *J.Phys. Chem. Lett.* **2015,** *6*, 693-699.

46. Mosconi, E.; Quarti, C.; Ivanovska, T.; Ruani, G.; De Angelis, F., Structural and electronic properties of organo-halide lead perovskites: a combined IR-spectroscopy and ab initio molecular dynamics investigation. *Phys. Chem. Chem.Phys.* **2014,** *16*, 16137-16144.

47. Ravi, V. K.; Santra, P. K.; Joshi, N.; Chugh, J.; Singh, S. K.; Rensmo, H.; Ghosh, P.; Nag, A., Origin of the Substitution Mechanism for the Binding of Organic Ligands on the Surface of CsPbBr₃ Perovskite Nanocubes. *J. Phys. Chem. Lett.* **2017,** *8*, 4988-4994.

48. Yin, W.-J.; Shi, T.; Yan, Y., Superior Photovoltaic Properties of Lead Halide Perovskites: Insights from First-Principles Theory. *J. Phys. Chem. C* **2015,** *119*, 5253-5264.

49. Ravi, V. K.; Markad, G. B.; Nag, A., Band Edge Energies and Excitonic Transition Probabilities of Colloidal CsPbX₃ (X = Cl, Br, I) Perovskite Nanocrystals. *ACS Energy Lett.* **2016,** *1*, 665-671.

Chapter 4

Surface Engineering of CsPbX$_3$ (X = Cl, Br, I) Nanocrystals for Improved Stability Towards Anion Exchange and Water Stability
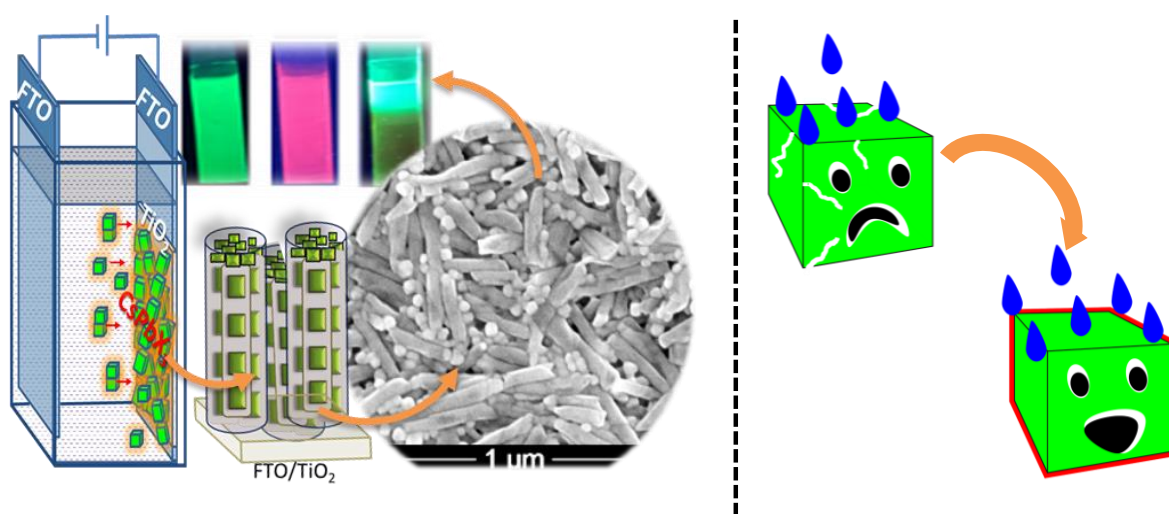
Abstract:

The lead halide perovskite nanocrystals show exciting optoelectronic properties but it has its own problems. The ease of anion exchange which gives advantage like easy tunability of the bandgap, also serves as a problem because of easy ion migration. This leads to problem like unwanted anion exchange between two CsPbX$_3$ nanocrystals and thus it defeats their purpose of using them in tandem solar cells or using a mixture of CsPbX$_3$ to obtain gamut of emission say white light. Further anion segregation in a mixed halide nanocrystal is also a major challenge that remains to be solved. Another problem these halide perovskite nanocrystals faces is due to their ionic nature. They are very unstable in polar solvent or when exposed to water/moisture. This is problematic since any real-life device would have to face some moisture content even when it is carefully fabricated and sealed. In this chapter, we have tried to mitigate some of the stability problem associated with the CsPbX$_3$ nanocrystals by engineering their surface to make it more stable. We have encapsulated the CsPbX$_3$ nanocrystals by two methods which are discussed in the subparts i.e. 4A and 4B of this chapter.

In Chapter 4A, we have coated the surface of the CsPbX$_3$ nanocrystals by PbSO$_4$-Oleate. This coating suppresses the anion exchange between the nanocrystal both in colloidal dispersion as well as when they are deposited as films. However, this coating is not sufficient enough to make the CsPbX$_3$ nanocrystals stable toward water and so we needed to find more robust way for protecting the CsPbX$_3$ nanocrystals.

In Chapter 4B, we have synthesized CsPbBr$_3$/ZnS core/shell structure which shows enhanced stability to water and light compared to pristine CsPbBr$_3$ nanocrystals. Having a crystalline inorganic semiconducting shell around the CsPbX$_3$ nanocrystals is desirable as it would not only protect the nanocrystals from external environment but also it would not hamper the charge transfer between the nanocrystals.

Chapter 4A

Capping of CsPbX$_3$ (X= Cl, Br, I) Nanocrystals by PbSO$_4$-Oleate to Suppress Anion Exchange
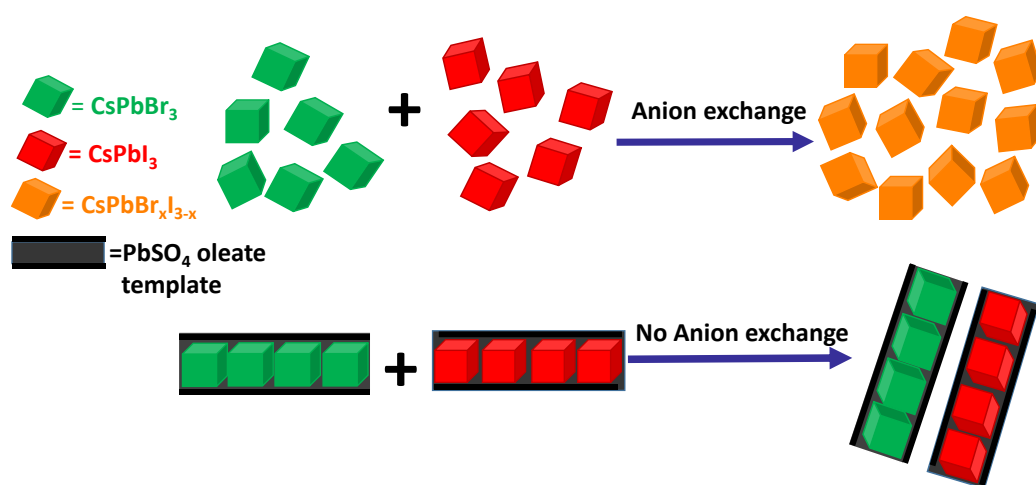
The work presented in this chapter has led to the following publication:

Ravi, V. K.; Scheidt, R. A.; Nag, A.; Kuno, M.; Kamat, P. V. *To Exchange or Not to Exchange*. Suppressing Anion Exchange in Lead Halide Perovskites with PbSO$_4$-Oleate Capping. *ACS Energy Lett.* **2018**, 8, 20, 4988-4994. Copyright permission has been taken from ACS publication for full paper.

Ravi, V. K.; Scheidt, R. A.; DuBose, J.; Kamat, P. V. Hierarchical Arrays of Cesium Lead Halide Perovskite Nanocrystals through Electrophoretic Deposition. *J. Am. Chem. Soc.* **2018**, 140, 28,8887-8894. Copyright permission has been taken from ACS publication for full paper.

Declaration:

This part of work is done in University of Notre Dame under the supervision of Prof. Prashant Kamat, as a part of my PhD program under the Bhaskara Advanced Solar Energy internship awarded by Indo-US Science Technology and Forum.

Abstract:

In chapter 2, we have seen that CsPbX$_3$ perovskite nanocrystals can be easily anion exchanged (even at room temperature, just by adding appropriate halide source) to give nanocrystals of different halide composition and thus have tunable bandgap, covering entire visible region. This ease of synthesis of compositionally different lead halide perovskite nanocrystals allows its utilization in tandem or layered fashion in either solar cells to absorb more solar spectrum or in light emitting diodes for having multicolour emission. However, the ease of halide ion exchange also poses a problem due to their high mobility. The obvious problem is keeping the lead halide perovskite nanocrystals intact without undergoing exchange of halide ions so that the original band structure is maintained for each layer of nanocrystals. In this chapter, we have successfully suppressed the halide ion exchange by capping CsPbBr$_3$ and CsPbI$_3$ nanocrystals with PbSO$_4$-Oleate to create a nanostructure assembly that inhibits the exchange of anions. Absorption and photoluminescence measurements show that the nanocrystals assemblies maintain their identity as either CsPbX$_3$ without undergoing any change in composition when they are mixed together. Further these PbSO$_4$-Oleate capped CsPbX$_3$ nanocrystals are electrophoretically deposited on the FTO/TiO$_2$ electrodes. Different halide composition of PbSO$_4$-Oleate capped CsPbX$_3$ nanocrystals can be mixed to give gamut of emission including white light both in colloidal dispersion as well as in films.

Graphical Abstract:
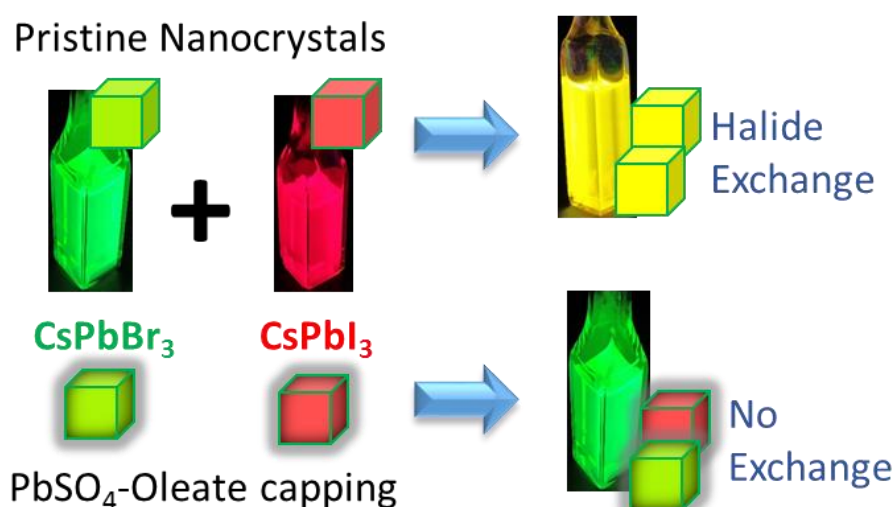
4A.1 Introduction:

Mixed halide perovskite nanocrystals (NCs) have attracted a lot of attention in recent years because of the ability to tune their bandgap through halide ion composition.[1-6] By tailoring the ratio of Cl$^-$ / Br$^-$ and Br$^-$ / I$^-$ it is possible to modulate the absorption and emission properties of metal halide perovskites across the entire visible region.[7] These unique composition dependent optical properties have been touted as a candidate for tandem solar cells and display devices.[8-11]

Metal halide perovskites are ionic in nature and the halide ion mobility within perovskite films has been studied in detail.[12-14] The migration of halide ions can also be visualized through spectral changes as the mixed halide films undergo phase segregation upon exposure to light.[15-17] The movement of these halide ions is also seen through the exchange of halide ions in NCs. For example, CsPbBr$_3$ NCs dispersions are able to undergo halide ion exchange with say lead chloride or lead iodides (or any halide source) salts to produce both mixed and completely exchanged CsPbCl$_3$ or CsPbI$_3$ NCs depending on the concentration of salts added.[18-20] The ability to readily exchange halide ions has also allowed for the creation of gradient structures with CsPbBr$_3$ at one side and CsPbI$_3$ at the other side of the same film.[21] Upon excitation these gradient structures direct the flow of charge carriers to the lowest bandgap region viz. the CsPbI$_3$ region, in the film which allows for efficient charge transfer.[22] However, the ease of halide ion exchange also poses a problem to create a tandem structure with layers of metal halide perovskites of different compositions due to their high mobility.[23] The obvious problem is keeping the lead halide perovskite NCs intact without undergoing exchange of halide ions so that the original band structure is maintained.

One way to suppress the exchange of halide ions is to cap the CsPbX$_3$ NCs with a non-halide layer. Use of bidentate ligands or polymer capping can provide stability to these NCs to some degree.[24] We followed an approach by capping the NCs with the PbSO$_4$-Oleate which was earlier reported to align the NCs in a linear fashion.[25, 26] Since the absorption and emission behaviour of perovskite NCs are dependent on the halide composition, we can monitor these spectral features to estimate the extent of halide ion exchange between CsPbX$_3$ NCs. We have chosen CsPbBr$_3$ and CsPbI$_3$ NCs as model system and discuss the role of PbSO$_4$-Oleate

capping on its optical properties and its ability to suppress anion exchange. We also found out that these capped NCs can be electrophoretically deposited on FTO/TiO$_2$ as an orderly aligned array. Further we show that the white emission can be achieved in dispersion and electrophoretically deposited film by mixing the different CsPbX$_3$ NCs in appropriate ratio.

4A.2 Experimental sections:

4A.2.1 Chemicals:

Cesium carbonate (Cs$_2$CO$_3$, Alfa Aesar, 99.9%), 1- octadecene (ODE, Sigma-Aldrich, 95%), oleylamine (OAm, Sigma Aldrich, 70% technical grade), oleic acid (OA, Sigma Aldrich, 90% technical grade), hexane (Sigma-Aldrich, 95% anhydrous), methyl acetate (MeAc, Sigma-Aldrich, 99.5% anhydrous), tetrabutylammonium hydrogen sulfate (TBAHS, Acros, 98%), lead(II) chloride (PbCl$_2$, Sigma-Aldrich, 99.999%), lead (II) bromide (PbBr$_2$, Sigma-Aldrich, 99.999%), lead (II) iodide (PbI$_2$, Sigma-Aldrich, 99.999%), acetone (Sigma-Aldrich, ≥99.5% ACS reagent), chloroform (CHCl$_3$, Fischer Scientific, 99.9% HPLC grade).

4A.2.2 Synthesis of pristine CsPbX$_3$ NCs:

Stock solution of cesium oleate (Cs-Oleate) is prepared by reacting 0.4 g cesium carbonate with oleic acid (1.25 mL) in 20 mL of ODE at 150 °C. The mixture is initially put under vacuum and N$_2$ (at least 3 times alternatively) to get rid of dissolved oxygen and moisture. The solution is then stored in a vial, in an inert atmosphere, for further use. PbX$_2$ (0.94 mmol), where X is the halide to be incorporated into the NC, is taken in a 50 mL 3 necked round bottom (RB) flask along with 25 mmol of ODE. The mixture is then degassed and put under N$_2$ alternatively (at least 3 times) to get rid of moisture and dissolved oxygen. 2.5 mL each OA and OAm are then added to the mixture and the temperature is increased to 130 °C to let the lead salts dissolve. The temperature is further increased to 180 °C and the previously prepared Cs-Oleate (pre-heated to 100 °C) is swiftly added to the reaction mixture and after 5 seconds the reaction is cooled using an ice-bath. The crude NCs are then washed twice with MeAc and finally redispersed in hexane for further use. These NCs are designated as CsPbX$_3$ NCs.

4A.2.3 Synthesis of PbSO$_4$-Oleate capped CsPbX$_3$ NCs:

The PbSO$_4$-Oleate capped NCs are prepared by following a reported method.[25] First, PbSO$_4$-Oleate are prepared by reacting 0.4 mL PbCl$_2$ (139 mg dissolved in 8 mL OAm and 0.1 mL OA), 0.2 ml TBAHS (424.4 mg in 10 ml acetone), 0.4 mL OA, and 10 mL CHCl$_3$. These are then precipitated by adding ethanol (30mL) and centrifuged at 7000 rpm for 5 min. The supernatant is discarded and the precipitate is redispersed in hexane (3mL). The prepared PbSO$_4$-Oleate dispersion are then added to the CsPbX$_3$ dispersion and allowed to self-assemble for 12 hours. It is then centrifuged at 1300 rpm and the supernatant is discarded while the resulting precipitate is redispersed in hexane and are designated as PbSO$_4$-Oleate capped CsPbX$_3$ NCs.

4A.2.4 Deposition of PbSO$_4$-Oleate capped CsPbX$_3$ NCs on FTO/TiO$_2$ electrodes:

TiO$_2$ is first coated on FTO substrate by doctor blading method and then annealed at 90 °C for 1 hour followed by 500 °C for 1 hour. Then these prepared, two electrodes are connected to a direct current (DC) power supply and dipped into a dispersion of PbSO$_4$-Oleate capped CsPbX$_3$ NCs. Depending on the time or the voltage applied, the film thickness (number of deposited NCs) can be controlled.

4A.2.5 Measurement of photoluminescence (PL) quantum Yield:

Room temperature PL quantum yield of NCs has been calculated by taking Fluorescein dye as reference dissolved in 0.1 M aqueous NaOH solution. The NCs are dispersed in hexane. The absorbance of Fluorescein dye and the NCs are kept below 0.1 at 470 nm while taking absorbance spectrum. To increase the signal to noise ratio, Fluorescein absorbance spectrum are taken repeatedly 5 times without taking the quartz cuvette out and then the spectrum is averaged out. Similarly, the absorbance of the NCs is also measured 5 times and then averaged in the same way. In case of PL, for all the samples, the NCs and the dye are excited at 470 nm keeping all the other parameters constant. Here again, 5 spectra for each sample are measured and averaged out. To calculate the PL quantum yield the following equation has been used:

$$QY_s = QY_{ref} \cdot \frac{F_s}{F_{ref}} \cdot \frac{A_{ref}(\lambda_{exc})}{A_s(\lambda_{exc})} \cdot \frac{n_s^2}{n_{ref}^2}$$

Where,

QY_s = Unknown PL quantum yield of sample.

QY_{ref} = Known PL quantum yield of reference (Here, for Fluorescein it is 0.91 in 0.1 M aqueous NaOH solution[27]).

F_s = Integrated PL intensity i.e. area under the PL Curve of the sample with fixed excitation wavelength.

F_{ref} = Integrated PL intensity i.e. area under the PL curve of the reference at fixed excitation wavelength.

$A_{ref}(\lambda_{exc})$ = Absorbance value of the reference in its absorbance spectrum at that fixed PL excitation wavelength.

$A_s(\lambda_{exc})$ = Absorbance value of the sample in its absorption spectrum at that fixed PL excitation wavelength.

n_s = Refractive index of the solvent in which sample is dispersed. Here, it is 1.3749 for toluene.

n_{ref} = Refractive Index of the solvent in which reference is dispersed. Here, it is 1.3333 for aqueous NaOH solution.

4A.2.6 Calculating concentration of the deposited films:

The concentration of PbSO$_4$-Oleate capped NCs are calculated using the Beer-Lambert's law:

$$A = \varepsilon \times C \times l$$

Where

A **=** Absorbance corresponding to the deposited NCs on the film. This is calculated by taking the absorbance of the dispersion at t = 0 (before any film deposition) and absorbance at t = t (after film deposition).

ε = The molar absorptivity. Values for molar absorptivity are taken from the reference.[28]

c = concentration of the deposited NCs.

l = length of the cuvette (1 cm).

For PbSO$_4$-Oleate capped CsPbBr$_3$ NC's:

$$1.47 = 3.83 \times 10^6 M^{-1} cm^{-1} \times c \times 1\ cm$$

$$c \cong 0.39\ \mu M$$

$$volume\ of\ solution = 3.1\ mL$$

$$\frac{0.39\ \mu moles}{1,000\ mL} \times 3.1\ mL = 1.2\ nmoles$$

$$Area\ of\ deposition = 1.5\ cm^2$$

$$\frac{Concentration}{Area} = \frac{1.2\ nmoles}{1.5\ cm^2} = 0.8\ \frac{nmoles}{cm^2}$$

This procedure is repeated for PbSO$_4$-Oleate capped CsPbI$_3$ NCs also where the molar absorptivity used is $2.4 \times 10^6\ M^{-1} cm^{-1}$. The concentration for these films are found to be $0.9\ \frac{nmoles}{cm^2}$.

4A.2.7 Characterization:

UV-visible absorption spectra are recorded on Cary 50 Bio UV-visible scanning spectrophotometer. PL spectra are recorded using Horiba Jobin Yvon Fluorolog 3 spectrophotometer. Time correlated single photon counting (TCSPC) data are recorded on Horiba Jobin Yvon single photon counting system, with nanoLED laser (370 nm). Transmission electron microscopy (TEM) images are recorded using a JEOL JEM 2100 F field emission transmission electron microscope at 200 kV.

4A.3 Results and Discussions:

4A.3.1 Capping of CsPbBr$_3$ and CsPbI$_3$ NCs with PbSO$_4$-Oleate:

Pristine CsPbBr$_3$ and CsPbI$_3$ NCs are prepared by following the hot injection method as discussed in the experimental section. A representative TEM image of CsPbBr$_3$ NCs is given along with the size distribution in Figure 4A.1a and 4A.1b. The NCs are of cubic morphology with average edge length ~ 11 nm. These NCs dispersion are then treated with the already prepared PbSO$_4$-Oleate dispersions (prepared in CHCl$_3$) to obtain a capping of PbSO$_4$-Oleate on the NCs.
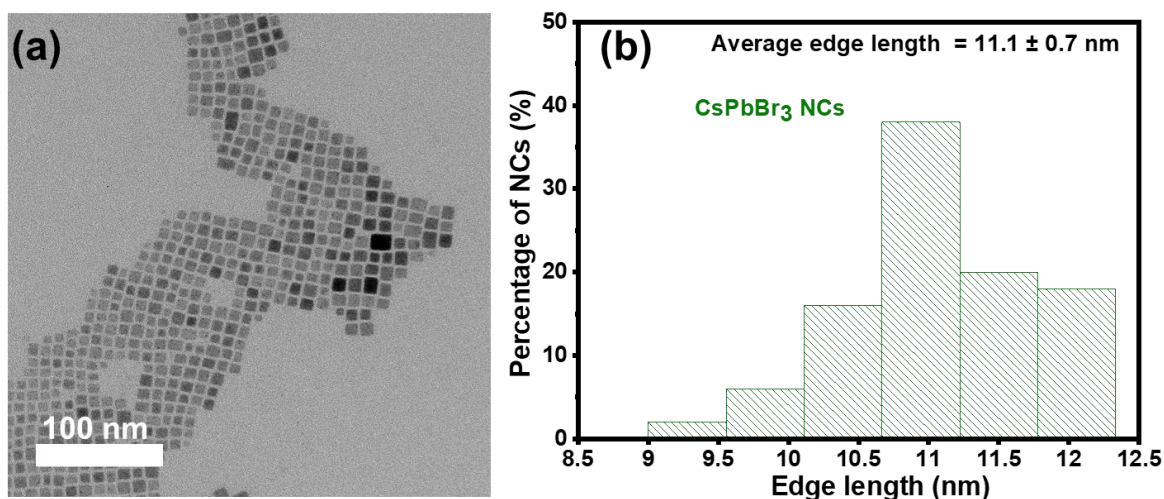
Figure 4A.1: (a) Representative TEM image of pristine CsPbBr₃ NCs. (b) Size distribution of pristine CsPbBr₃ NCs having an average edge length of ~ 11 nm.
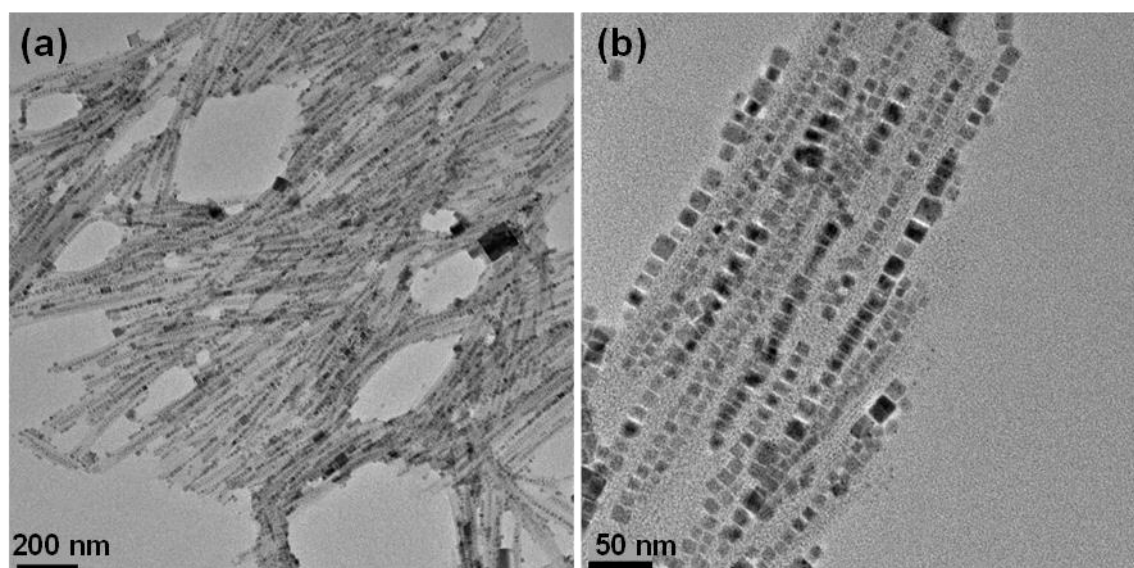
Figure 4A.2: Representative TEM images (a, b) of PbSO₄-Oleate capped CsPbBr₃ NCs at different magnification. The contrast difference around NCs can be seen and also the NCs appear to be assembled into linear chains.

As shown previously the capping of PbSO₄-Oleate also induces linear alignment of these NCs.[25, 26] Figure 4A.2a and 4A.2b at shows the representative TEM image of PbSO₄-Oleate capped CsPbBr₃ NCs, at different magnification, showing linear alignment of NCs. The details on the mechanism of such an alignment following the evaporation of solvent are presented previously.[25] It is interesting to note that the capping layer keeps the NCs well-dispersed with minimal inter-particle interactions.

4A.3.2 Excited state properties of PbSO₄-Oleate capped CsPbX₃ NCs:

Figure 4A.3 shows the PL spectra of CsPbBr$_3$ and CsPbI$_3$ NCs (absorption spectra in the inset) with and without the capping of PbSO$_4$-Oleate. As prepared pristine CsPbBr$_3$, and CsPbI$_3$ NCs dispersion in hexane, (shown by dotted curves) exhibit characteristic excitonic PL peak at 518 nm and 686 nm respectively (excitonic absorption peak at 500 nm for CsPbBr$_3$ and 665 nm for CsPbI$_3$ NCs). It is important to note that the PL features are retained following the capping of CsPbX$_3$ NCs with PbSO$_4$-Oleate (shown by solid curves). This confirms that the capping layer does not introduce any noticeable distortion in the band energy or the optical properties of these NCs. However, the absorbance and PL is little red shifted for PbSO$_4$-Oleate capped, CsPbBr$_3$ and CsPbI$_3$ NCs which may be due to increased electronic coupling because of their linear arrangement.
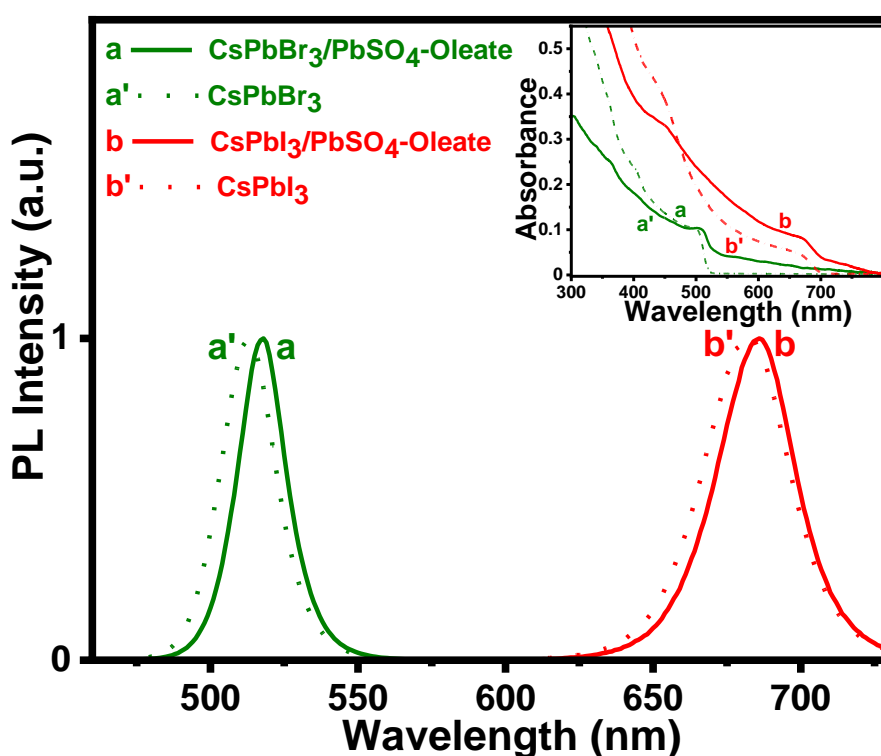
Figure 4A.3: PL spectra of PbSO$_4$-Oleate capped NCs compared with pristine CsPbX$_3$ NCs. The excitation wavelength is 370 nm. Inset shows the corresponding absorbance spectra. It can be seen that the absorbance of PbSO$_4$-Oleate capped NCs remained similar to that of pristine NCs but with a presence of scattering tail which is due to its reduced colloidal stability (increased effective size).

The PL lifetimes of these perovskite NCs, with and without PbSO$_4$-Oleate capping, are shown in Figure 4A.4. The decay parameters are analyzed through biexponential fit and are presented in Table 4A.1. Inherently, the CsPbI$_3$ has longer

lifetime than CsPbBr$_3$ NCs which is attributed to its higher dielectric constant of CsPbI$_3$, leading to the lower excitonic binding energy. It is evident that the capping with PbSO$_4$-Oleate increases the PL lifetime. For example, the average lifetime of CsPbBr$_3$ NCs increases from 13.3 ns to 16.9 ns upon capping with PbSO$_4$-Oleate. Reduction in surface defects through capping is likely to increase the PL lifetime due to a decrease in the possible number of trap states.
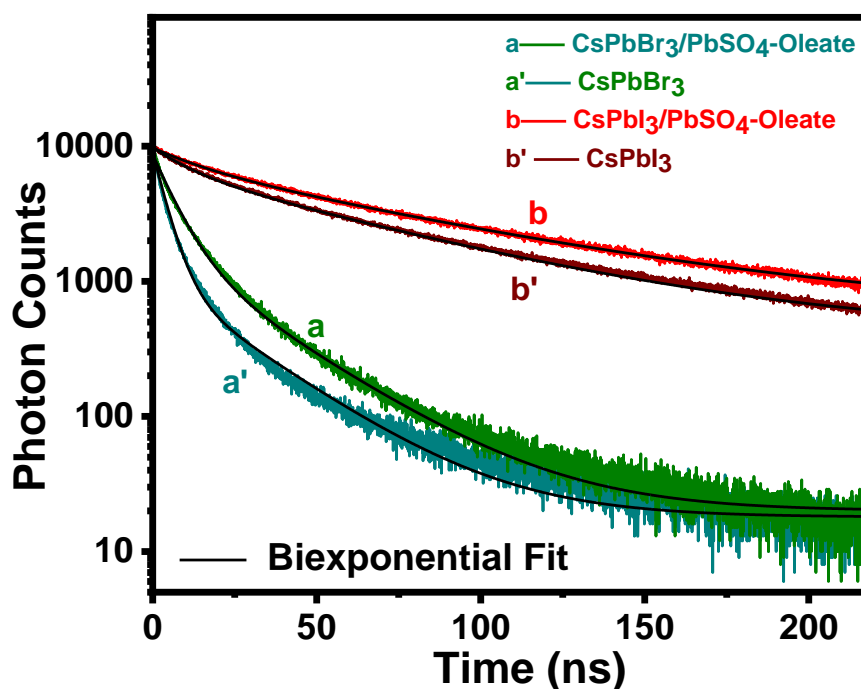
Figure 4A.4: PL decay of PbSO$_4$-Oleate capped NCs along with pristine samples. PL decays are recorded at their PL peak wavelength with excitation wavelength of 370 nm.

The absorbance and PL spectra used for the determination of PL quantum yield are presented in Figure 4A.5. Table 4A.1 compares the PL quantum yield, radiative and non-radiative rates of charge carrier recombination. We see a small decrease in the PL quantum yield when NCs are capped with PbSO$_4$-Oleate. It is likely that the scattering effects of the PbSO$_4$-Oleate capped perovskite NCs dispersion at the selected absorbance wavelength for PL quantum yield measurements introduces some error. We have not made any effort to exclude scattering effects in these calculations. However, increased PL lifetimes of PbSO$_4$-Oleate capped NCs show that radiative decay rate constants become smaller upon capping with PbSO$_4$-Oleate. In general, we can conclude that the PbSO$_4$-Oleate capping stabilizes the excited state by remediating the defects at the NC surface.
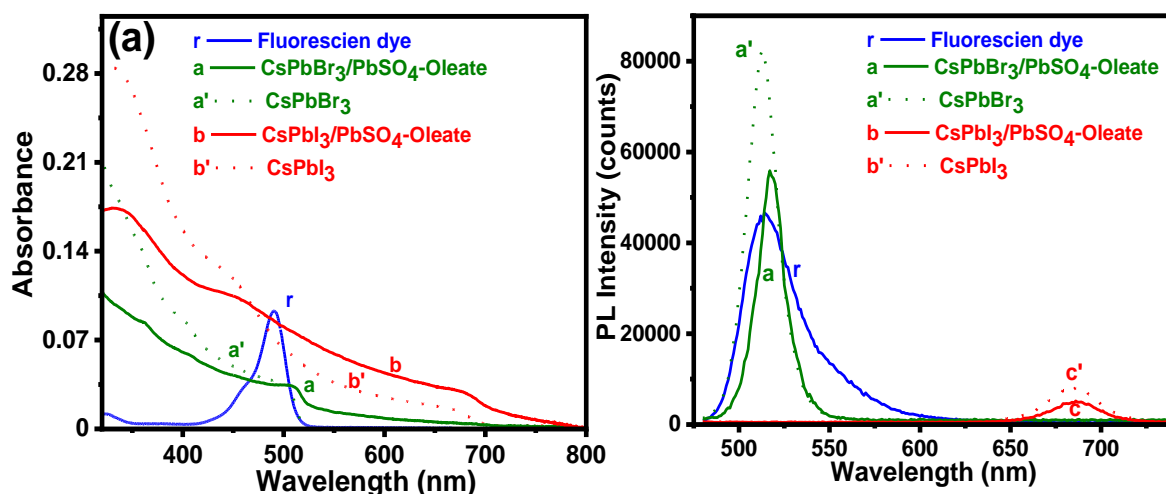
Figure 4A.5: UV-visible absorbance (a) and PL spectra (b) of CsPbX₃ NCs along with standard (Fluorescein) dye. Firstly, the PL quantum yield of CsPbBr₃ NCs are determined with reference to fluorescein dye and then the PL quantum yield of other NCs are determined using CsPbBr₃ as a reference. We acknowledge that there is error in estimation of the quantum yield of PbSO₄-Oleate capped NCs as these NCs shows scattering behaviour and thus exact value of absorbance cannot be determined. However, we would like to point out that the PL quantum yield remains similar if not increased for the PbSO₄-Oleate capped NCs thus suggesting that the quality of the PbSO₄-Oleate treated NCs remained similar to that of pristine NCs.

Table 4A.1: Excited state characteristics of PbSO₄-Oleate capped and pristine CsPbX₃ NCs.

Sample	Quantum Yield (Φ)	τ_{avg} ns	k_r $10^7 s^{-1}$	k_{nr} $10^7 s^{-1}$
CsPbBr₃/PbSO₄-Oleate	0.73	16.9	4.32	0.16
CsPbBr₃	0.95	13.3	7.14	0.04
CsPbI₃/PbSO₄-Oleate	0.06	74.1	0. 08	1.3
CsPbI₃	0.09	60.2	0. 15	1.5

$\tau_{avg} = 1/(k_r + k_{nr})$ and $k_r = (\Phi/\tau_{avg})$

4A.3.3 Halide ion exchange between CsPbX₃ NCs:

The CsPbX₃ NCs are sensitive to the surrounding environment and can undergo quick halide ion exchange or transform into lower dimensional phase when exposed to heat or moisture.[17, 19, 29] This instability of CsPbX₃ NCs in reactive chemical environment limits their use in light energy harvesting applications. Hence, it is

important to check whether the capping with PbSO$_4$-Oleate can provide enough chemical stability to overcome halide exchange problem between two CsPbX$_3$ NCs. It is earlier pointed out in chapter 2 of this thesis that the CsPbX$_3$ NCs easily undergoes anion exchange in colloidal dispersion as well as in films. Depending upon the concentration of halide ions in dispersion and exposure time it is possible to control the composition of mixed halide in the NCs. The same phenomenon of halide ion exchange occurs when dispersions of separately synthesized CsPbBr$_3$ and CsPbI$_3$ NCs are mixed together or two films of CsPbBr$_3$ and CsPbI$_3$ are made on top of each other.

To visualize the anion exchange, we have mixed pristine CsPbBr$_3$ and CsPbI$_3$ NCs dispersion and have recorded absorbance and PL spectra of the mixture.
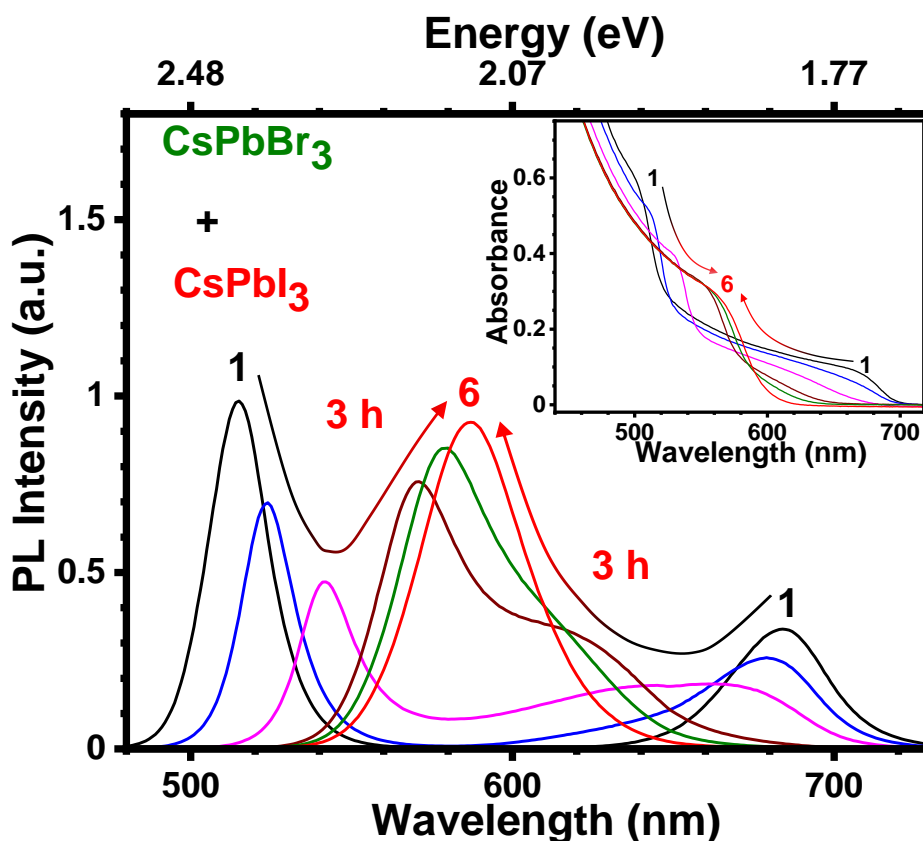
Figure 4A.6: PL spectra of the mixture of pristine CsPbBr$_3$ and CsPbI$_3$ NCs in hexane. The PL spectra changes with increasing time indicating the anion exchange between CsPbBr$_3$ and CsPbI$_3$ NCs. Peak "1" to peak "6" correspond to mixing time of 3 h. The excitation wavelength is 370 nm. Inset shows the absorption spectra for the same mixture. Here also the absorption profile changes where excitonic absorption peak corresponding to pristine CsPbBr$_3$ and CsPbI$_3$ NCs (peak "1") merge together to give excitonic absorption peak (peak "6") corresponding to some mixed halide, CsPbBr$_x$I$_{3-x}$ NCs composition.

In Figure 4A.6, at initial time of just mixing the samples of CsPbBr$_3$ and CsPbI$_3$ NCs (peak corresponding to "1"), the PL spectra of the mixture show two PL peaks corresponding to the individual PL peaks of CsPbBr$_3$ (515 nm) and CsPbI$_3$ (685 nm) NCs. After increasing the mixing time, the PL peak corresponding to CsPbBr$_3$ NCs shifts to longer wavelength while PL peak corresponding to CsPbI$_3$ NCs shifts to shorter wavelength. Finally, after 3 hours, both these peaks merge together to form a single PL peak (peak corresponding to "6") at 588 nm and no further change is observed. This shows the completion of anion exchange to give some mixed halide, CsPbBr$_x$I$_{3-x}$ NCs composition. Similar behaviour is seen in absorption spectra of the mixture shown in the inset of Figure 4A.6. We do not that the time required for complete exchange is dependent on the concentration of the NCs and also the stirring speed of the dispersion.
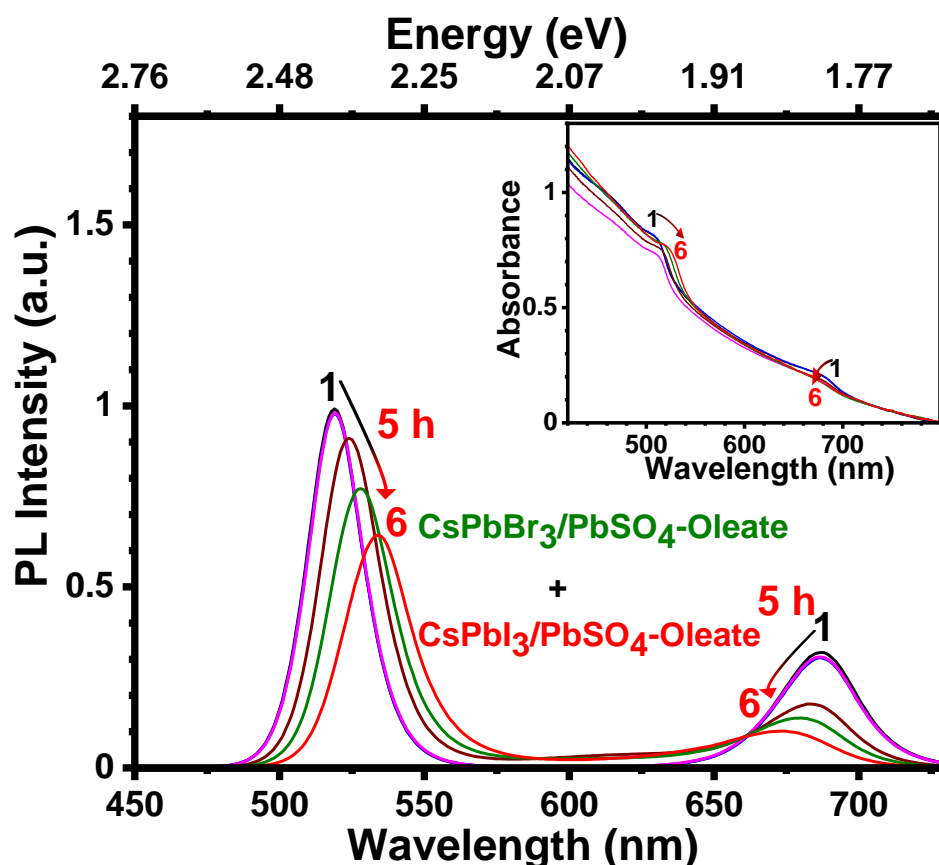
Figure 4A.7: PL spectra of the mixture of CsPbBr$_3$/PbSO$_4$-Oleate and CsPbI$_3$ PbSO$_4$-Oleate NCs in hexane. The shift in PL peak position is small (~ 30 nm) with increasing mixing time. Peak "1" to peak "6" correspond to mixing time of 5 h. The excitation wavelength is 370 nm. Inset shows the absorption spectra of the same mixture of NCs. It shows very small change in the absorption profile (little peak shift with decreasing intensity).

We then repeated the above experiments with $PbSO_4$-Oleate capped, $CsPbBr_3$ and $CsPbI_3$ NCs dispersion in hexane. Both absorption and PL spectra are recorded at different time intervals after mixing the two NCs dispersion as shown in Figure 4A.7. The dispersion is kept under slow stirring to ensure that the capping of $PbSO_4$-Oleate does not gets damaged. The PL and absorption (shown in inset) spectra show the characteristic excitonic feature corresponding to both $PbSO_4$-Oleate capped, $CsPbBr_3$ and $CsPbI_3$ NCs. The mixture shows very slow change upto 5 hours and after that there is no change in the PL and absorption spectra. For the PL spectra, there is some change with small spectral shift of ~ 30 nm for both $PbSO_4$-Oleate capped, $CsPbBr_3$ and $CsPbI_3$ NCs, with decreasing intensity. This change in the PL peak is not as drastic as in case of mixing of pristine $CsPbBr_3$ and $CsPbI_3$ NCs. Similarly, the absorption spectra shown no appreciable shift in excitonic peak position corresponding to individual $PbSO_4$-Oleate capped NCs. We proposed that this small shift in PL peak is due to the halide ion exchange between the poorly capped or uncapped NCs.
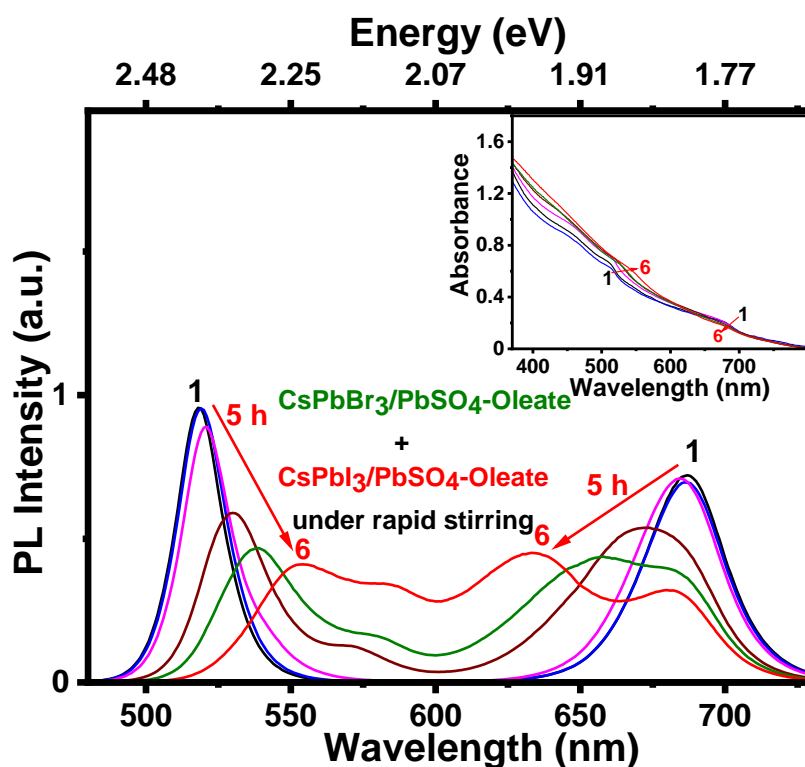
Figure 4A.8: The mixing of $PbSO_4$-Oleate capped, $CsPbBr_3$ and $CsPbI_3$ NCs under rapid stirring. The mixing time correspond to 5 h and excitation wavelength is 370 nm. The mixture shows appreciable anion exchange which is suggestive that rapid stirring indeed cause $PbSO_4$-Oleate capping to be partially destroyed.

The deterioration of the PbSO$_4$-Oleate capping under stirring could be another reason for this observed behaviour. Note that vigorous stirring results in larger shifts in the PL peaks as shown in Figure 4A.8.

Also, we recorded absorbance and PL spectra, presented in Figure 4A.9, for the NCs mixture of PbSO$_4$-Oleate capped CsPbBr$_3$ NCs and pristine CsPbI$_3$ NCs. It turns out that still anion exchange happens but now at a relatively slower rate. This confirms that that indeed capping of CsPbX$_3$ NCs by PbSO$_4$-Oleate suppresses the anion exchange between NCs.
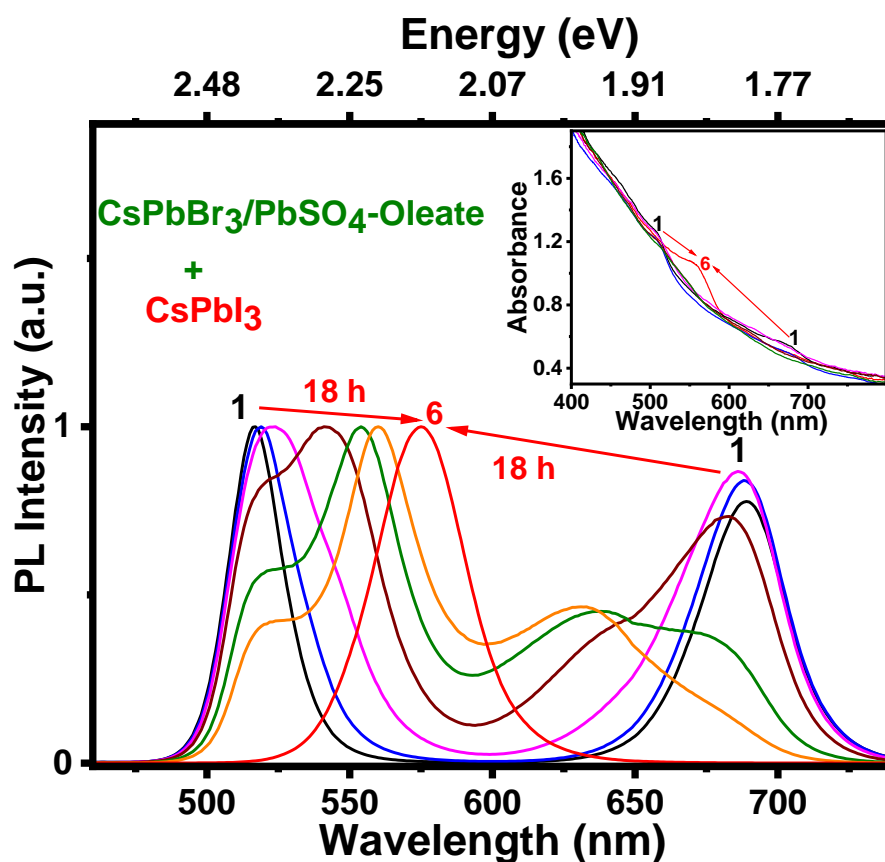
Figure 4A.9: The mixing of NCs where one is capped and other one is uncapped i.e. PbSO$_4$-Oleate capped CsPbBr$_3$ NCs mixed with pristine CsPbI$_3$ NCs. The mixing time correspond to 18 h and excitation wavelength is 370 nm. It is clear that the NCs still undergo anion exchange but at a slower rate than the pristine CsPbX$_3$ NCs.

The PL of mixed halide perovskites is dependent on the ratio of halide ions. For example, if CsPbBr$_3$ NCs or films are exposed to iodide we see a gradual shift of the absorption and PL peak towards red. Thus, we can use the PL peak as a measure to gauge the exchange of halide ions between the NCs. The change in PL

peak is an easier and better way to visualize halide ion exchange. Figure 4A. 10a shows the change in PL peak position of mixture of CsPbBr₃ and CsPbI₃ NCs along with the PbSO₄-Oleate capped, CsPbBr₃ and CsPbI₃ NCs. In case of mixture of pristine CsPbX₃ NCs, the PL peak corresponding to CsPbBr₃ and CsPbI₃ NCs converse together while in the case of PbSO₄-Oleate capped NCs, the PL peaks show a very small change during the mixing period. This confirms the protective role of PbSO₄-Oleate capping for the CsPbX₃ NCs.
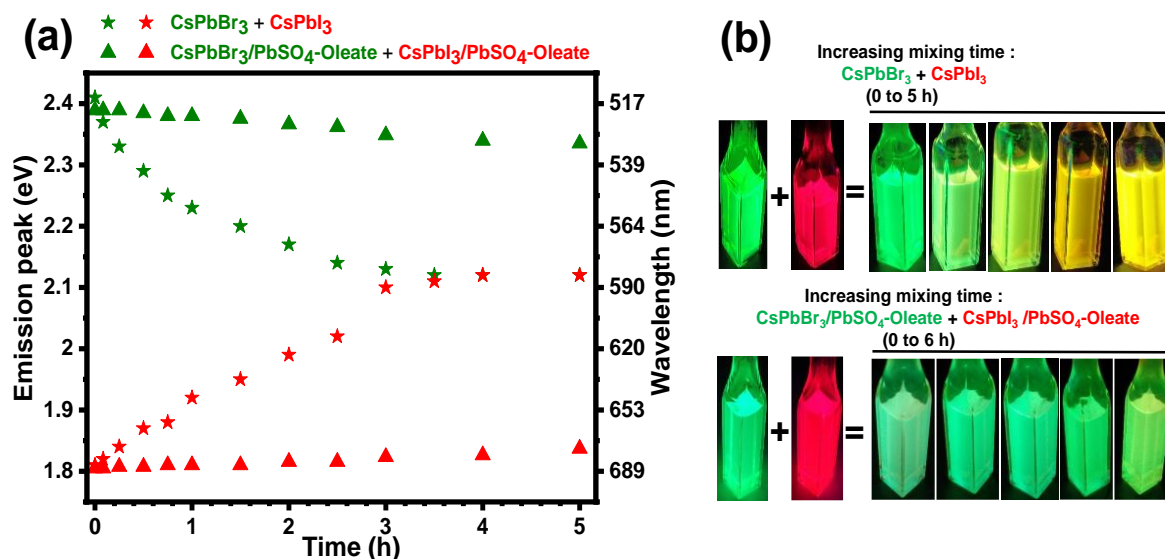
Figure 4A.10: (a) The PL peak change for the mixture of pristine, CsPbBr₃ and CsPbI₃ NCs dispersion in hexane (shown by green and red "★") and for PbSO₄-Oleate capped, CsPbBr₃ and CsPbI₃ NCs, ((shown by green and red "▲"), with increasing mixing time. The data is obtained from Figure 4A.6 and Figure 4A.7. (b) Photographs of the pristine and PbSO₄-Oleate capped, CsPbBr₃ and CsPbI₃ NCs under UV light (365 nm) at various mixing times.

In Figure 4.10b, the photograph of mixture of pristine NCs and PbSO₄-Oleate capped NCs are shown. While the pristine NCs mixture emission color changes from green to yellow signifying mixed halide perovskite NCs composition (initial color is green because the emission is dominated by high PLQY of CsPbBr₃ NCs), the emission color mixture of PbSO₄-Oleate capped NCs shows very slight change and it remained mainly as green emissive.

4A.3.4 Electrophoretic deposition (EPD):

One very interesting thing we found that these PbSO₄-Oleate capping can give net negative charge to CsPbX₃ NCs and they can be electrophoretically deposited on

electrodes. No prior reports are available on the EPD of the CsPbX$_3$ NCs. The EPD of semiconductor and metal nanoparticles provides a convenient way to deposit one or more layers of NCs within the mesoscopic TiO$_2$ film.[30-33] EPD are carried as shown in Figure 4A.11, where the NCs are deposited on the positive electrode signifying net negative charge on the NCs after the PbSO$_4$-Oleate capping. FTO electrodes coated with TiO$_2$ are dipped in the NCs dispersion and a DC voltage of 100 V is applied. With increasing time, the NCs from the dispersion gets deposited on the positive FTO electrode. The film on electrode became more or more colored as thickness increase whereas the NCs dispersion in the cuvette shows decrease in absorbance over time. This shows that the NCs from the dispersion leaves the dispersion and gets deposited on the electrode. We note that the film thickness can be increased by increasing applied voltage or increasing NCs concentration within the same deposition time. The absorbance of the NCs dispersion in the cuvette is recorded at time = 0 sec (before EPD) gives the initial concentration of the NCs dispersion while the absorbance recorded at time = t sec gives the concentration at that time which is smaller than the initial concentration.
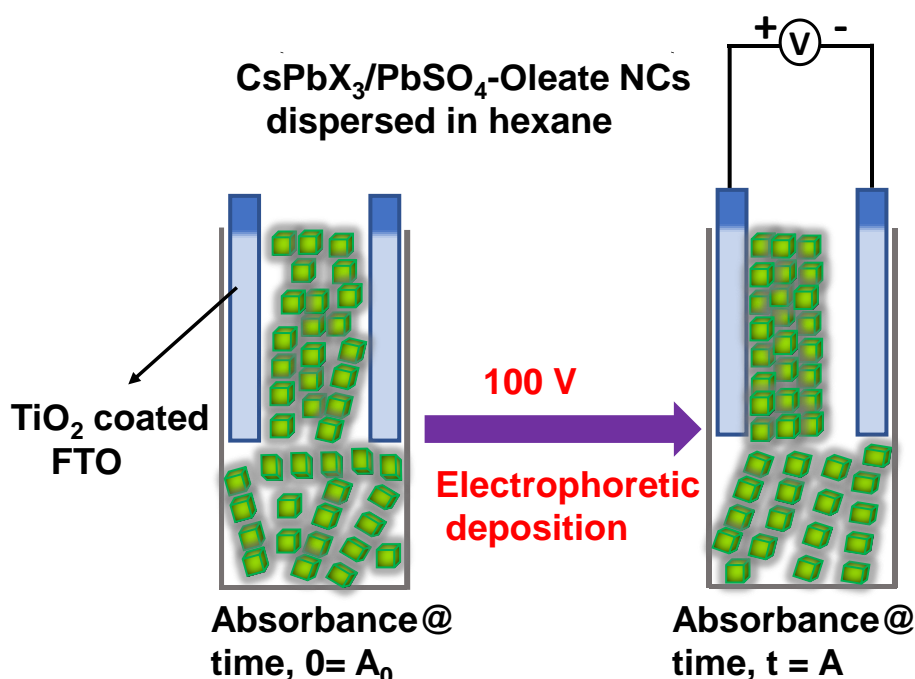
Figure 4A.11: Schematic of EPD of PbSO$_4$-Oleate capped CsPbBr$_3$ NCs on the TiO$_2$ coated FTO electrode. Electrode are dipped in the cuvette filled with NCs dispersion. With increasing time and voltage more and more NCs are deposited on the (+) ve electrode resulting in more coloration of the electrode while the NCs dispersion in the cuvette loses color.
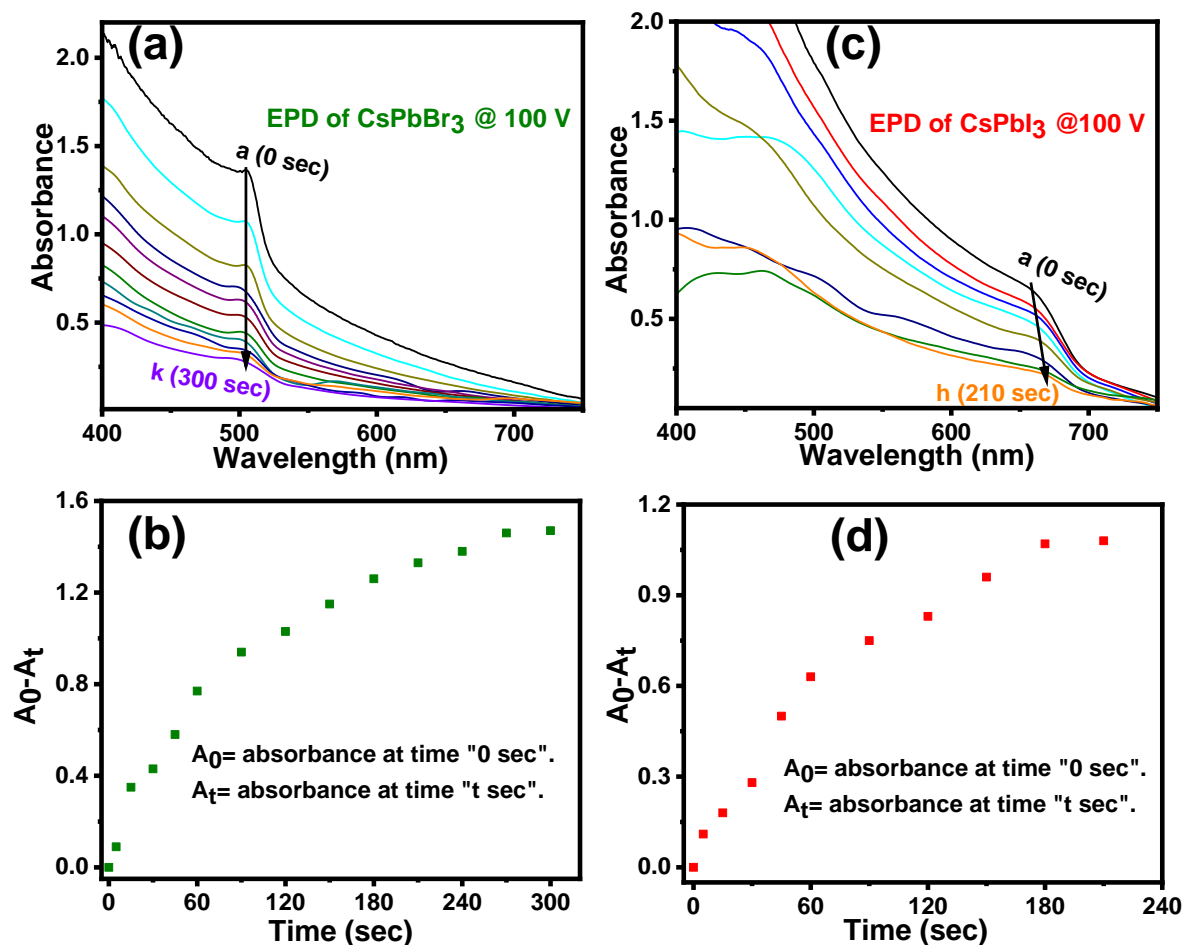
Figure 4A.12: UV-visible absorbance spectra of dispersion of (a) PbSO$_4$-Oleate capped CsPbBr$_3$ (c) PbSO$_4$-Oleate capped CsPbI$_3$ NCs at different time undergoing EPD. Panels (b) and (d) shows the difference in absorbance with time and corresponds to the number of NCs deposited on the electrode.

Figures 4A.12 shows the rate of deposition of NCs onto electrode surface as monitored from the disappearance of CsPbX$_3$ NCs dispersion absorbance in the cuvette. The difference absorbance of the dispersion is used to determine the amount of NCs deposited on the electrode surface. The absorption spectra recorded during EPD of these two samples of PbSO$_4$-Oleate capped, CsPbBr$_3$ and CsPbI$_3$ NCs are shown in Figure 4A.12a and 4A.12c respectively. Figures 4A.12b and 4A.12d shows the rate of deposition of NCs onto electrode surface as monitored from the disappearance of NCs dispersion absorbance. As can be seen from the traces in Figures 4A.12b and 4A.12d, within about 300 s it is possible to drive the NCs from the dispersion onto the electrode surfaces. This deposition dependence on time allows us to control the amount of NCs deposited on the electrode surface.

The total amount of NCs deposited on the electrode surface during deposition time is 0.8 nmole/cm^2 of PbSO$_4$-Oleate capped CsPbBr$_3$ NCs and 0.9 nmole/cm^2 of PbSO$_4$-Oleate capped CsPbI$_3$ NCs (calculation shown in the experimental section). The EPD method of deposition of NCs is quick and less tedious than conventional spin coating or vapor deposition methods. The convenience of achieving desired film thicknesses with ease allows deposition of multiple layers of different perovskite NCs. A representative bilayer film of CsPbX$_3$ NCs is made by EPD, first depositing PbSO$_4$-Oleate capped CsPbBr$_3$ NCs and then PbSO$_4$-Oleate capped CsPbI$_3$ NCs on TiO$_2$ coated FTO electrode. This film shows an additive absorbance feature, (feature of both PbSO$_4$-Oleate capped CsPbBr$_3$ NCs and PbSO$_4$-Oleate capped CsPbI$_3$ NCs) and remain stable over an extended period of time under ambient conditions as shown in Figure 4A.13.
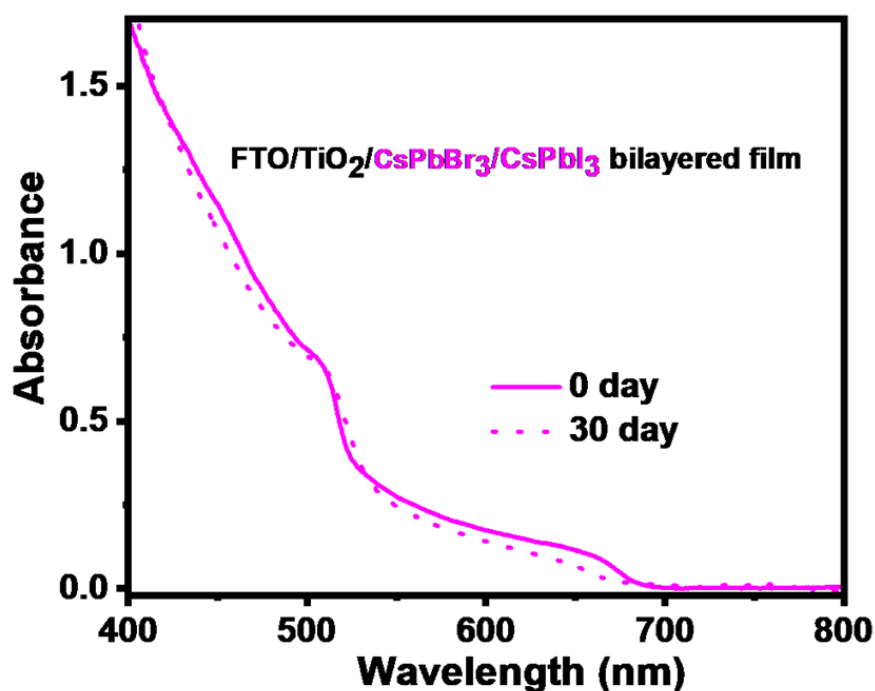
Figure 4A.13: UV-visible absorbance spectra showing the stability of the PbSO$_4$-Oleate capped CsPbBr$_3$/CsPbI$_3$ NCs layered film stored under ambient condition. The individual excitonic peaks for bromide and iodide are preserved indicating no intermixing of the NCs.

Interestingly, the shape of the EPD assembled PbSO$_4$-Oleate capped CsPbX$_3$ NCs remains linear and they are packed closely in linear arrays on the top of the TiO$_2$ film. In Figure 4A.14 we have shown schematic that depicts the initial alignment of PbSO$_4$-Oleate capped NCs in dispersion and their bundling to form larger nanorod

secondary arrays on the electrode surface. It is possible that charge neutralization of PbSO$_4$-Oleate capped CsPbX$_3$ NCs assembly near the electrode surface promotes their aggregation and form larger rods as they get deposited onto the electrode surface.
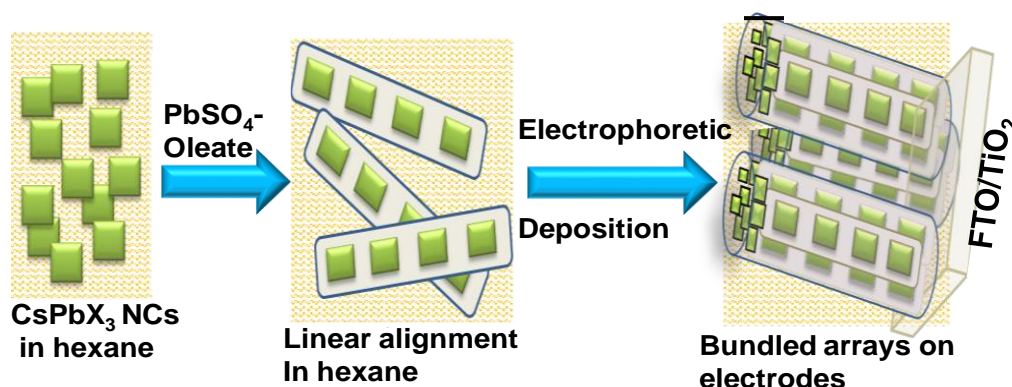
Figure 4A.14: Hierarchical assembly of PbSO$_4$-Oleate capped CsPbX$_3$ NCs. Illustration of alignment of CsPbX$_3$ NCs following PbSO$_4$-Oleate capping in hexane and as bundled array on the electrode surface following EPD.

For more details about the characterization of the EPD assembled film, optical properties, please see our published paper (Ravi et al., J. Am. Chem. Soc. **2018**, 140, 28,8887-8894.)

4A.3.5 Tunable emission including white light:

The composition dependent bandgap tuning makes metal halide perovskites attractive for achieving emission at a desired wavelength. However, as described earlier in the chapter, simply mixing two or more pristine CsPbX$_3$ NCs to obtain desired color is not possible because they would undergo anion exchange between themselves. However, now after PbSO$_4$-Oleate capping, it is possible to suppress the halide ion exchange between different CsPbX$_3$ NCs. The varying composition allows us to tune the emission of entire visible spectrum and the combination of the two or more of these suspensions can yield additional emissive colors. Examples of such color combination are shown in Figure 4A.15. We mixed blue emitting, PbSO$_4$-Oleate capped CsPbCl$_3$ NCs; green emitting, PbSO$_4$-Oleate capped CsPbBr$_3$ NCs and red emitting, PbSO$_4$-Oleate capped CsPbI$_3$ NCs to obtain different color both in colloidal dispersion as well in the EPD deposited films. We also further explored this feature to obtain white phosphor perovskites by mixing blue (CsPbCl$_3$), green

(CsPbBr$_3$), and red (CsPbI$_3$) emitting NCs capped with PbSO$_4$-Oleate. Figure 4A.16a shows the PL spectra of three separate dispersions of PbSO$_4$-Oleate capped, CsPbCl$_3$, CsPbBr$_3$ and CsPbI$_3$ NCs. As expected, they exhibit characteristic red (R), green (G), and blue (B) emission as a marker for the RGB display. Figure 4A.16b shows the resultant PL spectra when these NCs are mixed together.
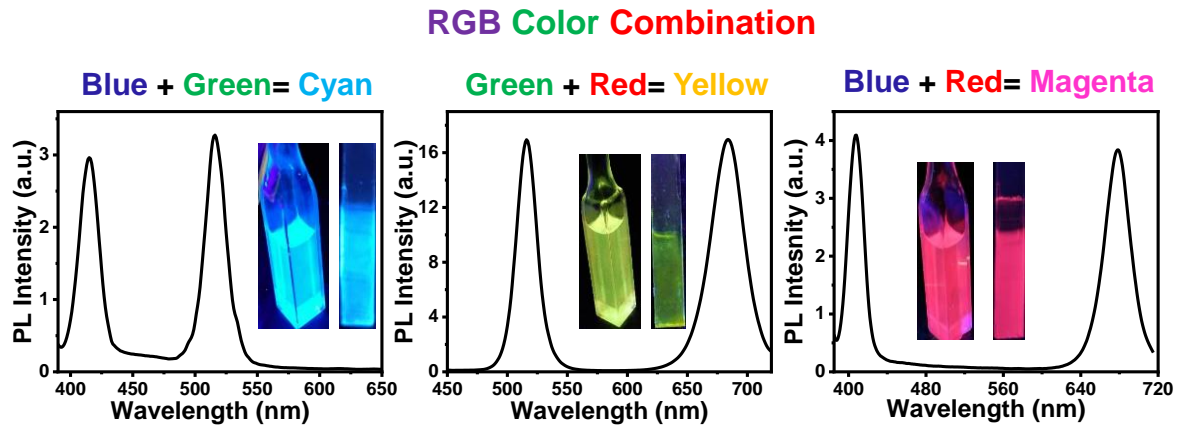
Figure 4A.15: Scheme showing RGB (Red, Green, and Blue) color combination. PbSO$_4$-Oleate capped CsPbX$_3$ NCs are mixed to generate different colors. Insets show the photographs of the colloidal dispersions and the deposited films on FTO/TiO$_2$ under UV light. The excitation wavelength is 370 nm.
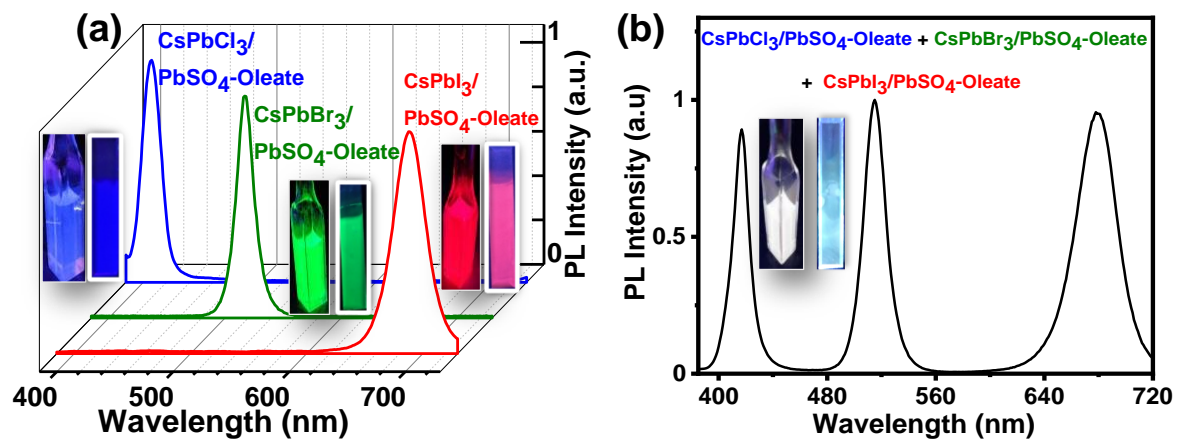
Figure 4A.16: (a) Individual PL spectra of PbSO$_4$-Oleate capped, CsPbCl$_3$, CsPbBr$_3$ and CsPbI$_3$ NCs. Inset shows the photograph of these NCs dispersion in hexane and on EPD deposited films under UV light. (b) Mixture of these three NCs together dispersion to produce white emission. This white emission is retained even in EPD deposited film. Photographs of suspensions and corresponding films under UV light are shown in insets. The excitation wavelength is 370 nm.

We have also made an effort to fill the spectral void in the emissions by introducing other CsPbX$_3$ mixed halide perovskite NCs with intermediate emission. The

resultant emission spectrum is shown in the Figure 4A.17a. The CIE diagram corresponding to the obtained spectrum is shown in Figure 4A.17b showing coordinates (0.29, 0.32) very close to ideal white light coordinates (0.33, 0.33). The ability to maintain relatively high emission shows that the most of the emission is retained despite the possibility of interparticle interactions in the excited state.
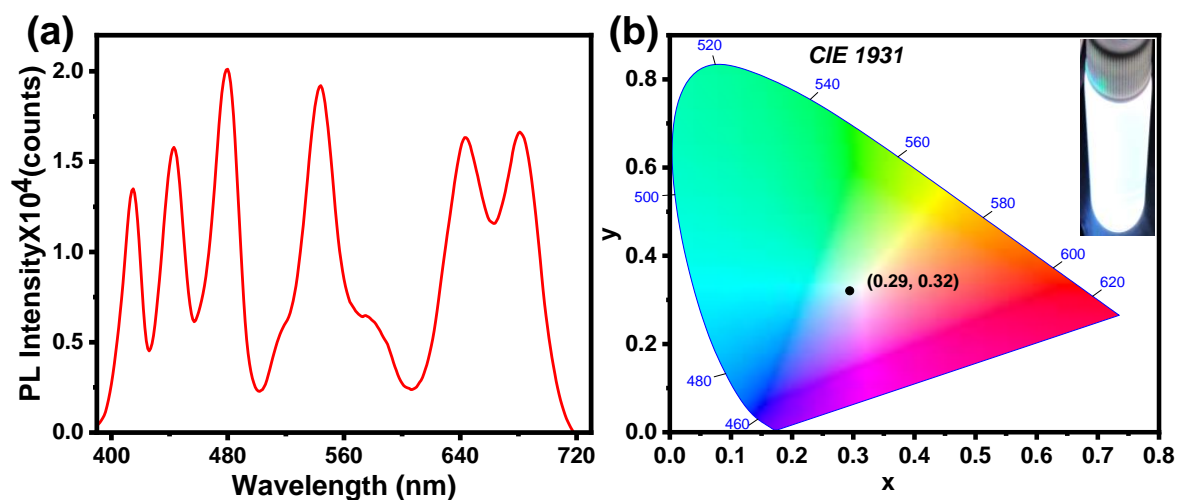
Figure 4A.17: (a) The PL spectrum shows the generation of white light by mixing different compositions of PbSO$_4$-Oleate capped CsPbX$_3$ NCs to have a better color purity of white light. (b) Color chromaticity of resultant white light is shown on CIE 1931.The inset shows the photograph of colloidal dispersion of NCs showing white light emission under UV light.

4A.4 Conclusions:

In this chapter, we have shown a convenient way to cap CsPbX$_3$ NCs with PbSO$_4$-Oleate. This strategy of capping offers a new approach to restrict the anions of CsPbX$_3$ NCs from undergoing anion exchange reactions when they are mixed together. Here for the first time, we have also shown that the PbSO$_4$-Oleate capped CsPbX$_3$ NCs can be electrophoretically deposited on the FTO/TiO$_2$ electrodes. This deposition method presents a very easy way to make films out of CsPbX$_3$ NCs where film thickness can be simply controlled by voltage and deposition time. The color obtained in dispersion by mixing PbSO$_4$-Oleate capped CsPbX$_3$ NCs remains unchanged even when deposited onto FTO/TiO$_2$ electrode surfaces because suppression of anion exchange between the films as well. This way, white emission can be obtained in dispersion as well as electrophoretically deposited film by mixing the different combination of PbSO$_4$-Oleate capped CsPbX$_3$ NCs, in appropriate

ratio. Thus, the capping strategy of CsPbX$_3$ NCs by PbSO$_4$-Oleate enables employment of wide array of tunable CsPbX$_3$ NCs for harvesting light energy while retaining the optical properties of individual CsPbX$_3$ NCs.

4A.5 References:

1. Beal, R. E.; Slotcavage, D. J.; Leijtens, T.; Bowring, A. R.; Belisle, R. A.; Nguyen, W. H.; Burkhard, G. F.; Hoke, E. T.; McGehee, M. D., Cesium Lead Halide Perovskites with Improved Stability for Tandem Solar Cells. *J. Phys. Chem. Lett.* **2016,** *7*, 746-751.

2. McMeekin, D. P.; Sadoughi, G.; Rehman, W.; Eperon, G. E.; Saliba, M.; Horantner, M. T.; Haghighirad, A.; Sakai, N.; Korte, L.; Rech, B.; Johnston, M. B.; Herz, L. M.; Snaith, H. J., A mixed-cation lead mixed-halide perovskite absorber for tandem solar cells. *Science* **2016,** *351*, 151-5.

3. Sutter-Fella, C. M.; Li, Y.; Amani, M.; Ager, J. W., 3rd; Toma, F. M.; Yablonovitch, E.; Sharp, I. D.; Javey, A., High Photoluminescence Quantum Yield in Band Gap Tunable Bromide Containing Mixed Halide Perovskites. *Nano Lett.* **2016,** *16*, 800-6.

4. Huang, H.; Bodnarchuk, M. I.; Kershaw, S. V.; Kovalenko, M. V.; Rogach, A. L., Lead Halide Perovskite Nanocrystals in the Research Spotlight: Stability and Defect Tolerance. *ACS Energy Lett.* **2017,** *2*, 2071-2083.

5. Kovalenko, M. V.; Protesescu, L.; Bodnarchuk, M. I., Properties and potential optoelectronic applications of lead halide perovskite nanocrystals. *Science* **2017,** *358*, 745.

6. Buriak, J. M.; Kamat, P. V.; Schanze, K. S.; Alivisatos, A. P.; Murphy, C. J.; Schatz, G. C.; Scholes, G. D.; Stang, P. J.; Weiss, P. S., Virtual Issue on Metal-Halide Perovskite Nanocrystals—A Bright Future for Optoelectronics. *Chem. Mater.* **2017,** *29*, 8915–8917.

7. Nedelcu, G.; Protesescu, L.; Yakunin, S.; Bodnarchuk, M. I.; Grotevent, M. J.; Kovalenko, M. V., Fast Anion-Exchange in Highly Luminescent Nanocrystals of Cesium Lead Halide Perovskites (CsPbX$_3$, X = Cl, Br, I). *Nano Lett.* **2015,** *15*, 5635-5640.

8. Kamat, P. V., Hybrid Perovskites for Multijunction Tandem Solar Cells and Solar Fuels. A Virtual Issue. *ACS Energy Lett.* **2018,** *3*, 28-29.

9. Eames, C.; Frost, J. M.; Barnes, P. R. F.; O'Regan, B. C.; Walsh, A.; Islam, M. S., Ionic Transport in Hybrid Lead Iodide Perovskite Solar Cells. *Nat. Commun.* **2015,** *6*, 7497.

10. Manser, J. S.; Christians, J. A.; Kamat, P. V., Intriguing Optoelectronic Properties of Metal Halide Perovskites. *Chem. Rev.* **2016,** *116*, 12956-13008.

11. Jesper Jacobsson, T.; Correa-Baena, J.-P.; Pazoki, M.; Saliba, M.; Schenk, K.; Gratzel, M.; Hagfeldt, A., Exploration of the Compositional Space for Mixed Lead Halogen Perovskites for High Efficiency Solar Cells. *Energy Environ. Sci.* **2016,** *9*, 1706-1724.

12. Hoke, E. T.; Slotcavage, D. J.; Dohner, E. R.; Bowring, A. R.; Karunadasa, H. I.; McGehee, M. D., Reversible Photoinduced Trap Formation in Mixed-Halide Hybrid Perovskites for Photovoltaics. *Chem. Sci.* **2015,** *6*, 613-617.

13. Slotcavage, D. J.; Karunadasa, H. I.; McGehee, M. D., Light-Induced Phase Segregation in Halide-Perovskite Absorbers. *ACS Energy Lett.* **2016,** *1*, 1199-1205.

14. Mosconi, E.; De Angelis, F., Mobile Ions in Organohalide Perovskites: Interplay of Electronic Structure and Dynamics. *ACS Energy Lett.* **2016,** *1*, 182-188.

15. Draguta, S.; Sharia, O.; Yoon, S. J.; Brennan, M. C.; Morozov, Y. V.; Manser, J. M.; Kamat, P. V.; Schneider, W. F.; Kuno, M., Rationalizing the Light-Induced Phase Separation of Mixed Halide Organic-Inorganic Perovskites. *Nat. Commun.* **2018,** *8*, 200.

16. Brennan, M. C.; Draguta, S.; Kamat, P. V.; Kuno, M., Light-Induced Anion Phase Segregation in Mixed Halide Perovskites. *ACS Energy Lett.* **2018,** *3*, 204-213.

17. Yoon, S. J.; Kuno, M.; Kamat, P. V., Shift Happens. How Halide Ion Defects Influence Photoinduced Segregation in Mixed Halide Perovskites. *ACS Energy Lett.* **2017,** *2*, 1507-1514.

18. Sadhanala, A.; Ahmad, S.; Zhao, B.; Giesbrecht, N.; Pearce, P. M.; Deschler, F.; Hoye, R. L. Z.; Gödel, K. C.; Bein, T.; Docampo, P.; Dutton, S. E.; De Volder, M. F. L.; Friend, R. H., Blue-Green Color Tunable Solution Processable Organolead

Chloride–Bromide Mixed Halide Perovskites for Optoelectronic Applications. *Nano Lett.* **2015,** *15*, 6095-6101.

19. Jang, D. M.; Park, K.; Kim, D. H.; Park, J.; Shojaei, F.; Kang, H. S.; Ahn, J.-P.; Lee, J. W.; Song, J. K., Reversible Halide Exchange Reaction of Organometal Trihalide Perovskite Colloidal Nanocrystals for Full-Range Band Gap Tuning. *Nano Lett.* **2015,** *15*, 5191-5199.

20. Guhrenz, C.; Benad, A.; Ziegler, C.; Haubold, D.; Gaponik, N.; Eychmüller, A., Solid-State Anion Exchange Reactions for Color Tuning of CsPbX3 Perovskite Nanocrystals. *Chem. Mater.* **2016,** *28*, 9033-9040.

21. Hoffman, J. B.; Schleper, A. L.; Kamat, P. V., Transformation of Sintered CsPbBr$_3$ Nanocrystals to Cubic CsPbI$_3$ and Gradient CsPbBr$_x$I$_{3−x}$ through Halide Exchange. *J. Am. Chem. Soc.* **2016,** *138*, 8603-8611.

22. Kim, M.-c.; Kim, B. J.; Son, D.-Y.; Park, N.-G.; Jung, H. S.; Choi, M., Observation of Enhanced Hole Extraction in Br Concentration Gradient Perovskite Materials. *Nano Lett.* **2016,** *16*, 5756-5763.

23. Braly, I. L.; Stoddard, R. J.; Rajagopal, A.; Uhl, A. R.; Katahara, J. K.; Jen, A. K. Y.; Hillhouse, H. W., Current-Induced Phase Segregation in Mixed Halide Hybrid Perovskites and its Impact on Two-Terminal Tandem Solar Cell Design. *ACS Energy Lett.* **2017,** *2*, 1841-1847.

24. Pan, J.; Shang, Y.; Yin, J.; De Bastiani, M.; Peng, W.; Dursun, I.; Sinatra, L.; El-Zohry, A. M.; Hedhili, M. N.; Emwas, A. H.; Mohammed, O. F.; Ning, Z.; Bakr, O. M., Bidentate Ligand-Passivated CsPbI$_3$ Perovskite Nanocrystals for Stable Near-Unity Photoluminescence Quantum Yield and Efficient Red Light-Emitting Diodes. *J Am. Chem. Soc.* **2018,** *140*, 562-565.

25. Zhang, X.; Lv, L.; Ji, L.; Guo, G.; Liu, L.; Han, D.; Wang, B.; Tu, Y.; Hu, J.; Yang, D.; Dong, A., Self-Assembly of One-Dimensional Nanocrystal Superlattice Chains Mediated by Molecular Clusters. *J. Am. Chem. Soc.* **2016,** *138*, 3290-3293.

26. Pan, A.; Jurow, M.; Zhao, Y.; Qiu, F.; Liu, Y.; Yang, J.; Urban, J. J.; He, L.; Liu, Y., Templated self-assembly of one-dimensional CsPbX$_3$ perovskite nanocrystal superlattices. *Nanoscale* **2017,** *9* , 17688-17693.

27. Porrès, L.; Holland, A.; Pålsson, L.-O.; Monkman, A. P.; Kemp, C.; Beeby, A., Absolute Measurements of Photoluminescence Quantum Yields of Solutions Using an Integrating Sphere. *J. Fluoresc.* **2006,** *16*, 267-273.

28. Ravi, V. K.; Markad, G. B.; Nag, A., Band Edge Energies and Excitonic Transition Probabilities of Colloidal CsPbX$_3$ (X = Cl, Br, I) Perovskite Nanocrystals. *ACS Energy Lett.* **2016,** *1*, 665-671.

29. Balakrishnan, S. K.; Kamat, P. V., Ligand Assisted Transformation of Cubic CsPbBr$_3$ Nanocrystals into Two-Dimensional CsPb$_2$Br$_5$ Nanosheets. *Chem. Mater.* **2018,** *30*, 74-78.

30. Islam, M. A.; Xia, Y.; Telesca, D. A.; Steigerwald, M. L.; Herman, I. P., Controlled Electrophoretic Deposition of Smooth and Robust Films of CdSe Nanocrystals. *Chem. Mater.* **2004,** *16*, 49-54.

31. Brown, P.; Kamat, P. V., Quantum Dot Solar Cells. Electrophoretic Deposition of CdSe−C$_{60}$ Composite Films and Capture of Photogenerated Electrons with nC$_{60}$ Cluster Shell. *J. Am. Chem. Soc.* **2008,** *130*, 8890-8891.

32. Smith, N. J.; Emmett, K. J.; Rosenthal, S. J., Photovoltaic cells fabricated by electrophoretic deposition of CdSe nanocrystals. *Appl. Phys. Lett.* **2008,** *93*, 043504.

33. Jasieniak, J.; Smith, L.; van Embden, J.; Mulvaney, P.; Califano, M., Re-examination of the Size-Dependent Absorption Properties of CdSe Quantum Dots. *J. Phys. Chem.* **2009,** *113*, 19468-19474.

Chapter 4B

CsPbBr$_3$/ZnS Core/Shell Type Nanocrystals for Enhanced Water Stability
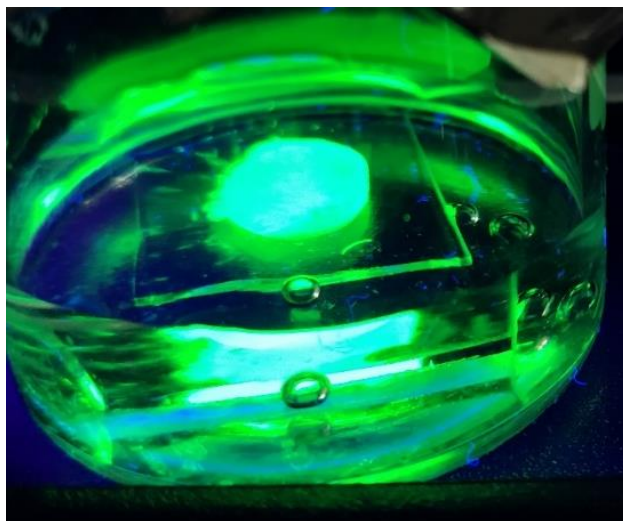
The work presented in this chapter has led to the following publication:

Ravi, V. K.; Saikia, S.; Yadav, S.; Nawale, V. V.; Nag, A. CsPbBr$_3$/ZnS Core/Shell Type Nanocrystals for Enhancing Luminescence Lifetime and Water Stability. *ACS Energy Lett.* **2020**, 5, 6, 1794-1796. Copyright permission has been taken from ACS publication for full paper.

Abstract:

In the previous chapter 4A, we have discussed about the suppression of anion exchange in CsPbX$_3$ nanocrystals by PbSO$_4$-Oleate coating. However, the capping was still not sufficient enough to protect the CsPbX$_3$ NCs from damage by water and light. Despite of extensive research on lead halide perovskites, there are a few reports addressing water instability issue. Core/shell heterostructure of CsPbX$_3$ NCs is desirable to overcome such problems. In this chapter, first we developed a strategy to stabilize the NCs under high temperature (~ 180 °C) so that it can be further processed for making core/shell heterostructures. Second part highlights conversion of already prepared CsPbBr$_3$ nanocrystals to CsPbBr$_3$/ZnS core/shell type nanostructure *via* treatment with a single molecular precursor namely, zinc diethyldithiocarbamate. We have developed CsPbBr$_3$/ZnS core/shell type nanostructure that showed enhanced water and photostability. Understanding of the band structure suggests formation of pseudo type II CsPbBr$_3$/ZnS core/shell type nanostructure where electron wavefunction gets confined within the core while hole wavefunction is delocalized over core and shell.

Graphical Abstract:

CsPbBr$_3$/ZnS core/shell

4B.1 Introduction:

Lead halide perovskite shows excellent optoelectronic properties[1-6] but they are prone to moisture, heat and light degradation.[7-10]. CsPbX$_3$ (X= Cl, Br, I) nanocrystals (NCs) also suffers from this fate and which impedes their commercial application. Literature survey reveals use of different inorganic and/or organic passivation/shell formation over lead halide perovskite NCs. There are reports of coating CsPbX$_3$ NCs with SiO$_2$, TiO$_2$, Al$_2$O$_3$, PbSO$_4$, CsPbBr$_x$ or polyhedral oligomeric silesquioxane to increase their stability against external environment.[11-16] However, the prior strategies have one problem or another like quenching of photoluminescence (PL), multiple NC cores are inside a single shell, and/or insulating shell that prevents the charge transport. A desirable way to improve the stability of the CsPbX$_3$ NCs is by coating the NCs by inorganic crystalline semiconducting shell to form a core/shell nanostructure.[17] It is known in literature for a long time where numerous examples of core/shell systems are present. Core/shell systems are advantageous because of better heat, light and moisture stability as compared to the core only NCs.[18] Moreover, core/shell nano-heterostructures help in separation of charge carriers due to formation of suitable band structure. Therefore, such nanostructures are considered as ideal candidates for important applications such as fluorescent biological labels, photovoltaics and catalysis.[19-23]

Making core/shell for other type of semiconductors like II-VI, III-V are routine technique and wide variety of literature are available on these.[24-28] Synthesis of core/shell structure of ionic perovskite NCs considered to be challenging because perovskite NCs are known to degrade under high processing temperature. Those methods do not work for halide perovskite NCs because of its inherent instability to high processing temperature to grow shell on seed NCs or polar solvent (another way of making core/shell by colloidal-atomic layer deposition). In this chapter, first we have stabilized the CsPbBr$_3$ NCs in dispersion at high temperature by addition of optimized amount of oleylammonium bromide (OAmBr). This stabilization of NCs in dispersion at high temperature is important to further grow shell on them. We then used, as synthesized CsPbBr$_3$ NCs as seeds, and treated it with zinc diethyldithiocarbamate (Zn(DDTC)$_2$) to form CsPbBr$_3$/ZnS core/shell type nanostructure. CsPbBr$_3$/ZnS core/shell type NCs shows enhanced aqueous- and photo-stability as compared to pristine CsPbBr$_3$ NCs. The Zn(DDTC)$_2$ treatment

appears to form CsPbBr$_3$/ZnS pseudo type-II core/shell NCs. The resulting core/shell type nanostructure retains the intense PL even when dipped inside water and can transfer holes to spiro-OMeTAD.

4B.2 Experimental Section:

4B.2.1 Chemicals:

Cesium carbonate (Cs$_2$CO$_3$, 99.9%, Sigma-Aldrich), lead (II) bromide (PbBr$_2$, 99.999%, Sigma-Aldrich), oleic acid (OA, 90%, Sigma-Aldrich), oleylamine (OAm, technical grade 70%, Sigma-Aldrich), 1-octadecene (ODE, technical grade 90%, Sigma-Aldrich), zinc diethyldithiocarbamate (Zn(DDTC)$_2$, 97%, Sigma-Aldrich), hydrobromic acid (HBr, 48% w/w in H$_2$O, Sigma-Aldrich), methyl acetate (MeAc, 99.98%, Sigma-Aldrich), toluene (Anhydrous, 99.99%, Sigma-Aldrich), TiO$_2$ paste (~30 nm, Sigma-Aldrich), ethanol (99 %, Rankem), spiro-OMeTAD (99.9%, Sigma-Aldrich), acetonitrile (99.9%, Sigma-Aldrich), 1-butanol (99.9%, Sigma-Aldrich), chlorobenzene (99.8%, Sigma-Aldrich), lithium bis(trifluoromethanesulfonyl) imide (Li-TFSI, 99.9%, Sigma-Aldrich), 4-tert-butyl pyridine (96 %, Sigma-Aldrich).

4B.2.2 Synthesis of cesium-oleate (Cs-Oleate):

Cs-Oleate stock solution is prepared by reacting Cs$_2$CO$_3$ (0.412 g) and OA (1.25 ml) in 20 mL ODE. The mixture is first degassed under vacuum and heated to 120 °C for removal of moisture. It is then further heated to 150 °C and continued until all Cs$_2$CO$_3$ reacted and turns to a transparent solution. It is then stored in a vial for further use.

4B.2.3 Synthesis of pristine CsPbBr$_3$ NCs:

Pristine CsPbBr$_3$ NCs are prepared by following the modified hot injection method[29] where 280 mg PbBr$_2$ is loaded in a three neck round bottom flask along with 20 mL ODE and 1:1 ratio of OAm:OA (2 mL of each). It is then put under alternate N$_2$ and vacuum for 1 h at 100 °C. After that, the reaction temperature is set to 180 °C. When the PbBr$_2$ completely solubilizes resulting in a transparent solution, hot injection of preheated Cs-Oleate has been done (2 mL) and immediately (approximately 5 sec) the reaction has been quenched by using an ice-water bath.

For the washing of the NCs, the crude NCs are first precipitated by centrifugation at 7000 rpm for 10 minutes. Toluene and MeAc are then added in 1:1 ratio to the

obtained precipitate and purified again via centrifugation under 11000 rpm for 5 minutes. The supernatant is discarded and then the final precipitate has been dried and stored in solid form (powders) for further use.

4B.2.4 Synthesis of OAmBr:

10 mL OAm, 1 mL HBr is loaded in a 25 mL three neck round bottom flask and heated to 80 °C under vacuum. The heating continued for 1 hour in N_2 environment. Then the heating is set to 120 °C and maintained for 2 hours under the same environment. Then at that temperature only, the resulting solution is collected in a N_2 filled vial tightly covered with septum. Whenever required, it has been heated at 80 °C to get a transparent yellow colored OAmBr solution as shown below and used in this form.

4B.2.5 Synthesis of CsPbBr₃/ZnS core/shell type NCs:

To prepare the CsPbBr₃/ZnS core/shell type NCs by treatment of CsPbBr₃ NCs with Zn(DDTC)$_2$, 15 mg CsPbBr₃ NCs powder is weighed and then dispersed in 3 mL ODE. Then the optimized amount of synthesized OAmBr (i.e. 20 µL for 15 mg CsPbBr₃ NCs) is added along with 16 mg of Zn(DDTC)$_2$ powder. The reaction mixture is then sonicated for 5 minutes to mix them completely and then heated at 120 °C for 1 hour using an oil bath. The product is washed first by centrifuging at 7000 rpm and discarding the supernatant. The precipitate is then dispersed in toluene and MeAc is added in equal volume and centrifuged again at 7000 rpm. Finally, the precipitate is dispersed in toluene for further use. This sample is referred as CsPbBr₃/ZnS core/shell type NCs. We also prepared a control sample where CsPbBr₃ sample heated only in presence of OAmBr, keeping all the parameters same (without the addition of Zn(DDTC)$_2$ powder). This sample is termed as CsPbBr₃-OAmBr NCs. Both the samples i.e. CsPbBr₃-OAmBr and CsPbBr₃/ZnS

core/shell type NCs shows reasonable colloidal stability in toluene where, the concentrated dispersions are stable upto 1 hour. After that, it slowly starts settling down. The dilute dispersions of the samples are colloidally stable for longer time than that.

4B.2.6. Deposition of NCs on glass, TiO₂ and spiro-OMeTAD substrates:

Films of CsPbBr₃/ZnS core/shell type NCs and CsPbBr₃-OAmBr NCs are made on the substrates by spin coating method. To prepare the films on glass substrate, NCs are directly spin coated on cleaned glass substrate at 200 rpm for 30 seconds. To prepare films on TiO₂, first TiO₂ paste in ethanol (0.504 g TiO₂ in 4.2 ml ethanol) is spin coated (1000 rpm for 20 seconds) on glass substrate and then the NCs are spin coated on that. Similarly, for making films on spiro-OMeTAD, a solution of spiro-OMeTAD (72.3 mg spiro-OMeTAD, 28.8 μL of 4-tert-butyl pyridine and 17.5 μL of Li-TFSI solution in 1 mL of chlorobenzene) is spin coated on glass substrate at 3000 rpm for 30 seconds and then subsequently NCs are deposited on that.

4B.2.7 Characterization:

Bruker D8 Advance X-ray diffractometer equipped with Cu Kα radiation of 1.54 Å is used to get powder X-ray diffraction (PXRD) data. UV-visible absorption spectra are recorded using Cary series UV-visible spectrophotometer. Steady state PL and PL decay measurements are carried out using FLS 980 (Edinburgh Instruments). The experimental PL decay plots are fitted with a bi-exponential decay equation, $y = A_1 e^{-x/\tau_1} + A_2 e^{-x/\tau_2}$; where A₁ and A₂ are the percentage contribution from lifetime τ_1 and τ_2 , respectively. Average lifetime is calculated by using the formula, $\tau_{avg} = \frac{\sum A_i \tau_i^2}{\sum A_i \tau_i}$. Transmission electron microscopy (TEM) images and high resolution TEM (HRTEM) images are captured by using a UHR FEG-TEM, JEOL JEM 2200FS field emission transmission electron microscope operated at 200 kV. Scanning electron microscopy (SEM) and energy dispersive X-ray spectroscopy (EDAX) measurements are performed on Zeiss Ultra Plus SEM instrument.

4B.3 Results and Discussion:

4B.3.1 Stability of colloidal CsPbBr₃ NCs against heat:

Core/shell heterostructure formation of NCs requires heating of the core NCs at higher temperatures (200 - 260 °C) for about 30 min or so. Unfortunately, such prolonged heat treatment of $CsPbBr_3$ NCs leads to the formation of Cs_4PbBr_6 impurity phase. So, the first challenge is to stabilize the $CsPbBr_3$ NCs dispersion for the high temperature processing. It was earlier reported that the oleylammonium ion binds to the surface of the $CsPbBr_3$ NCs.[30] The loss of oleylammonium along with Br^- from the surface of $CsPbBr_3$ NCs destabilizes the NCs dispersion at higher temperatures (>100 °C). To address this issue, we have added extra OAmBr to the pristine NCs dispersion and then heated the dispersion at 180 °C for 1 hour. This OAmBr addition is motivated by the work of Pradhan et al[31] adopted for the synthesis of $CsPbX_3$ NCs. As a control sample, we have also heated the $CsPbBr_3$ NCs dispersion without OAmBr keeping all other conditions same.

Figure 4B.1: PXRD patterns of pristine $CsPbBr_3$ NCs (red) along with the NCs when heated in absence (green) and presence (blue) of OAmBr at 180 °C for 1 hour. The NCs heated in absence of OAmBr gets degraded to mixture of phases of Cs_4PbBr_6 and $CsPb_2Br_5$, while the NCs heated in presence of OAmBr remains in orthorhombic phase of $CsPbBr_3$.

Figure 4B.1 shows the PXRD pattern of pristine CsPbBr$_3$ NCs, CsPbBr$_3$ NCs heated with OAmBr and a control sample of CsPbBr$_3$ NCs heated without the OAmBr. Also, the PXRD pattern of bulk CsPbBr$_3$, Cs$_4$PbBr$_6$ and CsPb$_2$Br$_5$ is given for the reference. In case of CsPbBr$_3$ NCs heated without the OAmBr, we can see lots of impurities phases present after heating for 1 hour. These impurities correspond to CsPb$_2$Br$_5$ and Cs$_4$PbBr$_6$. Further extending the heating of the reaction mixture, the CsPbBr$_3$ NCs completely breaks down to the white precipitate compound, mainly consisting of Cs$_4$PbBr$_6$, CsBr and PbBr$_2$. However, the CsPbBr$_3$ NCs heated with the optimized amount of OAmBr does not show such degradation and the orthorhombic phase is maintained.
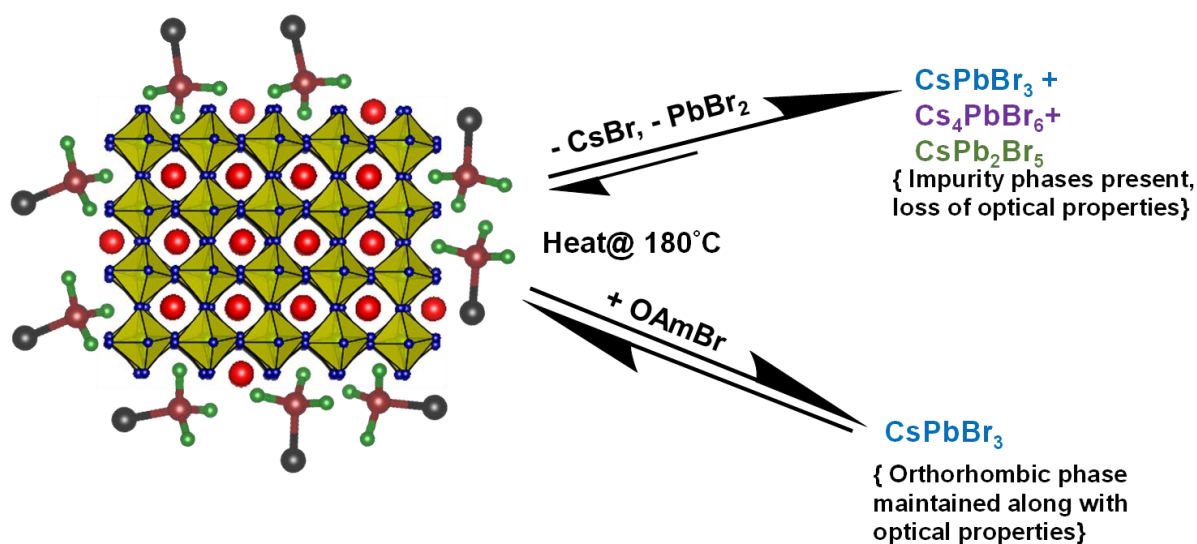
Figure 4B.2: Schematic showing the degradation mechanism when CsPbBr$_3$ NCs heated in absence of excess OAmBr while the NCs remains stable in its orthorhombic phase when heated in presence of little excess OAmBr.

The mechanism that we propose for the stabilization by excess OAmBr is that labile OAmBr gets detached from CsPbBr$_3$ NC surface while heating.[32] This disturbs the equilibria of adsorption and desorption of OAmBr from the surface of CsPbBr$_3$ NC. Once OAmBr gets detached, it leads to further loss of CsBr and PbBr$_2$ from the surface of NC and undergo surface reconstruction to give mixture of phases consisting of Cs$_2$Pb$_2$Br$_5$ and Cs$_4$PbBr$_6$. Excess addition of OAmBr maintains this equilibrium as shown in Figure 4B.2 and thus orthorhombic phase of the NCs remain preserved.

The UV-visible absorbance and PL spectra of pristine CsPbBr$_3$, CsPbBr$_3$ heated in presence of OAmBr and CsPbBr$_3$ heated without OAmBr are compared in Figure

4B.3. For the CsPbBr$_3$ NCs sample, heated in presence of excess OAmBr, the absorbance and PL profile remains similar to that of pristine CsPbBr$_3$ NCs whereas for the CsPbBr$_3$ sample heated without OAmBr, the absorbance profile is largely dominated by scattering behaviour and the PL is completely quenched. The quenching of PL is expected since the green emitting CsPbBr$_3$ NCs are degraded to other impurity phases as shown in figure 4B.1.
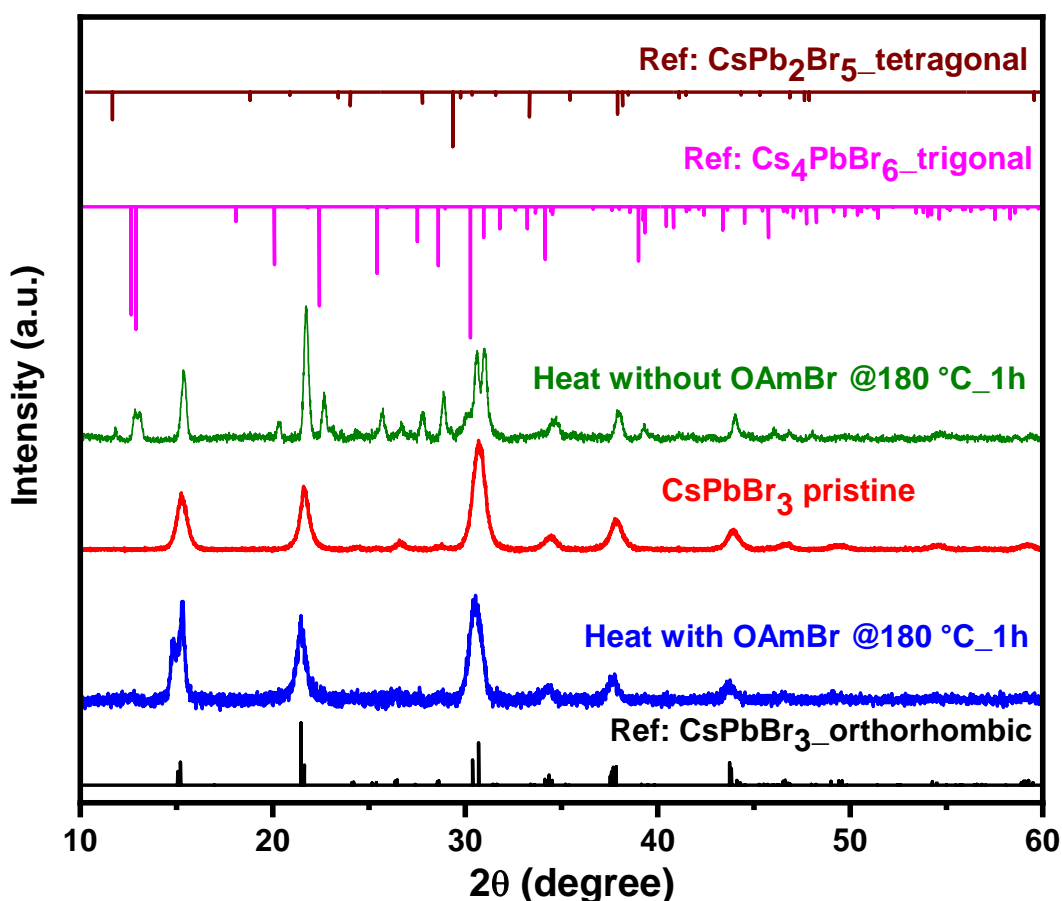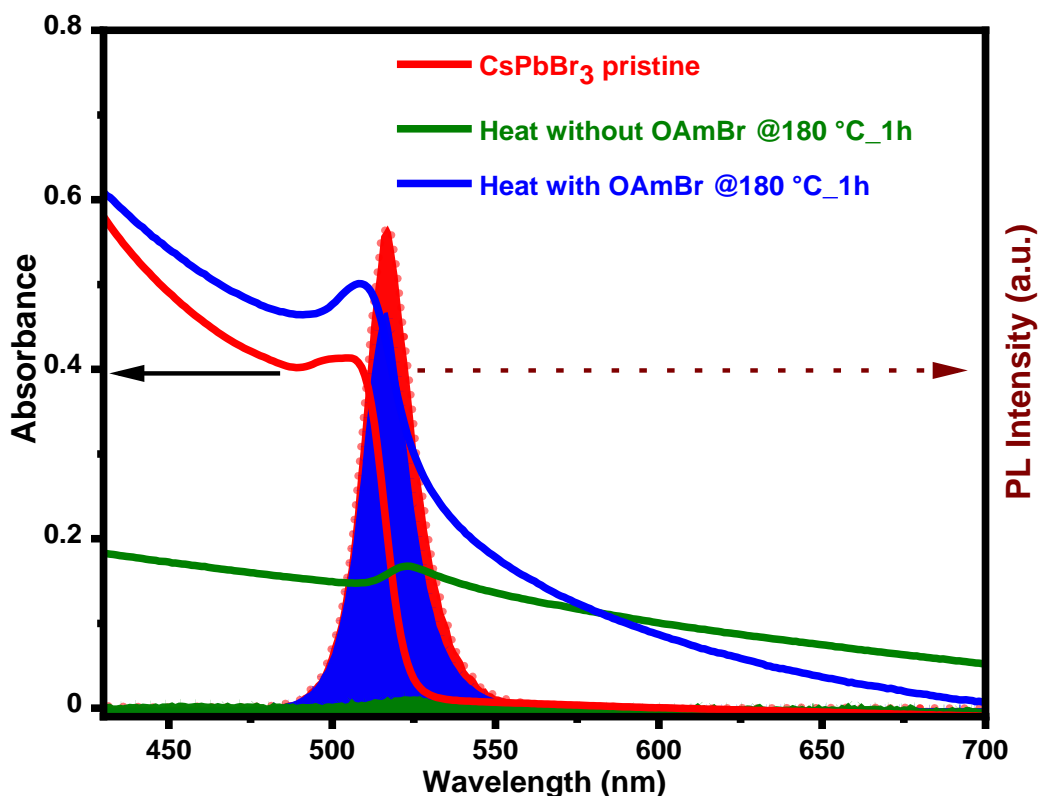

Figure 4B.3: UV-visible absorbance and PL spectra of pristine CsPbBr$_3$ NCs (red) along with the samples when heated in absence (green) and in presence (blue) of OAmBr at 180 °C for 1 h. For obtaining emission spectra, the samples are excited at 400 nm.

The PL decay profile for the pristine CsPbBr$_3$ NCs and the CsPbBr$_3$ NCs heated in presence of excess OAmBr are shown in the Figure 4B.4. The PL decay profiles are fitted with biexponential decay fit and both shows very similar lifetime values.

These analyses suggest that heating of the CsPbBr$_3$ NCs with excess OAmBr not only protect the orthorhombic crystal structure of the CsPbBr$_3$ NCs but also preserve the optical properties. This is a very important result as it gives us now a method where the CsPbBr$_3$ NCs dispersion can be stabilised at high temperature, which can be then processed further for making core/shell heterostructure. But note that the heat treatment of CsPbBr$_3$ NCs with excess

OAmBr leads to an increase in NCs size, which will be discussed in the next sub-section.
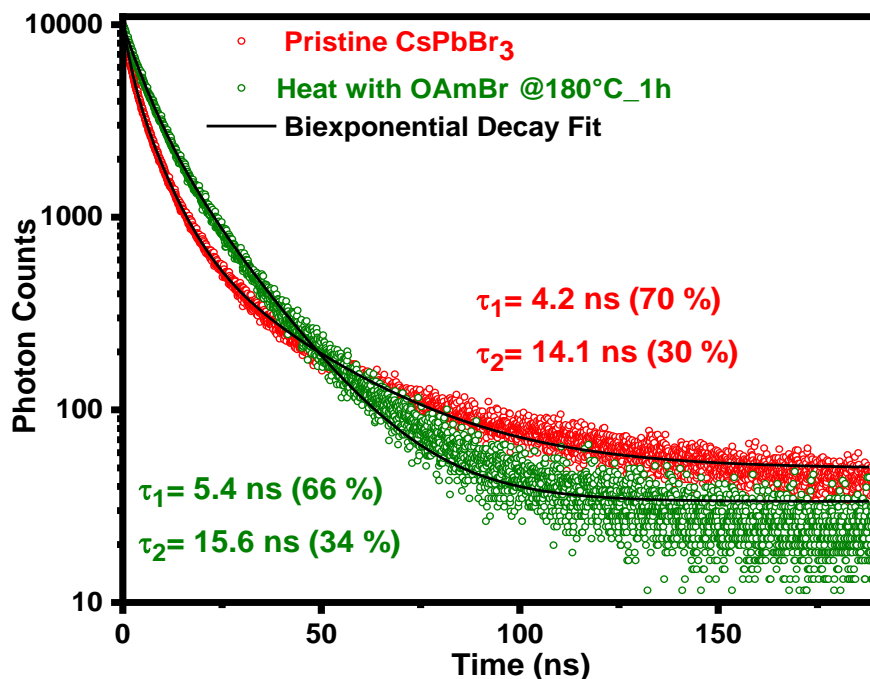
Figure 4B. 4: Comparison of PL decay of colloidal dispersion of pristine CsPbBr₃ NCs and CsPbBr₃-OAmBr NCs. Both the samples show similar decay profile and lifetime. PL decay lifetimes are obtained at the corresponding emission peak and the excitation wavelength used is 400 nm.

4B.3.2 CsPbBr₃/ZnS core/shell type NCs:

Now that we have tackled the heat stability of CsPbBr₃ NCs dispersion, we then proceeded for making shell on top of CsPbBr₃ NC. We have followed the modified protocol proposed by Dethlefsen et al.[33] to make ZnS shell on the CsPbBr₃ NCs.
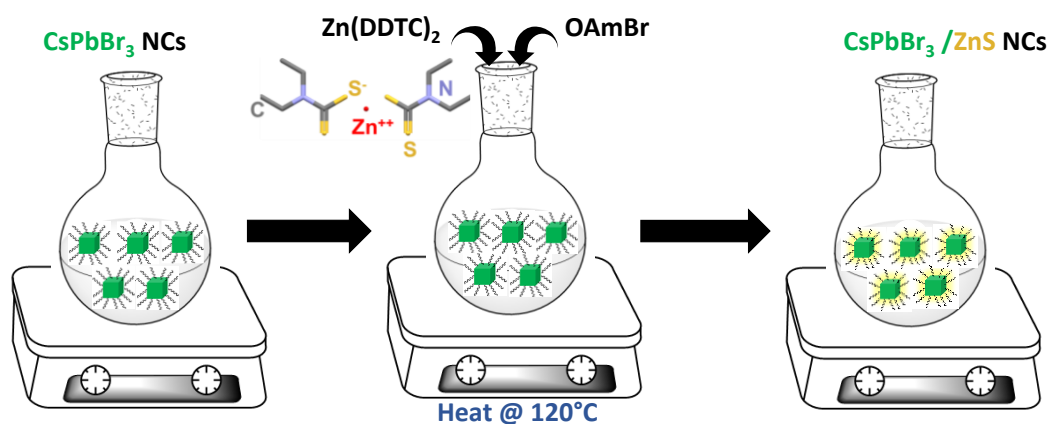
Figure 4B.5: Schematic of synthesis method used for the preparation of CsPbBr₃/ZnS core/shell type NCs.

$CsPbBr_3$ NCs are treated with $Zn(DDTC)_2$ and OAmBr at 120 °C for 1 hour forming a sample referred here as $CsPbBr_3$/ZnS core/shell NCs. The schematic for making $CsPbBr_3$/ZnS core/shell type NCs is shown in Figure 4B.5. We have used single molecular precursor $Zn(DDTC)_2$ for the growth of ZnS shell because $Zn(DDTC)_2$ slowly releases Zn and S at relatively lower temperature (~120 °C). The low temperature of shell growth and slow release of precursor ensures both the stability of $CsPbBr_3$ NCs and absence of separate nucleation of ZnS impurity phase. The control sample obtained after treating $CsPbBr_3$ NCs only with OAmBr is referred as $CsPbBr_3$-OAmBr NCs. In this case all other parameters are kept same except addition of $Zn(DDTC)_2$.
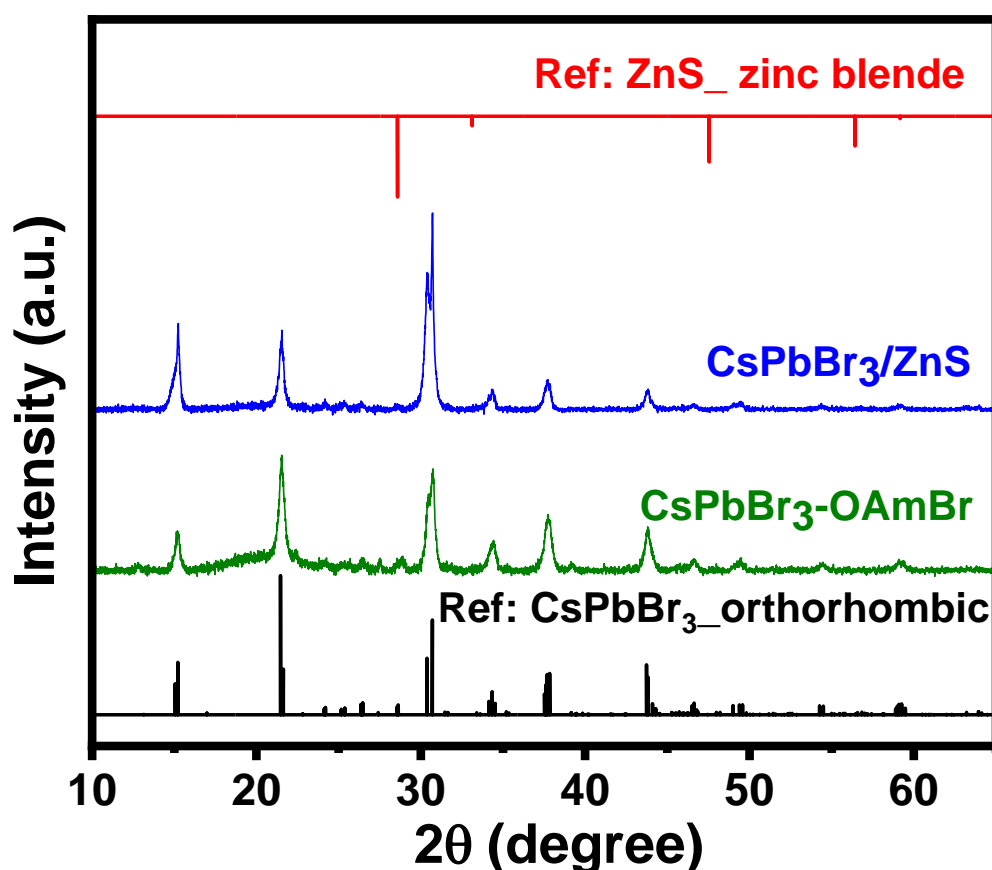
Figure 4B.6: PXRD patterns of $CsPbBr_3$/ZnS core/shell type NCs and $CsPbBr_3$-OAmBr NCs shows orthorhombic crystal structure is maintained in both the samples. Reference patterns $CsPbBr_3$ and ZnS are also shown for a comparison.

Figure 4B.6 compares the PXRD patterns of the $CsPbBr_3$/ZnS core/shell type NCs and the control sample $CsPbBr_3$-OAmBr NCs. For reference the bulk PXRD patterns of $CsPbBr_3$ and ZnS is provided. As shown in previous section that after heating the $CsPbBr_3$ NCs in presence of extra OAmBr does not affect its crystals

structure and it remain in orthorhombic phase. For the CsPbBr₃/ZnS core/shell type NCs structure remains unchanged after the shell formation and no impurity phase is found. However, from PXRD pattern, it is difficult to assign the CsPbBr₃/ZnS core/shell type structure. Core/shell structure with thin shell often does not show its contribution in the PXRD patterns. A lot of literature with good quality CdSe/ZnS NCs does not show contribution of thin shell in the PXRD patterns.[34]

The SEM image along with EDAX composition on the selected agglomerated region of NCs is shown in Figure 4B.7. It shows the presence of Zn and S along with the Cs, Pb and Br. Further, elemental mapping done on a rectangular area of a NC shows the uniform distribution of Cs, Pb, Br, Zn and S (Figure 4B.8).

The TEM images of CsPbBr₃ NCs, CsPbBr₃-OAmBr NCs and CsPbBr₃/ZnS core/shell type NCs are compared in Figure 4B.9. All the samples show distorted cubic morphology with average edge length of 10.8 ± 1.5 nm, 47.2 ± 9.1 nm and 48.7 ± 7.9 nm for CsPbBr₃ NCs, CsPbBr₃-OAmBr NCs and CsPbBr₃/ZnS core/shell type NCs, respectively. This suggests that heating the sample increases the NCs size as the NCs fuse together while heating. TEM image of CsPbBr₃/ZnS core/shell type NCs (Figure 4B.10) along with the HRTEM image of a NC (inset of Figure 4B.10) show lattice fringes corresponding to (020) planes of CsPbBr₃ and (200) planes of ZnS in zinc blende phase, confirming the core/shell interface.

Element	Atomic %
Cs	18.0 ± 0.3
Pb	18.2 ± 0.2
Br	55.1 ± 0.1
Zn	3.8 ± 0.3
S	4.9 ± 0.4
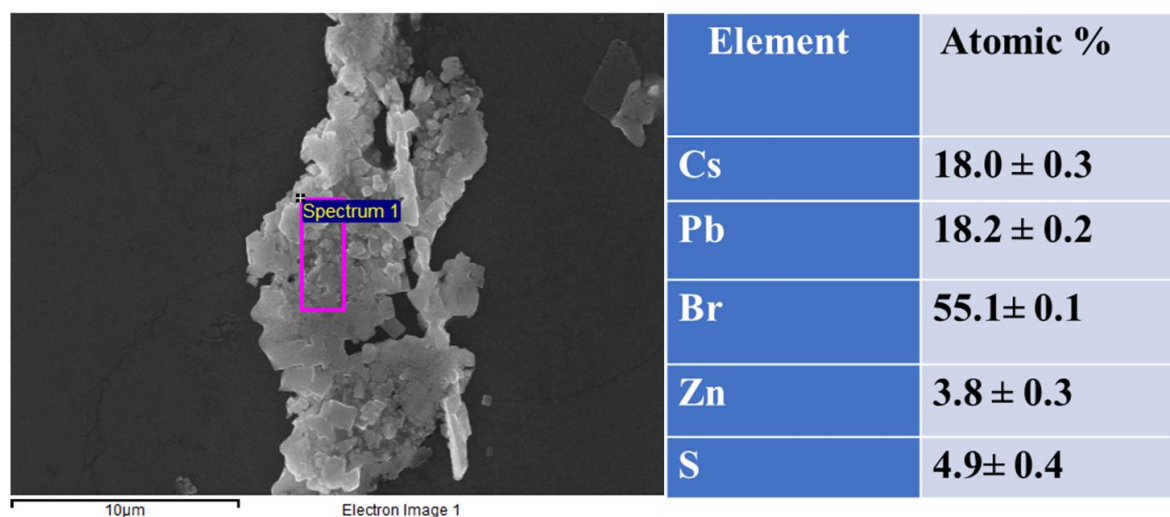
Figure 4B.7: SEM image of densely packed agglomerated region of CsPbBr₃/ZnS core/shell type NCs with an average size of ~ 49 nm and the EDAX measurement is performed on the same. EDAX measurement data on CsPbBr₃/ZnS core/shell type NCs shows atomic percentage of different elements as mentioned.
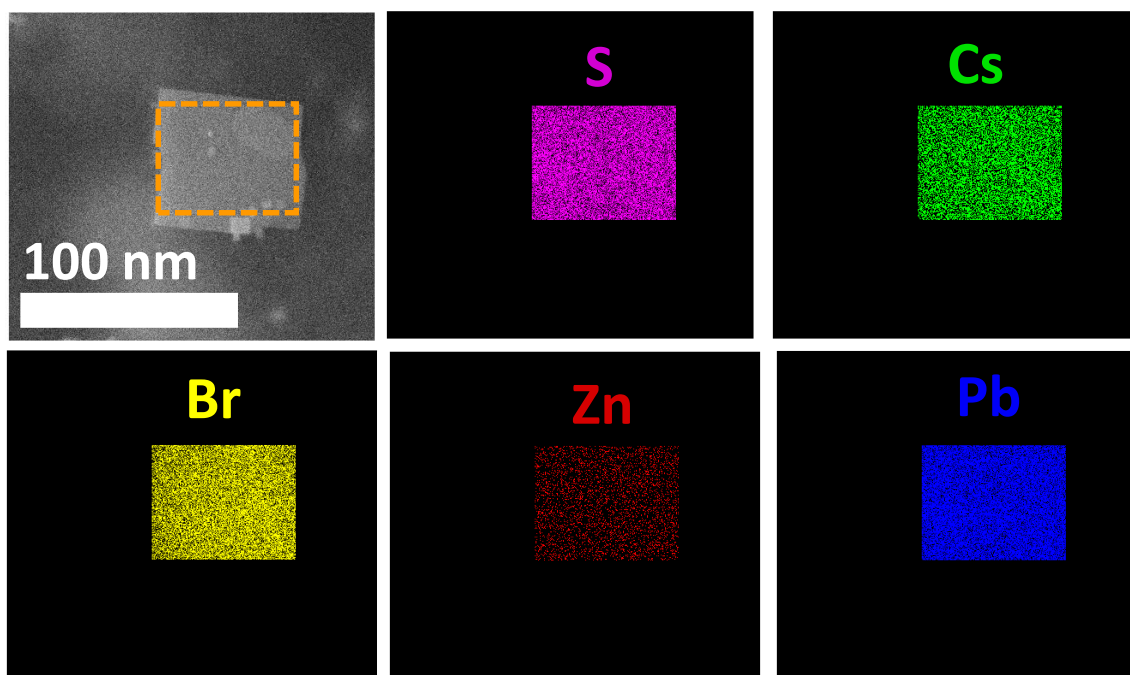
Figure 4B.8: Elemental mapping done on a CsPbBr₃/ZnS core/shell type NC shows Zn and S uniformly distributed along with Cs, Pb and Br. The area on which elemental mapping is done is highlighted by the orange rectangular box.
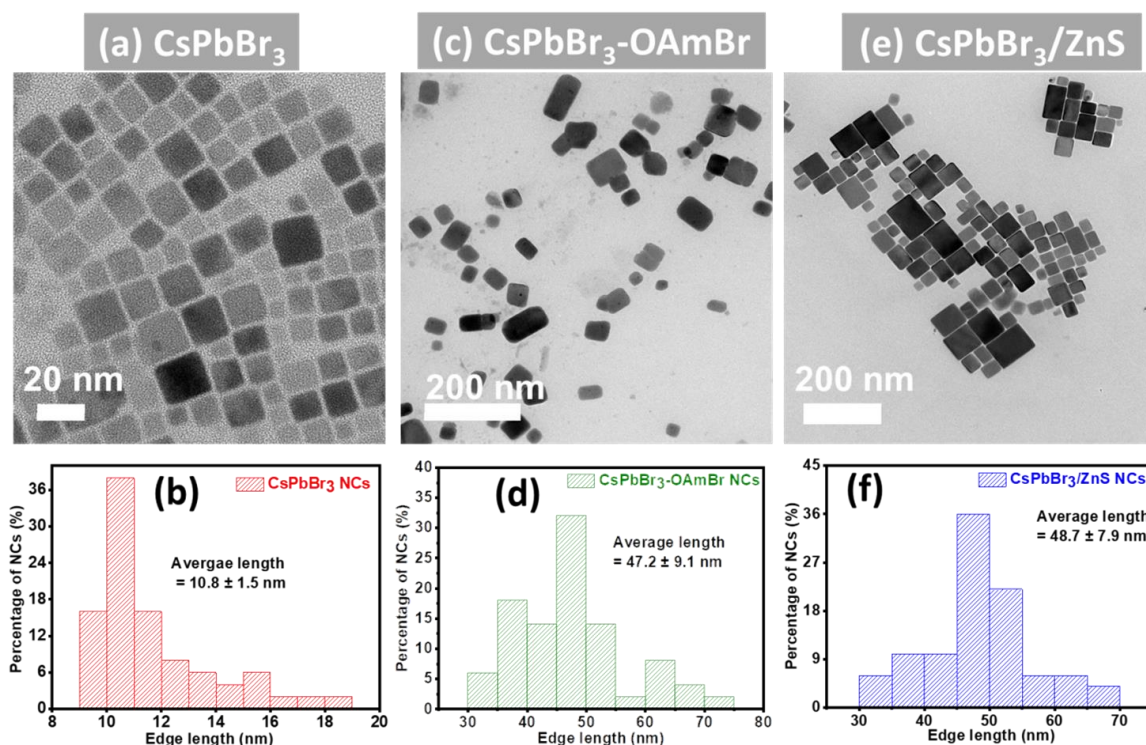
Figure 4B.9: TEM image and corresponding size distribution plot for (a-b) pristine CsPbBr₃ NCs, (c-d) CsPbBr₃-OAmBr NCs, and (e-f) CsPbBr₃/ZnS core/shell type NCs. It is to be noted that the heat treatment of the samples increases the size of the NCs from ~ 11 nm for pristine CsPbBr₃ NCs to ~ 48 nm for the heat-treated samples.
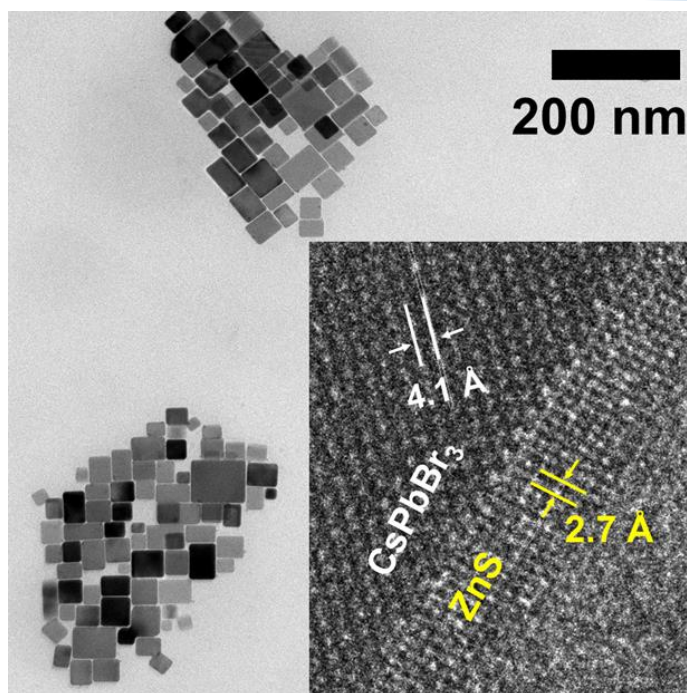
Figure 4B.10: TEM image of CsPbBr₃/ZnS core/shell type NCs showing cubic morphology. Inset shows HRTEM image of a NC near core/shell interface.
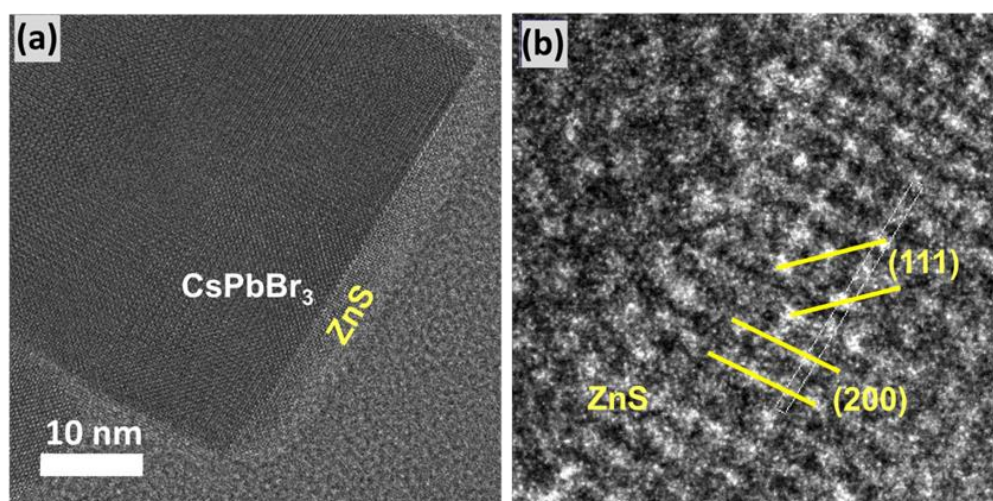
Figure 4B.11: TEM image of CsPbBr₃/ZnS core/shell type NCs. (b) Magnified part of same NC to show ZnS shell where planes are assigned to (111) and (200) of the zinc-blende phase of ZnS shell.

Also, in Figure 4B.11a, the HRTEM image of CsPbBr₃/ZnS core/shell NC and its magnified part (Figure 4.11b) is presented to show ZnS shell having (200) and (111) planes. However, we mention that the HRTEM image showing such interface is difficult to obtain for some other NCs of the sample, suggesting inhomogeneity in the shell growth (Figure 4B.12). Further improvement in the synthesis methodology is required to grow homogenous shell with a control over its thickness.
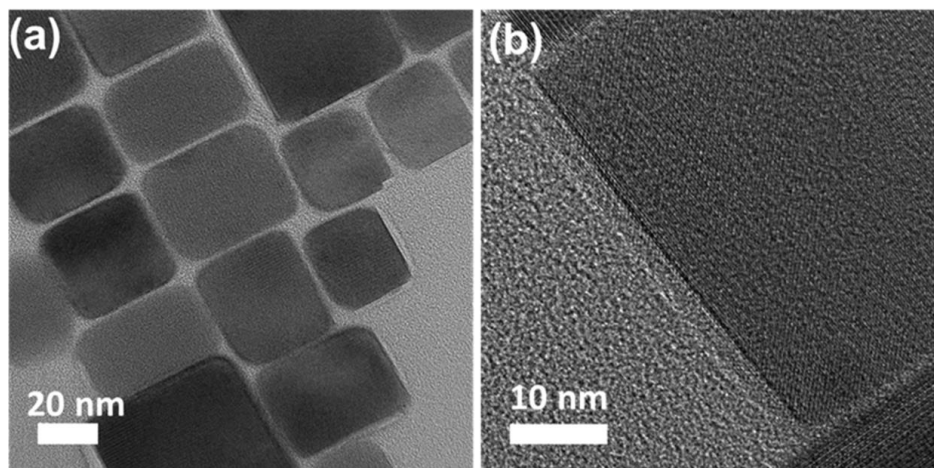
Figure 4B.12: (a) TEM image of CsPbBr₃/ZnS core/shell type NCs where we see a contrast between CsPbBr₃ and its edges indicating the ZnS shell. (b) HRTEM image of a part of NC showing the presence of shell of ZnS on CsPbBr₃. The contrast between core and shell material is inhomogeneous for different NCs, suggesting an inhomogeneity in shell growth. For NCs with clear contrast suggest thick enough ZnS shell, whereas, for other NCs, the shell is either thin or absent.

UV-visible absorption and PL peak (Figure 4B.13) of CsPbBr₃/ZnS core/shell type NCs show a small red shift (~ 5 nm) compared to CsPbBr₃-OAmBr NCs. This red shift might be because of spreading of electron and/or hole wavefunctions to the shell.[35]
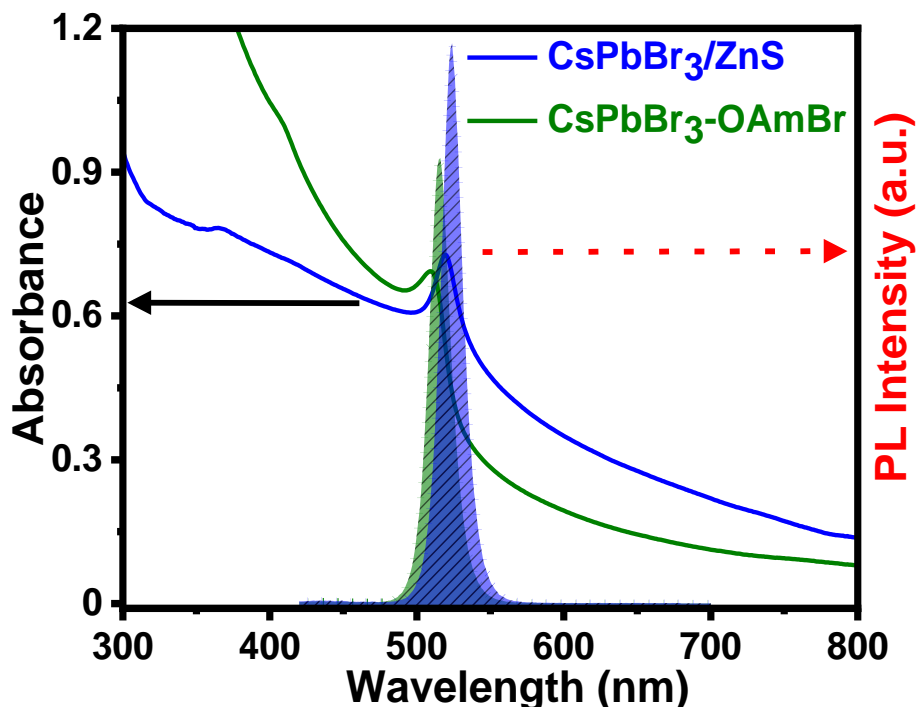
Figure 4B.13: UV-visible absorption and PL spectra showing little red shift for CsPbBr₃/ZnS core/shell type NCs. For obtaining emission spectra, the samples are excited at 400 nm.

Figure 4B.14 shows that the relative PL intensity slightly increases for the $CsPbBr_3$/ZnS core/shell type NCs as compared to the pristine $CsPbBr_3$ NCs and $CsPbBr_3$-OAmBr NCs. However, we would like to point out that this is just an estimation as it involves error in measuring PL quantum yield. This error is expected because of increased scattering effect in the heat-treated samples leading to error in measuring absorbance value.
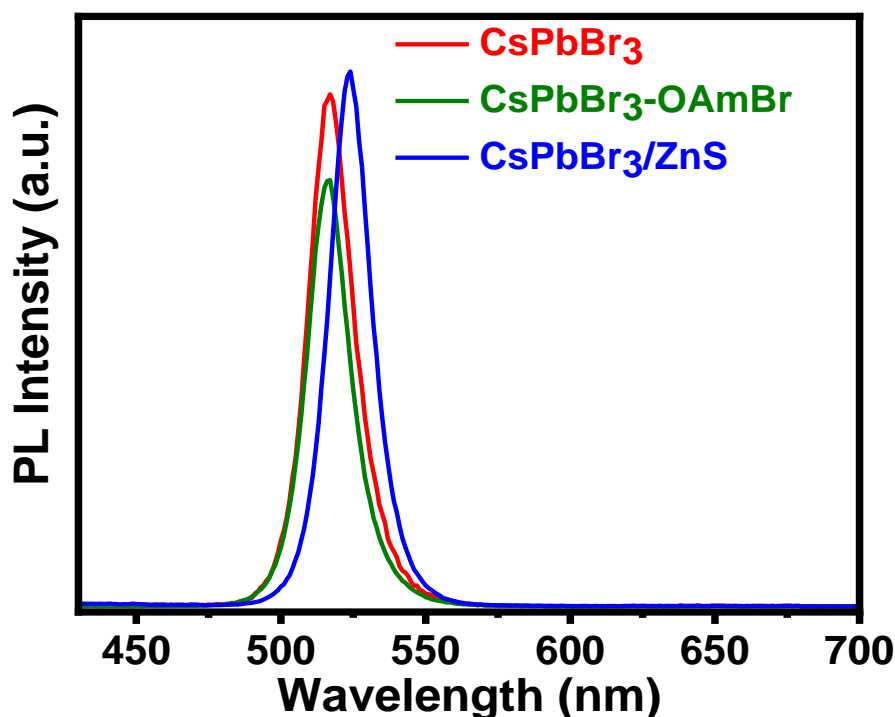
Figure 4B.14: PL spectra of pristine $CsPbBr_3$ NCs, $CsPbBr_3$-OAmBr NCs, $CsPbBr_3$/ZnS core/shell type NCs, after normalizing with absorbance at the excitation wavelength. The results suggest similar or slightly higher PL quantum yield for the core/shell sample. The samples are excited at wavelength of 400 nm.

Interestingly, a drastic increase in PL lifetime is observed for the core/shell NCs (Figure 4B.15). The average lifetime of $CsPbBr_3$/ZnS core/shell NCs is 102.6 ns, which is about 15 times longer than the average lifetime (7.2 ns) of $CsPbBr_3$-OAmBr NCs. These results confirm that the ZnS shell growth effectively modifies the electronic properties of the core. Prior report suggest that the valence band maximum (VBM) energies of both ZnS and $CsPbBr_3$ are similar, whereas, the conduction band minimum (CBM) of ZnS is at a significantly higher energy than that of $CsPbBr_3$.[36] So, there is a possibility of pseudo type-II band alignment at the core/shell interface where the hole is delocalized over both the core and shell, and electron is confined within the core (Figure 4B.16). Such pseudo type-II band

alignment can explain the significantly longer PL lifetime of CsPbBr₃/ZnS core/shell type NCs.
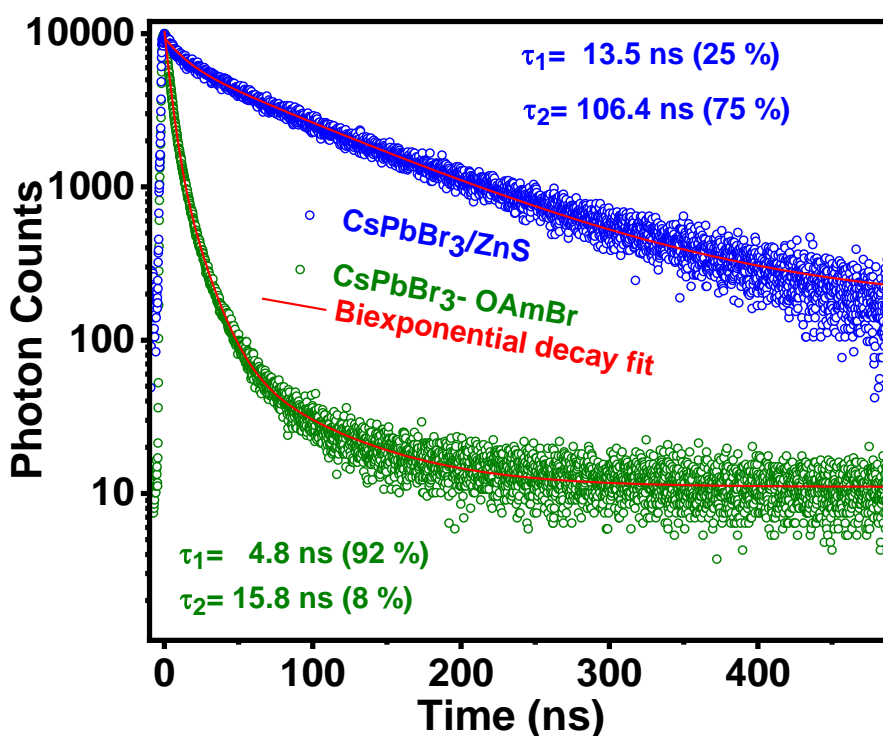
Figure 4B.15: Comparison of PL decay shows a huge increase in PL lifetime for CsPbBr₃/ZnS core/shell type NCs. PL decay lifetimes are obtained at the corresponding emission peak and the excitation wavelength used is 400 nm.
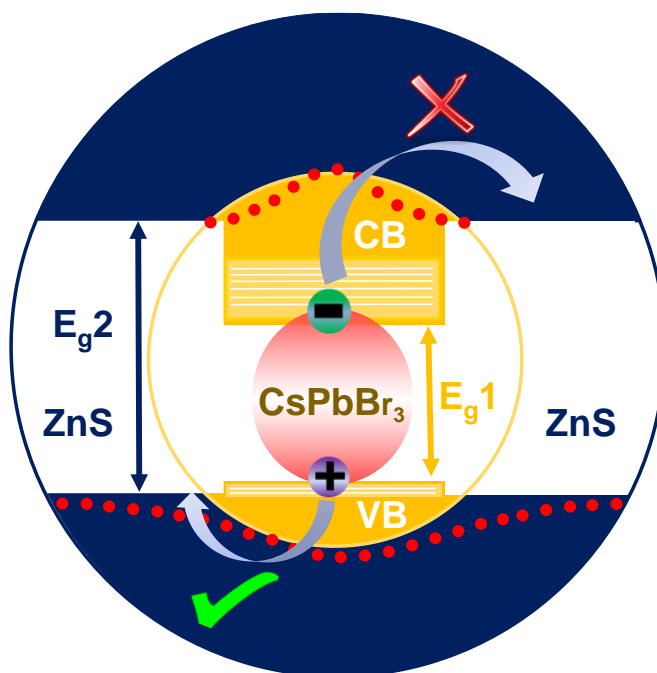
Figure 4B.16: Schematic showing pseudo type-II band alignment at the CsPbBr₃/ZnS core/shell interface, where the electron is confined inside the core but the hole is delocalized over both core and shell.

To verify the pseudo type-II band alignment further, we have made films of CsPbBr$_3$/ZnS core/shell type NCs, on glass, electron acceptor TiO$_2$ and hole acceptor spiro-OMeTAD (Figure 4B.17a). Interestingly, PL lifetimes of CsPbBr$_3$/ZnS core/shell type NCs remain comparable on both TiO$_2$ and glass substrates, suggesting suppression of electron transfer by the ZnS shell. Furthermore, PL decay of the CsPbBr$_3$/ZnS core/shell type NCs coated on spiro-OMeTAD becomes significantly faster, suggesting the hole delocalization over both core and shell materials, and therefore, can be transferred to suitable hole acceptors. PL decay of control sample i.e. of CsPbBr$_3$-OAmBr NCs on TiO$_2$ is much faster compared to the same NCs on glass substrate (see Figure 4B.17b), suggesting possibility of electron transfer from CsPbBr$_3$ NCs to TiO$_2$. The film on glass shows an average PL lifetime 9.3 ns, whereas the average lifetime decreases to 3.6 ns for the film on TiO$_2$. These PL decay trends support the proposed pseudo type-II core/shell structure, which is suitable for photodetectors applications.[35]
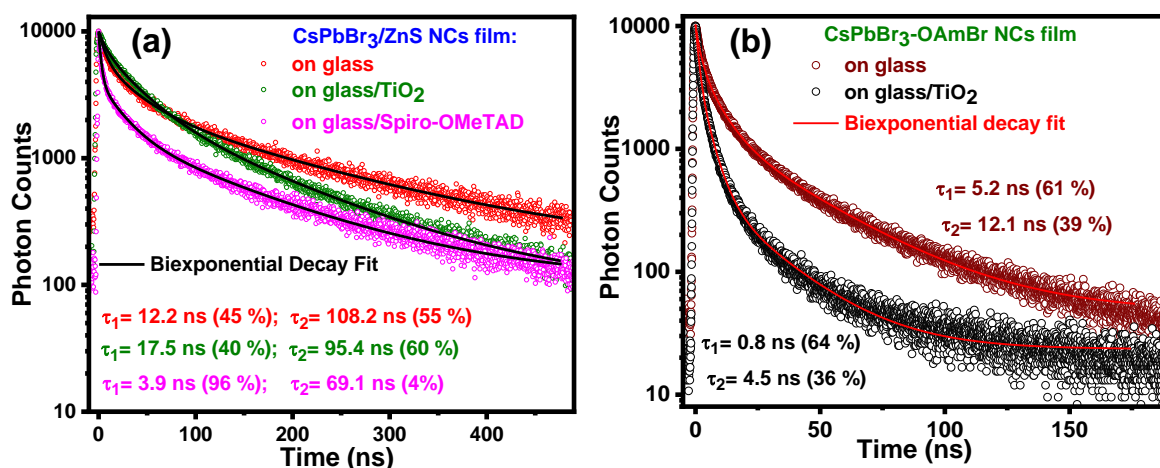
Figure 4B.17: (a) PL decay of CsPbBr$_3$/ZnS core/shell type NCs film deposited on glass, TiO$_2$, and spiro-OMeTAD. (b) Comparison of PL decay of CsPbBr$_3$-OAmBr NCs film on glass and on TiO$_2$ substrate. Bi-exponential PL decay and best fit parameters are given in the inset. PL decay lifetimes are obtained at their corresponding PL peak and the excitation wavelength used is 400 nm.

Finally, we have checked the effect of shell formation on aqueous and photo stability of NCs. Films of CsPbBr$_3$/ZnS core/shell type NCs and CsPbBr$_3$-OAmBr NCs are immersed in beakers full of water (to check for aqueous stability) and excited with white LED (50 mW) (to check for photostability). Figure 4B.18 shows the CsPbBr$_3$/ZnS core/shell type NCs remain highly emissive even after 48 hours, whereas PL of CsPbBr$_3$-OAmBr NCs disappears within 2 hours. Water stability tests

on powder of CsPbBr$_3$/ZnS core/shell type NCs and CsPbBr$_3$-OAmBr NCs are performed by mixing them with distilled water, and PL spectra are recorded at regular intervals of time. The NCs do not form a homogenous dispersion in water. This makes the quantitative estimation of PL intensity difficult. We have tried to minimize the error in estimation by vigorously shaking the sample just before measuring each PL spectrum. CsPbBr$_3$/ZnS core/shell type NCs retain about 54% of its initial PL intensity even after 48 hours, whereas the PL intensity of CsPbBr$_3$-OAmBr NCs quenches completely within 2 hours as shown in Figure 4B.19. CsPbBr$_3$ NCs in water is known to degrade to structurally lower dimensional counterpart Cs$_4$PbBr$_6$. The core/shell type structure of CsPbBr$_3$/ZnS NCs resists this degradation and the NCs remain emissive up to 4 days under continuous treatment of water.
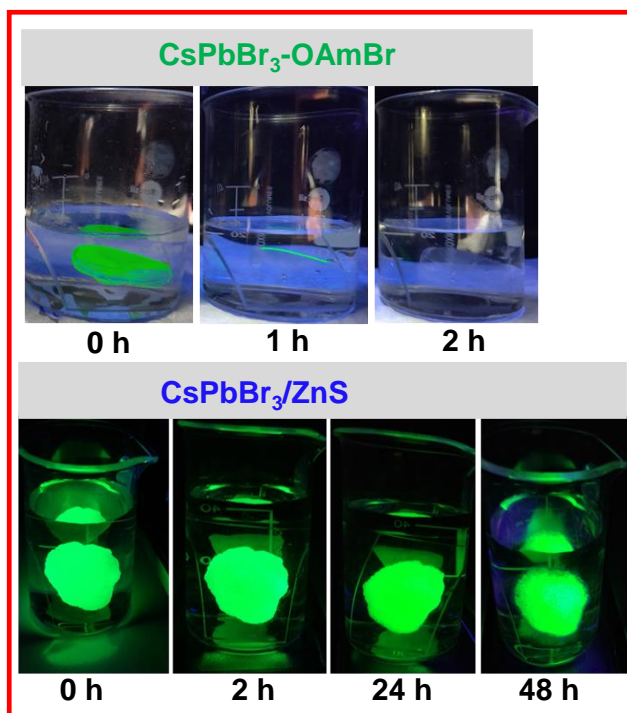
Figure 4B.18: Digital photographs of the films of CsPbBr$_3$/ZnS core/shell type NCs and CsPbBr$_3$-OAmBr NCs dipped in beakers full of water, and excited with UV lamp (365 nm).

To check the photostability of the NCs, we have dispersed the CsPbBr$_3$/ZnS core/shell type NCs and CsPbBr$_3$-OAmBr NCs in toluene, then irradiated them with 50 mW white LED continuously. PL spectra are recorded at different intervals of time which shows improved photo-stability of CsPbBr$_3$/ZnS core/shell type NCs compared to the CsPbBr$_3$-OAmBr NCs. As shown in Figure 4B.20, CsPbBr$_3$/ZnS

core/shell type NCs maintain about 80 % of its initial PL intensity even after 48 hours of continuous irradiation whereas intensity of CsPbBr$_3$-OAmBr NCs reduces to 20 % of its initial value.
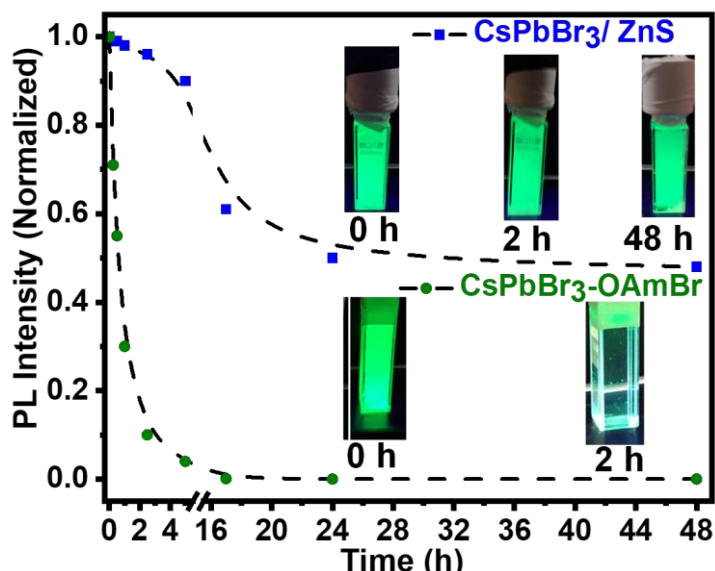
Figure 4B.19: Powders of CsPbBr$_3$/ZnS core/shell type NCs and CsPbBr$_3$-OAmBr NCs dispersed by vigorous shaking in distilled water. CsPbBr$_3$/ZnS core/shell type NCs retain about 54% of its initial PL intensity even after 48 h whereas the PL intensity of CsPbBr$_3$-OAmBr NCs quenches completely within 2 h. Inset shows digital photographs of the sample in the cuvette under UV light (365 nm).
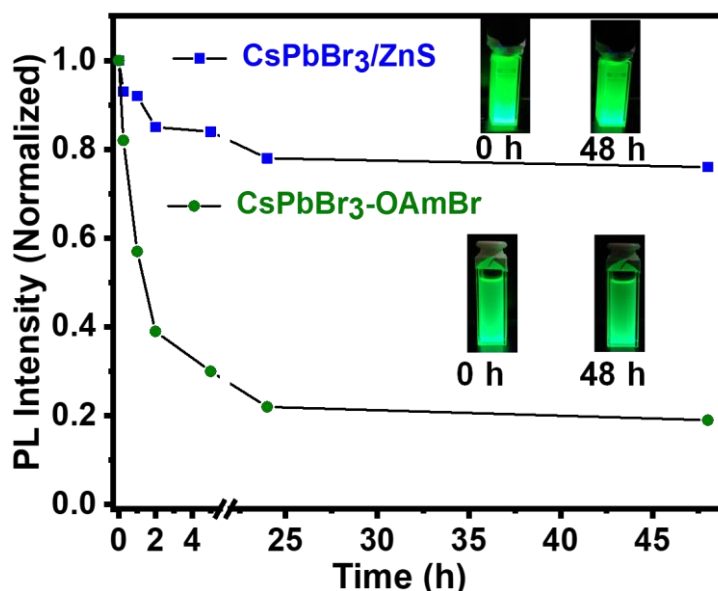
Figure 4B.20: PL intensity quenching of CsPbBr$_3$/ZnS core/shell type NCs compared with that of CsPbBr$_3$-OAmBr NCs. The NCs powder are dispersed in toluene and then irradiated with 50 mW white LED continuously and PL spectra are recorded at different intervals of time. Inset shows the corresponding photographs under UV light of 365 nm. CsPbBr$_3$/ZnS core/shell type NCs shows improved photostability compared to that of CsPbBr$_3$-OAmBr NCs.

4B.4 Conclusions:

We have shown that the addition of little extra amount of OAmBr to the CsPbBr$_3$ NCs dispersion helps it to maintain its orthorhombic phase even at high processing temperature. Then the CsPbBr$_3$/ZnS core/shell type NCs are synthesized by treating CsPbBr$_3$ seed NCs with single molecular precursor Zn(DDTC)$_2$ in presence of excess OAmBr. The shell growth over CsPbBr$_3$ NCs is not yet homogeneous. Interestingly, the CsPbBr$_3$/ZnS core/shell system of shows significant improvement in stability of sample when dipped inside a beaker of water. The shell formation also improves the photostability of CsPbBr$_3$/ZnS core/shell type NCs. PL lifetime of CsPbBr$_3$/ZnS core/shell type NCs increased significantly, suggesting a pseudo type-II band alignment at the core/shell interface. The holes are delocalized over both core and shell but the electrons are localized in the core only. This hole delocalization led to the transfer of holes from CsPbBr$_3$/ZnS core/shell type NCs to spiro-OMeTAD layer in a film. The success of obtaining CsPbBr$_3$/ZnS core/shell type nanostructure with enhanced stability to water and light, along with higher PL lifetime, would pave its way to use them for various applications like optically pumped LEDs, photodetectors and photocatalysis. We anticipate that this work would motivate future research on controlling the thickness and homogeneity of shell growth, along with device fabrication.

4B.5 References:

1. Protesescu, L.; Yakunin, S.; Bodnarchuk, M. I.; Krieg, F.; Caputo, R.; Hendon, C. H.; Yang, R. X.; Walsh, A.; Kovalenko, M. V., Nanocrystals of Cesium Lead Halide Perovskites (CsPbX$_3$, X = Cl, Br, and I): Novel Optoelectronic Materials Showing Bright Emission with Wide Color Gamut. *Nano Lett.* **2015,** *15*, 3692-3696.

2. Swarnkar, A.; Chulliyil, R.; Ravi, V. K.; Irfanullah, M.; Chowdhury, A.; Nag, A., Colloidal CsPbBr$_3$ Perovskite Nanocrystals: Luminescence beyond Traditional Quantum Dots. *Angew. Chem. Int. Ed.* **2015,** *54*, 15424-15428.

3. Yettapu, G. R.; Talukdar, D.; Sarkar, S.; Swarnkar, A.; Nag, A.; Ghosh, P.; Mandal, P., Terahertz Conductivity within Colloidal CsPbBr$_3$ Perovskite Nanocrystals: Remarkably High Carrier Mobilities and Large Diffusion Lengths. *Nano Lett.* **2016,** *16*, 4838-48.

4. Song, J.; Li, J.; Li, X.; Xu, L.; Dong, Y.; Zeng, H., Quantum Dot Light-Emitting Diodes Based on Inorganic Perovskite Cesium Lead Halides (CsPbX$_3$). *Adv. Mater.* **2015,** *27*, 7162-7.

5. Yakunin, S.; Sytnyk, M.; Kriegner, D.; Shrestha, S.; Richter, M.; Matt, G. J.; Azimi, H.; Brabec, C. J.; Stangl, J.; Kovalenko, M. V.; Heiss, W., Detection of X-ray photons by solution-processed lead halide perovskites. *Nat. Photon.* **2015,** *9*, 444-449.

6. Nedelcu, G.; Protesescu, L.; Yakunin, S.; Bodnarchuk, M. I.; Grotevent, M. J.; Kovalenko, M. V., Fast Anion-Exchange in Highly Luminescent Nanocrystals of Cesium Lead Halide Perovskites (CsPbX$_3$, X = Cl, Br, I). *Nano Lett.* **2015,** *15*, 5635-5640.

7. Akkerman, Q. A.; Rainò, G.; Kovalenko, M. V.; Manna, L., Genesis, challenges and opportunities for colloidal lead halide perovskite nanocrystals. *Nat. Mater.* **2018,** *17*, 394-405.

8. Kim, Y.; Yassitepe, E.; Voznyy, O.; Comin, R.; Walters, G.; Gong, X.; Kanjanaboos, P.; Nogueira, A. F.; Sargent, E. H., Efficient Luminescence from Perovskite Quantum Dot Solids. *ACS Appl. Mater. Interfaces* **2015,** *7*, 25007-25013.

9. Chen, X.; Hu, H.; Xia, Z.; Gao, W.; Gou, W.; Qu, Y.; Ma, Y., CsPbBr$_3$ perovskite nanocrystals as highly selective and sensitive spectrochemical probes for gaseous HCl detection. *J. Mater. Chem. C* **2017,** *5*, 309-313.

10. Meyns, M.; Perálvarez, M.; Heuer-Jungemann, A.; Hertog, W.; Ibáñez, M.; Nafria, R.; Genç, A.; Arbiol, J.; Kovalenko, M. V.; Carreras, J.; Cabot, A.; Kanaras, A. G., Polymer-Enhanced Stability of Inorganic Perovskite Nanocrystals and Their Application in Color Conversion LEDs. *ACS Appl. Mater. Interfaces* **2016,** *8*, 19579-19586.

11. Pan, J.; Sarmah, S. P.; Murali, B.; Dursun, I.; Peng, W.; Parida, M. R.; Liu, J.; Sinatra, L.; Alyami, N.; Zhao, C.; Alarousu, E.; Ng, T. K.; Ooi, B. S.; Bakr, O. M.; Mohammed, O. F., Air-Stable Surface-Passivated Perovskite Quantum Dots for Ultra-Robust, Single- and Two-Photon-Induced Amplified Spontaneous Emission. *J. Phys. Chem. Lett.* **2015,** *6*, 5027-5033.

12. Huang, H.; Chen, B.; Wang, Z.; Hung, T. F.; Susha, A. S.; Zhong, H.; Rogach, A. L., Water resistant CsPbX$_3$ nanocrystals coated with polyhedral oligomeric

silsesquioxane and their use as solid state luminophores in all-perovskite white light-emitting devices. *Chem. Sci.* **2016,** *7*, 5699-5703.

13. Palazon, F.; Akkerman, Q. A.; Prato, M.; Manna, L., X-ray Lithography on Perovskite Nanocrystals Films: From Patterning with Anion-Exchange Reactions to Enhanced Stability in Air and Water. *ACS Nano* **2016,** *10*, 1224-1230.

14. Li, G.; Rivarola, F. W. R.; Davis, N. J. L. K.; Bai, S.; Jellicoe, T. C.; de la Peña, F.; Hou, S.; Ducati, C.; Gao, F.; Friend, R. H.; Greenham, N. C.; Tan, Z.-K., Highly Efficient Perovskite Nanocrystal Light-Emitting Diodes Enabled by a Universal Crosslinking Method. *Adv. Mater.* **2016,** *28*, 3528-3534.

15. Wang, S.; Bi, C.; Yuan, J.; Zhang, L.; Tian, J., Original Core–Shell Structure of Cubic CsPbBr₃@Amorphous CsPbBrₓ Perovskite Quantum Dots with a High Blue Photoluminescence Quantum Yield of over 80%. *ACS Energy Lett.* **2018,** *3*, 245-251.

16. Ravi, V. K.; Scheidt, R. A.; Nag, A.; Kuno, M.; Kamat, P. V., To Exchange or Not to Exchange. Suppressing Anion Exchange in Cesium Lead Halide Perovskites with PbSO₄–Oleate Capping. *ACS Energy Lett.* **2018,** *3*, 1049-1055.

17. Reiss, P.; Protière, M.; Li, L., Core/Shell Semiconductor Nanocrystals. *Small* **2009,** *5*, 154-168.

18. Battaglia, D.; Li, J. J.; Wang, Y.; Peng, X., Colloidal Two-Dimensional Systems: CdSe Quantum Shells and Wells. *Angew. Chem. Int. Ed.* **2003,** *42*, 5035-5039.

19. Medintz, I. L.; Uyeda, H. T.; Goldman, E. R.; Mattoussi, H., Quantum dot bioconjugates for imaging, labelling and sensing. *Nat. Mater.* **2005,** *4*, 435-446.

20. Pellegrino, T.; Kudera, S.; Liedl, T.; Muñoz Javier, A.; Manna, L.; Parak, W. J., On the Development of Colloidal Nanoparticles towards Multifunctional Structures and their Possible Use for Biological Applications. *Small* **2005,** *1*, 48-63.

21. Greene, L. E.; Law, M.; Yuhas, B. D.; Yang, P., ZnO−TiO₂ Core−Shell Nanorod/P3HT Solar Cells. *J. Phys. Chem. Lett.* **2007,** *111*, 18451-18456.

22. Mora-Seró, I.; Bisquert, J.; Dittrich, T.; Belaidi, A.; Susha, A. S.; Rogach, A. L., Photosensitization of TiO₂ Layers with CdSe Quantum Dots: Correlation between Light Absorption and Photoinjection. *J. Phys. Chem. Lett.* **2007,** *111*, 14889-14892.

23. Kamat, P. V., Quantum Dot Solar Cells. Semiconductor Nanocrystals as Light Harvesters. *J. Phys. Chem. Lett.* **2008,** *112*, 18737-18753.

24. Hines, M. A.; Guyot-Sionnest, P., Synthesis and Characterization of Strongly Luminescing ZnS-Capped CdSe Nanocrystals. *J. Phys. Chem.* **1996,** *100*, 468-471.

25. Dabbousi, B. O.; Rodriguez-Viejo, J.; Mikulec, F. V.; Heine, J. R.; Mattoussi, H.; Ober, R.; Jensen, K. F.; Bawendi, M. G., (CdSe)ZnS Core−Shell Quantum Dots: Synthesis and Characterization of a Size Series of Highly Luminescent Nanocrystallites. *J. Phys. Chem. B* **1997,** *101*, 9463-9475.

26. Peng, X.; Schlamp, M. C.; Kadavanich, A. V.; Alivisatos, A. P., Epitaxial Growth of Highly Luminescent CdSe/CdS Core/Shell Nanocrystals with Photostability and Electronic Accessibility. *J. Am. Chem. Soc.* **1997,** *119*, 7019-7029.

27. Talapin, D. V.; Rogach, A. L.; Kornowski, A.; Haase, M.; Weller, H., Highly Luminescent Monodisperse CdSe and CdSe/ZnS Nanocrystals Synthesized in a Hexadecylamine−Trioctylphosphine Oxide−Trioctylphospine Mixture. *Nano Lett.* **2001,** *1*, 207-211.

28. Reiss, P.; Bleuse, J.; Pron, A., Highly Luminescent CdSe/ZnSe Core/Shell Nanocrystals of Low Size Dispersion. *Nano Lett.* **2002,** *2*, 781-784.

29. Li, X.; Wu, Y.; Zhang, S.; Cai, B.; Gu, Y.; Song, J.; Zeng, H., CsPbX₃ Quantum Dots for Lighting and Displays: Room-Temperature Synthesis, Photoluminescence Superiorities, Underlying Origins and White Light-Emitting Diodes. *Adv. Funct. Mater.* **2016,** *26*, 2435-2445.

30. Ravi, V. K.; Santra, P. K.; Joshi, N.; Chugh, J.; Singh, S. K.; Rensmo, H.; Ghosh, P.; Nag, A., Origin of the Substitution Mechanism for the Binding of Organic Ligands on the Surface of CsPbBr₃ Perovskite Nanocubes. *J Phys. Chem. Lett.* **2017,** *8*, 4988-4994.

31. Dutta, A.; Dutta, S. K.; Das Adhikari, S.; Pradhan, N., Phase-Stable CsPbI₃ Nanocrystals: The Reaction Temperature Matters. *Angew. Chem. Int. Ed.* **2018,** *57*, 9083-9087.

32. De Roo, J.; Ibanez, M.; Geiregat, P.; Nedelcu, G.; Walravens, W.; Maes, J.; Martins, J. C.; Van Driessche, I.; Kovalenko, M. V.; Hens, Z., Highly Dynamic Ligand Binding and Light Absorption Coefficient of Cesium Lead Bromide Perovskite Nanocrystals. *ACS Nano* **2016,** *10*, 2071-81.

33. Dethlefsen, J. R.; Døssing, A., Preparation of a ZnS Shell on CdSe Quantum Dots Using a Single-Molecular ZnS Precursor. *Nano Lett.* **2011,** *11*, 1964-1969.

34. Baranov, A. V.; Rakovich, Y. P.; Donegan, J. F.; Perova, T. S.; Moore, R. A.; Talapin, D. V.; Rogach, A. L.; Masumoto, Y.; Nabiev, I., Effect of ZnS shell thickness on the phonon spectra in CdSe quantum dots. *Phys. Rev. B* **2003,** *68*, 165306.

35. Lee, J.-S.; Kovalenko, M. V.; Huang, J.; Chung, D. S.; Talapin, D. V., Band-like transport, high electron mobility and high photoconductivity in all-inorganic nanocrystal arrays. *Nat. Nanotechnol.* **2011,** *6*, 348-352.

36. Ravi, V. K.; Markad, G. B.; Nag, A., Band Edge Energies and Excitonic Transition Probabilities of Colloidal CsPbX$_3$ (X = Cl, Br, I) Perovskite Nanocrystals. *ACS Energy Lett.* **2016,** *1*, 665-671.

Chapter 5

Colloidal BaZrS$_3$ Chalcogenide Perovskite Nanocrystals for Thin Film Device Fabrication

---
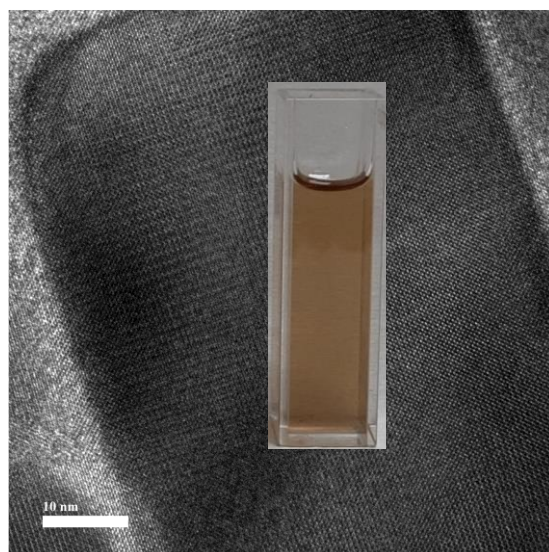
The work presented in this chapter has led to the following publication:

Ravi, V. K.; Yu, S. H.; Rajput, P. K.; Nayak, C.; Bhattacharyya, D.; Chung, D. C.; Nag, A. Colloidal BaZrS$_3$ Chalcogenide Perovskite Nanocrystals for Thin Film Device Fabrication. (Manuscript under review)

Declaration:

Field effect transistor devices are fabricated by Seong Hoon Yu and Dr. Dae Sung Chung at POSTECH, Korea.

Chapter 5
Colloidal BaZrS$_3$ Chalcogenide Perovskite Nanocrystals for Thin Film Device Fabrication

Abstract:

Barium Zirconium Sulfide, BaZrS$_3$ as a potential alternative of lead halide perovskite, has been proposed because of it is environmentally benign and are more stable than the lead halide perovskite. Theoretical optoelectronic properties of chalcogenide perovskites (e.g., BaZrS$_3$) are as good as that of halide perovskites (e.g., CH$_3$NH$_3$PbI$_3$). But the fabrication of optoelectronic devices is rarely reported, mainly because researchers still do not know how to prepare good quality thin films of chalcogenide perovskites. Here in this chapter, we report the colloidal BaZrS$_3$ nanocrystals (NCs, 40-60 nm) and their solution processed thin film transistors. The NCs exhibit thermal (15 – 673 K) and aqueous stability. BaZrS$_3$ NCs are first prepared using a solid-state synthesis route, and the subsequent surface modifications lead to colloidal dispersion of NCs in both polar N-methyl-2-pyrrolidinone and non-polar chloroform solvents. Colloidal BaZrS$_3$ NCs in chloroform is then used to make field effect transistors showing ambipolar properties with hole mobility 0.059 cm^{2}V^{-1}s^{-1} and electron mobility 0.017 cm^{2}V^{-1}s^{-1}. This first report of solution processed chalcogenide perovskite thin film with reasonable carrier mobility and strong optical absorption and emission, is expected to pave the way for future optoelectronic devices of chalcogenide perovskites.

Graphical Abstract:
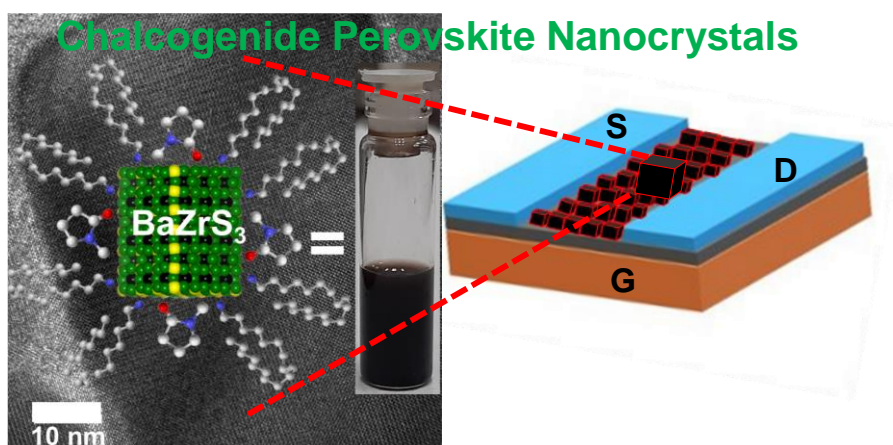
5.1 Introduction:

In the previous chapters, we have discussed the instability and toxicity issues of lead halide perovskite nanocrystals (NCs). We tackled some of those instability issues by doing the surface engineering of $CsPbX_3$ (X= Cl, Br, I) NCs. Ideally it is desired to develop new non-toxic and stable optoelectronic material. In this regard, we have explored a new class of material namely chalcogenide perovskite. Here, we prepare $BaZrS_3$ NCs for solution processed thin film device fabrication.

Oxide perovskites have long been exhibiting amazing properties including colossal magnetoresistance, ferroelectricity and multiferroics.[1, 2] But oxide perovskites are often not good semiconductors with wide band gap in the UV region, mainly because of the high electronegativity of oxygen. On the other hand, Pb-halide perovskites are recently proven to be excellent solution processed semiconductor with high solar cell efficiencies and other exciting optoelectronic properties.[3-10] But Pb toxicity and moisture/thermal instability remain as major challenges to overcome for this class of material.[11-17] Can chalcogenide (sulfide, selenide, and telluride) perovskites combine the good semiconducting properties of the halide perovskites with high stability and non-toxicity of oxide perovskite? This question re-ignited the study of chalcogenide perovskites, with first theoretical report of optoelectronic properties of chalcogenide perovskites appearing in the year 2015.[18] Subsequently, there are other theoretical studies suggesting high solar cell efficiency and photoelectrochemical water splitting of certain compositions of chalcogenide perovskites.[19-24] Some of the suggested chalcogenide perovskites compositions like $BaZrS_3$, $SrZrS_3$ and $SrHfS_3$ are experimentally synthesized in the form of their bulk powder.[20, 25-32] Also, 2D Ruddlesden−Popper and Dion–Jacobson type phases of chalcogenide perovskites are reported.[33-35] Optical properties in terms of strong light absorption and reasonable photoluminescence (PL) are also encouraging for their optoelectronic applications.[31, 32, 36]

But unfortunately, fabrication of thin films of chalcogenide perovskites, which is prerequisite for a typical optoelectronic device, remains very challenging till date. The major problem of material design is that the formation of $BaZrS_3$ and other chalcogenide compositions require a temperature > 600 °C. Physical methods such as sputtering and pulsed laser deposition (PLD) or chemical sulfurization of

BaZrO$_3$ thin film required multiple steps at temperatures ~ 900 °C or above, to achieve films of complex ternary chalcogenide compositions.[21, 37, 38] In this process non-stoichiometric compositions and also sometime impurity phases are observed. For example, the PLD grown (at 1150 °C) BaZrS$_3$ films also suffer from high level of sulfur vacancies resulting into high carrier density (10^{19} - 10^{20} cm^{-3}) that is undesired for optoelectronic applications.[37] Furthermore, it will be very challenging to incorporate such complex processes requiring temperature ~ 900 °C for fabricating desired interfaces in optoelectronic devices like solar cells. Till date, there is no chemical method reported for solution processed thin films of BaZrS$_3$. The obvious reason of this failure is that no solvent can survive the high synthesis temperature of BaZrS$_3$.

To overcome this difficulty, we employed a two-step process to achieve solution processed thin films (~50 nm thick) of BaZrS$_3$ NCs. In the first step, cube-shaped (edge length 40-60 nm) BaZrS$_3$ NCs are synthesized at 600 °C using a solid-state synthesis route. In the second step, we functionalize the surface of BaZrS$_3$ NCs achieving their colloidal dispersions either in polar solvents like N-methyl-2-pyrrolidinone or in non-polar solvents like chloroform. Then the field effect transistors (FETs) are fabricated to measure the charge transport characteristics of BaZrS$_3$ NCs films. FETs are fabricated with the solution processed thin films of BaZrS$_3$ NCs at room temperature. High thermal stability and aqueous stability of BaZrS$_3$ NCs are ensured, along with preliminary results of good photocatalytic activity of the NCs towards degradation of methylene blue dye.

5.2 Experimental Section:

5.2.1 Chemicals:

Barium sulfide (BaS, 99.9%, Sigma-Aldrich), sulfur (S, 99.998%, Sigma-Aldrich), zirconium powder (99%, Nanoshel), iodine (I$_2$, 99.9%, Rankem) oleylamine (OAm, technical grade 70%, Sigma-Aldrich), methyl acetate (anhydrous, 99.5%, Sigma-Aldrich), N-methyl-2-pyrrolidinone (90.7%, Sigma-Aldrich), chloroform (CHCl$_3$, ≥99 %, Sigma-Aldrich), methylene blue (Sigma-Aldrich), spiro-MeOTAD (99%, Sigma-Aldrich), acetonitrile (99.9%, Sigma-Aldrich), titanium diisopropoxide bis-(acetylacetonate) (99%, Sigma-Aldrich), 1-butanol (99.9%, Sigma-Aldrich)

chlorobenzene (99.8%, Sigma-Aldrich), lithium bis(trifluoromethanesulfonyl) imide (LITFSI, 99.9%, Sigma-Aldrich), FTO glasses (~7 Ω/sq, Sigma-Aldrich).

5.2.2 Solid-state synthesis of BaZrS₃ NCs powder:

Solid-state synthesis of BaZrS₃ NCs powder is done by following modified method of Niu et al.[31] Stoichiometric amount of BaS, Zr and S powders (BaS = 3 mmol, Zr = 3 mmol, and S = 6 mmol), and catalytic amount of iodine (25 mg) are taken inside a quartz tube. The quartz tube has length 20 cm, outer diameter of 20 mm and inner diameter of 18 mm. The tube containing the chemicals are then put under high vacuum of 5×10^{-6} mbar. Then the tube is sealed using oxy-acetylene torch and put inside a tubular furnace. The reaction is then carried out at 600 °C for 60 hours with heating rate of 1 °C/min and cooling rate of 0.5 °C/min. After the completion of reaction, the tube is taken out of the furnace and it is broken to take out the black-brown powder as shown in Figure 5.1. It is then further grinded to finer powder. These grinded powders are used for all characterization and surface modification.

5.2.3 Surface modification to form colloidal BaZrS₃ NCs dispersion:

To achieve colloidal dispersion of BaZrS₃ NCs, first we mix BaZrS₃ NCs powder with N-methyl-2-pyrrolidinone and then stirred the mixture at 120 °C for 6 hours to make it completely dispersible. It yields dark brownish dispersion which is then passed from 0.22 μm syringe filter without any aggregation to obtain stable dispersion of BaZrS₃ NCs in N-methyl-2-pyrrolidinone. Further to obtain colloidal dispersion of BaZrS₃ NCs in low boiling solvent like chloroform, we did a second round of surface modification by taking a mixture of BaZrS₃ NCs (400 mg) in N-methyl-2-pyrrolidinone 300 μL along with 100 μL OAm and heated it at 160 °C till the majority of solvent evaporates and it dries to form a thick paste. Then the dried paste is dispersed into chloroform, and passed through the syringe filter to obtain stable colloidal dispersion of BaZrS₃ in chloroform.

5.2.4 Characterization:

Powder X-ray diffraction (PXRD) patterns are recorded on Bruker D8 X-ray diffractometer with Cu Kα radiation of 1.54 Å. UV-visible-near infrared (NIR) diffused reflectance spectra of BaZrS₃ NCs powder are recorded using Shimadzu UV-3600 plus UV-VIS-NIR spectrophotometer. The reflectance data are converted to

absorbance data using Kubelka-Munk transformation. The UV-visible absorption spectra of colloidal dispersion is recorded using Cary series UV-visible spectrophotometer. Steady state photoluminescence (PL) measurements are carried out using FLS 980 (Edinburgh Instruments). Transmission electron microscopy (TEM) images and high resolution TEM (HRTEM) images are captured by using a UHR FEG-TEM, JEOL JEM 2200FS field emission transmission electron microscope operated at 200 kV. TEM sample for BaZrS₃ NCs powder is prepared by taking ~ 0.5 mg of sample in n-butanol (~ 1 mL) and then drop casted on carbon coated Cu TEM grid, while colloidal BaZrS₃ NCs are drop casted directly on the TEM grid. Light intensity is measured using HTC Instrument LX-101A Light Meter Luxmeter.

5.2.5 Aqueous stability and photocatalytic activity of BaZrS₃ NCs powder:

As prepared BaZrS₃ NCs powder is studied as a photocatalyst for the degradation of methylene blue dye in water, under sunlight irradiation (~70 mW /cm²). 100 ppm of methylene blue is prepared by dissolving 5 mg methylene blue in 50 mL Milli-Q water. The methylene blue solution is stirred in dark along with 20 mg BaZrS₃ NCs powder for 1 hour. This stirring promotes the chance for adsorption of dye on BaZrS₃ NCs powder. The degradation of methylene blue gets almost completed (ca. ~98 %) upon continuous irradiation of sun light over a period of 50 minutes. The photocatalytic dye degradation is repeated for multiple cycles, to test aqueous stability of BaZrS₃ NCs powder. The same BaZrS₃ NCs is reused for all the cycles, along with addition of fresh methylene blue for each cycle.

5.2.6 Thin film FET fabrication:

To form BaZrS₃ film, BaZrS₃ NCs dispersion in chloroform, has been passed through the 0.2 μm filter without clogging, and then spin-coated for 30 s at 2000 rpm. The FET device fabrication is carried out by Seong Hoon Yu and Dr. Dae Sung Chung in their laboratory (Department of Chemical Engineering, Pohang University of Science and Technology (POSTECH), Pohang, Korea 37673).

5.2.7 Fabrication of BaZrS₃ NCs sensitized solar cells:

BaZrS₃ NCs based solar cells are fabricated following a modified protocol used for fabrication of lead halide based solar cells.[39] Briefly, a FTO substrate (2.5 cm X 2.5

cm) is masked with Scotch tape leaving 5 mm on one side. Then the exposed area is etched by dropping Zn powder + HCl (3 M) and left it to react for 10 min. It is then washed and cleaned using ethanol/water bath. A blocking TiO$_2$ layer is made using a 0.15 M solution of titanium diisopropoxide bis- (acetylacetonate) in anhydrous 1-butanol. It is spin-casted at 2000 rpm for 40 s and then heat treated at 125 °C for 5 min. A mesoporous layer of TiO$_2$ is made using TiO$_2$ paste (size ~ 40 nm) having concentration C= 0.12 g/cm^3 in ethanol. It is spin-casted at 2000 rpm for 20 s by static coating and further annealed at 500 °C for 1 hour in a high-temperature oven. The BaZrS$_3$ NCs as an active layer is then deposited using colloidal dispersion of BaZrS$_3$ NCs in chloroform, through spin-coating. NCs having concentration around 20 mg/mL is used for deposition of single layer. It is then heated at 150 °C for 5 min and then dipped in MeOAc to get rid of organic part. The desired film thickness has been achieved by repeating the deposition and annealing cycles. Spiro-MeOTAD as hole transport layer is deposited through spin-coating at 3000 rpm for 30 s (Spiro-MeOTAD solution is made by mixing 72.3 mg Spiro-MeOTAD, 28.8 µL of 4-tert-butyl pyridine and 17.5 µL of Li-TFSI solution (520 mg Li-TSFI in 1 mL acetonitrile) in 1 mL of chlorobenzene). An 80 nm thick gold counter electrode is deposited using a thermal evaporator with a homemade mask of single cell area of 0.24 cm^2 at 10^{-6} Torr at a 5−10 Å/s deposition rate. Final contacts are made using silver paste.

5.3 Results and discussions:

5.3.1 Synthesis and morphology of BaZrS$_3$ NCs powder:

BaZrS$_3$ NCs powder are prepared using a slightly modified solid-state synthesis method reported by Niu et al.[31] The schematic of the reaction conditions is shown in Figure 5.1.

PXRD pattern of the product confirms the formation of phase pure BaZrS$_3$ NCs with orthorhombic crystal structure (distorted perovskite), as shown in Figure 5.2. UV-visible-NIR diffuse reflectance spectrum of BaZrS$_3$ NCs powder is measured, which is then converted to absorbance spectra by using Kubelka-Munk equation.[40] The absorption spectrum along with its corresponding Tauc plot is shown in Figure 5.3 suggest a direct band gap of 1.9 eV. Note that the finely grounded powder of BaZrS$_3$ NCs is used for absorption measurements.
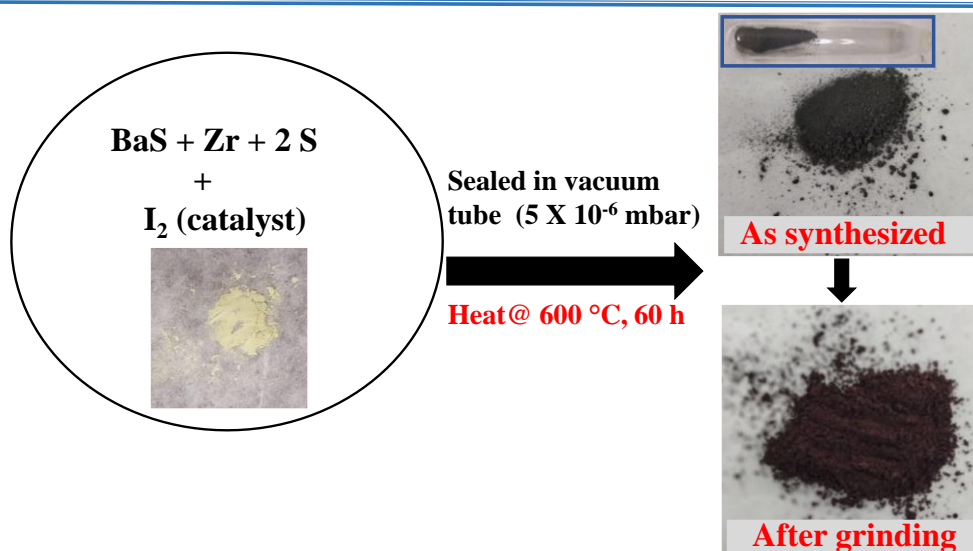
Figure 5.1: Schematic showing solid-state synthesis of BaZrS$_3$ NCs powder.
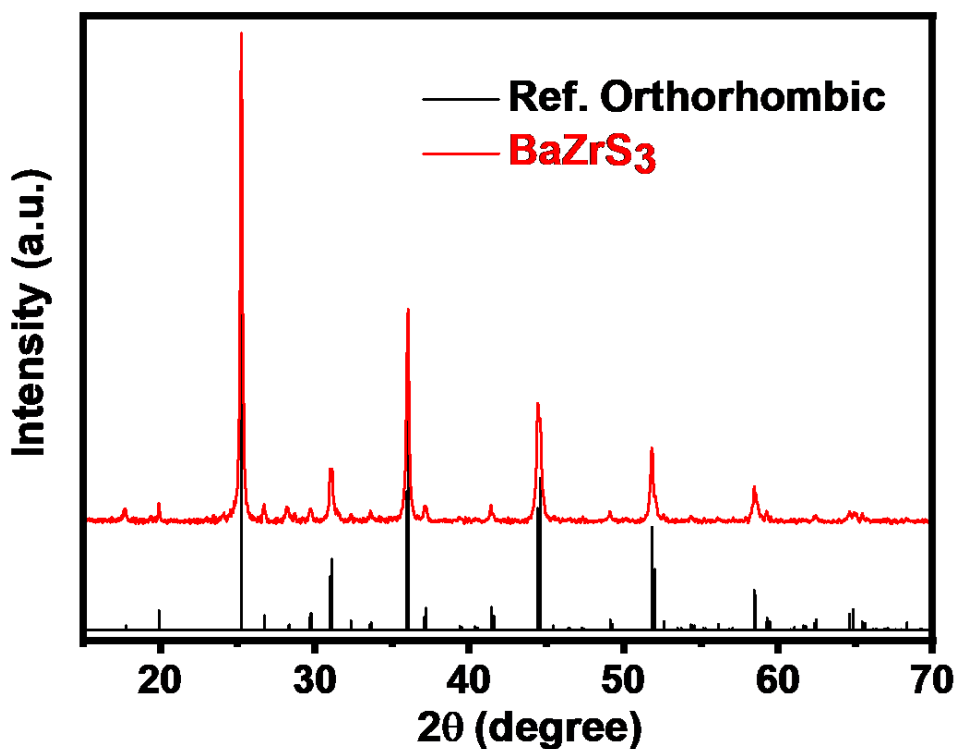
Figure 5.2: Comparison of PXRD pattern of BaZrS$_3$ NCs powder with that of reference pattern (00-015-0327) for orthorhombic phase of BaZrS$_3$.

PXRD peaks of BaZrS$_3$ powder in Figure 5.2 shows a small broadening suggesting possibility of formation NCs. Indeed, TEM image in Figure 5.4a shows the formation of NCs with cubic morphology. The edge lengths of the cubic NCs are around 40 to 60 nm. However, it is to be noted that some of the NCs agglomerate on TEM grid as shown Figure 5.4b.
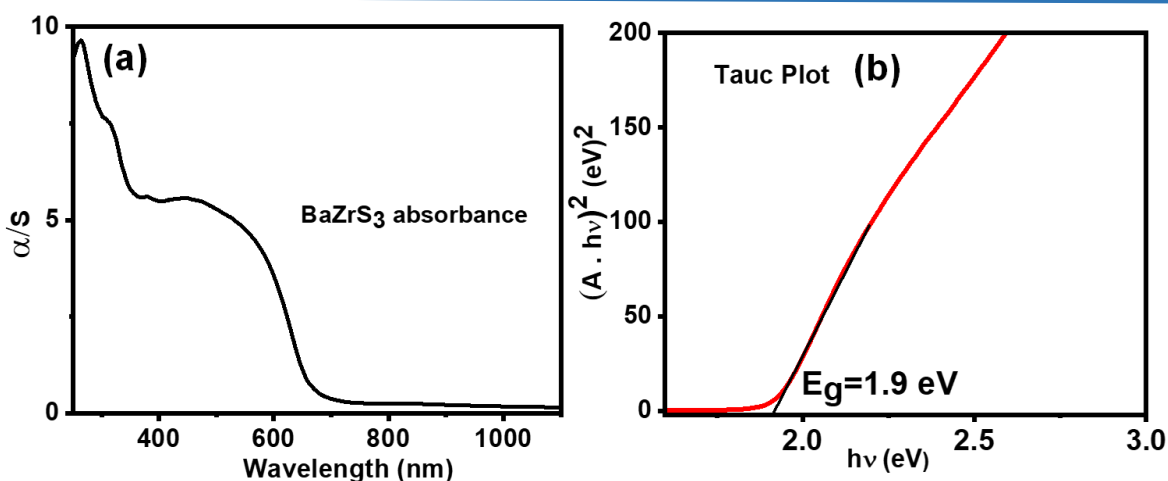
Figure 5.3: (a) The UV-visible-NIR absorption spectrum is obtained through Kubelka−Munk transformation from the measured diffused reflectance spectra of BaZrS₃ NCs powder, where α is the absorption coefficient and S is the scattering coefficient, (b) Tauc plot obtained from the corresponding absorption spectrum showing a direct bandgap of 1.9 eV. After the solid-state synthesis, the product is grounded, and the fine powder is used to measure absorption spectra.
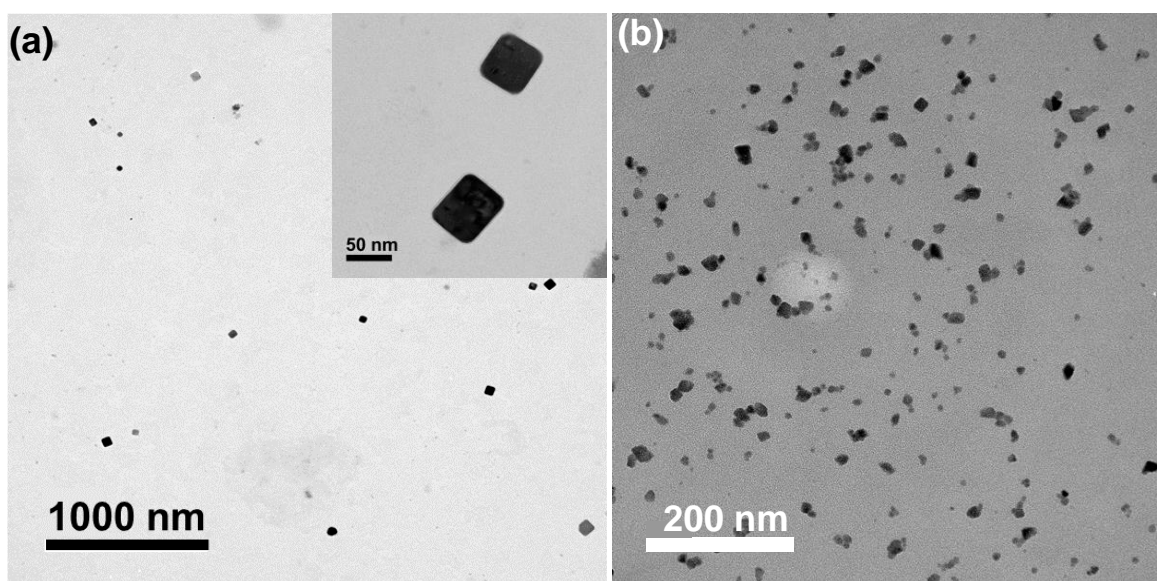
Figure 5.4: TEM image of BaZrS₃ NCs powder prepared by mixing the powder with n-butanol. (a) TEM image showing cube shaped BaZrS₃ NCs with edge lengths in the range of 40-60 nm. Inset shows the magnified image of NCs. (b) Many times, BaZrS₃ NCs shows irregular morphology and particles overlapped on each other.

HRTEM image in Figure 5.5a shows lattice fringes with interplanar distance 2.98 Å and 2.69 Å corresponding to the (004) and (220) planes of BaZrS₃ NCs respectively. Figure 5.5b shows the magnified HRTEM image of the same NC with the assignment of interplanar distance and the corresponding planes. Selected area electron diffraction (SAED) pattern of the NC in the inset of Figure 5.5a

demonstrates the single crystallinity of the sample. The diffraction spots can be assigned to the orthorhombic phase of $BaZrS_3$, similar to the powder XRD patterns in Figure 5.2. These TEM results are interesting because there is no prior report on the synthesis of $BaZrS_3$ NCs or any other chalcogenide perovskite NCs. More importantly, formation of NCs gives us the hope to make first ever solution processed films of chalcogenide perovskites.
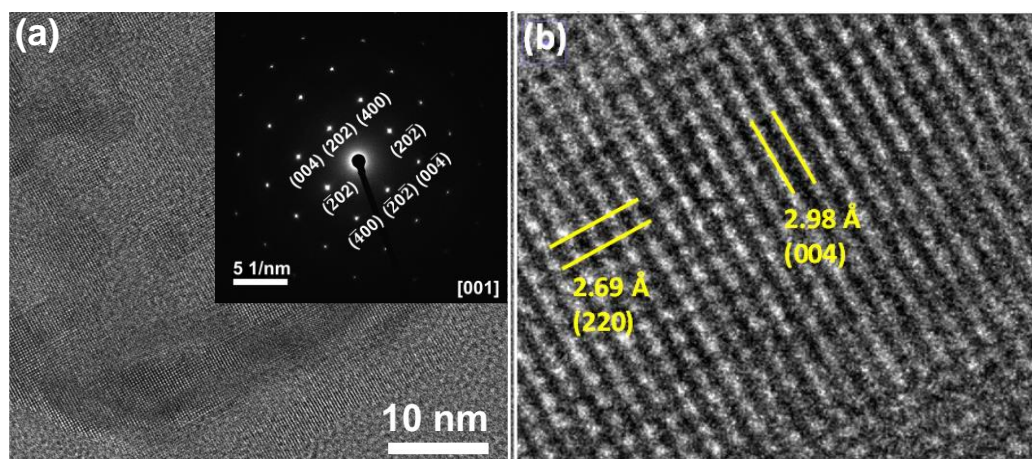
Figure 5.5: (a) HRTEM image of a single $BaZrS_3$ NC showing lattice fringes (b) magnified image of same to show the lattice fringes. Interplanar distances are marked, 2.98 Å and 2.69 Å corresponding to (004) and (220) planes of orthorhombic $BaZrS_3$ respectively. Note: Inset of Figure 5.5a shows the SAED pattern recorded on a different $BaZrS_3$ NC.

5.3.2 Stability of BaZrS₃ NCs powder:

To check the thermal stability of $BaZrS_3$ NCs, PXRD patterns are recorded at different temperatures. As shown in Figure 5.6a, the $BaZrS_3$ NCs remained in the orthorhombic phase throughout the temperature range, while heating up the sample from 298 K to 673 K. PXRD patterns recorded during the cooling of samples also show similar data (Figure 5.6b). These results show that $BaZrS_3$ NCs do not undergo any phase transition unlike the lead halide-based perovskites where they transform from orthorhombic to tetragonal to cubic phases with increasing temperatures.[41]

We have calculated the thermal volume expansion coefficient of $BaZrS_3$ NCs. Coefficient of volume thermal expansion, α_v at temperature T is defined as $\alpha_{v,T} = (1/V_{m,T}) \times (dV_{m,T}/dT)$ (at a constant pressure).[42] In the measured temperature range molar volume can be taken as linear function of temperature and is fitted with the linear equation as shown in Figure 5.7b.
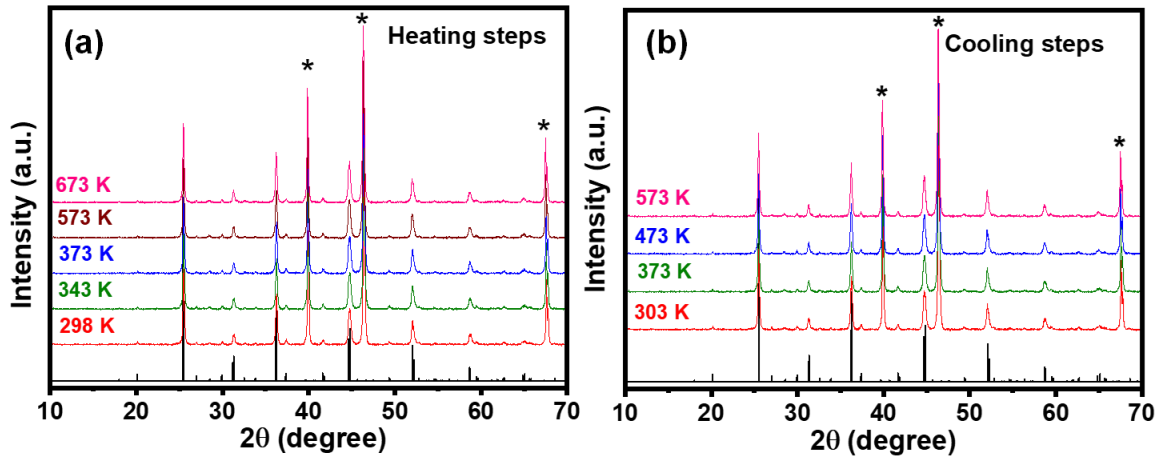
Figure 5.6: (a) Variable temperature XRD of BaZrS₃ NCs from room temperature to 673 K shows that the orthorhombic phase is maintained without any sign of degradation. (b) Cooling steps shown for the BaZrS₃ NCs coming from high temperature to room temperature. Peaks marked with "*" is due to Pt substrate.
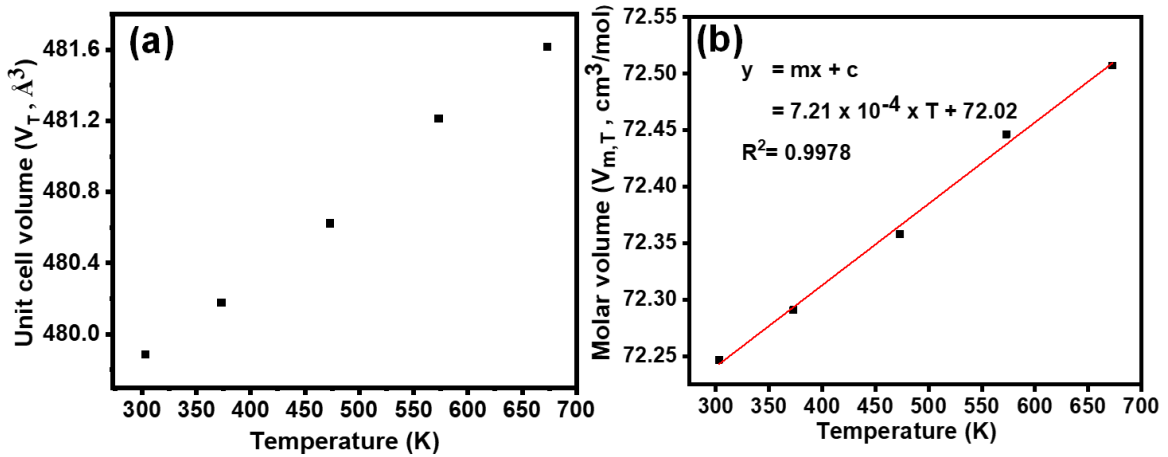
Figure 5.7: (a) It shows the variation of unit cell volume (V_T) of BaZrS₃ with increasing temperature determined using variable temperature PXRD. To obtain this, unit cell constants i.e. a, b and c are determined at each temperature and multiplied to give unit cell volume of orthorhombic crystal structure. (b) It shows the variation of molar volume ($V_{m,T}$) of BaZrS₃ with increasing temperature. Molar volume ($V_{m,T}$) are calculated as a function of temperature as $V_{m,T} = V_T \times N_A/Z$,[42] where V_T is the volume of the unit cell at temperature T, N_A is Avogadro number and Z is the number of formula unit per unit cell (for orthorhombic crystal structure, Z= 4).

The $\alpha_{v,T}$ at 300 K is then determined by dividing the slope (7.21×10⁻⁴) with molar volume at 303 K (72.32 cm³/mol) and is equal to, $\alpha_{v,303\,K} = 9.97×10^{-6}\,K^{-1}$. The thermal expansion coefficient serves as a design parameter for material having low thermal lattice conductivity and hence have application in designing thermoelectric materials.[43] This low thermal volume expansion of BaZrS₃ NCs gives an indication

that it could have low thermal conductivity which is recently reported by some groups.[44, 45]

After confirming the thermal stability of BaZrS₃ NCs over a wide temperature range, now we will discuss about the aqueous stability by testing photocatalytic activity of BaZrS₃ NCs in water. We have studied the photocatalytic activity of BaZrS₃ NCs powder by carrying out the degradation of methylene blue dye in distilled water, under sun light. Figure 5.8 shows the absorbance spectra of methylene blue at regular interval after irradiation of sunlight. Decrease in absorbance values shows the degradation of dye.
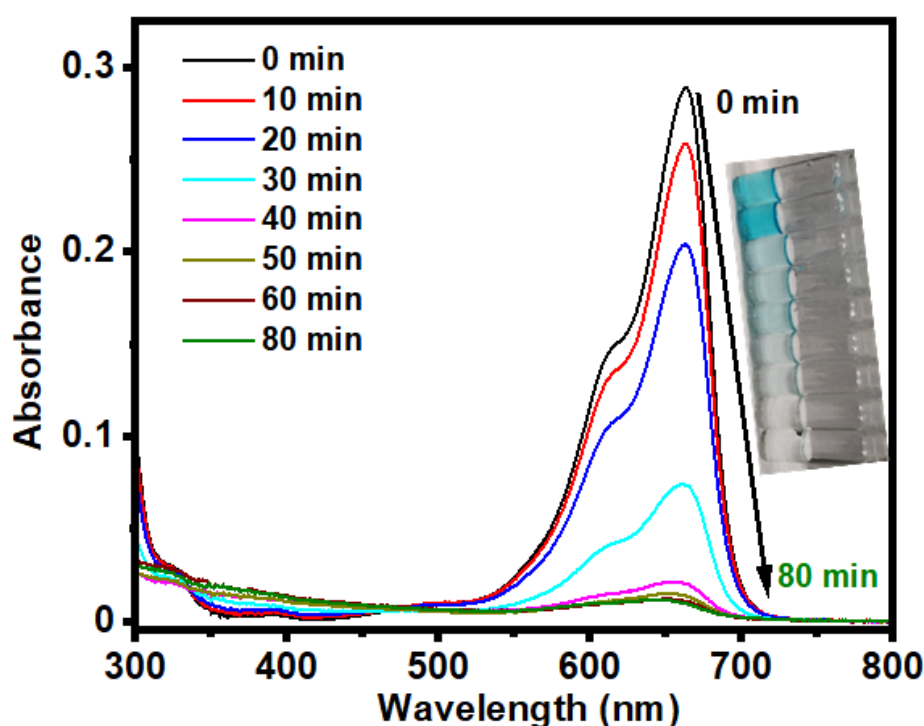
Figure 5.8: UV-visible absorption spectra of methylene blue dye in water at different irradiation times (using sunlight) in the presence of BaZrS₃ NCs. Inset shows digital photographs of methylene blue at different irradiation time.

Figure 5.9 shows the decrease in concentration of methylene blue with time. We find that BaZrS₃ NCs degrades almost 98 % of methylene blue within 50 min when exposed to sunlight. This preliminary photocatalytic activity of BaZrS₃ NCs is reasonably good compared to prior literature.[46, 47] Such photocatalytic performance probably arises from multiple factors like good solar light absorption capability of BaZrS₃ NCs, high surface to volume ratio of NCs, and reasonably good water stability.
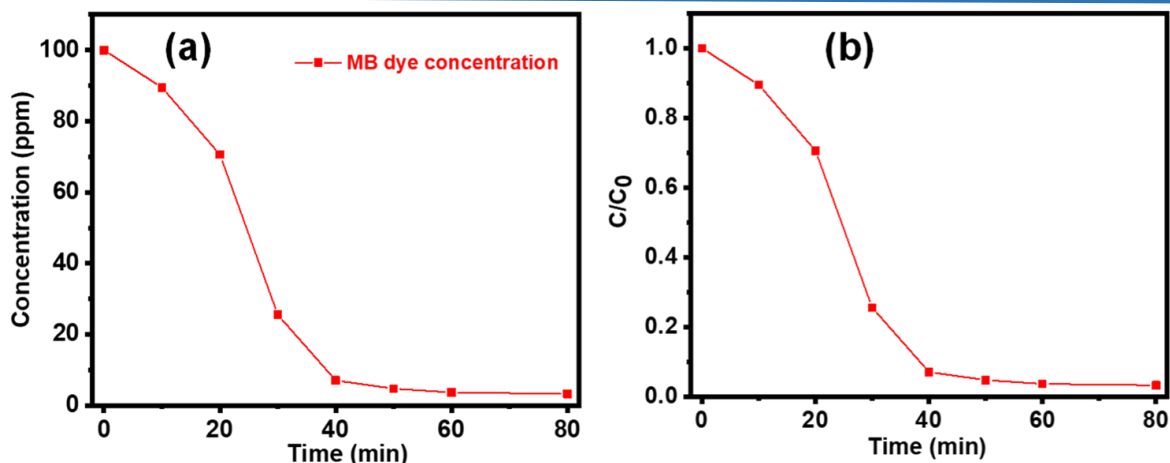
Figure 5.9: (a) Concentration of methylene blue (MB) dye with increasing time after sunlight irradiation. (b) Plot of C/C0 versus the irradiation time for the photodegradation of methylene blue dye in presence of BaZrS₃ NCs. Co is concentration of dye at time = 0 min and C is concentration at time = t min. These data are extracted from the UV-visible absorption spectra shown in Figure 5.8.
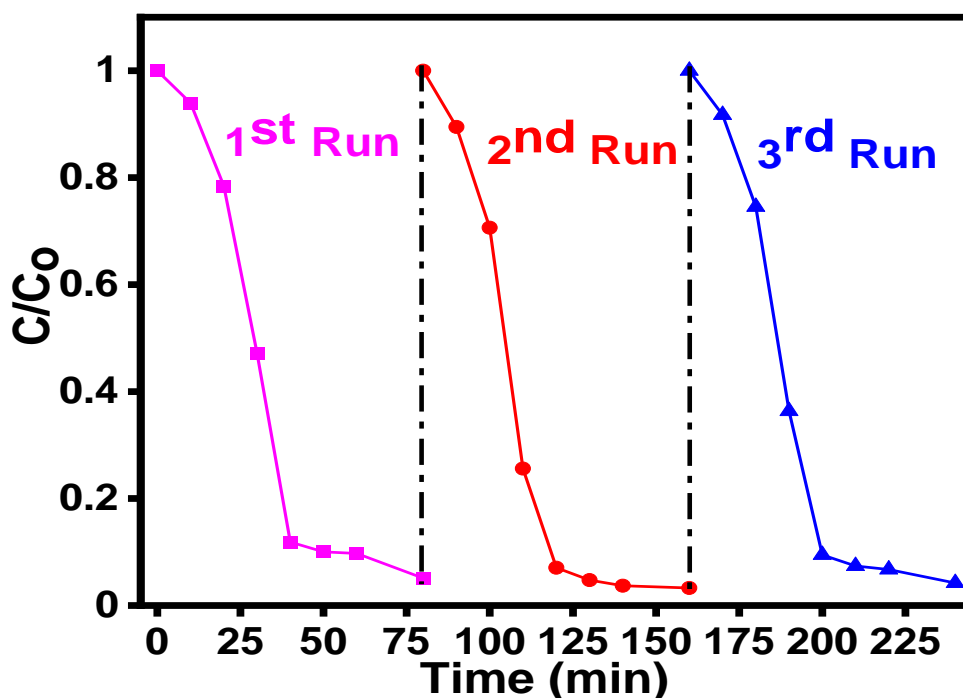
Figure 5.10: Testing water stability of BaZrS₃ NCs by measuring photocatalytic degradation of aqueous solution methylene blue dye in presence of the NCs. Reasonably good photocatalytic activity of BaZrS₃ NCs that remains largely unchanged over 3 cycles is observed.

To further check the water stability BaZrS₃ NCs, we show the recycling ability of the photocatalyst. Figure 5.10 shows that the photocatalytic performance of BaZrS₃ NCs for the degradation of methylene blue is stable for at least 3 cycles. However, we note that after several hours (10 to 12 hours) the BaZrS₃ NCs sample starts to

degrade in water as the water starts turning milky. In the dark, BaZrS₃ NCs powder (not a proper colloidal dispersion) in water is stable for a few days, as confirmed by PXRD pattern recorded after the water treatment.

5.3.3 Solution processability of BaZrS₃ NCs powder:

An important finding of the previous sub-section is that the BaZrS₃ powders are NCs of size around 40 – 60 nm. While the size may be too large to observe quantum confinement effect, the high surface to volume ratio could be utilized to make colloidal dispersion of NCs. Traditionally, colloidal synthesis yields NCs with their surfaces decorated with long-chain organic ligands or charged inorganic ligands, facilitating solution processed film fabrication.[48] Since, our BaZrS₃ NCs are prepared by solid-state synthesis, the NCs do not have any such surface ligands. Therefore, we needed to modify the surface of our pre-formed NCs to achieve solution processed BaZrS₃ NCs, which then can be utilized later to make thin film devices. Schematics in Figure 5.11 illustrate our strategy to functionalize the surface of NCs. BaZrS₃ NCs are first mixed with N-methyl-2-pyrrolidinone and then stirred at 120 °C for 6 hours to make it completely dispersible. It yields dark brownish dispersion which is then passed through 0.22 µm syringe filter without any clogging.
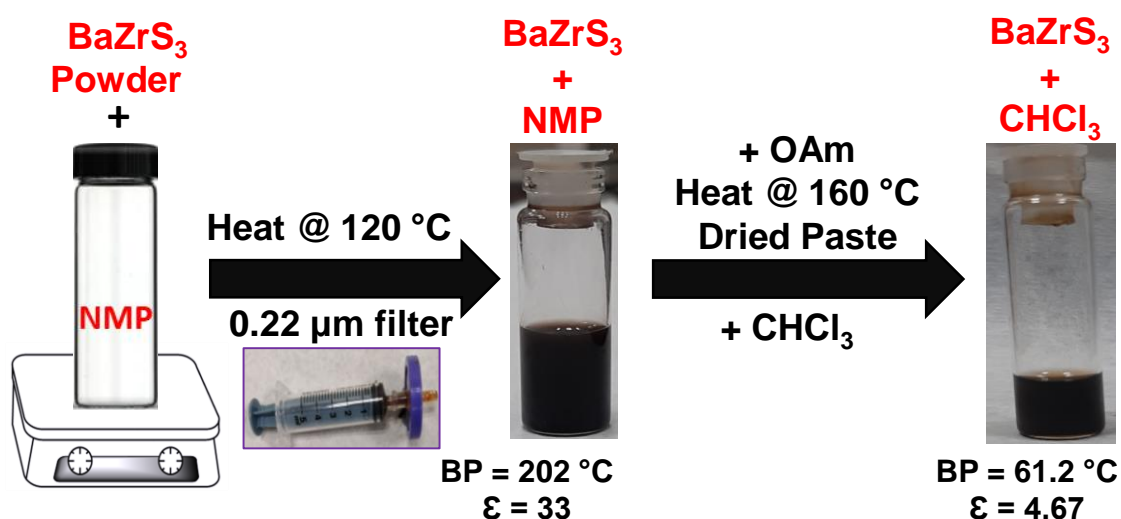
Figure 5.11: Schematic to make powder of BaZrS₃ NCs colloidally stable in N-methyl-2-pyrrolidinone (NMP) followed by treatment with oleylamine (OAm) to make dispersion in chloroform (CHCl₃). BP = boiling point and ε = dielectric constant.

PXRD pattern of the sample obtained by drop casting the dispersion in N-methyl-2-pyrrolidinone is shown in Figure 5.12. The PXRD pattern corresponds to BaZrS₃

NCs with orthorhombic phase without any impurity phase. This result confirms that the solution is nothing but colloidal dispersion of BaZrS$_3$ NCs in N-methyl-2-pyrrolidinone. The dispersibility of the BaZrS$_3$ NCs is attributed to the coordination of N-methyl-2-pyrrolidinone to the BaZrS$_3$ NCs. N-methyl-2-pyrrolidinone is known as a powerful coordinating solvent for 'd block' metals cations like Fe, Mn.[49, 50] N-methyl-2-pyrrolidinone has also been used to disperse transition metal dichalcogenide where it is believed that the interactions between the N-methyl-2-pyrrolidinone molecules and interactions between N-methyl-2-pyrrolidinone and transition metal dichalcogenide are of the similar nature.[51]
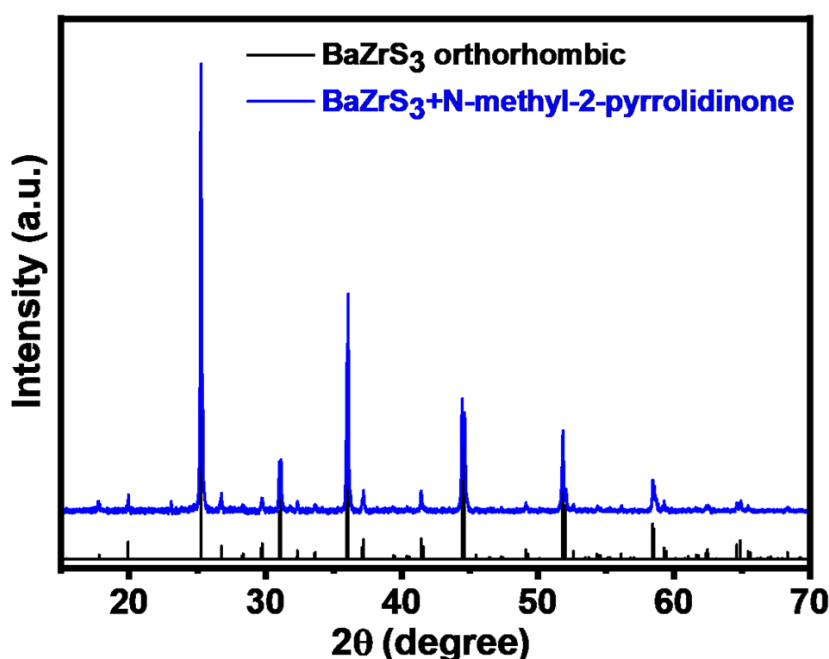
Figure 5.12: PXRD pattern recorded of the film made by drop casting colloidal dispersion of BaZrS$_3$ NCs on a glass slide.

The UV-visible absorption data (Figure 5.13a) of colloidal sample shows onset similar to the powder sample, but onset is less clear for dispersion because of the significantly reduced concentration of NCs in the dispersion. We have measured the extinction coefficient of colloidal BaZrS$_3$ NCs by using Beer-Lambert law as shown in Figure 5.13. The absorbance varies linearly with concentration of NCs. Using these data, we have calculated the extinction coefficient of BaZrS$_3$ NCs as 0.44×10^4 mg^{-1} cm^{-1} mL at 400 nm. For comparison, we note that the 11 nm sized CsPbI$_3$ NCs exhibit similar extinction coefficient (1.2×10^4 mg^{-1} cm^{-1} mL) at 400 nm.[52]
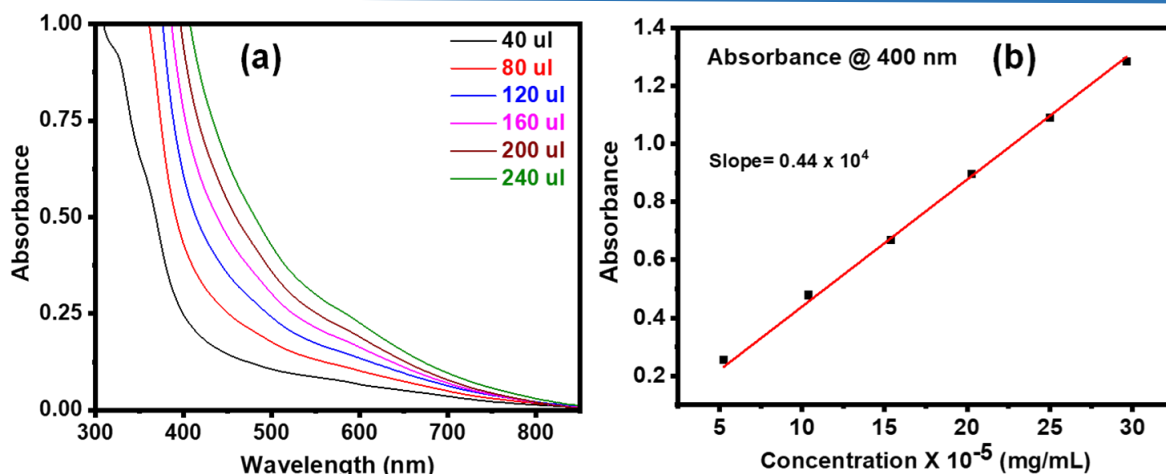
Figure 5.13: (a) UV-visible spectra of different concentrations of BaZrS₃ NCs dispersion in N-methyl-2-pyrrolidinone. (b) Plot of absorbance vs molar concentration (mg/mL) of BaZrS₃ NCs obtained by using the spectra in (a).

These results confirm the high absorption coefficient of the BaZrS₃ NCs, similar to Pb-halide perovskites, and agree with prior theoretical reports[18, 19] suggesting BaZrS₃ is having high absorption cross-section on par with lead halide perovskites.
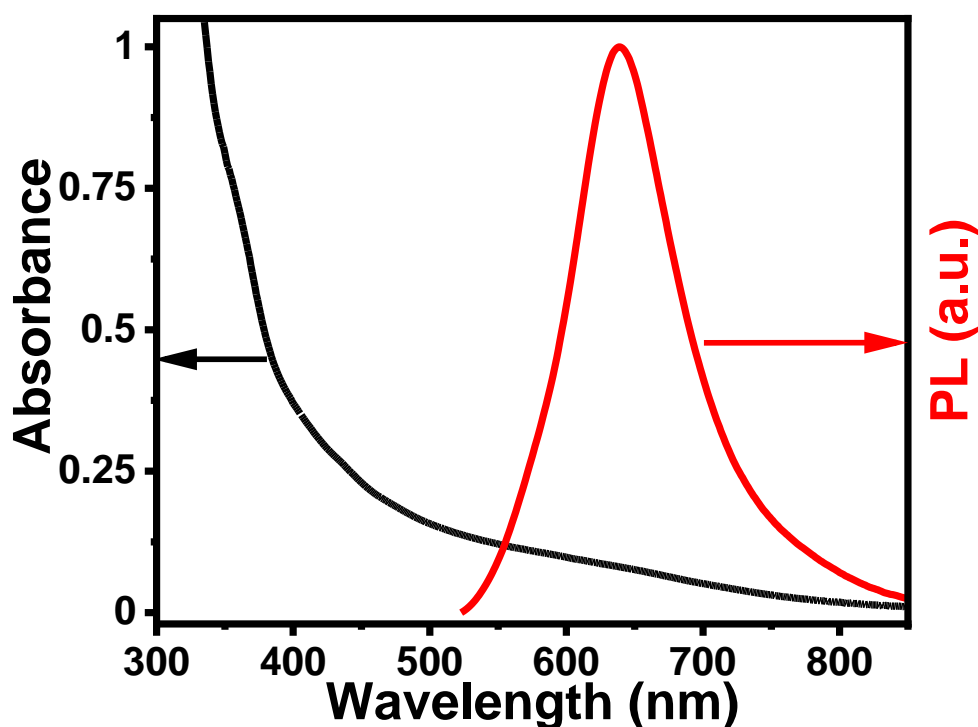
Figure 5.14: UV-visible absorbance and PL spectra of BaZrS₃ NCs dispersed in N-methyl-2-pyrrolidinone. The excitation wavelength used is 500 nm.

UV-visible absorption and PL spectra of the colloidal BaZrS₃ NCs in N-methyl-2-pyrrolidinone are shown in Figure 5.14. The PL signal is very weak for BaZrS₃ NCs powder (noisy data, not shown here), similar to prior report.[30, 31] Interestingly, PL

intensity increases significantly by making the dispersion of BaZrS$_3$ NCs in N-methyl-2-pyrrolidinone. Comparison of the PL and absorption data suggests that the PL is due to band-edge (or excitonic) emission. The increase in PL intensity for the dispersion is probably because of reduction of both non-radiative energy transfer and the radiative self-absorption processes in the dilute dispersion compared to the powder.[41] Since the PL quantum yield of our BaZrS$_3$ NCs is still rather low, such energy-transfer from more to less emitting NCs is expected to quench the PL significantly. Also, there is a possibility that N-methyl-2-pyrrolidinone might passivate the surface of NCs improving the PL intensity.
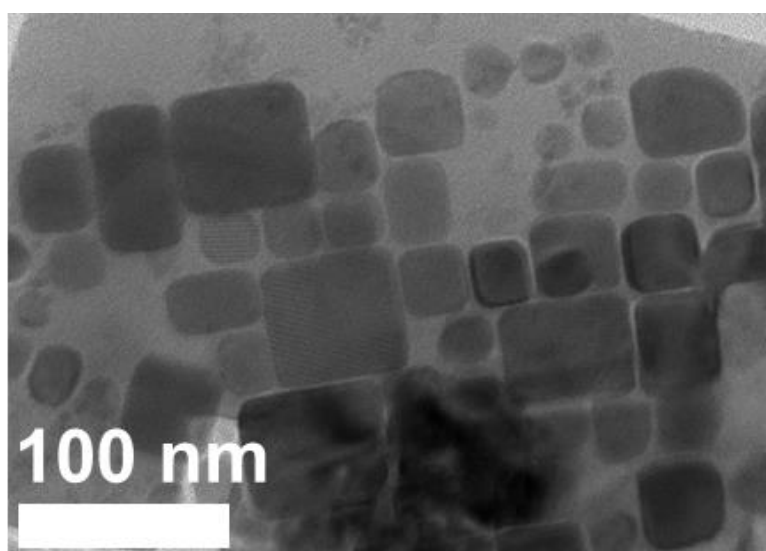
Figure 5.15: TEM image of BaZrS$_3$ NCs samples prepared from the chloroform dispersion of BaZrS$_3$ NCs, after treatment with N-methyl-2-pyrrolidinone and OAm.

While we could achieve the NC dispersion in N-methyl-2-pyrrolidinone, making thin films from this dispersion using standard techniques like spin coating is difficult because of the high boiling point of N-methyl-2-pyrrolidinone. Therefore, we did a second round of surface modification to disperse BaZrS$_3$ NCs into low-boiling solvents like chloroform. We take BaZrS$_3$ NCs (400 mg) in N-methyl-2-pyrrolidinone (300 μL) along with 100 μL OAm and heated it at 160 °C till the majority of solvent evaporates and it dries to form a thick paste. Then the dried paste is dispersed into chloroform. Figure 5.15 shows the TEM data of the sample taken from the chloroform dispersion. Cube shaped NCs are observed, implying that the treatment with the N-methyl-2-pyrrolidinone and OAm does not significantly change the morphology and size of BaZrS$_3$ NCs.

5.3.4 Thin film FET of BaZrS₃ NCs:

After achieving the colloidal dispersion of BaZrS$_3$ NCs in chloroform, now it can be used for making thin films. BaZrS$_3$ NCs FET is demonstrated with bottom gate-top contact geometry based on the solution process BaZrS$_3$ NCs. The FETs are fabricated by Dr. Dae Sung Chung and his student Seong Hoon Yu at POSTECH, Korea. Further details about the device fabrication, geometry and characterization can be found in our paper (Ravi et al., Colloidal BaZrS$_3$ Chalcogenide Perovskite Nanocrystals for Thin Film Device Fabrication, **Manuscript submitted**).

The BaZrS$_3$ NCs FETs exhibit ambipolar properties. It is capable of both hole and electron transport.
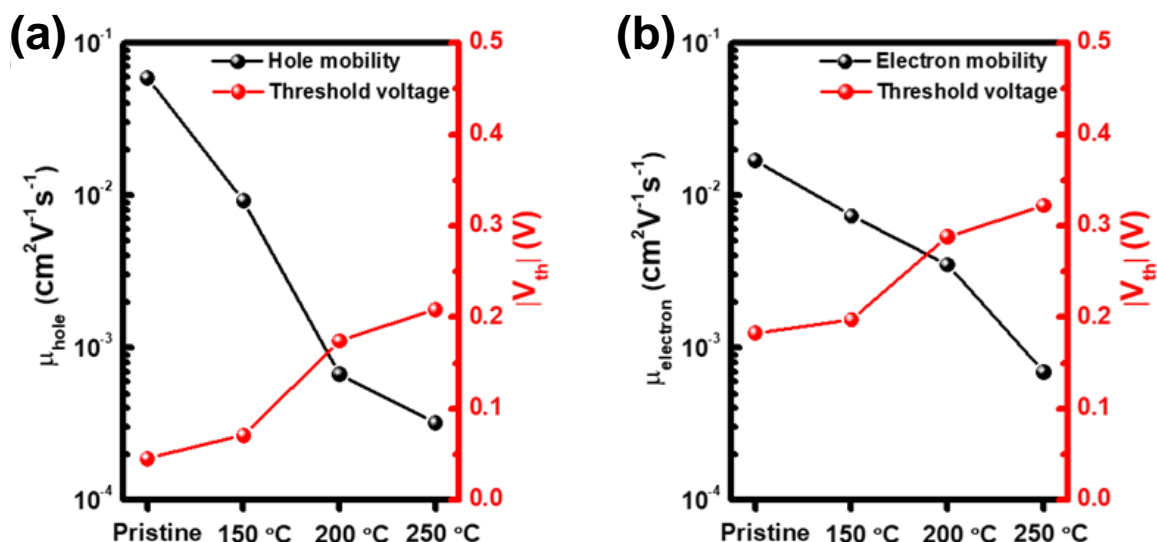
Figure 5.16: FET data showing changes in charge carrier mobility and threshold voltage of (a) p-type and (b) n-type FET as a function of annealing temperature.

With drain-source voltage (V$_{DS}$) of ± 0.1 V, it is found that the FET performances in terms of both mobility and threshold voltage (V$_{th}$) become worse at higher annealing temperatures of the BaZrS$_3$ NCs film. We speculate that this decrease is due to rough surface developed by the annealing process, which may hamper charge transport within BaZrS$_3$ NCs film. As summarized in Figure 5.16 a and 5.16b, there are clear trends of decreasing mobility and increasing V$_{th}$ when annealing temperature is increased, in both p- and n-type measurement regimes. BaZrS$_3$ NCs FET without any annealing (pristine) rendered the highest hole mobility of 0.059 cm^{2}V^{-1}s^{-1}, and also the highest electron mobility of 0.017 cm^{2}V^{-1}s^{-1}. Note that as far as we know, this is the first report of solution processed BaZrS$_3$ thin film device.

Long organic capping ligands like OAm hinders the charge transport in a NC film.[14] The size of our BaZrS$_3$ NCs is large (40-60 nm), reducing the surface-to-volume ratio or ligand-to-NC ratio. This large size of NCs, along with incomplete ligand coverage on the NC surface, possibly brings the NCs closer to each other in the film, allowing the charge transport.[53, 54] The carrier mobility values are expected to increase after a better surface modification of BaZrS$_3$ NCs.

5.3.5 Preliminary attempt at fabrication of solar cell of BaZrS$_3$ NCs:

Solar cells are fabricated from the colloidal dispersion of BaZrS$_3$ NCs in chloroform and by using it as an active layer. Figure 5.17 shows the planar architecture that is followed to make the solar cell device.

Figure 5.17: Planar architecture of fabricated solar cell device with layers from bottom to top as: FTO/ TiO2 / BaZrS3 NCs/ Spiro-MeOTAD/ Au.

Figure 5.18a shows the homemade mask of single cell area of (0.24 cm^2) made from tin foil and has been used for deposition of gold electrode. Figure 5.18b shows one of the representative solar cell devices. The fabricated solar cell devices are tested under the simulated solar spectrum of AM 1.5G and the power density of the light source has been fixed at 100 mW/cm^2 (In the lab of Dr. Nirmalaya Ballav, IISER Pune). Figure 5. 19 shows the Current density (J) –Voltage (V) curve of the solar cell devices employing BaZrS$_3$ NCs as light absorbing layer. As seen the current density (and voltage) increases with the number of BaZrS$_3$ NCs deposition layer and the maximum efficiency for this architecture is achieved for 6 layer having photovoltaic efficiency of 0.17 %. However, we do note that the thickness does not increase linearly with the increasing BaZrS$_3$ NCS deposition probably because the washing of previous layer when the next deposition is carried out.
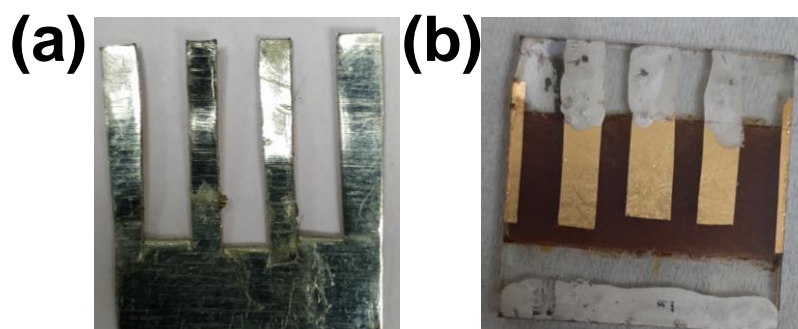
Figure 5.18: (a) Homemade mask made from steel having cut-out area of 0.24 cm^2 (8 mm X 3 mm). (b) A representative solar cell device.
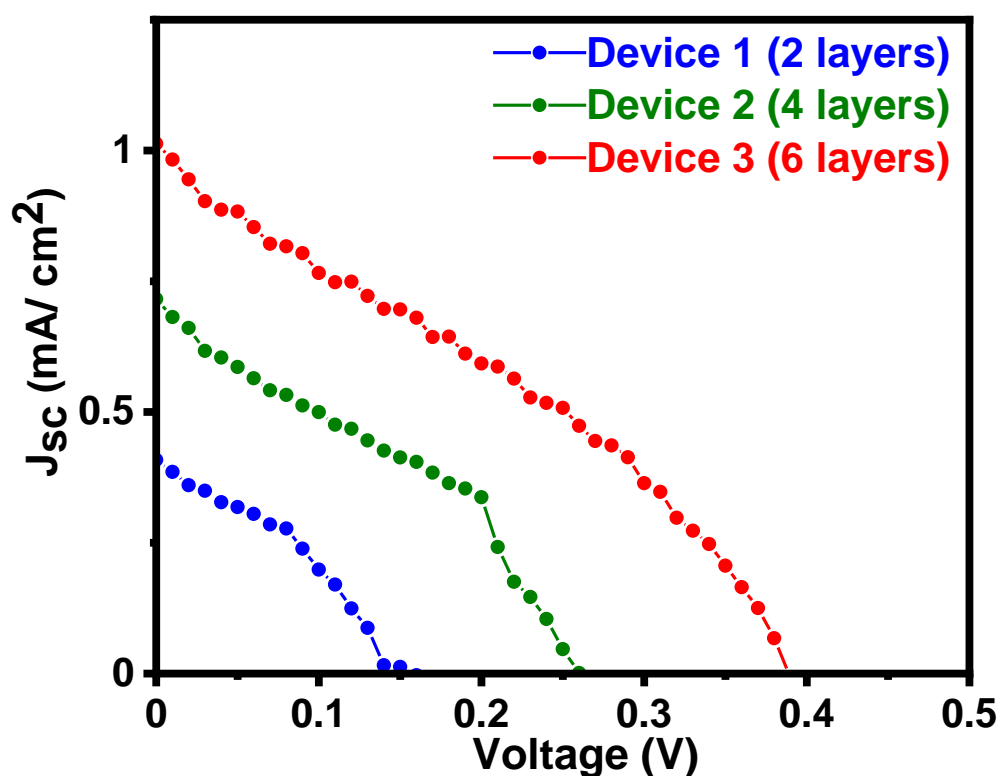
Figure 5.19: Current density−voltage curves (J−V) of various representative solar cell devices. Number of layers mentioned in legend refers to the number of times the BaZrS₃ NCs are spin-coated to increase the thickness.

Table 5.1: Solar cell parameters of BaZrS₃ NCs based devices having different thickness.

Device	J_{sc} (mA/cm^2)	V_{oc} (V)	FF (%)	Efficiency (%)
1	0.41	0.16	34	0.02
2	0.72	0.26	36	0.07
3	1.01	0.39	42	0.17

The low photovoltaic efficiency of this BaZrS$_3$ NCs based devices suggest that there is need of optimization of device architecture. Further treatment of BaZrS$_3$ NCs films for effective removal of organic ligand is also one of the ways to increase the efficiency.

5.4 Conclusions:

We have prepared BaZrS$_3$ chalcogenide perovskite NCs by employing solid-state synthesis resulting in the cube shaped NCs having edge length in the range of 40-60 nm. Structural stability of the NCs is confirmed using variable temperature PXRD (298 – 673 K). The NCs also serve as good photocatalysts (under sunlight) for methylene blue dye degradation in water. While the detailed photocatalytic activity can be studied in future, the present results confirm significantly improved water stability of bare BaZrS$_3$ chalcogenide perovskite NCs, compared to their metal halide perovskites. The size of the NCs are too big to observe quantum confinement effect, however the high surface to volume ratio is utilized not only for photocatalytic activity, but more importantly for solution processability. We developed desired surface chemistry for BaZrS$_3$ NCs making stable colloidal dispersion in both, polar solvent N-methyl-2-pyrrolidinone and non-polar solvent chloroform. The NCs dispersion in low-boiling chloroform is then spin coated to make thin films with thickness ~ 50 nm. These solutions processed thin films are then used to fabricate FET device in the bottom gate-top contact geometry. BaZrS$_3$ NCs show both p- and n-type ambipolar transistor behaviour with hole mobility 0.059 cm^{2}V^{-1}s^{-1}, and electron mobility 0.017 cm^{2}V^{-1}s^{-1}. So, the early results of charge carriers mobility values, along with their light absorbing power and moderate band-edge PL is encouraging for developing future optoelectronic devices of BaZrS$_3$ NCs and other related chalcogenide perovskite compositions. We also attempted to make solar cell devices based on BaZrS$_3$ NCs but the performance of the device is poor. Surely new strategy in making films, ligand removal and device architecture is needed for making more efficient solar cell. To the best of our knowledge, this is the first report of (i) any chalcogenide perovskite NCs, (ii) solution processed chalcogenide perovskite thin films, and (iii) FET of any chalcogenide perovskite system. So, the early results of carriers mobility values, along with their light absorbing power and

moderate band-edge PL is encouraging for developing future optoelectronic devices of BaZrS$_3$ NCs and other related chalcogenide perovskite compositions.

5.5 References:

1. Goto, T.; Kimura, T.; Lawes, G.; Ramirez, A. P.; Tokura, Y., Ferroelectricity and Giant Magnetocapacitance in Perovskite Rare-Earth Manganites. *Phys. Rev. Lett.* **2004,** *92*, 257201.

2. Ramesh, R.; Spaldin, N. A., Multiferroics: progress and prospects in thin films. *Nat. Mater.* **2007,** *6*, 21-29.

3. Kojima, A.; Teshima, K.; Shirai, Y.; Miyasaka, T., Organometal Halide Perovskites as Visible-Light Sensitizers for Photovoltaic Cells. *J. Am. Chem. Soc.* **2009,** *131*, 6050-6051.

4. Lee, M. M.; Teuscher, J.; Miyasaka, T.; Murakami, T. N.; Snaith, H. J., Efficient hybrid solar cells based on meso-superstructured organometal halide perovskites. *Science* **2012,** *338*, 643-647.

5. Shi, D.; Adinolfi, V.; Comin, R.; Yuan, M.; Alarousu, E.; Buin, A.; Chen, Y.; Hoogland, S.; Rothenberger, A.; Katsiev, K.; Losovyj, Y.; Zhang, X.; Dowben, P. A.; Mohammed, O. F.; Sargent, E. H.; Bakr, O. M., Low trap-state density and long carrier diffusion in organolead trihalide perovskite single crystals. *Science* **2015,** *347*, 519.

6. Manser, J. S.; Christians, J. A.; Kamat, P. V., Intriguing Optoelectronic Properties of Metal Halide Perovskites. *Chem. Rev.* **2016,** *116*, 12956-13008.

7. Akkerman, Q. A.; Rainò, G.; Kovalenko, M. V.; Manna, L., Genesis, challenges and opportunities for colloidal lead halide perovskite nanocrystals. *Nat. Mater.* **2018,** *17*, 394-405.

8. Pal, P.; Saha, S.; Banik, A.; Sarkar, A.; Biswas, K., All-Solid-State Mechanochemical Synthesis and Post-Synthetic Transformation of Inorganic Perovskite-type Halides. *Chem. Eur. J.* **2018,** *24*, 1811-1815.

9. Dutta, A.; Behera, R. K.; Pal, P.; Baitalik, S.; Pradhan, N., Near-Unity Photoluminescence Quantum Efficiency for All CsPbX$_3$ (X=Cl, Br, and I) Perovskite Nanocrystals: A Generic Synthesis Approach. *Angew. Chem. Int. Ed.* **2019,** *58*, 5552-5556.

10. Sheikh, T.; Nawale, V.; Pathoor, N.; Phadnis, C.; Chowdhury, A.; Nag, A., Molecular Intercalation and Electronic Two Dimensionality in Layered Hybrid Perovskites. *Angew. Chem. Int. Ed.* **2020,** 10.1002/anie.202003509.

11. Conings, B.; Drijkoningen, J.; Gauquelin, N.; Babayigit, A.; D'Haen, J.; D'Olieslaeger, L.; Ethirajan, A.; Verbeeck, J.; Manca, J.; Mosconi, E.; Angelis, F. D.; Boyen, H.-G., Intrinsic Thermal Instability of Methylammonium Lead Trihalide Perovskite. *Adv. Energy Mater.* **2015,** *5*, 1500477.

12. Babayigit, A.; Ethirajan, A.; Muller, M.; Conings, B., Toxicity of organometal halide perovskite solar cells. *Nat. Mater.* **2016,** *15*, 247-251.

13. Huang, H.; Bodnarchuk, M. I.; Kershaw, S. V.; Kovalenko, M. V.; Rogach, A. L., Lead Halide Perovskite Nanocrystals in the Research Spotlight: Stability and Defect Tolerance. *ACS Energy Lett.* **2017,** *2*, 2071-2083.

14. Pal, J.; Manna, S.; Mondal, A.; Das, S.; Adarsh, K. V.; Nag, A., Colloidal Synthesis and Photophysics of $M_3Sb_2I_9$ (M=Cs and Rb) Nanocrystals: Lead-Free Perovskites. *Angew. Chem. Int. Ed.* **2017,** *56*, 14187-14191.

15. Zhou, L.; Liao, J.-F.; Huang, Z.-G.; Wei, J.-H.; Wang, X.-D.; Li, W.-G.; Chen, H.-Y.; Kuang, D.-B.; Su, C.-Y., A Highly Red-Emissive Lead-Free Indium-Based Perovskite Single Crystal for Sensitive Water Detection. *Angew. Chem. Int. Ed.* **2019,** *58*, 5277-5281.

16. Li, M.; Zhou, J.; Zhou, G.; Molokeev, M. S.; Zhao, J.; Morad, V.; Kovalenko, M. V.; Xia, Z., Hybrid Metal Halides with Multiple Photoluminescence Centers. *Angew Chem. Int. Ed.* **2019,** *58*, 18670-18675.

17. Arfin, H.; Kaur, J.; Sheikh, T.; Chakraborty, S.; Nag, A., Bi^{3+}-Er^{3+} and Bi^{3+}-Yb^{3+} Codoped $Cs_2AgInCl_6$ Double Perovskite Near Infrared Emitters. *Angew. Chem. Int. Ed.* **2020,** 10.1002/anie.202002721.

18. Sun, Y.-Y.; Agiorgousis, M. L.; Zhang, P.; Zhang, S., Chalcogenide Perovskites for Photovoltaics. *Nano Lett.* **2015,** *15*, 581-585.

19. Bennett, J. W.; Grinberg, I.; Rappe, A. M., Effect of substituting of S for O: The sulfide perovskite $BaZrS_3$ investigated with density functional theory. *Phys. Rev. B* **2009,** *79*, 235115.

20. Meng, W.; Saparov, B.; Hong, F.; Wang, J.; Mitzi, D. B.; Yan, Y., Alloying and Defect Control within Chalcogenide Perovskites for Optimized Photovoltaic Application. *Chem. Mater.* **2016,** *28*, 821-829.

21. Kuhar, K.; Crovetto, A.; Pandey, M.; Thygesen, K. S.; Seger, B.; Vesborg, P. C. K.; Hansen, O.; Chorkendorff, I.; Jacobsen, K. W., Sulfide perovskites for solar energy conversion applications: computational screening and synthesis of the selected compound LaYS₃. *Energy Environ. Sci.* **2017,** *10*, 2579-2593.

22. Oumertem, M.; Maouche, D.; Berri, S.; Bouarissa, N.; Rai, D. P.; Khenata, R.; Ibrir, M., Theoretical investigation of the structural, electronic and thermodynamic properties of cubic and orthorhombic $XZrS_3$ (X = Ba,Sr,Ca) compounds. *J. Comput. Electron.* **2019,** *18*, 415-427.

23. Vonrüti, N.; Aschauer, U., Band-gap engineering in $AB(O_xS_{1-x})_3$ perovskite oxysulfides: a route to strongly polar materials for photocatalytic water splitting. *J Mater. Chem. A* **2019,** *7*, 15741-15748.

24. Buffiere, M.; Dhawale, D. S.; El-Mellouhi, F., Chalcogenide Materials and Derivatives for Photovoltaic Applications. *Energy Technol.* **2019,** *7*, 1900819.

25. Clearfield, A., The synthesis and crystal structures of some alkaline earth titanium and zirconium sulfides. *Acta Crystallogr.* **1963,** *16*, 135-142.

26. Nitta, T.; Nagase, K.; Hayakawa, S., Formation, Microstructure, and Properties of Barium Zirconium Sulfide Ceramics. *J. Am. Ceram. Soc.* **1970,** *53*, 601-604.

27. Wang, Y.; Sato, N.; Yamada, K.; Fujino, T., Synthesis of BaZrS₃ in the presence of excess sulfur. *J. Alloys Compd.* **2000,** *311*, 214-223.

28. Wang, Y.; Sato, N.; Fujino, T., Synthesis of BaZrS3 by short time reaction at lower temperatures. *J. Alloys Compd.* **2001,** *327*, 104-112.

29. Lee, C.-S.; Kleinke, K. M.; Kleinke, H., Synthesis, structure, and electronic and physical properties of the two SrZrS₃ modifications. *Solid State Sci.* **2005,** *7*, 1049-1054.

30. Perera, S.; Hui, H.; Zhao, C.; Xue, H.; Sun, F.; Deng, C.; Gross, N.; Milleville, C.; Xu, X.; Watson, D. F.; Weinstein, B.; Sun, Y.-Y.; Zhang, S.; Zeng, H., Chalcogenide perovskites – an emerging class of ionic semiconductors. *Nano Energy* **2016,** *22*, 129-135.

31. Niu, S.; Huyan, H.; Liu, Y.; Yeung, M.; Ye, K.; Blankemeier, L.; Orvis, T.; Sarkar, D.; Singh, D. J.; Kapadia, R.; Ravichandran, J., Bandgap Control via Structural and Chemical Tuning of Transition Metal Perovskite Chalcogenides. *Adv. Mater.* **2017,** *29*, 1604733.

32. Hanzawa, K.; Iimura, S.; Hiramatsu, H.; Hosono, H., Material Design of Green-Light-Emitting Semiconductors: Perovskite-Type Sulfide SrHfS$_3$. *J. Am. Chem. Soc.* **2019,** *141*, 5343-5349.

33. Wang, H.; Gou, G.; Li, J., Ruddlesden–Popper perovskite sulfides A$_3$B$_2$S$_7$: A new family of ferroelectric photovoltaic materials for the visible spectrum. *Nano Energy* **2016,** *22*, 507-513.

34. Niu, S.; Sarkar, D.; Williams, K.; Zhou, Y.; Li, Y.; Bianco, E.; Huyan, H.; Cronin, S. B.; McConney, M. E.; Haiges, R.; Jaramillo, R.; Singh, D. J.; Tisdale, W. A.; Kapadia, R.; Ravichandran, J., Optimal Bandgap in a 2D Ruddlesden–Popper Perovskite Chalcogenide for Single-Junction Solar Cells. *Chem. Mater.* **2018,** *30*, 4882-4886.

35. Cen, Y.-l.; Shi, J.-j.; Zhang, M.; Wu, M.; Du, J.; Guo, W.-h.; Liu, S.-m.; Han, S.-p.; Zhu, Y.-h., Design of Lead-Free and Stable Two-Dimensional Dion–Jacobson-Type Chalcogenide Perovskite A′La$_2$B$_3$S$_{10}$ (A′ = Ba/Sr/Ca; B = Hf/Zr) with Optimal Band Gap, Strong Optical Absorption, and High Efficiency for Photovoltaics. *Chem. Mater.* **2020,** *32*, 2450-2460.

36. Swarnkar, A.; Mir, W. J.; Chakraborty, R.; Jagadeeswararao, M.; Sheikh, T.; Nag, A., Are Chalcogenide Perovskites an Emerging Class of Semiconductors for Optoelectronic Properties and Solar Cell? *Chem. Mater.* **2019,** *31*, 565-575.

37. Wei, X.; Hui, H.; Zhao, C.; Deng, C.; Han, M.; Yu, Z.; Sheng, A.; Roy, P.; Chen, A.; Lin, J.; Watson, D. F.; Sun, Y.-Y.; Thomay, T.; Yang, S.; Jia, Q.; Zhang, S.; Zeng, H., Realization of BaZrS$_3$ chalcogenide perovskite thin films for optoelectronics. *Nano Energy* **2020,** *68*, 104317.

38. Comparotto, C.; Davydova, A.; Ericson, T.; Riekehr, L.; Moro, M. V.; Kubart, T.; Scragg, J., Chalcogenide Perovskite BaZrS$_3$: Thin Film Growth by Sputtering and Rapid Thermal Processing. *ACS Appl. Energy Mater.* **2020,** *3*, 2762-2770.

39. Ahn, N.; Son, D.-Y.; Jang, I.-H.; Kang, S. M.; Choi, M.; Park, N.-G., Highly Reproducible Perovskite Solar Cells with Average Efficiency of 18.3% and Best

Efficiency of 19.7% Fabricated via Lewis Base Adduct of Lead(II) Iodide. *J. Am. Chem. Soc.* **2015,** *137*, 8696-8699.

40. Eickhoff, T.; Grosse, P.; Theiss, W., Diffuse reflectance spectroscopy of powders. *Vib. Spectrosc.* **1990,** *1*, 229-233.

41. Corsepius, N. C.; DeVore, T. C.; Reisner, B. A.; Warnaar, D. L., Using Variable Temperature Powder X-ray Diffraction To Determine the Thermal Expansion Coefficient of Solid MgO. *J. Chem. Educ.* **2007,** *84*, 818.

42. Ni, J. E.; Case, E. D.; Schmidt, R. D.; Wu, C.-I.; Hogan, T. P.; Trejo, R. M.; Kirkham, M. J.; Lara-Curzio, E.; Kanatzidis, M. G., The thermal expansion coefficient as a key design parameter for thermoelectric materials and its relationship to processing-dependent bloating. *J. Mater. Sc.* **2013,** *48*, 6233-6244.

43. Osei-Agyemang, E.; Adu, C. E.; Balasubramanian, G., Ultralow lattice thermal conductivity of chalcogenide perovskite $CaZrSe_3$ contributes to high thermoelectric figure of merit. *npj Comput. Mater.* **2019,** *5*, 116.

44. Osei-Agyemang, E.; Balasubramanian, G., Understanding the Extremely Poor Lattice Thermal Transport in Chalcogenide Perovskite $BaZrS_3$. *ACS Appl. Energy Mater.* **2020,** *3*, 1139-1144.

45. Kuvarega, A. T.; Krause, R. W. M.; Mamba, B. B., Nitrogen/Palladium-Codoped TiO2 for Efficient Visible Light Photocatalytic Dye Degradation. *J Phys. Chem. C* **2011,** *115*, 22110-22120.

46. Zhang, Z.; Liang, Y.; Huang, H.; Liu, X.; Li, Q.; Chen, L.; Xu, D., Stable and Highly Efficient Photocatalysis with Lead-Free Double-Perovskite of $Cs_2AgBiBr_6$. *Angew. Chem. Int. Ed.* **2019,** *58*, 7263-7267.

47. Talapin, D. V.; Lee, J. S.; Kovalenko, M. V.; Shevchenko, E. V., Prospects of colloidal nanocrystals for electronic and optoelectronic applications. *Chem. Rev.* **2010,** *110*, 389-458.

48. Muñoz Iii, S. B.; Daifuku, S. L.; Sears, J. D.; Baker, T. M.; Carpenter, S. H.; Brennessel, W. W.; Neidig, M. L., The N-Methylpyrrolidone (NMP) Effect in Iron-Catalyzed Cross-Coupling with Simple Ferric Salts and MeMgBr. *Angew. Chem. Int. Ed.* **2018,** *57*, 6496-6500.

49. Ding, K.; Zannat, F.; Morris, J. C.; Brennessel, W. W.; Holland, P. L., Coordination of N-methylpyrrolidone to iron(II). *J. Organomet. Chem.* **2009,** *694*, 4204-4208.

50. Zhang, X.; Lai, Z.; Liu, Z.; Tan, C.; Huang, Y.; Li, B.; Zhao, M.; Xie, L.; Huang, W.; Zhang, H., A Facile and Universal Top-Down Method for Preparation of Monodisperse Transition-Metal Dichalcogenide Nanodots. *Angew. Chem. Int. Ed.* **2015,** *54*, 5425-5428.

51. Ravi, V. K.; Markad, G. B.; Nag, A., Band Edge Energies and Excitonic Transition Probabilities of Colloidal $CsPbX_3$ (X = Cl, Br, I) Perovskite Nanocrystals. *ACS Energy Lett.* **2016,** *1*, 665-671.

52. Swarnkar, A.; Chulliyil, R.; Ravi, V. K.; Irfanullah, M.; Chowdhury, A.; Nag, A., Colloidal $CsPbBr_3$ Perovskite Nanocrystals: Luminescence beyond Traditional Quantum Dots. *Angew. Chem. Int. Ed.* **2015,** *54*, 15424-15428.

53. Bi, Y.; Yuan, Y.; Exstrom, C. L.; Darveau, S. A.; Huang, J., Air Stable, Photosensitive, Phase Pure Iron Pyrite Nanocrystal Thin Films for Photovoltaic Application. *Nano Lett.* **2011,** *11*, 4953-4957.

54. Stolle, C. J.; Panthani, M. G.; Harvey, T. B.; Akhavan, V. A.; Korgel, B. A., Comparison of the Photovoltaic Response of Oleylamine and Inorganic Ligand-Capped $CuInSe_2$ Nanocrystals. *ACS Appl. Mater. Interfaces* **2012,** *4*, 2757-2761.

Thesis Summary and

Future Directions

Thesis Summary:

This thesis mainly discussed about the optoelectronic parameters, surface composition and strategy for providing stability to colloidal $CsPbX_3$ (X= Cl, Br, I) perovskite nanocrystals (NCs). These NCs have emerged as exciting material for optoelectronic applications because of their defect tolerant nature and thus reaching photoluminescence (PL) quantum yield near unity. One of the major problems that the $CsPbX_3$ NCs face is their instability in different reactive environments. A major portion of this thesis is employed on improving the stability of $CsPbX_3$ NCs by understanding and optimizing their surface chemistry. Thereafter, we introduced a new semiconducting material, $BaZrS_3$ chalcogenide perovskite NCs, which is non-toxic, stable and shows promising optoelectronic activity.
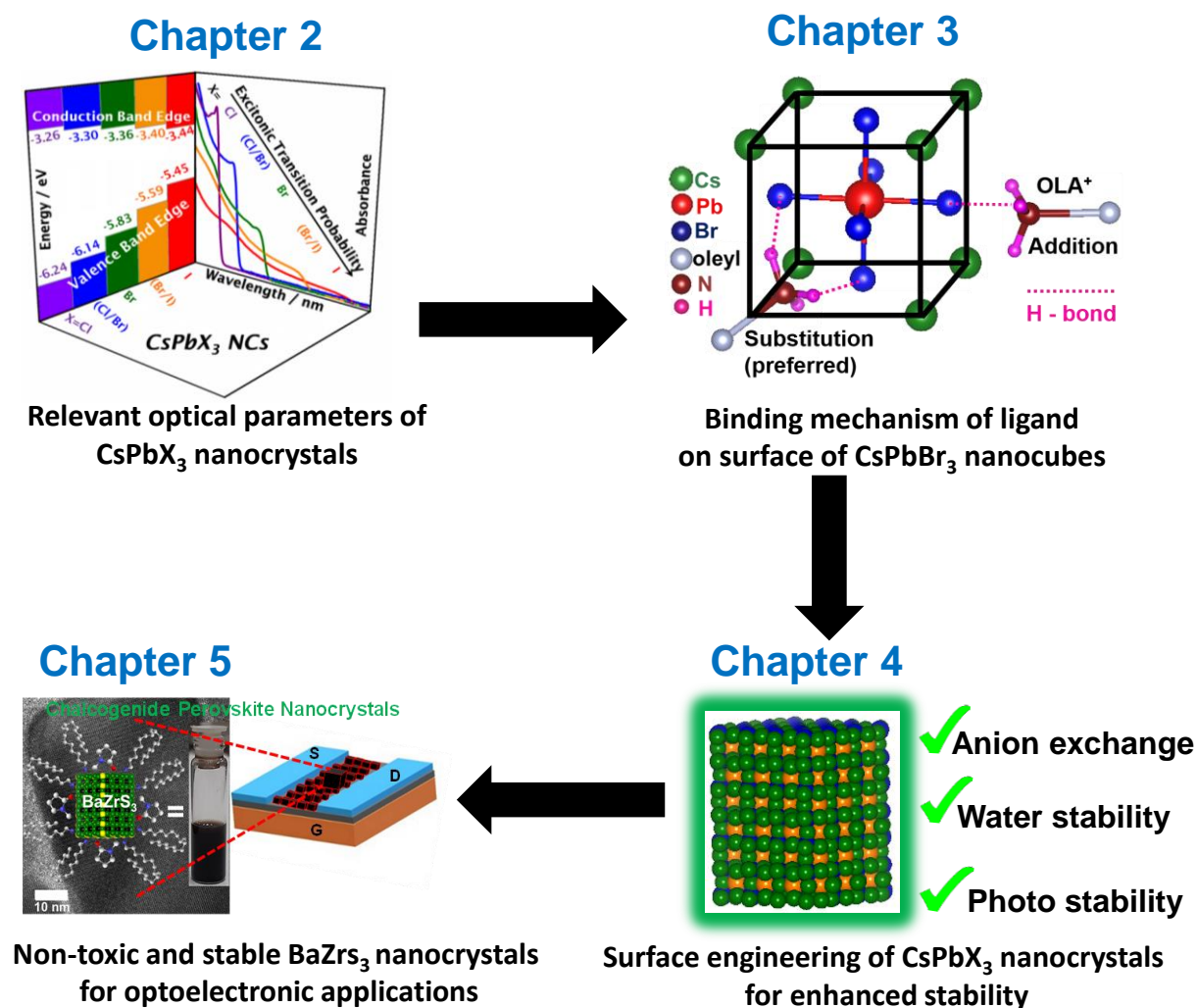
Figure F.1: Graphical summary of this thesis, starting from Chapter 2 to Chapter 5.

At first, we explored the challenges and opportunities in synthesizing $CsPbX_3$ NCs, followed by elucidation of important physical parameters like band edge energies and optical transition probabilities for different halide compositions. Subsequently, a variety of experimental and theoretical techniques are used to understand the nature of binding of organic ligands on the surface of $CsPbBr_3$ nanocubes. Relying on the understanding of this surface chemistry, we have developed two approaches to encapsulate $CsPbX_3$ NCs, thus improving their stability. In the first approach, $CsPbX_3$ NCs are capped with the $PbSO_4$-Oleate which prevents unwanted anion exchange between $CsPbX_3$ NCs with different halide (X) anions. Films of $PbSO_4$-Oleate capped $CsPbI_3$ NCs are then coated on another film of $PbSO_4$-Oleate $CsPbBr_3$ (or any other X) NCs by electrophoretic deposition method, without the exchange of halide ions between the two films. This suppression of anion exchange in films allowed us to tune the band gap of different films, achieving optically pumped white light emitting diode. The second surface coating approach is to prepare $CsPbBr_3$/ZnS core/shell structure, where the crystalline shell enhances the moisture/water stability of the NCs.

In the last chapter, a new kind of perovskite NCs, namely $BaZrS_3$ chalcogenide perovskite NCs are explored. Compared to their lead-halide counterparts, these NCs promise better stability and are environmentally benign. $BaZrS_3$ NCs are synthesized using solid-state method and then the surface of $BaZrS_3$ NCs are decorated appropriately achieving solution processed thin films with reasonably good carrier mobility.

From the data presented in this thesis, some key results of this thesis are:

1. Band edge energies and excitonic transition probability of $CsPbX_3$ NCs:

A trend in shift of bandgap of in $CsPbX_3$ NCs is explained by measuring valence band maxima (VBM) and conduction band minima (CBM) energy levels. Experimentally, it is shown that the halide contributes largely to the VBM and have little contribution to the CBM. Similarly, the measurement of the excitonic transition probabilities for different halide composition of $CsPbX_3$ NCs shows a decreasing trend from Cl to Br to I which is in support of observation of decreasing binding energies and increasing dielectric constant.

2. Unusual mechanism of binding of organic ligand to $CsPbBr_3$ NCs surface:

A new understanding of the binding of organic ligand on the surface of the $CsPbBr_3$ NCs is proposed in this thesis work. It is found that the oleylammonium ions act as binding ligands not by conventional adsorption mechanism but by substitution mechanism. It replaces some Cs^+ ions form the surface and substitute itself to have more hydrogen bonds with the Br^- on the surface and thus adopting more thermodynamically stable structure.

3. Encapsulation of $CsPbX_3$ NCs to overcome anion exchange and water degradation.

Two approaches have been shown in this thesis work for the encapsulation of the $CsPbX_3$ NCs. In the first approach, $CsPbX_3$ NCs are capped with $PbSO_4$-Oleate. These surface modified NCs show suppressed anion exchange compared to pristine $CsPbX_3$ NCs without any detrimental effect on their optoelectronic properties. Capping with $PbSO_4$-Oleate of $CsPbX_3$ NCs also enables electrophoretic deposition of these NCs on the electrodes. The suppression of anion exchange has direct application in tandem solar cell or layered emissive layers to obtain gamut of color including white light.

In the second approach, a core/shell type structure of $CsPbBr_3$/ZnS NCs has been synthesized having type II band structure. This shows enhanced water and light stability compared to pristine $CsPbX_3$ NCs. The enhancement in water and light stability would be next step for researchers to look for their applications in photocatalysis including water splitting reactions.

4. Non-toxic and stable $BaZrS_3$ NCs for thin film devices:

An environmentally benign and inherently more stable chalcogenide perovskite, $BaZrS_3$ NCs are synthesized and made into colloidal dispersion. To the best of our knowledge, this marks the first report of synthesizing colloidal dispersion of $BaZrS_3$ NCs. These NCs are then used for the fabrication of thin films and its related devices like field effect transistor (FET) and solar cell. This advancement in making good quality thin films would encourage future work to look into chalcogenide perovskite for possible optoelectronic applications.

Future Directions:

1. Opportunities for CsPbX$_3$ NCs:

A. Fabrication of blue light emitting diodes (LEDs):

One of the most active research problems right now in the field of CsPbX$_3$ NCs is to increase the efficiency and stability of blue LEDs. The green and red LEDs based on CsPbX$_3$ NCs have reached an external quantum efficiency (EQE) of 20 %, which is closer to their theoretical limit.[1, 2] However, the EQE of perovskite based blue LEDs is less than 10 %.[3-5] To obtain blue light emission, mixed halide Cl/Br composition is used which shows light and electric field induced phase segregation.[6, 7] This segregation causes different chloride and bromide rich region leading to impurity in the emitting color.
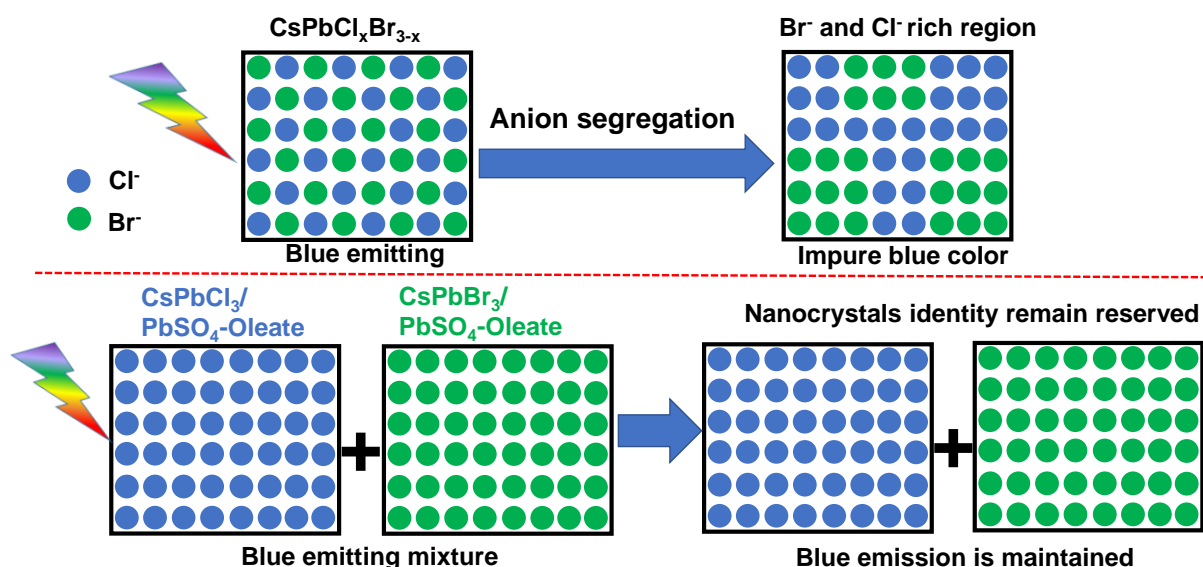
Figure F.2: Schematic showing anion segregation in case of pristine mixed halide NC leading to impurity in blue color. However, this can be avoided in case of mixture of CsPbCl$_3$ and CsPbBr$_3$ NCs used for blue emission capped with PbSO$_4$-Oleate.

One way to overcome this problem is with our approach of PbSO$_4$-Oleate capping of CsPbX$_3$ NCs as discussed in Chapter 4A. There we have shown that blue light can be achieved in colloidal dispersion as well in films by having a mixture of PbSO$_4$-Oleate capped, CsPbCl$_3$ and CsPbBr$_3$ NCs in appropriate ratio. Pure PbSO$_4$-Oleate capped CsPbCl$_3$ NCs (size ~ 11 nm) would have PL peak at 410 nm and pure PbSO$_4$-Oleate capped CsPbBr$_3$ NCs (size ~ 11 nm) would have PL peak at 515 nm. So, a mixture of these samples would have resultant PL somewhere in blue region. By carefully

optimizing the ratio of $PbSO_4$-Oleate capped, $CsPbCl_3$ NCs and $CsPbBr_3$ NCs it is possible to tune the PL peak all the way from 410 nm to 515 nm. We believe, this would be a novel approach as it can mitigate the problem of anion segregation as the NCs now maintain their individual identity without showing anion exchange or segregation.

B. Application in photocatalysis:

Lead halide perovskites have potential as photocatalysts because of the properties like high absorption coefficient with easily tunable bandgap and long charge carrier diffusion length.[8-11] There are some reports for the use of $CsPbBr_3$ NCs for photocatalytic CO_2 reduction,[12-14] and hybrid halide perovskite for splitting of HI[15, 16] and selective oxidation of alcohols.[17] However, the instability problem of lead halide perovskites in water makes it unsuitable for water splitting reaction and other aqueous based photocatalysis reactions.
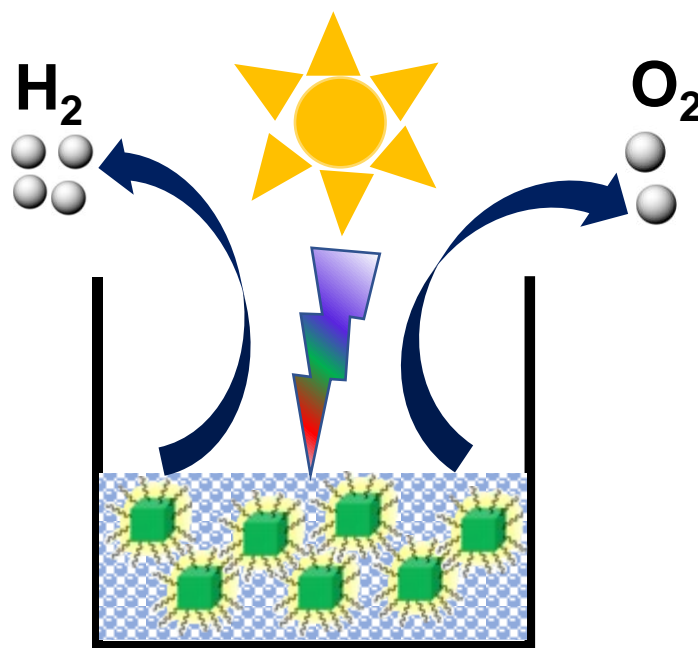
Figure F.3: Schematic showing application of $CsPbBr_3$/ZnS core/shell type NCs for photocatalytic water splitting reaction.

As shown in Chapter 4B, the $CsPbBr_3$/ZnS core/shell type NCs have enhanced stability in water. This makes them desirable for their use as photocatalysts in aqueous system including water splitting reactions. Also, the $CsPbBr_3$/ZnS core/shell NCs can shuttle the charge across the interface which was earlier a problem for other types of $CsPbBr_3$ encapsulation with silica[18] or polymer matrixes[19].

2. Opportunities for chalcogenide perovskite NCs:

A. Solar cells fabrication:

In Chapter 5 of this thesis, we made an attempt to make solar cell device using $BaZrS_3$ NCs. This was motivated by the fact that we were able to get colloidal dispersion of $BaZrS_3$ NCs which then can be used for making thin films. Also, the initial display of reasonable mobility values obtained from the FET devices suggested that it has a potential for the solar cell devices. However, the efficiency value that we got from our initial fabrication of solar cell devices is low. We suspect two main reasons behind it:

1. Improper washing of the $BaZrS_3$ NCs: N-methyl-2-pyrrolidinone and oleylamine as ligands are used for obtaining the colloidal dispersion which are then used for making thin films. This might cause problem in removing them from the NC surface and ultimately affecting the charge carrier transport. We believe that a better ligand for obtaining dispersion or better washing method to remove these long chain ligands would improve the efficiency of the fabricated solar cell device.

2. The device structure: The device stricture we followed is similar to that of lead halide perovskite based solar cell devices, where TiO_2 and spiro-OMeTAD are used as charge transport layers. We believe optimization in the device structure would further improve the efficiency.
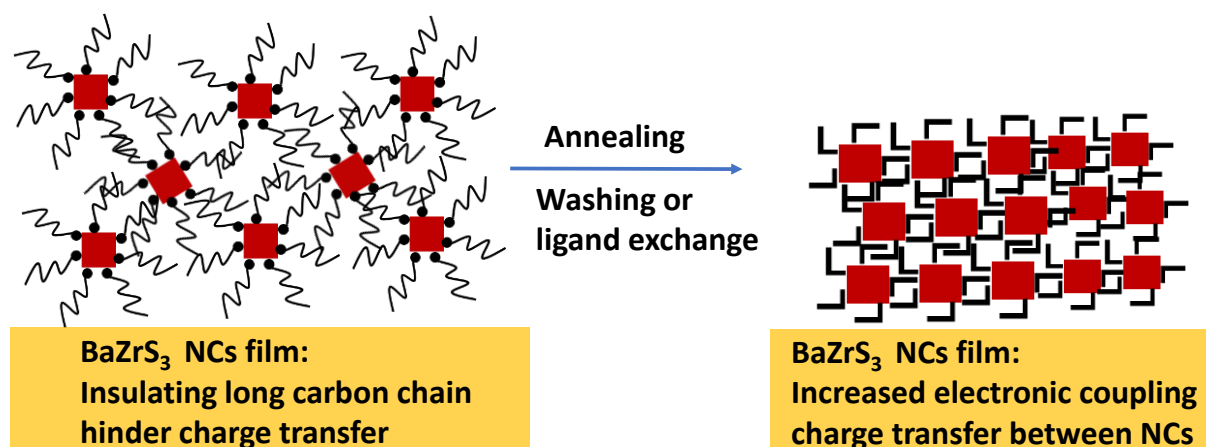
Figure F.4: $BaZrS_3$ NCs capped with long organic carbon chain ligand inhibiting charge transfer between NCs while proper annealing or washing or ligand exchange with shorter ligand would increase electronic coupling allowing efficient charge transfer between NCs.

B. Development of one step colloidal NCs:

Chalcogenide perovskite, $BaZrS_3$ is theoretically predicted to have optoelectronic properties on par with the lead halide perovskites. This is in alignment with their direct bandgap nature and high absorption coefficient. But it does not reflect in its PL property which indicates presence of defects, causing non radiative recombination of charge carriers. We observed that the PL response of $BaZrS_3$ NCs after modifying its surface with N-methyl-2-pyrrolidinone and oleylamine increases compared to the powder of $BaZrS_3$ NCs suggesting passivation of surface defects.

Ligand assisted colloidal synthesis is one of the prominent ways to make semiconductor NCs. It not only provides a great control over the size and shape but also passivates the defects by the ligands employed. This usually leads to high PL efficiency because of passivation of surface defects along with increased overlap between electron and hole wave functions owing to quantum confinement effect. Till now there is no such report on colloidal synthesis of $BaZrS_3$ NCs. We do believe that by appropriate choice of reactive precursor and the ligands, the colloidal synthesis of $BaZrS_3$ NCs would be feasible. This would allow researchers to study fundamental properties like quantum confinement effect on $BaZrS_3$ NCs along with their potential optoelectronic applications.
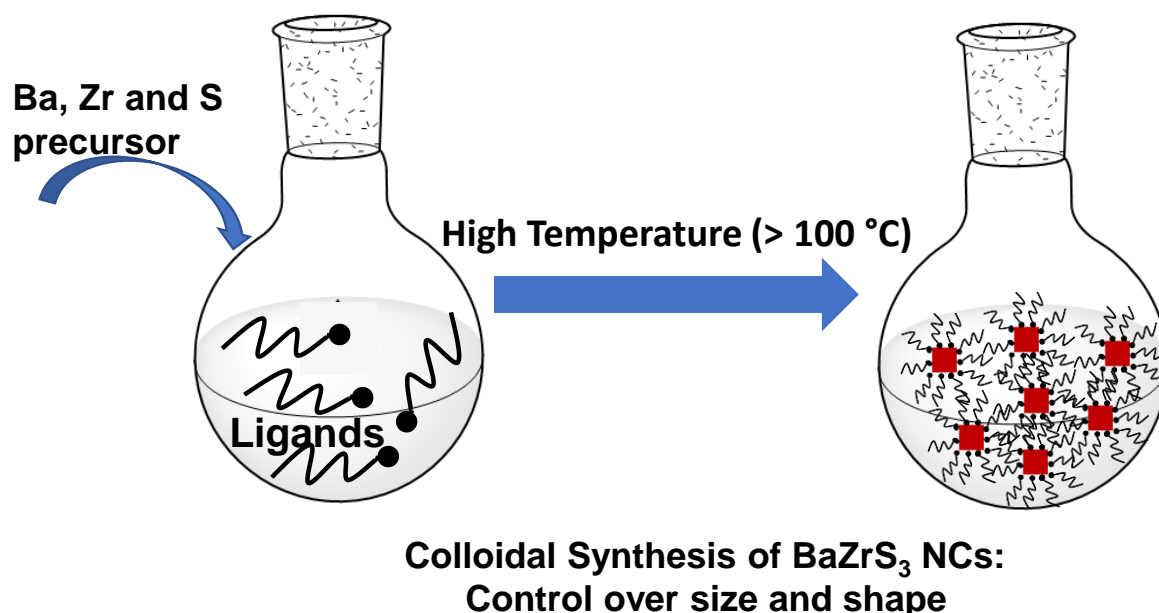
Figure F.5: Ligand assisted colloidal synthesis of $BaZrS_3$ NCs would allow control over size and shape thus control over optoelectronic properties.

References:

1. Lin, K.; Xing, J.; Quan, L. N.; de Arquer, F. P. G.; Gong, X.; Lu, J.; Xie, L.; Zhao, W.; Zhang, D.; Yan, C.; Li, W.; Liu, X.; Lu, Y.; Kirman, J.; Sargent, E. H.; Xiong, Q.; Wei, Z., Perovskite light-emitting diodes with external quantum efficiency exceeding 20 per cent. *Nature* **2018,** *562*, 245-248.

2. Chiba, T.; Hayashi, Y.; Ebe, H.; Hoshi, K.; Sato, J.; Sato, S.; Pu, Y.-J.; Ohisa, S.; Kido, J., Anion-exchange red perovskite quantum dots with ammonium iodine salts for highly efficient light-emitting devices. *Nat. Photon.* **2018,** *12*, 681-687.

3. Liu, Y.; Cui, J.; Du, K.; Tian, H.; He, Z.; Zhou, Q.; Yang, Z.; Deng, Y.; Chen, D.; Zuo, X.; Ren, Y.; Wang, L.; Zhu, H.; Zhao, B.; Di, D.; Wang, J.; Friend, R. H.; Jin, Y., Efficient blue light-emitting diodes based on quantum-confined bromide perovskite nanostructures. *Nat. Photon.* **2019,** *13*, 760-764.

4. Li, Z.; Chen, Z.; Yang, Y.; Xue, Q.; Yip, H.-L.; Cao, Y., Modulation of recombination zone position for quasi-two-dimensional blue perovskite light-emitting diodes with efficiency exceeding 5%. *Nat. Commun.* **2019,** *10*, 1027.

5. Vashishtha, P.; Ng, M.; Shivarudraiah, S. B.; Halpert, J. E., High Efficiency Blue and Green Light-Emitting Diodes Using Ruddlesden–Popper Inorganic Mixed Halide Perovskites with Butylammonium Interlayers. *Chem. Mater.* **2019,** *31*, 83-89.

6. Li, G.; Rivarola, F. W. R.; Davis, N. J. L. K.; Bai, S.; Jellicoe, T. C.; de la Peña, F.; Hou, S.; Ducati, C.; Gao, F.; Friend, R. H.; Greenham, N. C.; Tan, Z.-K., Highly Efficient Perovskite Nanocrystal Light-Emitting Diodes Enabled by a Universal Crosslinking Method. *Adv. Mater.* **2016,** *28*, 3528-3534.

7. Brennan, M. C.; Draguta, S.; Kamat, P. V.; Kuno, M., Light-Induced Anion Phase Segregation in Mixed Halide Perovskites. *ACS Energy Lett.* **2018,** *3*, 204-213.

8. He, M.; Zheng, D.; Wang, M.; Lin, C.; Lin, Z., High efficiency perovskite solar cells: from complex nanostructure to planar heterojunction. *J. Mater. Chem. A* **2014,** *2*, 5994-6003.

9. Kazim, S.; Nazeeruddin, M. K.; Grätzel, M.; Ahmad, S., Perovskite as light harvester: a game changer in photovoltaics. *Angew. Chem. Int. Ed.* **2014,** *53*, 2812-2824.

10. Wu, K.; Liang, G.; Shang, Q.; Ren, Y.; Kong, D.; Lian, T., Ultrafast Interfacial Electron and Hole Transfer from $CsPbBr_3$ Perovskite Quantum Dots. *J. Am. Chem. Soc.* **2015,** *137*, 12792-12795.

11. Li, X.; Wu, Y.; Zhang, S.; Cai, B.; Gu, Y.; Song, J.; Zeng, H., $CsPbX_3$ Quantum Dots for Lighting and Displays: Room-Temperature Synthesis, Photoluminescence Superiorities, Underlying Origins and White Light-Emitting Diodes. *Adv. Funct. Mater.* **2016,** *26*, 2435-2445.

12. Xu, Y.-F.; Yang, M.-Z.; Chen, B.-X.; Wang, X.-D.; Chen, H.-Y.; Kuang, D.-B.; Su, C.-Y., A $CsPbBr_3$ Perovskite Quantum Dot/Graphene Oxide Composite for Photocatalytic CO_2 Reduction. *J. Am. Chem. Soc.* **2017,** *139*, 5660-5663.

13. Kong, Z.-C.; Liao, J.-F.; Dong, Y.-J.; Xu, Y.-F.; Chen, H.-Y.; Kuang, D.-B.; Su, C.-Y., Core@Shell $CsPbBr_3$@Zeolitic Imidazolate Framework Nanocomposite for Efficient Photocatalytic CO_2 Reduction. *ACS Energy Lett.* **2018,** *3*, 2656-2662.

14. Shyamal, S.; Dutta, S. K.; Das, T.; Sen, S.; Chakraborty, S.; Pradhan, N., Facets and Defects in Perovskite Nanocrystals for Photocatalytic CO_2 Reduction. *J. Phys. Chem. Lett.* **2020,** *11*, 3608-3614.

15. Park, S.; Chang, W. J.; Lee, C. W.; Park, S.; Ahn, H.-Y.; Nam, K. T., Photocatalytic hydrogen generation from hydriodic acid using methylammonium lead iodide in dynamic equilibrium with aqueous solution. *Nat. Energy* **2016,** *2*, 16185.

16. Wang, X.; Wang, H.; Zhang, H.; Yu, W.; Wang, X.; Zhao, Y.; Zong, X.; Li, C., Dynamic Interaction between Methylammonium Lead Iodide and TiO_2 Nanocrystals Leads to Enhanced Photocatalytic H_2 Evolution from HI Splitting. *ACS Energy Lett.* **2018,** *3*, 1159-1164.

17. Huang, H.; Yuan, H.; Janssen, K. P. F.; Solís-Fernández, G.; Wang, Y.; Tan, C. Y. X.; Jonckheere, D.; Debroye, E.; Long, J.; Hendrix, J.; Hofkens, J.; Steele, J. A.; Roeffaers, M. B. J., Efficient and Selective Photocatalytic Oxidation of Benzylic Alcohols with Hybrid Organic–Inorganic Perovskite Materials. *ACS Energy Lett.* **2018,** *3*, 755-759.

18. Wang, H.-C.; Lin, S.-Y.; Tang, A.-C.; Singh, B. P.; Tong, H.-C.; Chen, C.-Y.; Lee, Y.-C.; Tsai, T.-L.; Liu, R.-S., Mesoporous Silica Particles Integrated with All-Inorganic $CsPbBr_3$ Perovskite Quantum-Dot Nanocomposites (MP-PQDs) with High

Stability and Wide Color Gamut Used for Backlight Display. *Angew. Chem. Int. Ed.* **2016,** *55*, 7924-7929.

19. Huang, H.; Chen, B.; Wang, Z.; Hung, T. F.; Susha, A. S.; Zhong, H.; Rogach, A. L., Water resistant $CsPbX_3$ nanocrystals coated with polyhedral oligomeric silsesquioxane and their use as solid state luminophores in all-perovskite white light-emitting devices. *Chem. Sci.* **2016,** *7*, 5699-5703.

List of All Publications

Included in the Thesis:

- **Ravi, V. K.**; Markad, G. B.; Nag, A. Band Edge Energies and Excitonic Transition Probabilities of Colloidal $CsPbX_3$ (X = Cl, Br, I) Perovskite Nanocrystals. *ACS Energy Lett.* **2016,** 1, 665−671.

- **Ravi, V. K.;** Santra, P. K.; Joshi, N.; Chugh, J.; Singh, S. K.; Rensmo, H.; Ghosh, P.; Nag, A. Origin of Substitution Mechanism for the Binding of Organic Ligands on the Surface of $CsPbBr_3$ Perovskite Nanocubes. *J. Phys. Chem. Lett.* **2017,** 8, 4988-4994.

- **Ravi, V. K.**; Scheidt, R. A.; Nag, A.; Kuno, M.; Kamat, P. V. To Exchange or Not to Exchange. Suppressing Anion Exchange in Cesium Lead Halide Perovskites with $PbSO_4$-Oleate Capping. *ACS Energy Lett.* **2018,** 3, 1049−1055.

- **Ravi, V. K.**; Scheidt, R. A.; DuBose, J.; Kamat, P. V. Hierarchical Arrays of Cesium Lead Halide Perovskite Nanocrystals through Electrophoretic Deposition. *J. Am. Chem. Soc.* **2018,** 140, 8887−8894.

- **Ravi, V. K.**; Saikia, S.; Yadav, S.; Nawale, V. V.; Nag, A. $CsPbBr_3$/ZnS Core/Shell Type Nanocrystals for Enhancing Luminescence Lifetime and Water Stability. *ACS Energy Lett.* **2020,** 5, 1794-1796.

- **Ravi, V. K.**; Yu, S. H.; Rajput, P. K.; Nayak, C.; Bhattacharyya, D.; Chung, D. C.; Nag, A. Colloidal $BaZrS_3$ Chalcogenide Perovskite Nanocrystals for Thin Film Device Fabrication. **(Manuscript submitted)**.

Not Included in the Thesis:

- **Ravi, V. K.**; Swarnkar, A.; Chakraborty, R.; Nag, A. Excellent green but less impressive blue luminescence from $CsPbBr_3$ Perovskite Nanocubes and Nanoplatelets. *Nanotechnology* **2016,** 27, 325708.

List of All Publications

➢ Swarnkar, A.; Chulliyil, R.; **Ravi, V. K**.; Irfanullah, M.; Chowdhury, A.; Nag, A. Colloidal $CsPbBr_3$ Perovskite Nanocrystals: Luminescence Beyond Traditional Quantum Dots. *Angew. Chem., Int. Ed.* **2015,** 54, 15424−15428.

➢ Aneesh, J.; Swarnkar, A.; **Ravi, V. K**.; Sharma, R.; Nag, A.; Adarsh, K.V. Ultrafast Exciton Dynamics in Colloidal $CsPbBr_3$ Nanocrystals: Biexciton Effect and Auger Recombination. *J. Phys. Chem. C* **2017,** 121, 4734−4739**.**

➢ Sarkar, S.; **Ravi, V. K**.; Banerjee, S.; Yettapu, G.V.; Markad, G.B.; Nag, A.; Mandal, P. Terahertz Spectroscopic Probe of Hot Electron and Hole Transfer from Colloidal $CsPbBr_3$ nanocrystals. *Nano Lett.* **2017,** 17, 5402−5407.

➢ Swarnkar, A.; **Ravi, V. K**.; Nag, A. Beyond Colloidal Cesium Lead Halide Perovskite Nanocrystals: Analogous Metal Halides and Doping. *ACS Energy Lett.* **2017,** 2, 1089−1098.

➢ Mondal, A.; Aneesh, J.; **Ravi, V. K**.; Sharma, R.; Mir, W.J.; Beard, M.C..; Nag, A.; Adarsh, K.V. Ultrafast exciton many body interactions and hot-phonon bottleneck in colloidal cesium halide perovskite nanocrystals. *Phys. Rev. B* **2018,** 98, 115418.

➢ Haque, A.; **Ravi, V. K.**; Shankar, G.S.; Sarkar, I.; Nag, A.; Santra, P.K. Internal Heterostructure of Anion-Exchanged Cesium Halide Nanocubes. *J. Phys. Chem. C* **2018,** 122, 13399−13406.

➢ **Ravi, V. K**.; Singhal, N.; Nag, A. Initiation and Future Prospects of Colloidal Metal halide Double Perovskite Nanocrystals: Cs_2AgBiX_6 (X=Cl, Br, I). *J. Mater. Chem. A* **2018,** 6, 21666−21675.

➢ **Ravi, V. K**.; Mondal, B.; Nawale, V.; Nag, A. *Don't Let the Lead Out:* New Material Chemistry Approaches for Sustainable Lead Halide Perovskite Solar Cells. **(Manuscript submitted)**

Copyrights and

Permissions

Copyrights and

Permissions

JOHN WILEY AND SONS LICENSE
TERMS AND CONDITIONS

Jul 24, 2020

This Agreement between IISER Pune -- Vikash Ravi ("You") and John Wiley and Sons ("John Wiley and Sons") consists of your license details and the terms and conditions provided by John Wiley and Sons and Copyright Clearance Center.

License Number	4875260961205
License date	Jul 24, 2020
Licensed Content Publisher	John Wiley and Sons
Licensed Content Publication	Israel Journal of Chemistry
Licensed Content Title	Spectroelectrochemistry of Quantum Dots
Licensed Content Author	Alvaro Colina, Aranzazu Heras, Juan V. Perales-Rondon, et al
Licensed Content Date	May 3, 2019
Licensed Content Volume	59
Licensed Content Issue	8
Licensed Content Pages	16
Type of use	Dissertation/Thesis
Requestor type	University/Academic

Format	Print and electronic

Portion	Figure/table

Number of figures/tables	1

Will you be translating?	No

Title	Synthesis, Surface Engineering and Stability of CsPbX3 (X = Cl, Br, I) and BaZrS3 Perovskite Nanocrystals

Institution name	Indian Institute of Science Education and Research, Pune

Expected presentation date	Oct 2020

Portions	Figure 1

Requestor Location	IISER Pune IISER Pune Campus Dr. Homi Bhabha Road Pune, Pune 411008 India Attn: IISER Pune

Publisher Tax ID	EU826007151

Total	0.00 USD

Terms and Conditions

TERMS AND CONDITIONS

This copyrighted material is owned by or exclusively licensed to John Wiley & Sons, Inc. or one of its group companies (each a"Wiley Company") or handled on behalf of a society with which a Wiley Company has exclusive publishing rights in relation to a particular work (collectively "WILEY"). By clicking "accept" in connection with completing this licensing transaction, you agree that the following terms and conditions apply to this transaction (along with the billing and payment terms and conditions established by the Copyright Clearance Center Inc., ("CCC's Billing and Payment terms and conditions"), at the time that

ELSEVIER LICENSE
TERMS AND CONDITIONS

Jul 24, 2020

This Agreement between IISER Pune -- Vikash Ravi ("You") and Elsevier ("Elsevier")
consists of your license details and the terms and conditions provided by Elsevier and
Copyright Clearance Center.

License Number	4875230734488
License date	Jul 24, 2020
Licensed Content Publisher	Elsevier
Licensed Content Publication	Elsevier Books
Licensed Content Title	Handbook of Crystal Growth
Licensed Content Author	Katsuhiro Tomioka,Takashi Fukui
Licensed Content Date	Jan 1, 2015
Licensed Content Pages	45
Start Page	749
End Page	793
Type of Use	reuse in a thesis/dissertation
Portion	figures/tables/illustrations
Number of figures/tables/illustrations	1

Format	both print and electronic
Are you the author of this Elsevier chapter?	No
Will you be translating?	No
Title	Synthesis, Surface Engineering and Stability of CsPbX3 (X = Cl, Br, I) and BaZrS3 Perovskite Nanocrystals
Institution name	Indian Institute of Science Education and Research, Pune
Expected presentation date	Oct 2020
Portions	Figure 1
Requestor Location	IISER Pune IISER Pune Campus Dr. Homi Bhabha Road Pune, Pune 411008 India Attn: IISER Pune
Publisher Tax ID	GB 494 6272 12
Total	0.00 USD

Terms and Conditions

INTRODUCTION

1. The publisher for this copyrighted material is Elsevier. By clicking "accept" in connection with completing this licensing transaction, you agree that the following terms and conditions apply to this transaction (along with the Billing and Payment terms and conditions established by Copyright Clearance Center, Inc. ("CCC"), at the time that you opened your Rightslink account and that are available at any time at http://myaccount.copyright.com).

GENERAL TERMS

2. Elsevier hereby grants you permission to reproduce the aforementioned material subject to the terms and conditions indicated.

3. Acknowledgement: If any part of the material to be used (for example, figures) has appeared in our publication with credit or acknowledgement to another source, permission must also be sought from that source. If such permission is not obtained then that material

THE AMERICAN ASSOCIATION FOR THE ADVANCEMENT OF SCIENCE LICENSE TERMS AND CONDITIONS

Jul 24, 2020

This Agreement between IISER Pune -- Vikash Ravi ("You") and The American Association for the Advancement of Science ("The American Association for the Advancement of Science") consists of your license details and the terms and conditions provided by The American Association for the Advancement of Science and Copyright Clearance Center.

License Number	4875270379692
License date	Jul 24, 2020
Licensed Content Publisher	The American Association for the Advancement of Science
Licensed Content Publication	Science
Licensed Content Title	Hydroxylation of the surface of PbS nanocrystals passivated with oleic acid
Licensed Content Author	Danylo Zherebetskyy,Marcus Scheele,Yingjie Zhang,Noah Bronstein,Christopher Thompson,David Britt,Miquel Salmeron,Paul Alivisatos,Lin-Wang Wang
Licensed Content Date	Jun 20, 2014
Licensed Content Volume	344
Licensed Content Issue	6190
Volume number	344

Issue number	6190
Type of Use	Thesis / Dissertation
Requestor type	Scientist/individual at a research institution
Format	Print and electronic
Portion	Figure
Number of figures/tables	1
Title	Synthesis, Surface Engineering and Stability of CsPbX3 (X = Cl, Br, I) and BaZrS3 Perovskite Nanocrystals
Institution name	Indian Institute of Science Education and Research, Pune
Expected presentation date	Oct 2020
Portions	Figure 2
Requestor Location	IISER Pune IISER Pune Campus Dr. Homi Bhabha Road Pune, Pune 411008 India Attn: IISER Pune
Total	0.00 USD

Terms and Conditions

American Association for the Advancement of Science TERMS AND CONDITIONS

Regarding your request, we are pleased to grant you non-exclusive, non-transferable permission, to republish the AAAS material identified above in your work identified above,

Copyright Clearance Center | Marketplace™

Order Number: 1050536
Order Date: 24 Jul 2020

Payment Information

Vikash Ravi
vikashkumar.ravi@students.iiserpune.ac.in
Payment method: Invoice

Billing Address:
Mr. Vikash Ravi
IISER Pune
IISER Pune Campus
Dr. Homi Bhabha Road
Pune, Pune 411008
India

+91 2025908464
vikashkumar.ravi@students.iiserpune.ac.in

Customer Location:
Mr. Vikash Ravi
IISER Pune
IISER Pune Campus
Dr. Homi Bhabha Road
Pune, Pune 411008
India

Order Details

1. Chemical communications

Billing Status:
Open

Order license ID	1050536-1
Order detail status	Completed
ISSN	1364-548X
Type of use	Republish in a thesis/dissertation
Publisher	ROYAL SOCIETY OF CHEMISTRY
Portion	Image/photo/illustration

0.00 USD
Republication Permission

LICENSED CONTENT

Publication Title	Chemical communications	Country	United Kingdom of Great Britain and Northern Ireland
Author/Editor	Royal Society of Chemistry (Great Britain)	Rightsholder	Royal Society of Chemistry
Date	01/01/1996	Publication Type	e-Journal
Language	English		

REQUEST DETAILS

Portion Type	Image/photo/illustration	Distribution	Worldwide
		Translation	Original language of publication
Number of images / photos / illustrations	1	Copies for the disabled?	No
Format (select all that apply)	Print,Electronic	Minor editing privileges?	Yes
Who will republish the content?	Not-for-profit entity		

Duration of Use	Life of current edition	**Incidental promotional use?**	No
Lifetime Unit Quantity	Up to 499		
Rights Requested	Main product	**Currency**	USD

NEW WORK DETAILS

Title	Synthesis, Surface Engineering and Stability of CsPbX3 (X = Cl, Br, I) and BaZrS3 Perovskite Nanocrystals	**Institution name**	Indian Institute of Science Education and Research Pune
		Expected presentation date	2020-10-01
Instructor name	Dr. Angshuman Nag		

ADDITIONAL DETAILS

The requesting person / organization to appear on the license	Vikash Kumar Ravi

REUSE CONTENT DETAILS

Title, description or numeric reference of the portion(s)	N/A	**Title of the article/chapter the portion is from**	N/A
Editor of portion(s)	N/A	**Author of portion(s)**	Royal Society of Chemistry (Great Britain)
Volume of serial or monograph	N/A		
Page or page range of portion	N/A	**Issue, if republishing an article from a serial**	N/A
		Publication date of portion	1996-01-01

2. Chemical communications

<div style="float:right">

Billing Status:
Open

</div>

Order license ID	1050536-2
Order detail status	Completed
ISSN	1364-548X
Type of use	Republish in a thesis/dissertation
Publisher	ROYAL SOCIETY OF CHEMISTRY
Portion	Image/photo/illustration

0.00 USD
Republication Permission

LICENSED CONTENT

Publication Title	Chemical communications	**Country**	United Kingdom of Great Britain and Northern Ireland
Author/Editor	Royal Society of Chemistry (Great Britain)		
		Rightsholder	Royal Society of Chemistry
Date	01/01/1996	**Publication Type**	e-Journal
Language	English		

REQUEST DETAILS

Portion Type	Image/photo/illustration	**Distribution**	Worldwide

Number of images / photos / illustrations	1	**Translation**	Original language of publication
Format (select all that apply)	Print,Electronic	**Copies for the disabled?**	No
Who will republish the content?	Not-for-profit entity	**Minor editing privileges?**	Yes
Duration of Use	Life of current edition	**Incidental promotional use?**	No
Lifetime Unit Quantity	Up to 999		
Rights Requested	Main product	**Currency**	USD

NEW WORK DETAILS

Title	Synthesis, Surface Engineering and Stability of CsPbX3 (X = Cl, Br, I) and BaZrS3 Perovskite Nanocrystals	**Institution name**	Indian Institute of Science Education and Research, Pune
		Expected presentation date	2020-10-01
Instructor name	Dr. Angshuman Nag		

ADDITIONAL DETAILS

The requesting person / organization to appear on the license	Vikash Kumar Ravi

REUSE CONTENT DETAILS

Title, description or numeric reference of the portion(s)	Fig. 6 Cation exchange mediated synthesis of doped, alloyed, segmented, and core/shell heterostructures.	**Title of the article/chapter the portion is from**	Synthesis of tailor-made colloidal semiconductor heterostructures
		Author of portion(s)	Royal Society of Chemistry (Great Britain)
Editor of portion(s)	N/A		
Volume of serial or monograph	54	**Issue, if republishing an article from a serial**	52
Page or page range of portion	7115	**Publication date of portion**	2018-05-28

Total Items: 2

Subtotal: 0.00 USD

Order Total: 0.00 USD

Copyright Clearance Center | Marketplace™

Order Number: 1050545
Order Date: 24 Jul 2020

Payment Information

Vikash Ravi
vikashkumar.ravi@students.iiserpune.ac.in
Payment method: Invoice

Billing Address:
Mr. Vikash Ravi
IISER Pune
IISER Pune Campus
Dr. Homi Bhabha Road
Pune, Pune 411008
India

+91 2025908464
vikashkumar.ravi@students.iiserpune.ac.in

Customer Location:
Mr. Vikash Ravi
IISER Pune
IISER Pune Campus
Dr. Homi Bhabha Road
Pune, Pune 411008
India

Order Details

1. Dalton transactions

Billing Status:
Open

Order license ID	1050545-1
Order detail status	Completed
ISSN	1477-9234
Type of use	Republish in a thesis/dissertation
Publisher	ROYAL SOCIETY OF CHEMISTRY
Portion	Image/photo/illustration

0.00 USD
Republication Permission

LICENSED CONTENT

Publication Title	Dalton transactions	**Country**	United Kingdom of Great Britain and Northern Ireland
Author/Editor	Royal Society of Chemistry (Great Britain)		
		Rightsholder	Royal Society of Chemistry
Date	01/01/2003		
		Publication Type	e-Journal
Language	English		

REQUEST DETAILS

Portion Type	Image/photo/illustration	**Distribution**	Worldwide
		Translation	Original language of publication
Number of images / photos / illustrations	1		
		Copies for the disabled?	No
Format (select all that apply)	Print,Electronic		
		Minor editing privileges?	Yes
Who will republish the content?	Not-for-profit entity		
		Incidental promotional use?	No
Duration of Use	Life of current edition		

Lifetime Unit Quantity	Up to 999	**Currency**	USD
Rights Requested	Main product		

NEW WORK DETAILS

Title	Synthesis, Surface Engineering and Stability of CsPbX3 (X = Cl, Br, I) and BaZrS3 Perovskite Nanocrystals	**Institution name**	Indian Institute of Science Education and Research, Pune
		Expected presentation date	2020-10-01
Instructor name	Dr. Angshuman Nag		

ADDITIONAL DETAILS

The requesting person / organization to appear on the license	Vikash Kumar Ravi

REUSE CONTENT DETAILS

Title, description or numeric reference of the portion(s)	Fig. 1 Schematic representation of the covalent bond classification. X-type ligands are one-electron donors, L-type ligand are Lewis bases and Z-type ligands are Lewis acids.	**Title of the article/chapter the portion is from**	From ligands to binding motifs and beyond; the enhanced versatility of nanocrystal surfaces
		Author of portion(s)	Royal Society of Chemistry (Great Britain)
Editor of portion(s)	N/A	**Issue, if republishing an article from a serial**	34
Volume of serial or monograph	45	**Publication date of portion**	2016-07-20
Page or page range of portion	13278		

Total Items: 1

Subtotal: 0.00 USD

Order Total: **0.00 USD**

Copyright Clearance Center | Marketplace™

Order Number: 1050589
Order Date: 24 Jul 2020

Payment Information

Vikash Ravi
vikashkumar.ravi@students.iiserpune.ac.in
Payment method: Invoice

Billing Address:
Mr. Vikash Ravi
IISER Pune
IISER Pune Campus
Dr. Homi Bhabha Road
Pune, Pune 411008
India

+91 2025908464
vikashkumar.ravi@students.iiserpune.ac.in

Customer Location:
Mr. Vikash Ravi
IISER Pune
IISER Pune Campus
Dr. Homi Bhabha Road
Pune, Pune 411008
India

Order Details

1. Philosophical transactions

Billing Status:
Open

Order license ID	1050589-1
Order detail status	Completed
ISSN	1471-2962
Type of use	Republish in a thesis/dissertation
Publisher	ROYAL SOCIETY
Portion	Image/photo/illustration

0.00 USD
Republication Permission

LICENSED CONTENT

Publication Title	Philosophical transactions	**Country**	United Kingdom of Great Britain and Northern Ireland
Author/Editor	Royal Society	**Rightsholder**	The Royal Society (U.K.)
Date	01/01/1997	**Publication Type**	e-Journal
Language	English	**URL**	https://royalsociety.org/journals/

REQUEST DETAILS

Portion Type	Image/photo/illustration	**Distribution**	Worldwide
Number of images / photos / illustrations	1	**Translation**	Original language of publication
Format (select all that apply)	Print,Electronic	**Copies for the disabled?**	No
Who will republish the content?	Not-for-profit entity	**Minor editing privileges?**	No

Duration of Use	Life of current edition	**Incidental promotional use?**	No
Lifetime Unit Quantity	Up to 999	**Currency**	USD
Rights Requested	Main product		

NEW WORK DETAILS

Title	Synthesis, Surface Engineering and Stability of CsPbX3 (X = Cl, Br, I) and BaZrS3 Perovskite Nanocrystals	**Institution name**	Indian Institute of Science Education and Research Pune
		Expected presentation date	2020-10-01
Instructor name	Dr. Angshuman Nag		

ADDITIONAL DETAILS

The requesting person / organization to appear on the license	Vikash Kumar Ravi

REUSE CONTENT DETAILS

Title, description or numeric reference of the portion(s)	Figure 1. The LaMer model of nucleation and growth.	**Title of the article/chapter the portion is from**	Continuous-flow hydrothermal synthesis for the production of inorganic nanomaterials.
Editor of portion(s)	N/A		
Volume of serial or monograph	373	**Author of portion(s)**	Royal Society
Page or page range of portion	N/A	**Issue, if republishing an article from a serial**	N/A
		Publication date of portion	2015-12-28

The Royal Society (U.K.) Terms and Conditions

Out of Copyright - any journal requested with a Publication date older than 70 years.

Total Items: 1

           Subtotal: 0.00 USD

Order Total: **0.00 USD**

JOHN WILEY AND SONS LICENSE
TERMS AND CONDITIONS

Jul 24, 2020

This Agreement between IISER Pune -- Vikash Ravi ("You") and John Wiley and Sons ("John Wiley and Sons") consists of your license details and the terms and conditions provided by John Wiley and Sons and Copyright Clearance Center.

License Number	4875320266721
License date	Jul 24, 2020
Licensed Content Publisher	John Wiley and Sons
Licensed Content Publication	Journal of the American Ceramic Society
Licensed Content Title	A Thin Film Approach to Engineering Functionality into Oxides
Licensed Content Author	Mark A. Zurbuchen, Andreas Schmehl, Xiaoqing Pan, et al
Licensed Content Date	Aug 12, 2008
Licensed Content Volume	91
Licensed Content Issue	8
Licensed Content Pages	26
Type of use	Dissertation/Thesis
Requestor type	University/Academic

Format	Print and electronic
Portion	Figure/table
Number of figures/tables	1
Will you be translating?	No
Title	Synthesis, Surface Engineering and Stability of CsPbX3 (X = Cl, Br, I) and BaZrS3 Perovskite Nanocrystals
Institution name	Indian Institute of Science Education and Research, Pune
Expected presentation date	Oct 2020
Portions	Figure 2
Requestor Location	IISER Pune IISER Pune Campus Dr. Homi Bhabha Road Pune, Pune 411008 India Attn: IISER Pune
Publisher Tax ID	EU826007151
Total	0.00 USD

Terms and Conditions

Dear Dr. Kumar Ravi,

Thank you for contacting ACS Publications Support.

Your permission requested is granted and there is no fee for this reuse. In your planned reuse, you must cite the ACS article as the source, add this direct link <https://pubs.acs.org/doi/10.1021/nl5048779>, and include a notice to readers that further permissions related to the material excerpted should be directed to the ACS.

Sincerely,

Budimir Jelic
ACS Publications
Customer Services & Information
Website: https://help.acs.org
Incident Information:

I would like to reuse one of the figure from the given below paper in my introduction part of the thesis. I pledge to give the proper citations and credits.

Details:

Link of the paper: https://pubs.acs.org/doi/10.1021/nl5048779

Title of paper: Nanocrystals of Cesium Lead Halide Perovskites ($CsPbX_3$, X = Cl, Br, and I): Novel Optoelectronic Materials Showing Bright Emission with Wide Color Gamut.

Figure: 1, Figure no 2

Detail Where the content will be used:

Thesis Author: Vikash Kumar Ravi

Title of thesis: Synthesis, Surface Engineering and Stability of $CsPbX_3$ (X = Cl, Br, I) and $BaZrS_3$ Perovskite Nanocrystals

presentation date: October 2020

Institute: IISER Pune

Please grant me permission to do so. I would be very thankful of you for this

Regards

Vikash Kumar ravi

Dear Dr. Kumar Ravi,

Thank you for contacting ACS Publications Support.

Your permission requested is granted and there is no fee for this reuse. In your planned reuse, you must cite the ACS article as the source, add this direct link <https://pubs.acs.org/doi/10.1021/acscentsci.8b00201>, and include a notice readers that further permissions related to the material excerpted should be directed to the ACS.

Sincerely,

Budimir Jelic
ACS Publications
Customer Services & Information
Website: https://help.acs.org

Incident Information:

Incident #:	3698462
Date Created:	2020-07-24T13:50:54
Priority:	3
Customer:	Vikash Kumar Ravi
Title:	Reuse of image for thesis_non profit
Description:	Dear ACS Team,

I would like to reuse one of the figure from the given below paper in my introduction part of the thesis. I pledge to give the proper citations and credits.
Details:
Link of the paper: https://pubs.acs.org/doi/10.1021/acscentsci.8b00201
Title of paper: All-Inorganic Metal Halide Perovskite Nanocrystals: Opportunities and Challenges.
Figure: 1, Figure no 1
Detail Where the content will be used:
Thesis Author: Vikash Kumar Ravi
Title of thesis: Synthesis, Surface Engineering and Stability of CsPbX3 (X = Cl, Br, I) and
BaZrS3 Perovskite Nanocrystals
presentation date: October 2020
Institute: IISER Pune
Please grant me permission to do so. I would be very thankful of you for this
Regards
Vikash Kumar ravi

SPRINGER NATURE LICENSE
TERMS AND CONDITIONS

Jul 24, 2020

This Agreement between IISER Pune -- Vikash Ravi ("You") and Springer Nature ("Springer Nature") consists of your license details and the terms and conditions provided by Springer Nature and Copyright Clearance Center.

License Number	4875330192142
License date	Jul 24, 2020
Licensed Content Publisher	Springer Nature
Licensed Content Publication	Nature Materials
Licensed Content Title	Genesis, challenges and opportunities for colloidal lead halide perovskite nanocrystals
Licensed Content Author	Quinten A. Akkerman et al
Licensed Content Date	Feb 19, 2018
Type of Use	Thesis/Dissertation
Requestor type	non-commercial (non-profit)
Format	print and electronic
Portion	figures/tables/illustrations
Number of figures/tables/illustrations	1
High-res required	no

Will you be translating?	no
Circulation/distribution	500 - 999
Author of this Springer Nature content	no
Title	Synthesis, Surface Engineering and Stability of CsPbX3 (X = Cl, Br, I) and BaZrS3 Perovskite Nanocrystals
Institution name	Indian Institute of Science Education and Research, Pune
Expected presentation date	Oct 2020
Portions	Figure 2
Requestor Location	IISER Pune IISER Pune Campus Dr. Homi Bhabha Road Pune, Pune 411008 India Attn: IISER Pune
Total	0.00 USD

Terms and Conditions

Springer Nature Customer Service Centre GmbH
Terms and Conditions

This agreement sets out the terms and conditions of the licence (the **Licence**) between you and **Springer Nature Customer Service Centre GmbH** (the **Licensor**). By clicking 'accept' and completing the transaction for the material (**Licensed Material**), you also confirm your acceptance of these terms and conditions.

1. Grant of License

1. 1. The Licensor grants you a personal, non-exclusive, non-transferable, world-wide licence to reproduce the Licensed Material for the purpose specified in your order only. Licences are granted for the specific use requested in the order and for no other use, subject to the conditions below.

1. 2. The Licensor warrants that it has, to the best of its knowledge, the rights to license reuse of the Licensed Material. However, you should ensure that the material you are requesting is original to the Licensor and does not carry the copyright of

SPRINGER NATURE LICENSE
TERMS AND CONDITIONS

Jul 24, 2020

This Agreement between IISER Pune -- Vikash Ravi ("You") and Springer Nature ("Springer Nature") consists of your license details and the terms and conditions provided by Springer Nature and Copyright Clearance Center.

License Number	4875331284561
License date	Jul 24, 2020
Licensed Content Publisher	Springer Nature
Licensed Content Publication	Science China Materials
Licensed Content Title	Photo-stability of CsPbBr3 perovskite quantum dots for optoelectronic application
Licensed Content Author	Junsheng Chen 陈俊生 et al
Licensed Content Date	Sep 20, 2016
Type of Use	Thesis/Dissertation
Requestor type	non-commercial (non-profit)
Format	print and electronic
Portion	figures/tables/illustrations
Number of figures/tables/illustrations	1
Will you be translating?	no

Circulation/distribution	500 - 999
Author of this Springer Nature content	no
Title	Synthesis, Surface Engineering and Stability of CsPbX3 (X = Cl, Br, I) and BaZrS3 Perovskite Nanocrystals
Institution name	Indian Institute of Science Education and Research, Pune
Expected presentation date	Oct 2020
Portions	Figure 7
Requestor Location	IISER Pune IISER Pune Campus Dr. Homi Bhabha Road Pune, Pune 411008 India Attn: IISER Pune
Total	0.00 USD

Terms and Conditions

Springer Nature Customer Service Centre GmbH
Terms and Conditions

This agreement sets out the terms and conditions of the licence (the **Licence**) between you and **Springer Nature Customer Service Centre GmbH** (the **Licensor**). By clicking 'accept' and completing the transaction for the material (**Licensed Material**), you also confirm your acceptance of these terms and conditions.

1. Grant of License

1. 1. The Licensor grants you a personal, non-exclusive, non-transferable, world-wide licence to reproduce the Licensed Material for the purpose specified in your order only. Licences are granted for the specific use requested in the order and for no other use, subject to the conditions below.

1. 2. The Licensor warrants that it has, to the best of its knowledge, the rights to license reuse of the Licensed Material. However, you should ensure that the material you are requesting is original to the Licensor and does not carry the copyright of another entity (as credited in the published version).

1. 3. If the credit line on any part of the material you have requested indicates that it was reprinted or adapted with permission from another source, then you should also

Dear Dr. Ravi,

Thank you for contacting ACS Publications Support.

Your permission requested is granted and there is no fee for this reuse. In your planned reuse, you must cite the ACS article as the source, add this direct link https://pubs.acs.org/doi/abs/10.1021/acs.jpcc.7b03389, and include a notice to readers that further permissions related to the material excerpted should be directed to the ACS.

If you have any further queries please do not hesitate to contact us.

Sincerely,
Dimitrije Bozovic
ACS Publications
Customer Services & Information
Website: https://help.acs.org
Incident Information:

Incident #:	3698518
Date Created:	2020-07-24T14:18:24
Priority:	3
Customer:	Vikash Kumar Ravi
Title:	Reuse of image for thesis_non profit
Description:	Dear ACS Team,

I would like to reuse one of the figure from the given below paper in my introduction part of the thesis. I pledge to give the proper citations and credits.
Details:
Link of the paper: https://pubs.acs.org/doi/10.1021/acs.jpcc.7b03389
Title of paper: From CsPbBr3 Nano-Inks to Sintered CsPbBr3–CsPb2Br5 Films via Thermal Annealing: Implications on Optoelectronic Properties.
Figure: 1
Detail Where the content will be used:
Thesis Author: Vikash Kumar Ravi
Title of thesis: Synthesis, Surface Engineering and Stability of CsPbX3 (X = Cl, Br, I) and BaZrS3 Perovskite Nanocrystals
presentation date: October 2020
Institute: IISER Pune
Please grant me permission to do so. I would be very thankful of you for this
Regards
Vikash Kumar ravi

SPRINGER NATURE

Biological impact of lead from halide perovskites reveals the risk of introducing a safe threshold

Author: Junming Li et al

Publication: Nature Communications

Publisher: Springer Nature

Date: Jan 21, 2020

Copyright © 2020, Springer Nature

Creative Commons

Band Edge Energies and Excitonic Transition Probabilities of Colloidal CsPbX3 (X = Cl, Br, I) Perovskite Nanocrystals

Author: Vikash Kumar Ravi, Ganesh B. Markad, Angshuman Nag

Publication: ACS Energy Letters

Publisher: American Chemical Society

Date: Oct 1, 2016

Copyright © 2016, American Chemical Society

PERMISSION/LICENSE IS GRANTED FOR YOUR ORDER AT NO CHARGE

This type of permission/license, instead of the standard Terms & Conditions, is sent to you because no fee is being charged for your order. Please note the following:

- Permission is granted for your request in both print and electronic formats, and translations.
- If figures and/or tables were requested, they may be adapted or used in part.
- Please print this page for your records and send a copy of it to your publisher/graduate school.
- Appropriate credit for the requested material should be given as follows: "Reprinted (adapted) with permission from (COMPLETE REFERENCE CITATION). Copyright (YEAR) American Chemical Society." Insert appropriate information in place of the capitalized words.
- One-time permission is granted only for the use specified in your request. No additional uses are granted (such as derivative works or other editions). For any other uses, please submit a new request.

BACK   CLOSE WINDOW

Origin of the Substitution Mechanism for the Binding of Organic Ligands on the Surface of CsPbBr3 Perovskite Nanocubes

ACS Publications
Most Trusted. Most Cited. Most Read.

Author: Vikash Kumar Ravi, Pralay K. Santra, Niharika Joshi, et al

Publication: Journal of Physical Chemistry Letters

Publisher: American Chemical Society

Date: Oct 1, 2017

Copyright © 2017, American Chemical Society

ACS Publications
Most Trusted. Most Cited. Most Read.

To Exchange or Not to Exchange. Suppressing Anion Exchange in Cesium Lead Halide Perovskites with PbSO4–Oleate Capping

Author: Vikash Kumar Ravi, Rebecca A. Scheidt, Angshuman Nag, et al

Publication: ACS Energy Letters

Publisher: American Chemical Society

Date: Apr 1, 2018

Copyright © 2018, American Chemical Society

PERMISSION/LICENSE IS GRANTED FOR YOUR ORDER AT NO CHARGE

This type of permission/license, instead of the standard Terms & Conditions, is sent to you because no fee is being charged for your order. Please note the following:

- Permission is granted for your request in both print and electronic formats, and translations.
- If figures and/or tables were requested, they may be adapted or used in part.
- Please print this page for your records and send a copy of it to your publisher/graduate school.
- Appropriate credit for the requested material should be given as follows: "Reprinted (adapted) with permission from (COMPLETE REFERENCE CITATION). Copyright (YEAR) American Chemical Society." Insert appropriate information in place of the capitalized words.
- One-time permission is granted only for the use specified in your request. No additional uses are granted (such as derivative works or other editions). For any other uses, please submit a new request.

BACK   CLOSE WINDOW

ACS Publications
Most Trusted. Most Cited. Most Read.

Hierarchical Arrays of Cesium Lead Halide Perovskite Nanocrystals through Electrophoretic Deposition

Author: Vikash Kumar Ravi, Rebecca A. Scheidt, Jeffrey DuBose, et al

Publication: Journal of the American Chemical Society

Publisher: American Chemical Society

Date: Jul 1, 2018

Copyright © 2018, American Chemical Society

Copyright Clearance Center

RightsLink®

Home | Help | Email Support | Sign in | Create Account

CsPbBr3/ZnS Core/Shell Type Nanocrystals for Enhancing Luminescence Lifetime and Water Stability

ACS Publications
Most Trusted. Most Cited. Most Read.

Author: Vikash Kumar Ravi, Sajid Saikia, Shivam Yadav, et al

Publication: ACS Energy Letters

Publisher: American Chemical Society

Date: Jun 1, 2020

Copyright © 2020, American Chemical Society

PERMISSION/LICENSE IS GRANTED FOR YOUR ORDER AT NO CHARGE

This type of permission/license, instead of the standard Terms & Conditions, is sent to you because no fee is being charged for your order. Please note the following:

- Permission is granted for your request in both print and electronic formats, and translations.
- If figures and/or tables were requested, they may be adapted or used in part.
- Please print this page for your records and send a copy of it to your publisher/graduate school.
- Appropriate credit for the requested material should be given as follows: "Reprinted (adapted) with permission from (COMPLETE REFERENCE CITATION). Copyright (YEAR) American Chemical Society." Insert appropriate information in place of the capitalized words.
- One-time permission is granted only for the use specified in your request. No additional uses are granted (such as derivative works or other editions). For any other uses, please submit a new request.

BACK   CLOSE WINDOW